A NONHYDROLYTIC SOLUTION-PHASE SYNTHESIS OF LITHIUM NIOBATE NANOSTRUCTURES

by

Bryan D. Wood
Bachelor of Science, Simon Fraser University 2005

THESIS SUBMITTED IN PARTIAL FULFILLMENT OF THE REQUIREMENTS FOR THE DEGREE OF

MASTER OF SCIENCE

In the
Department of Chemistry

SIMON FRASER UNIVERSITY

Summer 2009

APPROVAL

Name: **Bryan D. Wood**

Degree: **Master of Science**

Title of Thesis: **A Nonhydrolytic Solution-Phase Synthesis of Lithium Niobate Nanostructures**

Examining Committee:

Chair: **Erika Plettner**
Associate Professor

_____

Byron D. Gates
Senior Supervisor
Assistant Professor and Canada Research Chair in Surface Chemistry

_____

Zuo-Guang Ye
Supervisor
Professor & Associate Chair

_____

David Vocadlo
Supervisor
Associate Professor and Canada Research Chair in Chemical Biology

_____

Tim Storr
Internal Examiner
Assistant Professor

Date Defended/Approved: August-12-2009

Declaration of
Partial Copyright Licence

ABSTRACT

A new soft chemical approach to synthesize nanoscale crystals of $LiNbO_3$ has been developed. This technique was developed with the intention of producing a material for use as an optical probe in second harmonic generation microscopy. Nanocrystals of $LiNbO_3$ were synthesized in < 24 h from a single-source metal organic precursor that decomposes at 360 °C in a solution of coordinating molecules. A longer reaction time led to the formation of pronounced rod structures up to 50 nm in length through a process of directed aggregation. The process precursors, products, and by-products are described in detail using a variety of spectroscopic methods in order to elucidate the mechanism of $LiNbO_3$ formation and to evaluate how the process can be further improved.

Keywords: lithium niobate, $LiNbO_3$, solution-phase, nonhydrolytic decomposition, alkoxides, coordinating solutions, nanocrystals, directed aggregation, nonlinear, triphenylphosphine oxide

Subject Terms: solution-phase synthesis, colliod synthesis

TABLE OF CONTENTS

LIST OF FIGURES

LIST OF TABLES

CHAPTER 1 – MOTIVATION FOR THE PURSUIT OF LITHIUM NIOBATE NANOCRYSTALS IN SECOND HARMONIC GENERATION MICROSCOPY

1.1 Introduction

The long-term research goal for this project is to prepare nanocrystalline materials that are capable of efficient second harmonic generation (SHG) at visible wavelengths. These crystals are intended to function as optical probes in a rapidly growing field of laser microscopy. The specific target of this research is to claim a portion of the growing niche among the methods for imaging biological samples and processes *in vivo*.[1, 2] In general, this research also fulfills part of the increasing demand for methods to prepare nanoscale photonic, electronic, and mechanical materials for function in devices. [1, 3-7] This demand stems from the continued miniaturization of devices and their components. In this work, the solution-phase synthesis of $LiNbO_3$ nanocrystals is explored as a method to achieve these objectives. In the following Chapter, the reasons for exploring SHG microscopy will be discussed starting with a brief and simplified introduction to the theory of frequency doubling. The background is then applied more specifically to the case of nanoscaled crystals and how they can be optimized in shape to facilitate SHG efficiency. Finally, this section will close with a description of the structure of $LiNbO_3$, and the reason for its choice among a list of alternative starting materials.

1.2 An Overview of the Processes in Multiphoton Microscopy (MFM)

Several techniques have been coupled with an optical microscope for the contrast enhancement of cellular structures. By far, the most commonly applied technique is two-photon excited fluorescence microscopy (TPEF)[2] that can occur in naturally occurring molecules and tissues such as NADH[3] (nicotinamide adenine dinucleotide) and collagen, respectively. Additional dyes (fluorophores) are usually added because the intrinsic signal strength is typically low. Signal enhancement can be improved by implementing higher concentrations of dyes with better quantum yields. TPEF starts with the simultaneous absorption of two photons, that excites an electron (in the fluorophore) to a higher electronic state (S_2, V_i in **Figure 1.1**). The absorption is then accompanied by a non-radiative internal conversion from the current electronic state to an upper vibrational level of a lower electronic state (e.g., V_3 in S_1). The fluorescence emission results from the energy released as the electron returns to one of the vibrational levels of the original ground state

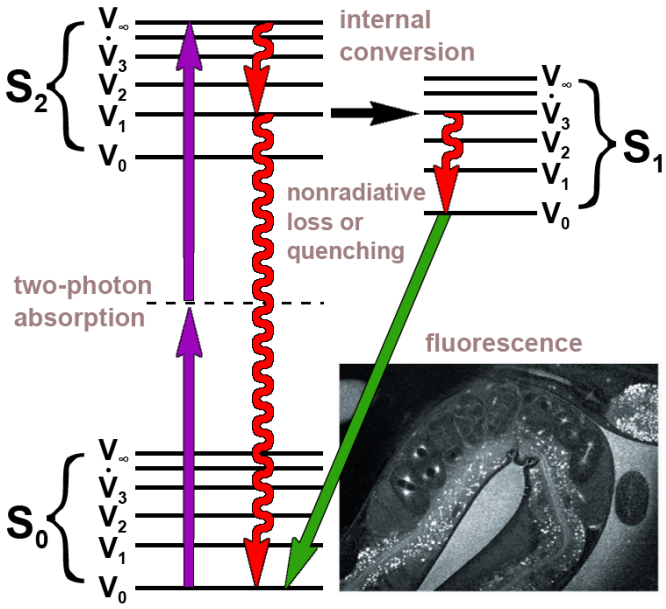

Figure 1.1 **A Jablonski diagram that displays the process of fluorescence. The attached TPEF image was obtained through the use of dyes by Campagnola (reprinted with permission from the Biophysical Society © 2002).[1] Bright areas display the tubulin structures within a worm and eight of its embryos.**

(e.g., S_0, V_0). One of the major problems facing this process is a result of the described fluorescence mechanism. Photonic energy is not conserved in this process because there are several points where energy is lost as heat. Notably, they occur as the electron falls to the lowest vibrational level of the excited state (e.g., S_1,V_0) prior to fluorescence, and to the lowest vibrational level of the ground state. Since this process is happening rapidly in a localized area, local heating occurs. The relatively short excitation wavelengths used in this technique are also more effectively scattered [$I_{scat.} \alpha (I_0/ \lambda^4)$]. Scattered radiation when coupled with heating results in photodegradation of the surrounding tissues and dye molecules. These effects typically appear in the dyes after $10^6 - 10^8$ photons and in less than 10^5 photons for naturally fluorescing host tissues.[4] The resulting tissue damage usually limits the time frame of the analysis and also restricts the technique to use on dead tissue samples. Another disadvantage is that the emission band is broad (up to 100 nm wide).[2,5] If an intrinsic source emits close to that of the chosen fluorophore it becomes difficult to tell them apart (distinguish between the tissues). In addition, as a result of a wide complexity in excitation peak shapes, emission wavelengths, and quantum yields, there is an overwhelming amount of fluorophores available for purchase. The market is flooded with options that can make decisions difficult to make. In short, TPEF provides good emission intensities, but it's application for imaging living cells and real-time biological processes is restricted by unavoidable tissue damage.

Since the initial demonstration of fluorescent semiconducting nanocrystals (a.k.a. quantum dots; QD) there has been a rapid surge in their use for imaging

biological structures by multiphoton fluorescence microscopy (MFM). Its rapid acceptance comes as a result of solving many of the preceding issues in TPEF, including high yields, sharp emission patterns, and a higher damage threshold than organic dyes.[4] Since longer excitation wavelengths can be used, MFM has also been applied to living tissue samples[3] and imaging can be performed for longer periods of time. The origin of an emission from an otherwise inactive bulk semiconductor occurs as a result of nanoscale quantum confinement. The photoexcitation process generates an electron and hole within the semiconductor that are each "confined" to remain in specific (or "quantized") energy levels.

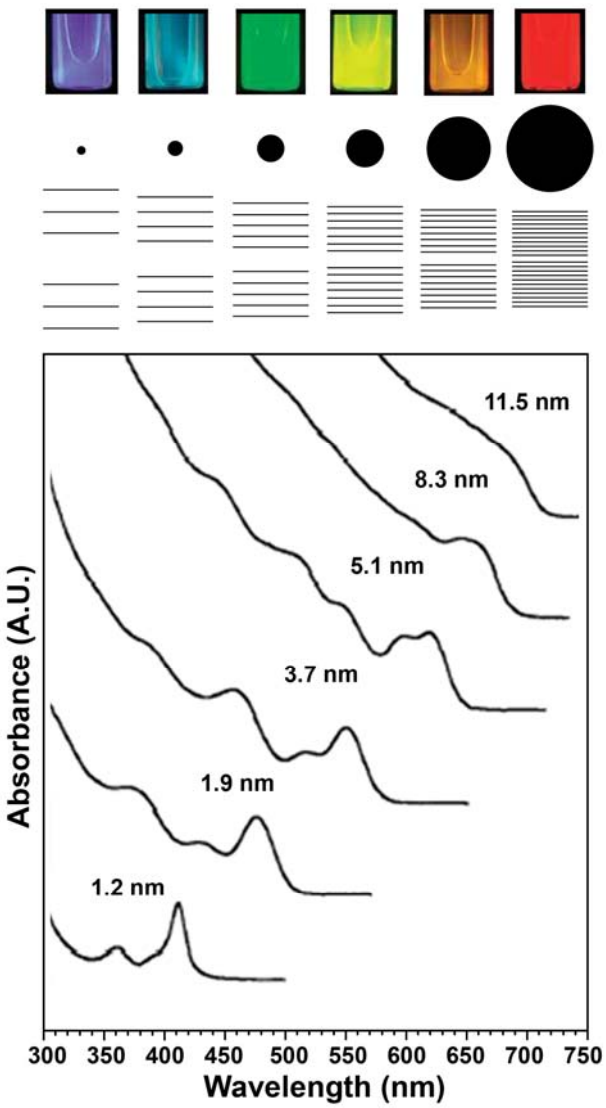

Figure 1.2 **Absorption spectrum of CdSe quantum dots displaying the absorption bands, that then reemit to produce the luminescence shown above. The displayed data is that of Bawendi (spectral data reprinted with permission from the American Chemical Society © 1993).[6] Hypothetical energy level diagrams have also been shown that display a decreasing band-gap as the size of the nanocrystal is increased. The band gap gives rise to the observed fluorescence.**

Quantum confinement does not occur in the case of bulk materials because a photoinduced electron and hole are part of a band that represents the loss of individuality for a number of molecular orbitals. As matter is added and the size of the nanocrystal increases, new energy states are added that cause the HOMO-LUMO (or band-gap) to shrink (**Figure 1.2**). That effect is due to the increasing similarity of energy level wavefunctions as more orbitals are added to the system. As a consequence of nanocrystal growth, the fluorescence excitation and emission are red-shifted. This effect demonstrates that simple size and material considerations can be used to tune the emission to generate a wide range of wavelengths (from 400 nm to 2 um).[5] Within an ordinary band, electron-hole pairs have a larger degree of thermal freedom (mobility) allowing them a longer lifetime before they recombine. As nanoscale dimensions are approached, there are less available states for occupation and those states are energetically spaced further apart. As a result, the electron and hole have a short range of mobility and a short lifetime before recombination. The short lifetime results in high yielding fluorescence (denoted by high extinction coefficients, $>10^5$), and the discrete electronic states generate very low bandwidth emissions (20-30 nm).[5] High intensities and narrow bandwidths lessen the possibility of spectral overlap with intrinsic sources. By implementing two sets of different sized nanocrystals, simultaneous multicolored images can also be easily constructed.[10, 11] Some of the negative aspects of these materials are that the emission is troubled by a "blinking" problem whereby the emission is not continuous.[2, 10, 13] While lower excitation wavelengths reduce the amount of tissue damage, the process still

involves an excited electron that has been shown in living tissues to react and form harmful singlet oxygen.[7] Toxicity is also a serious concern since many semiconductors contain heavy metal atoms like cadmium and lead. The release of Cd^{2+} from cadmium-based QDs has been shown to result in cell-death.[7,8] Different surface coatings, either molecular or material-based, are being explored and show promise for stabilizing the surface of the QDs such that less Cd^{2+} is released.[7,8] Semiconducting QDs offer a number of advantages over the use of organic dyes in TPEF, but the toxic effects of cadmium remain a topic of concern.

Second harmonic generation (SHG) microscopy is another competitive technique for imaging biological samples. SHG arises from naturally occurring compounds in the body with a high degree of regularity (and noncentrosymmetry) in their structure. Those materials include the more commonly referenced collagen and myosin tissues, as well as cellular microtubules.[9] At this stage, the process can be viewed as a optical transmutation whereby two photons of long wavelength source light (infrared) are coupled to re-emit as a single photon at half the wavelength (typically visible) (**Figure 1.3**). Little or no photoinduced tissue damage occurs as a result of SHG because the process produces little to no waste heat and it does not involve an excited-state electron.[1,10] Also, the long source-laser wavelengths are not as prone to scattering. The lack of tissue damage and the long source-laser wavelengths mean that SHG microscopy is applicable for use on living tissue samples,[11] and imaging is possible at deeper tissue depths than TPEF.[12] SHG is also attractive because the emission bandwidth is small,[2] and the wavelength of the emission is tuneable by adjusting

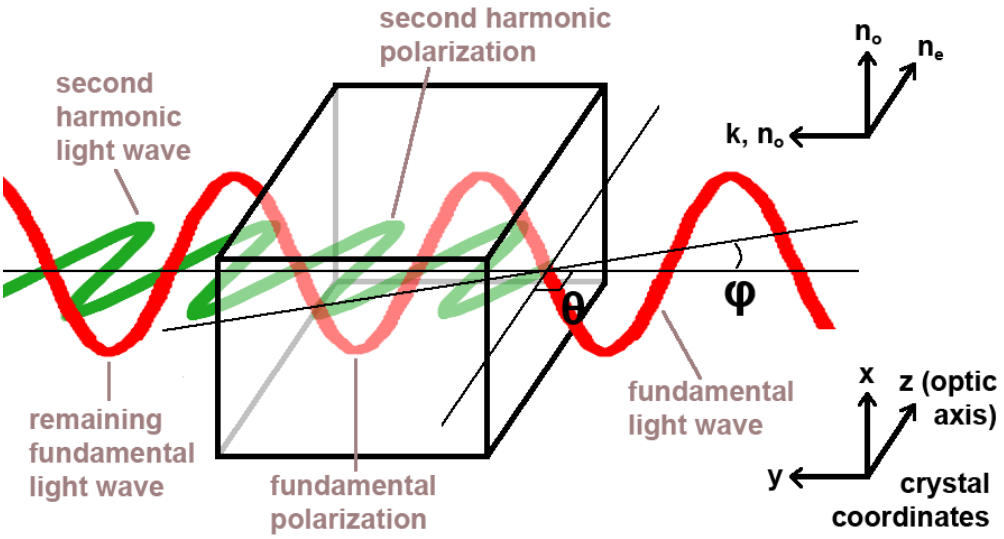

Figure 1.3 **The SHG process with respect to the crystallographic (x, y, z) coordinate frame and the laser propogation direction (k, θ, φ). The crystal is shown with one compositionally unique axis (i.e., a uniaxial crystal displayed) indicated by the presence of n_o and n_e. Angle θ is found within the kz-plane, and angle φ represents the angle out of the kz-plane. Angle φ has been exaggerated for clarity, and is not represented in the fundamental beam. In the experiment the crystal converts some of the incident laser light into a second harmonic beam.**

the source wavelength. This contrasts with semiconducting QDs where a change in the emission wavelength requires new dots. Unlike QDs, the detected signal is always continuous, and never suffers from blinking.[4] The emitted SHG occurs as a well-defined and orientationally-dependant polarization that can be mathematically related back to the structural orientation of the emitter.[2, 9] This property allows for the generation of 3D images with high resolution.[8, 19] With these positive characteristics the field is awaiting the possibility of using the technique to image processes in real-time. The delay in this progress is related, in part, to the fact that intrinsic SHG biomaterials emit such a low intensity that long integration times are necessary for the required data. A further drawback of the application is that the SHG signal deteriorates as temperature is increased.[13]

The cause of this effect is a change in the physical structure of the emitting tissue as a result of thermal motion.

To address the need for higher field intensities, the SHG microscopy field is looking towards contrast agents that are currently in the form of organic dyes and metallic nanoparticles.[14] The majority of biological imaging with SHG employs the use of organic dyes whose chiral shape lends to an increase in the second harmonic sensitivity of a localized area. Although the dye is present throughout the sample, it only generates localized SHG enhancement because rotational freedom in solution forms an essentially achiral optical environment. Cellular interfaces impose a peudo-orientation on the dyes, and that creates a localized region of accentuated noncentrosymmetry. The most commonly referenced type of dyes in the literature are the styryls,[16, 18, 22] that have been mentioned to increase SHG intensities from 1-2 orders of magnitude relative natural sources.[15] The drawback is that the organic dyes are susceptible to photobleaching that can lead to tissue damage in the surrounding area.[9] The metallic nanocrystals function in a very different way because the crystal itself represents an achiral composition of atoms that are not capable of SHG.[10,15] The origin of SHG in these structures is scattering at the interface between the nanocrystal and the surrounding medium where inversion symmetry is broken.[15] The metallic nanocrystals function by absorbing light to create a resonating surface oscillation of electrons (i.e., a surface plasmon is generated) at a frequency that depends on the shape of the crystal and the type of material.[16] The SHG that scatters from a bulk surface is normally weak, but the surface

plasmon can significantly enhance the second harmonic output when the resonance frequency coincides with the frequency of the incident laser light.[6, 23] Like the semiconducting QDs, the size and shape dependence of the metal plasmon resonance can be used to create a tuneable emission.[16] Metal nanoparticles can be used alone for SHG or they can be chosen to amplify the local electric field around a pre-existing structure or dye.[9] For the purposes of SHG, the metal particles are troubled by a loss of SHG intensity as a result of changes in the particle shape that occur by photoinduced heating.[17] Heating under illumination may also result in tissue damage if it becomes significant enough.

Alternative possibilities for contrast enhanced SHG microscopy are the long-term goal of this research. The use of nonlinear optical (NLO) nanocrystals as local SHG emitters has received much less attention than deserved in this field. Only five research articles have addressed (although very subtly) this type of enhancement to date. The nonlinear optical materials used in these articles include $KNbO_3$,[18] ZnO,[19] and β-BaB_2O_4[20] nanorods, and $Fe(IO_3)_3$[4] and $KTiOPO_4$[21] nanocrystals. $Fe(IO_3)_3$ and ZnO are two interesting members of this list because they are not normally used in macroscale frequency doubling. Similar to the metal nanoparticles, these NLO nanocrystals produce a surface-based SHG signal, but they additionally generate a signal from the bulk of the material. On the basis of an additional bulk signal, it can be assumed that the overall SHG in NLO nanocrystals would exceed that of metallic nanoparticles. The ideal shape that yields the best proportion of bulk and surface material for the highest overall

SHG yield is still unknown. Anisotropic crystal morphologies of NLO nanocrystals, such as those of $KNbO_3$ and β-BaB_2O_4, do help to enhance the crystal surface area and the surface derived SHG as a result. Zhao found that the SHG efficiency of the synthesized β-BaB_2O_4 rods was nearly 10 times that of nanocrystals 80 nm in diameter.[20] In a comparison between intrinsic and dye-based SHG methods, NLO nanocrystals are not as impacted by temperature effects. As inorganic materials they also have a higher photostability such that they do not degrade or invoke photodamage in the surrounding tissues. Similar to the former cases of SHG microscopy, orientational information can be obtained from the nanocrystals.[4,21] The inorganic oxides are also noteworthy for their biological stability and if there is a possibility of degradation, the components are relatively inert although several of the cations like, Nb^{5+} and Ti^{4+}, may act as oxidants. On the basis of composition, fewer toxicity concerns are certain to surround the use of typical NLO nanocrystals (**Appendix 1.1**) relative to semiconducting QDs. With such a short list of literature precedence, little is described about the variables that would impact the efficiency of the process, but one point can still be made. The SHG intensity will be larger than that of intrinsic SHG sources because of larger crystal dipoles relative to biological sources. More about SHG nanocrystals will be described in the sections to come.

1.3 Light and the Nonlinear Material Response

Light incident and travelling through a substance is best described as a travelling sinusoidal wave. In reality this wave is composed of numerous wavelengths depending on the bandwidth of the laser, but for simplicity, it is

assumed to be monochromatic in this work. The alternating phase of this applied field (a.k.a. fundamental wave) exerts a force on the electron clouds around atoms or regions within a crystal. The electron clouds track the alternating phase in an oscillatory fashion as the fundamental passes through the material. These charge oscillations, or polarizations within the crystal then emanate their own electric field in a converse effect (**Figure 1.4**).[22] In general, the total induced polarization, P(t), caused by the applied field, E(t), can be described by the sum of all its frequency components according to the equation in **Figure 1.5**. In most cases, the material response to light is described in terms of the first term, $\chi^{(1)}E(t)$, that highlights a linear proportionality between the electric field and the polarization. The susceptibility, χ, in this equation describes how easily a material is polarized by an applied field. Typically, the values of the susceptibility drop greatly with order such that $\chi^{(1)} >> \chi^{(2)} >> \chi^{(3)}$ etc.[23] In some materials, however, terms of higher field proportionality (i.e., "nonlinear" proportionality) are not negligible and they create polarizations of the 2nd and 3rd harmonic, respectively (**Figure 1.5**). Usually, if one is interested in producing a second or third harmonic, intense

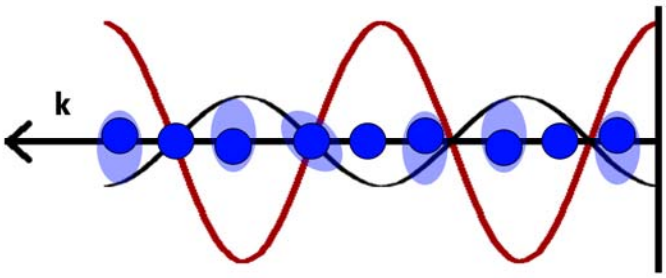

Figure 1.4 **Schematic showing the generation of a linear polarization in the lattice of a generic crystal. The size of the atoms (blue) relative the fundamental polarization (red) has been exaggerated to display the cause and effect of polarization. Here, the electron clouds are shown to distort to generate a polarization that oppses the applied field.**

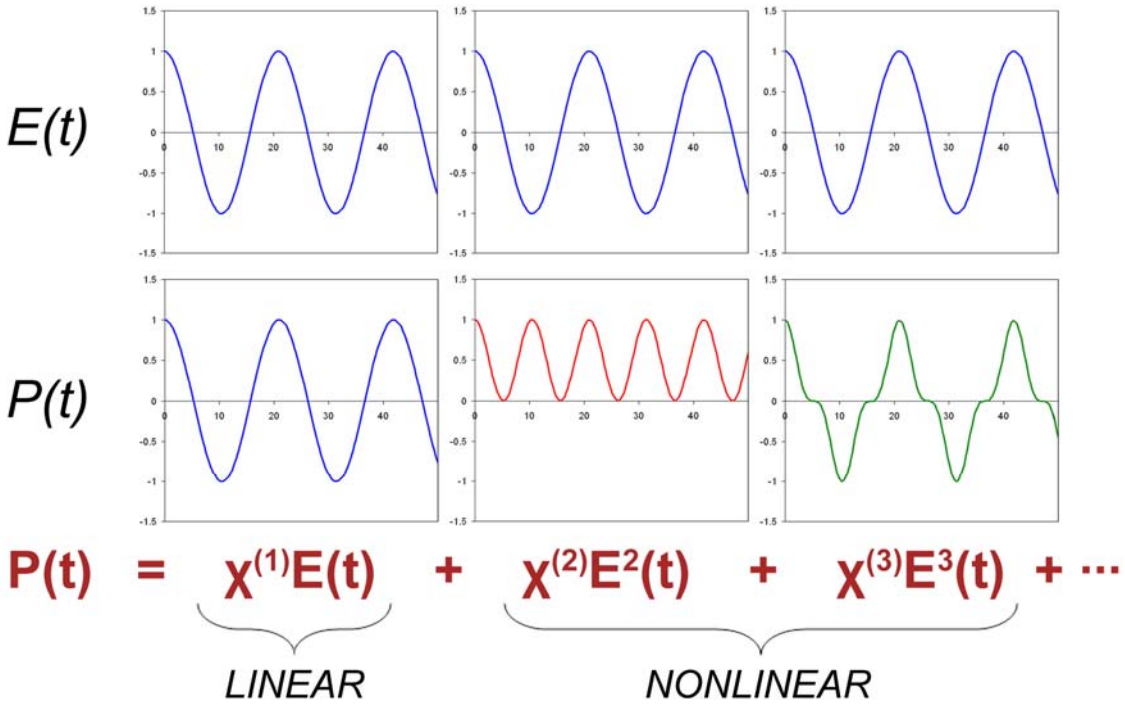

Figure 1.5 The total polarization generated in a nonlinear optical material. On top is shown the applied field, and immediately below are the individual polarization responses that contribute to the total polarization. Note that the amplitudes have not been scaled to reflect the difference in susceptibility values. This was done to magnify the shape of the higher order responses.

electric fields are used to offset the small value of the harmonic susceptibility. In the second term, the fundamental gives rise to a polarization at twice the frequency of the source field. The photon generated by this polarization is therefore the second harmonic wave.

The polarization itself is an electric displacement that travels through the crystal at a speed that is dictated by its orientation relative to the crystal axes. When the polarization is generated parallel to an axis its translational speed varies depending on the index of refraction it experiences in that plane:

$$v_P = \frac{c}{n} \tag{1}$$

The translational speed, v_p, in the above expression is called the phase velocity of the polarization, c is the speed of light in vacuum, and n is the index of refraction for a given direction in the medium. In anisotropic materials, at least one crystallographic direction is compositionally different, and that gives rise to multiple indicies of refraction for certain crystals. In one type of crystal, called uniaxial, a wave can experience indicies called n_o (o for ordinary) and n_e (e for extraordinary). The extraordinary index is ordinarily associated with the compositionally unique crystallographic axis. Often this axis is designated as the *c*-axis. If the crystal in **Figure 1.3** is uniaxial (and φ is 0^o), note that the fundamental oscillates in the *a*-axis so it experiences pure n_o. The generated second harmonic would then oscillate in the *c*-axis, experiencing pure n_e. In biaxial crystals each axial plane has its own unique composition and index. Here, the indicies are referred to as n_a, n_b, and n_c in association with each unique crystallographic axis. If the crystal in **Figure 1.3** is biaxial then the fundamental is said to experience n_a while the second harmonic experiences n_c (with $\varphi = 0^o$). It is important to note that a polarization can also be generated to travel through the crystal under a mixed index (e.g., between n_e and n_o). Polarizations of a mixed index occur when the laboratory and crystallographic frames of reference do not coincide. In the case of **Figure 1.3**, this is true because φ is nonzero, and it forces the fundamental to experience a little of n_e and the second harmonic polarization to experience a little of n_o. The true index experienced is a

trigonometric mixture of n_e and n_o. This type of angle-tuning methodology will be discussed in more detail shortly.

The wavevector, k, rather than the phase velocity is used to describe the nature of the generated wave because it further incorporates the polarization frequency. The wavevector is related to the phase velocity (v_P) and wavelength (λ) by the following equation:[24]

$$k = \frac{\omega}{v_P} = \frac{n\omega}{c} = n\left(\frac{2\pi}{\lambda}\right) \tag{2}$$

Here, ω, is the number of wave oscillations per unit time (angular frequency) and n is the index of refraction along which the beam is polarized. The wavevector will be discussed further when the efficiency of the second harmonic beam is addressed.

1.4 Selection Rules for SHG

Second harmonic generation can only be produced from systems that lack inversion symmetry. This restriction can be met at the interface of two materials or within single materials whose composition is noncentrosymmetric. Boyd [25] has provided a simple mathematical proof of this concept by considering the polarization that gives rise to the second harmonic:

$$\vec{P}(t) = \chi^{(2)}\vec{E}^2(t) \tag{3}$$

In a centrosymmetric material, the material composition is indifferent regardless of direction. Therefore, if the direction of the applied field, E(t), is switched to –E(t), the polarization will also change sign:

$$-\vec{P}(t) = \chi^{(2)}[-\vec{E}(t)]^2 \tag{4}$$

Simplifying we find:

$$-\vec{P}(t) = \chi^{(2)}\vec{E}^{\,2}(t) \tag{5}$$

The above equality is only true if the value of the second order susceptibility, $\chi^{(2)}$ is zero. This result implies that there is no possibility for a second harmonic wave in centrosymmetric materials.

1.5 The Nonlinear Susceptibility, $\chi^{(2)}$

As a three-wave process, each with a possibility of three different directions of polarization (x,y,z), $\chi^{(2)}$ in **equation (3)** represents a 3x3x3 cubic matrix.[24] Each cell represents one of the $3^3 = 27$ possible configurations of polarization. Since a cubic matrix is difficult to draw or do calculations with, it is represented instead as a 3x6 matrix, whereby a third of the combinations have been removed because nine values represent duplicate orientations of the electric field [e.g., $E_x(t)E_y(t) = E_y(t)E_x(t)$]. The rows represent x (1), y (2), and z (3) orientations of the second harmonic, respectively, and the six columns represent

the six unique orientations of the fundamental polarization that are xx (1), yy (2), zz (3), yz (4), xz (5), and xy (6), respectively:

$$\begin{bmatrix} d_{11} & d_{12} & d_{13} & d_{14} & d_{15} & d_{16} \\ d_{21} & d_{22} & d_{23} & d_{24} & d_{25} & d_{26} \\ d_{31} & d_{32} & d_{33} & d_{34} & d_{35} & d_{36} \end{bmatrix}$$

The intensity of the polarization giving rise to the second harmonic wave is dependant on the size of the 18 unique d-values (d_{il}) referred to as nonlinear coefficients. For crystal symmetry reasons, a number of these values will be zero. Tables of these matricies with nonzero values are given in a number of references and are listed according to symmetry.[25,26] For a given fundamental beam configuration, there will always be a specific mathematical combination of coefficients that produces a single "effective" nonlinear coefficient, d_{eff}. This value enables a direct comparison between materials because it directly scales the magnitude of the electric field to give the magnitude of the second harmonic polarization. The formulas for calculating d_{eff} from d_{il} are tabulated in the literature.[26] To explain these concepts more clearly, consider the following second harmonic susceptibility for $LiNbO_3$ (crystal class $3m$[26]) at 1058 nm:[27]

$$\begin{bmatrix} 0 & 0 & 0 & 0 & -4.88 & -2.58 \\ -2.58 & 2.58 & 0 & -4.88 & 0 & 0 \\ -4.88 & -4.88 & -34 & 0 & 0 & 0 \end{bmatrix}$$

From tables, the value of d_{eff} for the simple case of same-plane fundamental waves is:[25]

$$d_{eff} = d_{31}\sin\theta - d_{22}\cos\theta \sin 3\varphi \quad (6)$$

Angle θ in **equation (6)** represents the angle of incidence for the fundamental waves relative the optic axis and φ represents the crystal rotation angle. If we take the case where the fundamental enters with $\theta = 90^{o}$ and $\varphi = 0^{o}$ the second term is 0 and the value of d_{eff} is -4.88 pm/V (case of **Figure 1.3**). What this situation represents is an electric field directed along the *b*-axis (90^{o} from *c*-axis, i.e., z) and plane polarized in the *a*-axis (note the 1 in d_{31}). This orientation of polarizations results in a second harmonic plane-polarized in the *c*-axis (denoted by 3 in d_{31}) with a magnitude equal to:

$$\left|\vec{P}(t)\right| = 2d_{eff}\left|\vec{E}^{2}(t)\right| \quad (7)$$

A large polarization is preferred, so large values of d_{eff} should be sought. At this point, it looks as though there is complete freedom in φ because the value of d_{eff} is indifferent as φ changes. In the following sections it will be clear that this is not the case and that only particular combinations of angles θ and φ will lead to efficient SHG.

1.6 Optimization of the Bulk Second Harmonic Response

An efficient second harmonic response is produced when the intensity of the fundamental beam is high, the material has a high nonlinear susceptibility, the phase velocities of the fundamental waves and the second harmonic wave are equal, and when the crystal has a sufficient optic axis length.[23,25,26] These requirements are summarized by a number of authors[26, 27, 29, 30] in the following equation for the lower-limit of conversion efficiency:

$$\eta_{SHG} = \frac{I_{2\omega}}{I_{\omega}} = A\left(I_{\omega} d_{eff}^{2} L^{2}\right)\left[\frac{\sin(\Delta kL/2)}{(\Delta kL/2)}\right]^{2} \qquad (8)$$

Here, I_{ω} and $I_{2\omega}$ are the intensities of the fundamental and generated second harmonic beam, d_{eff} is the effective nonlinear susceptibility, Δk is the wavevector mismatch between the fundamental and generated second harmonic beam, and L is the crystal length with respect to the direction of propagation. The variable A is a scaling term that is different depending on the derivation applied by the author.

From this expression and the preceding discussion, it is apparent that a high nonlinear coefficient, d_{eff}, results in a relatively high efficiency in the second harmonic response. Since the susceptibility, d_{eff}, acts to transform the magnitude of a particular applied field into a second harmonic polarization, a larger value would indicate the creation of a more intense second harmonic. This was previously described in **equation (7)**.

In **equation (8)** it is also appears that an intense fundamental beam and

long crystal lengths will also produce favourable efficiencies. An intense incident field is necessary, despite SHG dependence on the square of the electric field, because of the small value of high order susceptibilities like $\chi^{(2)}$. While the efficiency also appears to be directly proportional to the length of the crystal, this is slightly misleading. The benefit is seen only when the crystal is long in the direction of propagation, and when the generated polarizations are produced with synchronous phases. Initially when the fundamental enters the crystal, a second harmonic is generated and it begins to propagate through the crystal. As the fundamental travels through the crystal, new second harmonic polarizations are continuously generated. If the index of refraction is different for the fundamental and the second harmonic, they propagate through the material at different rates [**equation (1)**]. After a time, or after a certain crystal length, the newly generated second harmonic will no longer coincide constructively with the phases of earlier polarizations. So if “phasematching” is not established the process will not be as efficient because part of the crystal length actually contributes to destroying the SHG. Constructive interference only dominates when the new polarizations are generated up to a half cycle ahead of the existing polarization. In the remaining half of the cycle, waves are generated with opposing phase to the waves created in the first half of the cycle. Due to the half cycle of positive overlap, the period of coherence, π, occurs over a specific crystal length:

$$L_c = \frac{\pi}{\Delta k} \tag{9}$$

L_c is the effective crystal length that is pertinent to the discussion of efficiency in **equation (8)**. A phase difference of π will develop in a length of time (or distance L_c) based on how closely matched the phase velocities are (**Figure 1.6**). In the top image of **Figure 1.6**, the fundamental laser polarization has a greater phase velocity than the second harmonic, and that has resulted in the production of new second harmonic polarizations that are ahead of the existing polarization. New polarizations are created from 0 to 4π out-of-phase over the entire crystal length resulting in the rise and fall of the SHG intensity twice. The effective crystal length is only from 0 to π where constructive interference amplifies the existing second harmonic polarization. In the bottom image of **Figure 1.6** the phase velocity difference is improved such that the entire

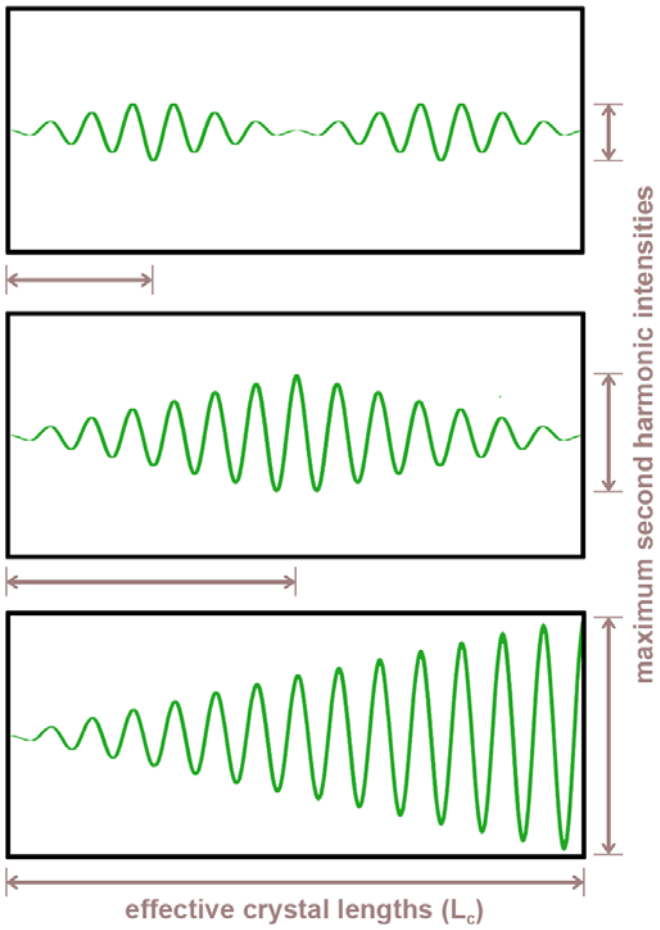

Figure 1.6 **The second harmonic polarization intensity as a function of crystal depth when the fundamental polarization travels through the crystal at a different phase velocity than the second harmonic (top and middle). When the rate of propagation of the polarizations are matched (bottom), the second harmonic intensity grows as a result of constructive interference over the entire crystal length.**

crystal length is useful for generating SHG (i.e., L_c exceeds the physical crystal length). The phase velocity difference is expressed by the difference in wavevectors, *Δk*, that were introduced earlier in **equation (2)**:

$$\Delta k = k_{2\omega} - 2k_{\omega} = 0 \tag{10}$$

The subscripts in the above equation are used to help signify the wavevectors of the second harmonic (2ω) and the fundamental polarizations (ω). The factor of 2 appears in the above expression due to the fact that the second harmonic has twice the frequency as the fundamental wave.

The degree of phasematching, Δk, also appears directly in **equation (8)**. The term outlined in the square brackets of **equation (8)** is analogous to the function (sin x)/x, where x = ΔkL/2. The function has a maxima in the limit where ΔkL/2 goes to 0. Since the length of the crystal, L, must be nonzero, optimal efficiency is only found for Δk = 0. This fact was demonstrated in **equation (10)**. Conceptually, the notion of Δk is less vague when written in terms of the differences in index of refraction (Δn) because the difference in phase velocities is zero [**equation (1)**] when the second harmonic and the fundamental experience the same index. **Equation (10)** can be written in terms of the index of refraction by substitution with **equation (2)** to yield:[23]

$$\Delta k = \frac{4\pi}{\lambda_{\omega}}\left(n_{2\omega} - n_{\omega}\right) \tag{11}$$

Methods of establishing the $\Delta n = 0$ condition are the topic of the following section.

1.7 Further Phasematching Discussion

Phasematching is undoubtedly the most important factor in an efficient nonlinear optical process. Consequently, the forms of phasematching and the influence of experimental conditions on phasematching will be briefly addressed. Phasematching can be affected by the source-beam angle of incidence, the process temperature (thermooptic effect), pressure (photoelastic effect), and the frequency and amplitude of the electric field (photorefractive effect).[26] The flexibility, tolerance, or adjustable range that a given material has to the preceding factors is highly important to choosing the right SHG material for a specific application.

As previously discussed, phasematching is the process of equalizing the phase velocities of the fundamental and second harmonic polarizations. The process could, however, alternatively be described as offsetting dispersion with birefringence. Dispersion is a frequency dependant change in an index of refraction and birefringence is the existence of more than one index of refraction in a material. A large birefringence does not necessarily imply a benefit, since it is merely a compromise to dispersion.

In one type of phasematching, called *noncritical phasematching*, the fundamental beam is always polarized along the crystal axis with the largest index of refraction (**Figure 1.7**). If any one index is evaluated in **Figure 1.7** as a

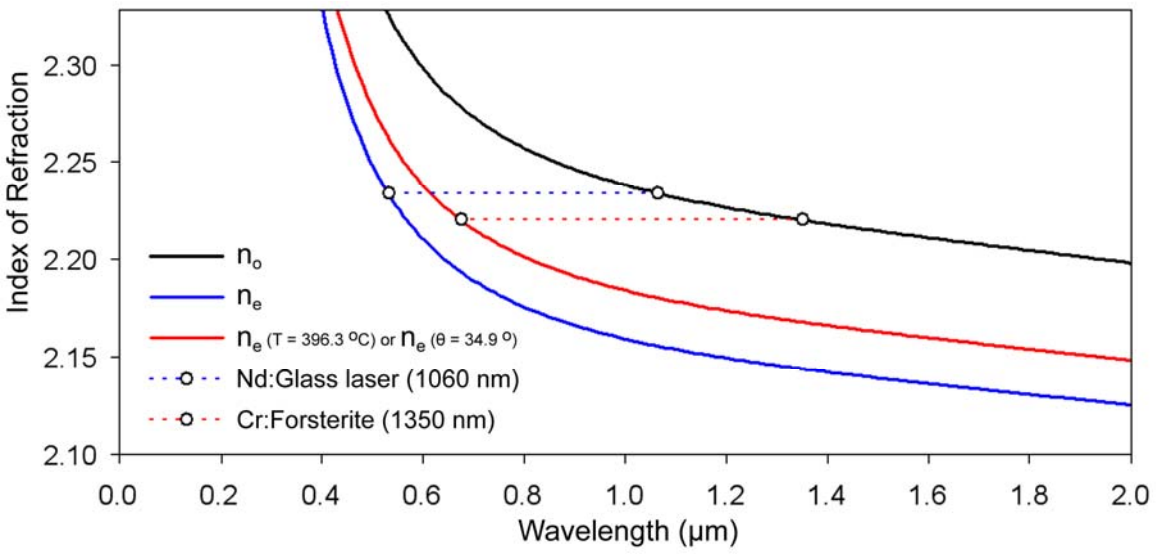

Figure 1.7 **The use of birefringence to offset the property of dispersion. At 32 °C $LiNbO_3$ is capable of phasematching a Nd:Glass laser perfectly because the index of the second harmonic and the fundamental waves are equal. For the Cr:Forsterite laser, $n_o \neq n_e$ for the second harmonic and the fundamental waves, but temperature or angle tuning adjusts the value of n_e such that phasematching can be achieved.**

function of the fundamental and second harmonic frequency, the effect of dispersion is apparent. By **equation (1)**, the phase velocity of the second harmonic will be far too slow because it will always experience a higher index of refraction. To achieve phasematching in spite of frequency, the experiment must make use of birefringence. If a high (i.e., slow) index plane is applied to the fast fundamental polarization and the low index plane (fast) carries the slower second harmonic polarization, $\Delta k = 0$ can be satisfied. In the case of $LiNbO_3$, this is a fundamental beam with polarization along either the *a*- or *b*-axis where $n_o(\omega) = 2.234$ (1060 nm, T = 32.2 °C) (**Figure 1.7**). Under these conditions, the birefringence of $LiNbO_3$ offsets dispersion perfectly such that a second harmonic at 530 nm experiences $n_e(2\omega) = 2.234$ while polarized in the *c*-axis (see **Appendix 3.1**). Note that this is the case described earlier in the calculation of

d_{eff}. The phasematched condition is also specific to the temperature of 32.2 ^{o}C, but there is an inherent temperature tolerance that is material dependant. The name “noncritical” has been given to all cases where the laboratory and crystal coordinate axes are identical because the second harmonic efficiency is not as affected by changes in the temperature, angle of incidence, or wavelength in this geometry (**Appendix 1.1**).

If the laser source was switched to a Cr:Forsterite laser (1350 nm, T = 32.2 ^{o}C), $n_o(\omega) \neq n_e(2\omega)$ in $LiNbO_3$ and the second harmonic output is limited as a result. A perfect phasematching condition can, however, be made for this laser if the conditions of the experiment are changed. For example, phasematching can be made by increasing the temperature to 396.3 ^{o}C (see **Appendix 3.1**). This temperature-tuned crystal is still considered a state of noncritical phasematching because the fundamental is still directed along a principle axis in the crystal. Temperature tuning is made possible by structural rearrangements that accompany a change in temperature. Temperature adjustment causes the relative composition along given crystallographic directions to change enough such that the indicies of refraction are modified. In the case of $LiNbO_3$, NbO_6 octahedra tilt to elongate the *ab*-plane.[28] Based on a difference in bonding along each crystal direction, the stress-strain response of a crystal may also result in structural distortions. The resulting pressure can be expected to impact the indicies of refraction.

Since 396.3 ^{o}C is an extreme temperature, one may be more apt to use the second type of phasematching called *critical phasematching*. In this method,

the angle of incidence [θ from **equation (6)**] is tilted such that the second harmonic polarization experiences a trigonometric mixture of n_o and n_e while the fundamental polarization remains in the *a*- or *b*-plane (along n_o). Since travel along n_o is slower than that along n_e in $LiNbO_3$, angle tuning has the effect of slowing the phase velocity of the second harmonic wave. For the case described, take the instance when a Cr:Forsterite laser (1350 nm, T = 32.2 ^oC) is polarized along the *a*-axis (n_o = 2.220). The second harmonic becomes phasematched with the fundamental polarization when the angle of incidence (θ) for the laser is tilted 34.9^o into the *b*-axis (see **Appendix 3.1**). At this angle, the second harmonic polarization no longer experiences pure n_e. The second harmonic experiences roughly 33% n_o (2.278) from the *b*-axis and 67% n_e (2.194) from the *c*-axis, and the blend shows a net index of 2.220. Critical phasematching received its name as a result of very narrow temperature, angle, and wavelength restrictions relative noncritical phasematching. A great example of this definition was provided by Boyd for $KNbO_3$.[25] In a 1 cm crystal the critically matched angular tolerance is just 0.036^o compared to 1.3^o for the noncritically matched system.

If critical phasematching is to be used, the SHG will also be limited by a phenomenon known as spatial walk-off (a.k.a. Poynting vector walk-off).[26] Spatial walk-off is defined when the induced polarization and the fundamental polarization diverge by an angle called the walk-off angle (ρ). The walk-off angle has a similar consequence to the case of a nonideal coherence length, whereby the generated SHG is only pumped over a limited distance. Here though, the

distance of coherence is called the aperture length and it is a restriction imposed only by experimental design:

$$L_a = \sqrt{\pi} r_0 / \rho \tag{12}$$

Here L_a is the effective length of coherence, r_0 is the radius of the driving beam, and ρ is the walk-off angle based on the choice of critical phasematching. The walk-off angle may or may not be significant depending on the choice of material (**Appendix 1.1**). Note that if the beam radius is larger, the electric field will still overlap with the electric polarization over a greater distance despite ρ. The minimum radius of the laser beam will be restricted by the surface damage threshold for a material. If the beam becomes too concentrated by decreasing r_0, physical damage can occur to the crystal and frequency-doubling capacity will degrade as a result of a number of factors including scattering from stress-generated cracks, absorption by photoreduced centers, or from compositional or structural changes (e.g., due to Li_2O volatilization).[26] The definition of walk-off length also highlights the fact that a highly confined laser beam is not ideal for systems intended to be critically phasematched. Too broad of a beam may also lead to less efficient SHG by dispersing the laser intensity.

1.8 The Strengths and Weaknesses of Nanocrystals for SHG

Perhaps one of the biggest questions enveloping the synthesis of NLO nanocrystals for use as SHG emitters is whether or not the nanocrystals can be efficient enough to be of practical use. The lengths of the crystals are so short

that the resulting polarization will certainly be small. Also, the crystals themselves may exhibit noncentrosymmetry, but a powder, or pile of randomly oriented small crystals appears fairly isotropic in composition. Randomly positioned crystals are analogous to the situation of SHG dyes in solution. These dyes only emit at the surfaces of cells where inversion symmetry is broken. A locally generated second harmonic wave in one nanocrystal is not likely to travel far before it destructively interferes with another second harmonic wave in a neighbouring crystal. Since the crystal orientations are random in a powder, it is highly unlikely that the beams from neighbouring nanocrystals will exhibit any kind of coherence. In the case of powders, Dougherty and Kurtz explain that the net efficiency is effectively zero (10^{-9} to 10^{-14} % efficiency).[29] Despite this dismal appearance, the following section will address how to improve this outcome and the benefits of NLO nanocrystals will be discussed in relation to the theory formerly discussed.

The major obstacle to overcome with respect to efficiency is to implement a method of disrupting the isotropic nature of the powder; otherwise, high efficiency situations will be limited to the observation of single nanocrystals. Single nanocrystal measurements have been shown in one case to have a four-order improvement in efficiency (i.e., 10^{-5} %).[18] In the desired application, however, there will be many emitting nanocrystals to consider, so there is a need to impose some type of communal orientation. There are a number of methods of imposing order. The first method is to change the morphology of the crystal. Anisotropic crystal morphologies, such as rods and disks, lead to a natural gravity induced pseudo-orientation. The process of self-orientation, in this case,

is a result of a lower potential energy for a rod lying flat relative to standing on one end. The orientation of the crystals could be further improved as a result of pressure applied by shaking, tapping, or pressing the sample. Anisotropic structures within the body may not be a wise decision though. For example, it is well known that the fiber-like structure of asbestos is the chief property related to the cause of a number of respiratory illnesses. By far the most promising method of alignment is to target a pyroelectric material. These materials exhibit a spontaneous polarization that will align with an applied electric field if the material is suspended and has free rotation. Within the pyroelectric materials, a special class exists called whereby the spontaneous polarization can be switched to align with an applied field. This property, called ferroelectricity, would be more useful in this case because crystals with restricted motion can still be aligned. This type of alignment methodology has been used in other research with success.[30] Out of the 32 different crystal point groups, 18 are capable of SHG, and out of those, only 10 are pyroelectric and capable of exhibiting ferroelectricity.[31] The scope of the search in this research should be limited to the 10 pyroelectric point groups, which still represent a large number of possible crystals. Magnetic materials and their alignment through the use of magnetic fields do not apply in this research. Magnetic materials are poor optical materials due to a lack of transparency due to free electrons that efficiently absorb a broad spectrum of wavelengths. Anisotropic crystal morphologies and ferroelectric materials stand the best chance to overcome the loss of SHG as a result of random crystal orientations.

A further obstacle in this work is to ensure that the polarization of the fundamental is aligned in the appropriate direction. The above methods of orienting nanocrystals, in particular ferroelectricity, will facilitate overcoming this challenge. By knowing the direction of the applied field, and the direction of the polar axis in the nanocrystal, the orthogonal direction will preferentially expose the remaining *ab*, *bc*, or *ac* co-planes. With respect to phasematching, this situation still exhibits a 2-dimensional disorder that harms SHG efficiency, but with further discussion it will become clear that this will make little difference. If we do wish to reduce the directionality of the SHG system by another degree, we can impose the scope of this research to ferroelectric crystals with only one unique axis (i.e., indifferent about the polar axis). By applying this restriction to the 10 pyroelectric point groups, the orthogonal, monoclinic, and triclinic crystals are removed and the list of suitable materials is reduced to just 6 point groups. For example, in the case of $LiNbO_3$ (point group 3m), the laser can be incident anywhere in the *ab*-plane for noncritical phasematching because the index of refraction is indifferent about the polar *c*-axis.

As challenging as it sounds for establishing efficient SHG with NLO nanocrystals, these crystals do have a number of advantages. For one, they have a high surface-area to volume ratio that leads to a significant amount of surface induced SHG.[32] Chan and coworkers[7] found that d_{31} and d_{33} in their 62 x 667 nm ZnO nanorods were 2.8 and 18 pm/V relative to 2 and 7 pm/V for the bulk, respectively. They attributed this enhancement in the nanocrystals to a surface effect because the values of d_{31} and d_{33} were found to increase with

crystal anisotropy. Nakayama also found d_{eff} values larger than expected for the bulk.[18] Slight dispersion differences aside, d_{eff} was found to be ~9.1 pm V^{-1} (2ω = 502 nm) that is slightly higher than the bulk value of 8.62 pm V^{-1} (2ω = 491 nm).[33] These cases of SHG from nanocrystals show that the effective nonlinear susceptibility is increased relative to the bulk as a result of surface induced SHG. Higher susceptabilities were previously described to result in more efficient SHG.

So far the literature focus has been on typical NLO materials like $KNbO_3$,[18] β-BaB_2O_4,[20] and $KTiOPO_4$,[21] but these articles have still not addressed the key advantage of nanocrystalline NLO materials. The key benefit is that phasematching considerations are loosened to near nonexistence. Since the scale of the crystal is much smaller than the wavelength of light used, there will generally be a length of coherence (L_a or L_c) much greater than the length of the nanocrystal. As a numerical example, consider an extreme case of wavevector mismatch where an Er:Glass laser (1540 nm) is to be frequency doubled by $LiNbO_3$ at 21 ^oC. Here the index difference, Δn, between the fundamental (2.213) and second harmonic (2.179) waves in **equation (10)** is 0.03. This difference equates to a coherence length, L_c, of ~11 μm. In terms of the 1-5 cm long crystals that are normally used for SHG, this result would be detrimental since it utilizes only 0.1 % of the crystals frequency doubling capacity (e.g., **Figure 1.6**). If a 5 nm crystal was used, the coherence length is ~2000 times the length of the crystal such that by the time the fundamental beam leaves the crystal, the generated harmonic is only 0.001 radians out of phase with the existing harmonic. Essentially, the nanocrystal is sufficiently phasematched for optimal

performance. The flexible phasematching condition also means that nonlinear coefficients like d_{33} are available for use. In $LiNbO_3$, d_{33} = 34 pm/V (1058 nm) but the subscripts signify that the fundamental and the second harmonic are both polarized in the *c*-axis. Due to dispersion this polarization configuration results in a very large index mismatch (Δn), and subsequently a very short coherence length. However, relative to a nanocrystal, this distance is insignificant and phasematching is still obtained. At the nanoscale, the phasematching temperature, angular, and wavelength tolerances also improve greatly. This fact is demonstrated in Bonacina's nanocrystalline $Fe(IO_3)_3$ where every crystal was observed to emit without any method of imposing preferred orientation.[4] In that work, the bandwidth of the emission spectrum was also able to show that the nanocrystals doubled the entire bandwidth of the fundamental beam. This equates to an outstanding ability of the $Fe(IO_3)_3$ nanocrystals to create SHG over at least a 50 nm range of wavelengths.[4] Essentially, the result is that the phasematched condition is highly flexible, and it can permit a wide degree of experimental conditions.

1.9 Adequate Materials for SHG Nanocrystals

A wide variety of NLO crystals are available for the generation of visible light from infrared or near-infrared lasers. An extensive table of competitive and commercially available SHG crystals has been made available for the readers benefit (**Appendix 1.1**). However, considering the preceding arguments, the tabulated d_{eff} and the phasematching considerations are not necessarily the maximum values that can be achieved at the nanoscale. The quoted

transparency regions are also likely to change as a result of quantum confinement. In a beneficial way, quantum confinement necessitates a higher energy absorption edge as the crystal size shrinks, but it is not known what happens at the lower energy limit of transparency. Damage thresholds of the crystal are also not a concern anymore, because most biological samples are too sensitive for the use of intense laser fields; especially those intense enough to damage an inorganic crystal. In order of importance then, a summary of the remaining material requirements are:

1) high nonlinear optical coefficient(s)
2) high transparency to infrared and visible wavelengths
3) anisotropic crystal morphology
4) morphology long in the direction of SHG propagation
5) a ferroelectric material if possible

To this list can be added several biologically imposed requirements, which are:

6) water stability[34]
7) pH stability
8) water dispersability
9) low toxicity

Table 1.1 A selection of materials from Weber[27] that have nonlinear optical coefficients greater than 12 pm/V for the emission of visible SHG wavelengths. Crystal classes highlighted in grey are not ferroelectric classes.

Material	crystal class	d_{il}	d_{il} value (pm/V)	2ω (nm)	Bulk (nm) Transparency
$LiNbO_3$	3m	d_{33} =	34.0	529	350-5000
		d_{33} =	31.8	659	
$KTiOPO_4$	mm2	d_{33} =	13.7	530	350-4500
$KNbO_3$	mm2	d_{33} =	19.6	532	400-4500
$LiTaO_3$	3m	d_{33} =	16.4	529	400 -
β-BaB_2O_4	3m	d_{22} =	13.4	530	190-3500
$InPS_4$	-4	d_{36} =	20.0	532	-
		d_{31} =	26.3	532	
$AgGaS_2$	-42m	d_{36} =	23.4	532	500-13000
$BaTiO_3$	4mm	d_{31} =	15.7	532	400 -
		d_{15} =	17.0	532	
$LiInO_2$	mm2	d_{33} =	15.8	532	-
α-ZnS	6mm	d_{33} =	13.8	532	340 -
β-ZnS	-43m	d_{36} =	20.7	529	-

The maximum available nonlinear coefficient is the main concern for efficiency. **Table 1.1** has been created with this concen in mind. This short list was constructed from the values of Weber,[27] and it considers all materials exhibiting a nonlinear coefficient above 12 pm/V for a second harmonic in the visible spectrum. Absent from this list are a few four-element compounds that were considered to be a challenging stoichiometry to obtain in such a preliminary study. Also absent are some members of the II-IV and III-V families of semiconductors that have exceptionally high nonlinear coefficients, but they have equally poor transparency in the visible spectrum. The final exception to this list was the removal of all cadmium, lead, mercury and arsenic compounds that are

a concern for toxicity. In the remaining table of interest, $LiNbO_3$ stands out as a material with a very strong qualification because of a high nonlinear optical coefficient (d_{33} of 34 pm/V at 1058 nm), a broad transparency, and a ferroelectric nature (see **Section 1.10**). The biological factors are more difficult to address, but our title compound shows high acid resistance and water stability. In our research, we have determined that acids can slightly modify the surface, possibly by a shallow proton exchange for surface-bound lithium. A short-term toxicity study was also performed and cells that ingested $LiNbO_3$ were still alive following one week (unpublished work of Professor Vincent Semetey, Institut Curie, Centre de Recherche, France). The dispersability in aqueous media is fair, but real application will probably be superseded by application of a thin silica surface. Due to the widespread use of silica in gas and liquid chromatography columns, the methods of changing silica surface chemistry are well understood.[5]

1.10 Structure and the Ferroelectric Property of Lithium Niobate

$LiNbO_3$ is part of the trigonal crystal system. The simplest repeat unit of the crystal structure is a rhombohedral unit cell composed of two formula units (Z = 2). According to the near-stoichiometric data (Li/Nb ≈ 1) presented by Iyi,[35] the unit cell dimensions for this structure are each 5.493 Å and the angles between the *a*-, *b*-, and *c*-axes are also equivalent at 55.5°. The rhombohedral cell is, however, rarely used to describe the structure of $LiNbO_3$. Typically, the structure is described in terms of a larger hexagonal unit cell (Z = 6) that has a more useful set of axes and a conceptually simpler structure for visualization. For this type of unit cell, the *a*- and *b*-axes are now 5.149 Å and separated by 120°, but they are

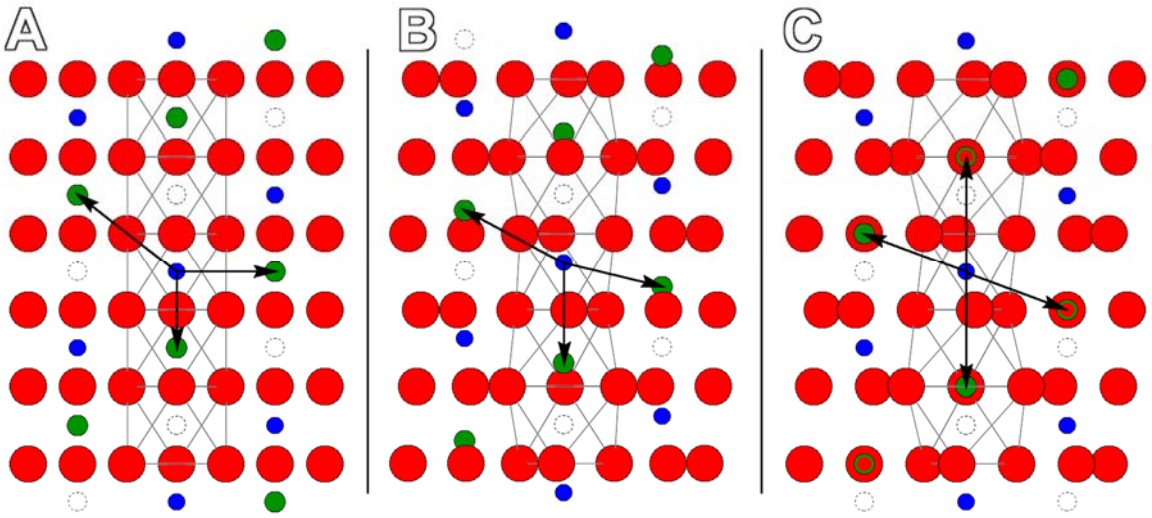

Figure 1.8 **Three edge-sharing stacks of oxygen octahedra in LiNbO3 are shown in: (A) an imaginary hexagonal lattice, (B) a true distorted hexagonal lattice and (C) a high-temperature lattice (~1180 °C). Relative atomic sizes for Nb (blue), Li (green) and O (red) are shown. Empty octahedral sites are shown in white. By observation, (A) and (B) are both noncentrosymmetric. Also, (B) is the only case where the dipole vectors add to result in a net polarization. Therefore (B) identifies that LiNbO3 is a ferroelectric material.**

coplanar with the oxygen layers in the crystal. The *c*-axis lies 90^{o} out of the *ab*-plane and has changed to 13.858 Å. The *c*-axis is special in this representation because it is oriented along the highest symmetry element of the structure; a three-fold rotation axis. This axis also represents the direction of an intrinsic dipole moment for the structure.

To better understand the structure and origin of this dipole moment it is easiest to construct a simplfied view of the structure from basic principles. In this pseudo-$LiNbO_3$ structure, the lattice is built of hexagonally stacked layers of close packed oxygen atoms (red) in the *ab*-plane (**Figure 1.8A**). The metals, lithium (green) and niobium (blue) have radius ratios of 0.46 and 0.53, respectively (see **Appendix 3.2**). These values illustrate that both metals are ideally suited for filling the octahedral sites ($r_M/r_O > 0.414$) in this lattice. The ABA

stacking sequence of oxygen layers creates a series of face-sharing octahedral sites along the *c*-axis. Thin black lines have been drawn in **Figure 1.8** to highlight each of the octahedra. The octahedra are connected by face-sharing interactions to form chains along the *c*-axis (three adjacent chains are shown). Each of these chains is joined to six adjacent chains by edge-sharing. Two-thirds of the octahedra are filled equally by lithium and niobium atoms in a highly periodic arrangement. From the bottom up in the chain highlighted in **Figure 1.8A**, a vacant octahedral site is followed by a lithium, then niobium octahedra and so on. The six encircling chains can be thought of as copies of this chain shifted up and down in an alternating fashion about the center stack. This means that each vacant octahedra is surrounded in the *ab*-plane by lithium and niobium octahedra only. Likewise, the lithium and niobium sites are surrounded by alternating vacancies and the corresponding alternate cation. As a result of the cation distribution, this mock structure of $LiNbO_3$ lacks an inversion center. The dipole arrows in **Figure 1.8A** add vectorally to zero to also reveal that this structure is nonpolar.

The process of creating the true structure of $LiNbO_3$ [R3c (#161)] from this pseudo-structure is a short process. The metal-metal distance between lithium and niobium in the face-sharing configuration of octahedra[36] is short (see **Appendix 3.3**) and that results in coulombic repulsion. As a result of this force, both cations displace towards the vacant sites above and below for niobium and lithium, respectively (**Figure 1.8B**). In addition to the shifting of metal atoms, the oxygen atoms also move. The oxygen atoms above the niobium atoms and

below the lithium atoms, spread to accommodate the new metal positions. The true oxygen packing is, therefore, described by distorted hexagonal layers. While both metals are displaced, the heavier and highly charged Nb^{5+} ion moves relatively little compared to that of the more labile Li^{+} ion. Each lithium atom of 1 electron charge moves down 0.481 Å creating a dipole of -2.31 D. Each Nb^{5+} atom moves 0.255 Å creating an opposing dipole of +6.12 D. A net dipole of +3.81 D is created for the pair of ions as a result of this movement, which can be confirmed visually by the vector addition of dipole arrows in **Figure 1.8B** (also see **Appendix 3.4**). The presence of a dipole in absence of an applied field classifies $LiNbO_3$ as a ferroelectric material. The lack of inversion symmetry is still maintained in **Figure 1.8B** and that is why it is capable of SHG.

A second structural phase exists for $LiNbO_3$ at temperatures greater than the ferroelectric phase transition temperature [R℅c (#167) at $T_c \geq 1180\ ^{o}C$].[37] In this paraelectric phase (**Figure 1.8C**), the lithium atoms displace so far that they insert into the oxygen layer below. The oxygen atoms of the *ab*-plane spread further in this structure as a result of the insertion and this is revealed by a growth in the unit cell *a*- and *b*-axes from 5.15 Å to 5.29 Å.[37] On the contrary, the niobium cations return to the center of their octahedra as a result of symmetrical coulombic forces from the surrounding LiO_3 layers. The symmetrical cation positions in the structure do not result in a spontaneous dipole as in the low temperature phase (see vectors **Figure 1.8C**). The high symmetry also renders the formation of an inversion center for the structure so SHG is not possible.

From this discussion, $LiNbO_3$ has been shown to be a ferroelectric crystal that will be stable at biologically relevant temperatures. This property, in addition to several others listed in **Section 1.9** contributed to the choice of $LiNbO_3$ as the introductory material for study in this research.

1.11 Concluding Remarks

Several multiphoton microscopy techniques are being coupled with an optical microscope for the purpose of imaging biological samples. Among them, SHG is a promising candidate because of the absence of photobleaching and its potential for high resolution imaging deep within tissues. The use of SHG in imaging applications is likely to catch on if a suitable probe can be found to increase the SHG emitted from the samples. In this Chapter, we addressed the possibility of using a nonlinear optical nanocrystal as such a probe. Among a list of available materials, $LiNbO_3$ appears to be the most suitable because of high nonlinear optical coefficients, a broad visible and infrared transparency, ferroelectricity, and the prospect of stability and safety in a biological sample.

CHAPTER 2 – AN IN-DEPTH DESCRIPTION OF THE SOLUTION-PHASE PROCESS

2.1 Introduction

In the preceding Chapter, it was established that the chosen method to synthesize $LiNbO_3$ should have a goal of producing anisotropic structures with a direction of anisotropy along the direction of the intended fundamental beam. Since the d_{33} nonlinear coefficient is of the greatest interest here, *a*- or *b*-axis growth is the most desirable result because d_{33} requires a fundamental beam polarized in the plane of the *c*-axis (therefore incident in the *a*- or *b*-plane). If alignment methods are going to be employed, then the chosen synthesis should also be capable of forming independent (free or non-fused) nanocrystals with single ferroelectric domains. In this section a comprehensive review of the current methods for producing nanocrystalline $LiNbO_3$ is introduced. These methods are then discussed in relation to their potential for achieving the desired crystalline morphology. Our methodology and justification behind the chosen solution-phase approach is also described here.

2.2 The Current Methods of Synthesizing $LiNbO_3$ Nanocrystals

The production of nanocrystals for efficient SHG microscopy will rely on the ability of the chosen synthesis to produce independent nanocrystals with a morphology that emphasizes specific crystal directions. The most common

routes to make nanoscale crystals of $LiNbO_3$ today can be summarized as secondary processes. By one method, the cutting debris from melt-grown boules of $LiNbO_3$ are crushed by high-energy mechanical milling to produce powders containing nanocrystals. Ball milling is popular because it is a simple, cost effective, and scalable method of producing independent nanocrystals.[38] Since the process pulverizes the crystal, the size distribution broadens and there is a loss of any anisotropic morphology that could benefit SHG.

Various etching methods applied to masked wafers or thin films are among the more advanced techniques used today to produce submicron $LiNbO_3$ features. In three examples, light or electron beams can been used to produce thin-film $LiNbO_3$ features by ordinary lithographic techniques,[39] by selectively curing a photosensitive Li-Nb precursor[42, 43] or by writing ferroelectric domains.[44-46] Depending on the technique used, the modified portions of the wafer are then selectively etched with the use of acidic or organic solvents to reveal a patterned $LiNbO_3$ structure. These techniques allow the creation of highly controlled morphologies with specific crystallographic orientations. The dominant crystal orientation is a consequence of using thin-films that have been prepared by substrate-dependant epitaxial growth. The downfall of selective etching techniques is that they are typically more costly, less scalable, and the etched feature is typically composed of nanoscale crystal aggregates that make up the thin film. Neither of these classical methods is, therefore, suitable for producing $LiNbO_3$ with a fine control of size and morphology.

Syntheses that do not require a post-production modification to achieve

nanoscale dimensions are primary processes. These types of processes are more desirable, since post-production processing of $LiNbO_3$ becomes increasingly difficult as the targeted product dimension is reduced. A complete and up-to-date review of all the available techniques to produce nanocrystalline $LiNbO_3$ is tabulated in **Appendix 1, Table 1.2**. Most of these methods produce aggregates of isotropically shaped nanocrystals. Only two processes from this list can be highlighted as capable of producing independent crystals of $LiNbO_3$; the hydrothermal and the templated sol-gel method. These methods have also been shown to be capable of controlling the crystal morphology.

Templating methods rely on the presence of a matrix to confine the growth of the $LiNbO_3$ crystals. The templating method works very well at producing polycrystalline structures with a highly regular and elongate morphology. The technique is, however, restricted because of difficulties in removing the templating material in each case. Although the problem of template removal goes almost unmentioned, our work with porous alumina membranes have shown (via XPS) that they are very difficult to remove by the typical application of KOH. As an interesting example of how misleading the literature can be, Zhao *et al*.[40] make the following comment about their X-ray powder diffraction analysis: "*The templates do not disturb the measurements because their walls consist of amorphous alumina.*" This statement is misleading because Zhao also states that the membranes are easily and completely removed. Also, sometimes the removal of substrate leads to the partial destruction of the templated material. Again, Zhao *et al*.[48] are misleading by omitting the methodology by which

macroporous silicon membranes are “selectively etched.” Considering the formation of macroporous silicon templates occurs electrochemically in dilute HF, it is reasonable to assume similar conditions would be necessary for its complete removal. However, the HF also etches the *c*-axis of $LiNbO_3$.

The hydrothermal technique is notable for the low temperature and facile production of small and independent crystals with some degree of shape control. The process can be aqueous or non-aqueous, but it does require the use of a bomb reactor. Its potential with $LiNbO_3$ was realized as early as 1993 by producing $LiNbO_3$ nanocrystals that were slightly aggregated, fairly homogenous in size, and elongate in shape.[41] In a second report, Niederberger *et al.*[42] showed the technique is capable of producing very small, independant crystals of $LiNbO_3$ 20-60 nm in diameter. Most recently, the technique is now integrating the use of surfactants that can be selective in their surface coordination such that product morphology can be fine-tuned.[43] Capping of the nanoparticle surface by coordinating molecules appears, in the least, to be capable of producing isolated $LiNbO_3$ crystals.

Aside from the methods for producing $LiNbO_3$ above, there exists a separate body of literature that showed independent metal oxide nanocrystals could be produced with a high degree of control over the resulting morphology through the use of organometallic precursors and non-aqueous coordinating solutions. Nonhydrolytic solution-phase methods, such as these, are commonly found to result in single crystals of high compositional quality and excellent crystallinity.[52, 53] These reactions occur at ambient pressures in an inert

atmosphere and are non-aqueous because of the precursor water sensitivity and the need for higher reaction temperatures for crystallinity. The produced nanocrystals are independent, homogenous in size, and exhibit a specific morphology that is controllable based on reaction parameters. A review of metal oxide production by this method is provided by Park *et al.*[44] and Jun *et al.*[45] The nonhydrolytic solution-phase synthesis of $LiNbO_3$ nanocrystals was pursued in this research because of its prospect of achieving our goals towards an efficient NLO nanocrystal. As a previously unexplored route to $LiNbO_3$, it was also hoped to have an impact in the large research community who study this material. In the following section, the theory of solution-phase syntheses are described with an in-depth focus on the reaction parameters that contribute to affecting the product morphology.

2.3 The LaMer-Dinegar Mechanism for Nanocrystal Formation

Lamer and Dinegar[46] were the first to outline the theory that is the groundwork for the solution-phase production of nanoparticles. In their experiment they clearly outlined three stages that can be referred to as decomposition, nucleation, and growth. A fourth stage, aging, can also be considered as an informal part of this process.[47] The key point that Lamer and Dingar highlight is to isolate discrete nucleation and growth stages if a single particle size and shape is to be isolated. Once separated this process provides a proven method for designing specific particle morphologies. The nucleation stage of any material will always result in the formation of isotropically-shaped particles, but complex structures, such as, disks, rods, wires, tetrapods, and various

polyhedra, can result from subsequent growth when the reaction parameters have been properly controlled.

Regardless of the reaction taking place, the process always begins with the formation of a homogenous solution of the product precursor. Once formed, a reaction is initiated thermally by the rapid injection of this solution into a hot solvent, or chemically by the rapid injection of a reactant into this solution. The capping agent can be present in the precursor solution or as part of the solution to receive the injected precursor. For a select few examples, there is no injection step. Instead the precursor is dissolved in the coordinating solution and the temperature is simply increased. The thermally initiated reaction that results from either of these methods can be referred to as the decomposition stage of the process. During this stage the precursor decomposes or reacts to form small soluble “particles” called monomers (**Figure 2.1**). Eventually, with an increase in temperature, the solution becomes saturated with these monomers, but they remain dissolved. The monomers remain dissolved because the potential energy of a precipitated particle is still greater than the potential energy of the saturated state.[44] The monomers at this point do form small solids, but they are redissolved on account of their high surface energy. Nucleation occurs in a rapid “burst” once the critical concentration limit is reached (**Figure 2.1**). The critical monomer concentration represents the point where the energy of precipitation matches the energy imposed by saturation. Soon, the rate of nucleation plateaus in the limit where the rate of monomer production exactly matches their rate of consumption by nucleation. Once the monomer concentration returns to a point below the

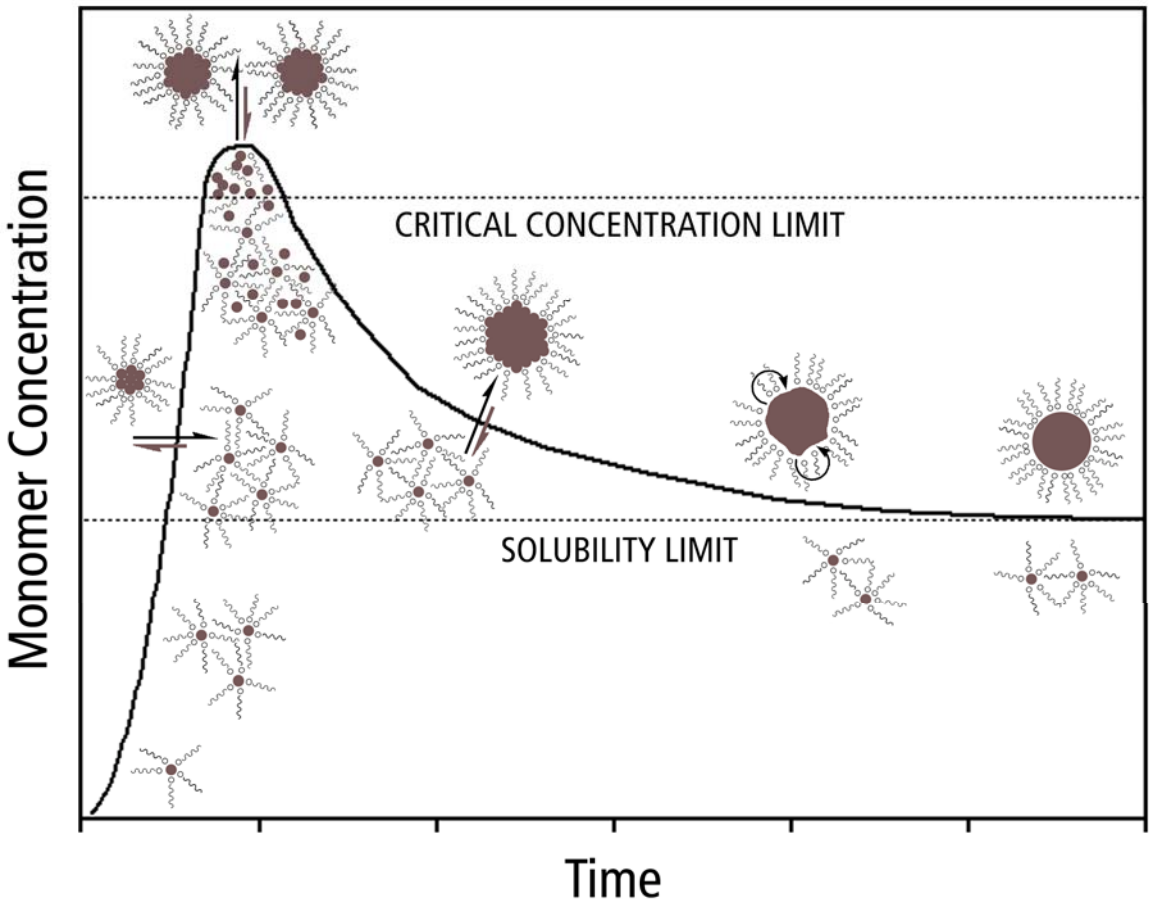

Figure 2.1 **The reaction profile of a typical solution-phase reaction. As time progresses, heat contributes to decomposition of the precursor that results in an increase in dissolved monomer concentration (shown beneath the curve). Once the solubility limit is reached, suspended aggregates appear, but are not stable enough to persist (solids are above the curve). Nucleation occurs once the critical monomer concentration is reached. Subsequent growth occurs until the monomer concentration returns to the solubility limit. Late in the scheme, Ostwald ripening acts to smoothen the surface.**

critical saturation point for nucleation, no further nuclei are formed.

Since the nuclei consist primarily of surface atoms, their shape is dynamically changing in an attempt to minimize their surface energy.[44] For a given material, a minimum chemical potential is found in shapes that exhibit a closed shell configuration of atoms.[48] Typically, this minimum occurs in one of a few “magic sizes” for the nuclei. The crystal unit cell could be one example of

such a closed shell configuration, but faceted crystals such as a 111-faceted tetrahedron (for cubic crystals) can also satisfy this condition. Many of the initial particles formed during nucleation do not survive the length of the reaction because of their high surface energy. Despite a closed shell configuration, many of these initial particles are so small that they contain a multitude of surface atoms and consequently, a high surface energy. These particles gradually redissolve to form soluble monomers. The shape of the nuclei that do persist affects the final shape of the crystal.

After nucleation, the monomers in solution are deposited on the surfaces of the nuclei during a growth stage. Smaller nuclei experience more rapid deposition as a result of a higher surface energy. As a result, the particle size distribution generally narrows during growth.[44] The growth stage continues until the system returns to normal levels of saturation.[46] The presence of the capping molecules and the choice of reaction parameters during this period affect the shape of the resulting nanocrystals. Many of these variables are discussed in more detail in the sections that follow.

Once normal saturation levels are approached, the aging stage begins. During this process, thermally driven crystallization continues and material is redistributed over the surfaces of growing particles to form lower energy surfaces. The redistribution of material is a process commonly referred to as Ostwald ripening,[44] and it is thermodynamically driven by a difference in potential energy between high and low surface energy sites.[49] More generally, the process is a mass transfer from smaller particles to larger particles, or from long crystal

axes to short crystal axes in order to produce lower energy spherical shapes.[52, 58, 60] Without the surface capping ligands, aging would also see the fusing of nanocrystals as a result of a natural self-assembly in attempt to minimize surface energy.[49] As a result of the aging process, a slight broadening of the particle-size distribution is typically encountered.[44]

2.4 Reaction Parameters that Influence Particle Size and Shape

In the preceding section, four primary stages for a solution-phase nanocrystal synthesis were discussed. Here, the reaction variables that affect those stages will be discussed in more detail. An understanding of their effect will lead to the choice of suitable conditions for producing the desired morphology in $LiNbO_3$. This theory will further benefit discussions, in **Chapter 4**, where the product morphology is analyzed.

2.4.1 Material Based Considerations

It is necessary to clarify that not all materials can be formed into intricate shapes by the solution-phase reaction. The ability of shaping a material starts with the chemical makeup of the crystal itself. In each crystal, there exists a number of crystallographic planes that can differ based on a number of factors, including, but not exclusive to, the charge of surface atoms, the degree of atom valency, and atom density. These factors combine to create a unique surface energy for each plane of a different composition (**Figure 2.2**). High surface energy planes are more unstable and reactive, and this facilitates naturally higher rates of material deposition. This growth disparity can lead to the formation of

anisotropic nanocrystal morphologies. Unilateral growth to form rods and wires is, therefore, limited to materials that exhibit a unique high surface energy composition in at least one direction.[50] Cubic crystal structures, with a centrosymmetric composition, cannot be synthesized as 1D structures by this technique. The most that can be done with cubic structures is to generate faceted symmetrical shapes of different sizes. The underlying consideration here, is that the shaping process starts with the material. Anisotropic structures will only form in materials with an anisotropic composition.

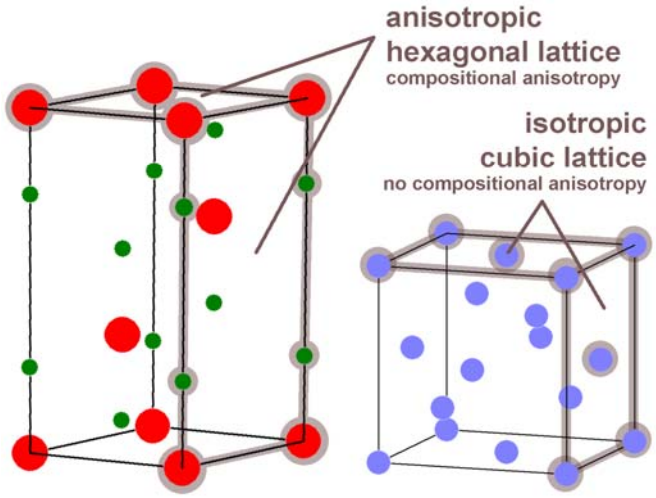

Figure 2.2 Hexagonal Li_2O (left) and cubic Si (right) lattices. The difference in surface composition in the Li_2O lattice creates planes with different surface energies, and this property is required to make anisotropic crystal morphologies by the solution-phase synthesis. In Si, the highlighted planes are compositionally indifferent.

2.4.2 Temperature and Time

In order to create a product with a single size and morphology there is a strict need to carefully regulate both temperature and reaction time. Rates, such as the decomposition, nucleation, diffusion, and dissolution rates of this reaction, involve time that is dependant on temperature through the Arrhenius equation. By constructing the appropriate temperature profile for a reaction, the first step has been made towards synthesizing nanocrystals of a specific form. The choice

of a temperature profile is, however, the most complex variable in a solution-phase reaction.

For the formation of monodisperse crystals the rate of temperature increase is important. If the critical saturation level in the solution is reached at a lower temperature, as a result of a low ramp rate, it can be expected that the decomposition rate will also be slow. If the monomer supply rate is slow, the rate of nucleation will also remain slow because it is dependant on the amount of monomers in solution. A slow rate of nucleation results in a prolonged nucleation stage and a poor separation of nucleation and growth. **Figure 2.3** shows the effect of ramping rate on the shape of the nucleation stage of the reaction profile. It is shown along with data from Yin *et al*.[49] who studied the effect of ramp rate on the synthesis of γ-Fe_2O_3 nanocrystals. With a prolonged nucleation, growth begins at different times for the nuclei produced. The result is a large standard

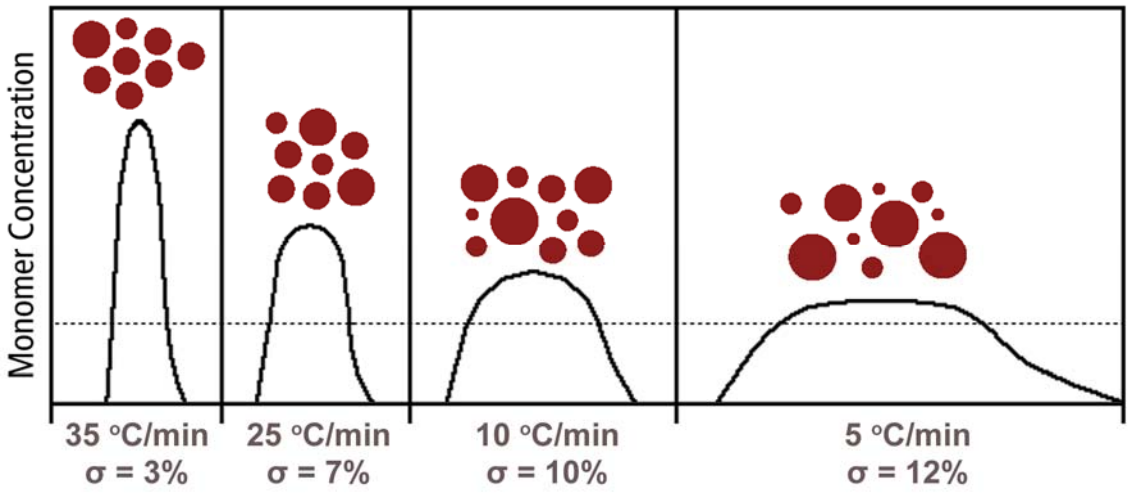

Figure 2.3 **The nucleation stage of the reaction profile as a function of reaction temperature ramping rate. The observed effect of increasing ramp rate is to shorten the nucleation event and it results in a narrowing of the particle size distribution. The assumption of these graphs are that the maximum reaction temperature has been met prior to the critical monomer saturation limit (dashed line).**

deviation (σ) in the particle sizes produced for reactions of a lower ramp rate. The average particle size in each reaction did not seem to change though.

The maximum temperature of reaction is critical to the growth phase of the reaction. Temperature will determine whether or not the growth phase will be thermodynamically or kinetically controlled, and one of either of these growth regimes can be chosen by adjusting temperature appropriately. The underlying cause of this control is an ability to regulate the production of monomers available for growth.[51] At high temperatures there is a rapid production of monomers in solution that leads to fast kinetic (anisotropic) growth on specific high surface-energy planes. At lower temperatures, the rate of monomer production is slower. Therefore, monomers deposit over a longer period of time where they typically deposit to create a more thermodynamically stable surface. In the case of a low reaction temperature, spherical particles typically result. Peng[48] has shown that this is the case in the synthesis of CdSe. In that work, it was shown that a high rate of monomer production in solution leads to rapid growth on specific planes to form elongated shapes.

Limitations do exist for the kinetic model. Temperature can only be used to increase the monomer flow up to a given point; thereafter, thermodynamic growth dominates (**Figure 2.4**). The break-down of the kinetic model can be associated back to the material-based considerations previously described. If substantial enough, heat can contribute to an equalization of surface-energies for anisotropic materials. Consequently, the driving force for anisotropic deposition is lost. An example of this is found in the synthesis of Mn_3O_4 by Seo *et al*.[52] By increasing

Figure 2.4 The kinetic and thermodynamic growth model contributing to (from left to right) nanocrystals, nanoeggs, nanorods, and nanowires. Technically, both the top and bottom axes can be considered "temperature." They have been labelled this way to distinguish between excessive temperatures leading to a loss of surface energy anisotropy (top), and to the regular thermal increase in monomer production (bottom).

the reaction temperature from 270 ^{o}C to 350 ^{o}C, aspect ratios of the product fell from 3 to 2.

The mechanism of temperature-based growth control is not only related to the rate of monomer production, but also to the binding equilibrium of the capping agent. The surface coordination of the capping molecules in solution are involved in a dynamic equilibrium between a dissociated and a bound form.[53] The equilibrium can be viewed as follows, where *L* is a surface coordinating ligand, and *S* denotes a precursor molecule, the surface of a monomer, or the surface of a nuclei:

$$L + S \rightleftharpoons SL + heat \qquad (13)$$

Despite the organization of capping molecules at the surface being entropically disfavourable, the enthalpic gain, denoted by a *heat* term in **equation (13)**, is large as a result of significant molecule-to-molecule Van der Waals bonding and dipole-dipole or coloumbic interactions at the surface of the

monomer or nanocrystal. As a result, the equilibrium is expected to favour the bound form under average laboratory conditions.

Physically, heat acts to destabilize the surface by forcing the equilibrium [**equation (13)**] towards a free molecule or exposed surface. Once exposed the monomers are more subject to nucleation, and the crystal planes are more likely to grow as a consequence. During nucleation, heat destabilizes the saturated monomer solution by exposing the surfaces of the monomer. This destabilization has the effect of lowering the critical monomer concentration for nucleation and leads to less nucleated material in a more brief nucleation event.[44] During this event, few particles are produced, but more material remains for growth on their surfaces (**Figure 2.5**). The outcome of the reaction is a larger crystal size relative to lower temperature conditions where more nuclei grow by deposition with less material. Park *et al*. provide an example of the temperature effect on **equation (13)** by modifying the solvent they used during the reaction.[54] The solvents, 1-hexadecene (bp = 274 ^{o}C), 1-octadecene (b.p. = 317 ^{o}C), and 1-eicosene (b.p. = 330 ^{o}C), can safely be considered as isomorphous non-interacting solvents for comparison in this example. The difference in their boiling point is responsible for the production of 5, 12, an 16 nm diameter nanocrystals, respectively. Interestingly, there was also an unreported linear relationship between the boiling point and the crystal size for the five solvents they studied.

During growth, heat destabilizes the planes that have the lowest binding coefficients for the capping agent. These planes are the first to be exposed to growth followed by the higher energy planes as the maximum reaction

temperature is increased. The presence of the capping agent equilibrium facilitates the naturally occurring material-based kinetic growth and hinders the kinetic model breakdown at higher temperature. More about this will be described later in this Chapter.

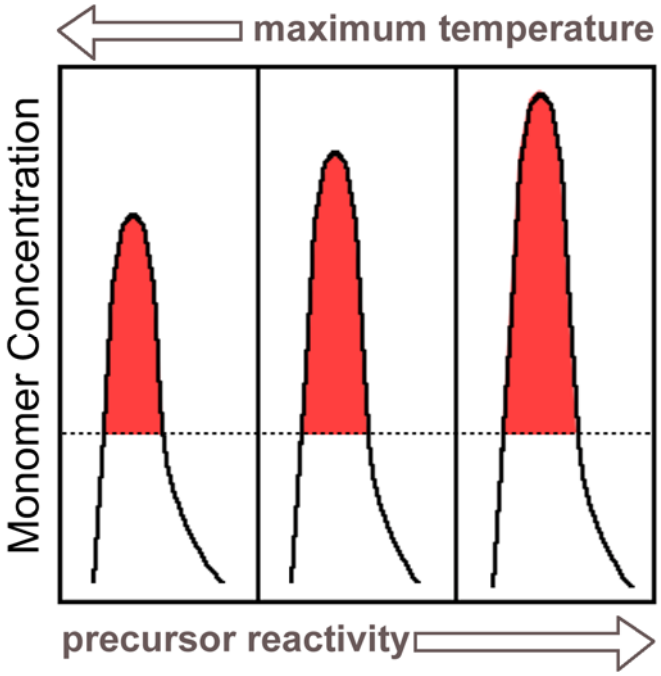

Figure 2.5 **The effect of maximum reaction temperature and precursor reactivity on the nucleation stage of the reaction profile. The critical monomer concentration (dashed line) is shown at the same level to emphasize the size of the nucleation event (red). Higher maximum temperatures destabilize the saturated condition by exposing the surfaces of the monomers. Destabilization acts to lower the critical monomer concentration limit causing nucleation at a lower reaction temperature. At a given temperature, a higher precursor reactivity results in a higher rate of monomer production. The rate of nucleation therefore matches the rate of monomer production at a higher level.**

The overall reaction time is the only aspect of time that is truly an independent and adjustable solution-phase synthesis variable. The reaction time can be stopped anywhere during the growth process to isolate nanocrystals of various sizes, or after the growth process and during some time in the aging process. The semiconducting QDs synthesized by Bawendi *et al.*[6] are a good example of how time can be used as a variable. They were able to produce 1.2 to 11.5 nm diameter nanocrystals simply by stopping the reaction at different times mid-

growth.[12] The reaction was haulted in their work by periodically withdrawing aliquots of the solution and cooling them. When nanocrystals are experimentally given more time to develop, effects of the aging stage start to take place. One may consider a longer aging period if crystallinity is slow to develop, or cut the stage short to avoid possible morphological changes to the crystal. Ostwald ripening, depicted in **Figure 2.1**, is one such process that modifies the shape of the crystal by redepositing nucleated material in more energetically favourable surface sites. If anisotropic structures were formed, Ostwald ripening acts to slowly reduce the aspect ratio. Another process of aging is aggregation. Given time at high temperatures, capping agents cannot completely prevent the periodic aggregation of nanocrystal surfaces. This process reduces the total amount of exposed high energy surfaces, and thus reduces the overall energy of the system.

In a small selection of materials, temperature can also be used to select between the growth of two or more different phases. This property of polymorphism is common for Mn and group 10 chalcogenides (e.g., CdSe, ZnS) that exhibit a cubic zinc blende or a hexagonal wurzite crystal structure based on the conditions maintained for the growing crystal. At lower temperatures the zinc blende polymorph is more stable and at higher temperatures the wurzite polymorph is more stable. By changing the temperature mid-reaction, the second polymorph starts to grow off the first polymorph leading to complex branched and tetrapod structures.[55] Beyond these materials, a number of oxide phases also exist and can be triggered to grow based on temperature conditions. In an

excellent example of polymorphism and the temperature effect, Tang synthesized HfO_2 at 360 ^oC and 400 ^oC.[56] As a result of this temperature change the stable crystalline phase changed from tetragonal to monoclinic. While both phases exhibit compositional anisotropy, the surface energies of the tetragonal planes are not sufficiently different at 360 ^oC to promote anisotropic growth. As a result, the product of this synthesis was 5.5 nm spherical crystals. At 400 ^oC, one monoclinic plane remained more chemically reactive and 3.4 x 7.6 nm long rods resulted. In order to conserve mass, one can also see that roughly 2.5 times the number of nanocrystals must form at lower temperatures, which is consistent with the fact presented earlier that heat promotes nucleation by destabilizing the monomer solution.

With respect to the synthesis of anisotropic $LiNbO_3$ nanocrystals, the targeted synthesis should have a high enough temperature to sustain a high production of monomers and achieve a crystalline product, but also low enough to ensure surface-energy anisotropy is not lost. Organometallic precursors used in solution-phase syntheses typically required temperatures of at least 200 ^oC to initiate decomposition.[57] Suitable crystallinity cannot be achieved, however, for $LiNbO_3$ outside the range of 350-600 ^oC.[58] At the low end of this range, the temperature is too low to permit ion mobility, and at the high-end of this range lithium mobility becomes so great it begins to be volatilized and seriously affect the product stoichiometry. Unfortunately, the solvent choice for a nonhydrolytic reaction become increasingly limited as the maximum reaction temperature is increased. Furthermore, our studies in the synthesis of γ-Fe_2O_3 indicate that the

capping agent also needs to have high temperature resistance in addition to a low volatility in order to remain present and active during the course of the reaction. Sterically guarded phosphine-oxides appeared to be the logical choice for our reaction because of their prevalent history in the nonhydrolytic synthesis of numerous metals, semiconductors, and oxides. Their popularity for use as a capping agent is the result of a high thermal stability[59] in absence of O_2, and they are polar leading to the formation of homogenous solutions with the precursor. Triphenylphosphine oxide (TPPO; dec. >360 ^{o}C) was used in the majority of our reactions as an inexpensive alternative to the more commonly applied trioctylphosphine oxide (TOPO) system.

2.4.3 The Precursor Choice and Concentration

The choice of precursor has a direct influence on the rate of decomposition. By choosing a more reactive compound or one that decomposes along a more energetically favourable pathway, the rate of monomer production can be increased. If the rate of monomer production is increased during the decomposition stages of the reaction, the rate of nucleation can be expected to equal the rate of decomposition at an overall higher monomer concentration **(Figure 2.5)**. The highlighted area under the nucleation curve of **Figure 2.5** is proportional to the amount of material nucleated, so it can also be expected to be proportional to the number of nuclei produced. A larger amount of material is nucleated through the use of more reactive precursors leaving less material for deposition onto the nuclei during the growth stage. Therefore, the final crystal size can be expected to be smaller. The relationship precursor has to maximum

temperature is found in **equation (13).** Both reactive precursors and heat lead to higher concentrations of monomer in solution.

As an example of the precursor effect, Joo *et al*. and Tang substituted chlorides for bromides in identical syntheses of ZrO_2[60] and HfO_2[56] nanocrystals, respectively. The crystal diameter was observed to change from 4.1 nm to 2.9 nm for ZrO_2 and from 5.5 to 3.7 nm for HfO_2. Since, bromine is a better leaving group than chlorine, the decomposition reaction is accelerated with the use of bromides. Similarly, Trentler *et al*. also found a reduction in particle size for the synthesis of TiO_2, upon switching from TiF_4 to $TiCl_4$, $TiBr_4$ and TiI_4.[61] In another example by the Hyeon group, a 1:2 mol ratio of precursor/oleic acid solution yielded 9-nm diameter crystals with $Fe(oleate)_3$[54] compared to 7-nm diameter crystals with a more reactive precursor such as $Fe(CO)_5$.[62] Hyeon's group realized the potential of such nucleation-loving ($Fe(CO)_5$) and growth-loving ($Fe(oleate)_3$) precursors and combined them in specific quantities to finely tune the synthesis of γ-Fe_2O_3 with diameters from 6 to 15 nm.[63]

The effect of precursor concentration has never been described independently. It is always mentioned in relation to the capping agent concentration in the form of a precursor-to-capping agent ratio, and therefore, its effect can be expected to be opposite to the well-documented changes in capping agent concentration (see the following section for more information).

A number of precursor decomposition pathways are also described in the literature. The most ideal and commonly applied cases yield the desired oxide and purely gaseous by-products. Common types of nonhydrolytic decomposition

pathways have been described in the articles by Vioux[57] and Pinna.[64] Reactions involving purely acetate or conjugate acid-based precursors are also common [e.g., Hyeon's Fe(oleate)$_3$], but the mechanism has not been explained. CO_2 gas is, however, known to be one of the by-products.

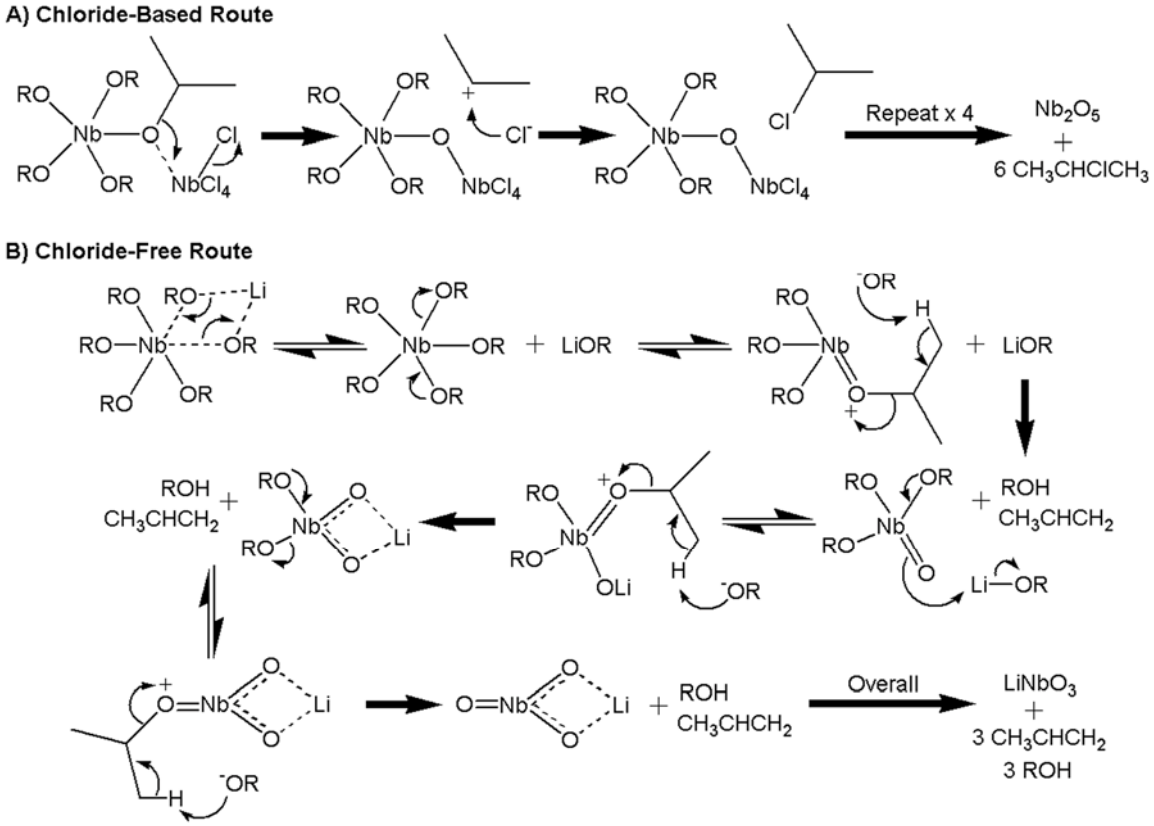

Figure 2.6 The alkyl-halide (A) and alkene/alcohol (B) decomposition reactions for $LiNb(OPr^i)_6$. $LiOPr^i$ is not shown in (A) because it undergoes a metathesis reaction to leave as inert LiCl.

In our work, we decided to use $LiNb(OPr^i)_6$ as an alkoxide in either an alkyl-halide (**Figure 2.6A**) or ester/alkene-alcohol elimination reaction (**Figure 2.6B**). This alkoxide has a more favorable decomposition pathway for the described reactions because of a more stable cation intermediate compared with primary alkoxides of lithium and niobium.[44,61] By stabilizing the carbocation, the

reaction progesses because the forward-direction of the equilibria is favoured. Based on previous kinetic arguments, a more reactive precursor should be chosen where the synthesis of anisotropic structures are sought. More reactive precursors maintain a high rate of monomer production at the maximum reaction temperature favouring the rapid growth of high energy planes.[48] We also chose this precursor deliberately because its metal stoichiometry is equal to our product stoichiometry, thus it is a single-source precursor. At the scale of our reaction, there would be considerable difficulty in accurately weighing the required quantities of individual metal compounds (especially the low-mass Li-compounds) for the appropriate stoichiometry. In $LiNbO_3$, the compositional purity is known to influence the optical properties greatly.[65,66] Unfortunately, the commercial availability and purity of our chosen precursor is an issue and the synthesis of our own precursor was an essential aspect of this project.

2.4.4 The Capping Agent Concentration

The influence of capping agent concentration can be understood from **equation (13)** previously introduced in this Chapter. If the concentration of capping agent increases in solution, the equilibrium adjusts to further favour the bound state (*SL*). In the bound state, the precursor is more stable against decomposition and a saturated solution of monomers can be stabilized causing the critical concentration for nucleation to be elevated. Based on this argument, fewer crystals form during the nucleation event, but more material remains in solution to be deposited during the growth stage. This leads to the synthesis of larger nanocrystals. Furthermore, the capping agent also coordinates to the

precursor, and the precursor stability increases with increasing capping agent concentration. The influence of increasing precursor stability was previously discussed and correlated with the formation of larger nuclei. Stabilization of the precursor and the monomer concentration both act to limit the number of crystals produced during nucleation and result in the growth of larger crystals.

A number of examples displaying the influence of the capping agent is available in the literature. In two reports by Hyeon, an increase in capping agent concentration resulted in larger nanoparticles. Using $Fe(oleate)_3$ in a 1:1, 1:2, and 1:3 mole ratio with oleic acid they produced 11, 12, and 14 nm diameter nanocrystals in 1-octadecene.[54] Using $Fe(CO)_5$ in a 1:1, 1:2, and 1:3 mole ratio of oleic acid, particle sizes of 4, 7, and 11 nm in diameter were synthesized in octyl ether, respectively.[62] These results were corroborated by Yin *et al*.[49] who further noted that the use of 1:1, 1:2, and 1:3 molar ratios also caused an increase in the decomposition temperature. In their work, the decomposition temperature of the precursor increased from 265 ^{o}C to 280 ^{o}C and 288 ^{o}C and nanocrystals of 4, 7, and 12 nm were formed, respectively. Tuning the particle size by capping agent concentration is not always a viable option. At high concentrations of capping agent small nanocrystals form, but a reduced amount of growth also results in broader size distributions,[49] and at low capping agent concentration the nanocrystals may be unstable against aggregation over time. Aggregation is known to occur with γ-Fe_2O_3 nanocrystals if they were rinsed too thoroughly in the purification stage. Despite its very weak donor capability, the rinsing solvent, ethanol, is capable of displacing oleic acid at the surface when

present in excess concentrations. Readdition of oleic acid after purification can aid with stability.

Capping agent concentration not only affects the nucleation stage, but also the growth stage. In general, its presence slows the growth of crystal planes by blocking monomer access to the surface. The effect of concentration on the growth stage may not be that apparent because an increase in the capping agent concentration (*L*) normally promotes *SL* formation while the high reaction temperature at growth normally reduces *SL* in the preceding equilibrium [**equation (13)**].

In our work, TPPO was the chosen capping molecule. Pure phosphine oxide reactions have been shown capable of producing small monodisperse nanoparticles of group IV oxides despite a fairly small precursor to capping agent ratio (1:10 to 1:12).[66, 70, 71] The unusually small nanocrystals that result from these reactions have not been explained in relationship to the theory of coordinating solution reactions.[44] Perhaps, growth is so hindered in these cases that the reaction teeters at the critical point for nucleation until most of the available precursor has been nucleated. Whatever the cause, a pure TPPO solution seemed a sensible method of generating nanoscale crystals.

2.4.5 The Type of Capping Agent

There are two types of capping agent, selective and non-selective, and they differ in how well they bind to the surfaces of the nanocrystal. Selective capping agents are characterized by a strong surface coordination. This strong coordination is typically confined to crystal faces with the highest surface energy.

By blocking “selective” planes, these types of capping molecules force deposition to the remaining exposed surfaces. Non-selective capping agents show no preferred coordination to any particular plane in the nanocrystal. They are characterized as weakly coordinating and they are more easily displaced as a result. With these types of capping molecules all the crystal planes show roughly equal coordinating strength.

In any reaction, the choice of capping agent type and design depends on the intended product and its desired morphology. Depending on the type of capping agent, these nuclei can be directed to form dots or anisotropic structures during the growth stage. The choice of selective capping at the right concentration should be the target of syntheses that aim to create elongate rod-like structures because these capping agents selectively direct deposition to a given set of planes. Nonselective capping can, however, produce anisotropic structures if the material exhibits strong compositional anisotropy and the reaction temperature is low enough that distinct surface energies still exist. In most cases, the latter point is not true and spherical crystals result. The choice of head group or coordinating moiety on the capping agent is purely material dependent. For example, a selective capping molecule for γ-Fe_2O_3, like oleic acid, is not a selective capping molecule in the synthesis of gold nanocrystals because of a chemical and physical difference between the surfaces of the two materials.

In the work of Jun *et al*., anisotropic TiO_2 structures were produced using lauric acid as a selective capping agent.[67] The strong binding affinity of the

<001> face for lauric acid resulted in an enhanced growth on the remaining <101> set of planes with an increasing concentration of lauric acid. As the precursor to capping agent mole ratio decreased from 2:1 through 1:4 a more complete growth retardation was observed for the <001> planes.[45] As the capping agent concentration was increased, bullet shapes changed to rods and branched rods that exhibited a decreasing amount of growth in the 001 direction. In this example, the effect of capping agent concentration was also observable. Higher concentrations of capping agent led to rods with a greater length and diameter, as fewer nuclei are generally created under these conditions. In the synthesis of Mn_3O_4, $W_{18}O_{49}$ and TiO_2 rods, Seo *et al*.[52] employed both selective and non-selective capping agents, however, the selective oxygen-donor, oleic acid, was decomposed during the reaction to provide the necessary oxygen. After decomposition the solution was left with a large amount of non-selective oleylamine to regulate growth. Due to its non-selective behavior, the high energy planes [[38] for TiO_2 and Mn_3O_4, and <010> for $W_{18}O_{49}$] [52] were not blocked, and they exhibited the highest growth rates. The direction of anisotropy for the rods was, therefore, in the direction defined by these planes.

The molecular design of the capping agent allows the production of varying degrees of coordinating ability. Thankfully, a wide range of capping agents are available for direct purchase, but the properties that influence their behavior need to be understood in order to make an appropriate choice of capping agent for a particular product. As a general rule, atom interactions between the surface and the capping agent should be paired to create hard-hard

or soft-soft interactions. In other words, small highly charged surface cations form more effective orbital overlap with equally small and highly charged anions. Likewise, large and polarizable cations with a low oxidation state prefer an equal anionic counterpart. This general rule explains the preference of the lower

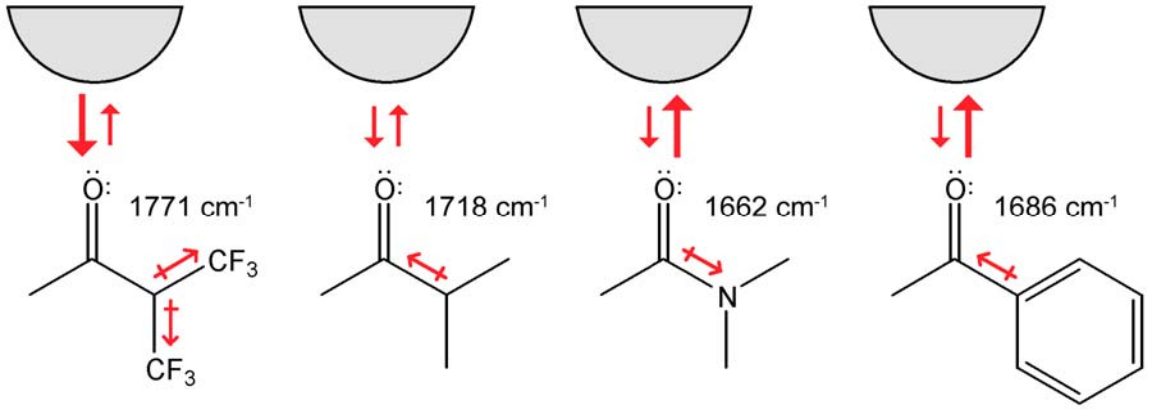

Figure 2.7 **An example of the factors that contribute to a "selective" versus "nonselective" capping agents in a solution-phase synthesis. Each of the four molecules is represented as participating in a binding equilibrium [equation (13)]. Selective capping agents (e.g., dimethylacetamide) are those that favour the bound-state as a result of factors such as resonance and inductive effects (denoted by dipole arrows). The donor ability of each molecule is signified by the energy of carbonyl stretching frequency.**

transition metal series like gold or platinum to sulfur and nitrogen-donors respectively, while Fe^{3+} or Nb^{5+} prefer oxygen-donors. Within the set of oxygen, nitrogen, or sulfur-donors, the resonance, and induction properties of the molecule can be tuned to further increase the bonding capabilities and the "selective" nature of the molecule. As an example, **Figure 2.7** shows a series of ketone-donors that are accompanied by their carbonyl stretching frequencies. These frequencies qualitatively indicate the amount of electron density that the molecule is capable of placing in the C=O bond. More electron density signifies an easier surface donation, and it arises as a result of resonance and induction

support present in the backbone of the molecule. Upon surface coordination each capping molecule would obtain a formal positive charge on the carbonyl carbon. Those molecules capable of supporting the charge better, will have a higher proportion of the bound state, *SL*, in **equation (13)**. In this case, acetophenone and dimethylacetamide support the formal charge better as a result of induction and resonance contributing to electron rich C=O bonds. Relatively speaking, acetophenone and dimethylacetamide are considered the more selective capping agents out of **Figure 2.7**.

Triphenylphosphine oxide (TPPO) is a nonselective capping agent because of a relatively weak coordinating ability in the phosphoryl head-group. Our use of TPPO at high temperatures is, therefore, expected to promote the presence of the free-ligands (*L*) and surfaces (*S*) more than through the use of a stronger capping agent. Coordination complexes between TPPO and various hard metal centers are well established,[68,69] and the complexes identify that the molecule would behave as an adequate capping agent for metals such as Nb^{5+} and Li^{+} on the surface of $LiNbO_3$. The donor strength of the phosphoryl group in TPPO (1193 cm^{-1})[70,71] is also comparable to the more commonly applied TOPO (1195 cm^{-1}),[72] but they differ significantly in their degree of steric hinderance. Our product will be anisotropic, as in the case of Seo *et al.*,[52] if $LiNbO_3$ contains enough surface energy anisotropy at the chosen reaction temperature.

2.4.6 The Steric Hindrance of the Capping Agent

The design of the capping molecule can also be chosen or modified to exhibit a varying degree of steric bulk. A limited selection of literature is available

to describe the effect of sterics alone because a change in the molecules backbone generally also implies an associated change in donor strength. The effect of sterics is clear though. A greater amount of steric bulk hinders both nucleation and growth by effectively separating the reactive monomers in solution.[53] Under the influence of bulky capping agents, the monomers in solution are less likely to aggregate to form nuclei because they are spaced further apart. Like capping agent concentration, this will result in increasing the critical monomer concentration. Fewer and smaller nuclei result in nucleation and there remains a large amount of material to be deposited for growth. While the growth stage may involve the deposition of a lot of material, bulky capping agents reduce the possibility that the monomers will encounter the surface of a particle. Therefore the growth stage becomes prolonged and it leads to highly spherical crystals with a narrow size distribution. The decomposition temperature of the reaction precursor is also shown to increase as the steric bulk of the capping agent is increased.[49] This result can be rationalized as an effect caused by a decreased tendency to cross-react two precursor molecules when they are spatially separated by bulky capping groups. If the precursor is more stable, larger nanocrystals would also result.

In Yin's work, octanoic, lauric, and oleic acid were compared in the synthesis of γ-Fe_2O_3.[49] Although the length of the carbon chain increases in this series, each of these acids has a carbonyl stretching frequency of 1711 cm^{-1} indicating that the backbone of the acid provides equivalent inductive support for

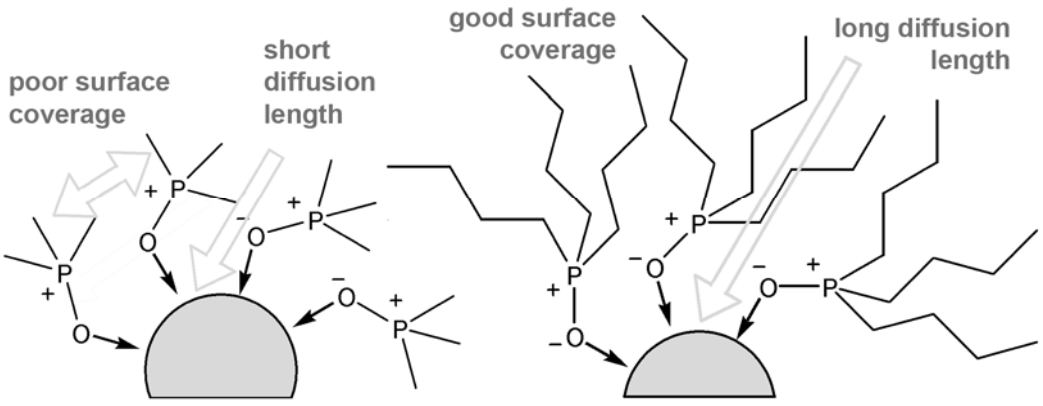

Figure 2.8 **Growth regulating attributes of the steric bulk in capping agents. Broad cone-angles and short backbone length couple to create a low surface capping density and short monomer diffusion lengths, respectively. This results in a less regulated and more rapid growth phase. Longer capping agents lead to better coverage and longer monomer diffusion lengths that slow the process of growth.**

coordination. The nanocrystals that formed were 6, 9, and 12 nm in diameter, respectively, for the three acids. Also, the crystal size distribution was narrowest when longer alkyl chains were used. The results of this synthesis were caused by a small nucleation an improved growth regulation by larger capping agents. In a slightly less ideal example, Park used tributyl-, triphenyl-, and trioctylphosphine to synthesize 2, 5, and 7 nm diameter Ni nanoparticles under equivalent reaction conditions.[73] The trend in crystal size is not completely the result of a steric effect because each capping agent also has a slightly different donor strength.

Two aspects of TPPO sterics make it noticeably different from TOPO; cone angle and the length of the capping agent extending from the surface. With a large rigid Tolman cone angle, TPPO is unable to densely pack on the surface of the nanocrystals (**Figure 2.8**). The large cone angle would result in openings in the capped surface where monomers can still collect. This point identifies that

the rate of growth will be faster for TPPO-capped surfaces than a more densely coated TOPO surface. In addition, the length of the capping agent is relatively short. If TPPO dissociates from a surface, a solvated monomer does not have far to travel before it can be deposited, whereas if TOPO dissociates from a surface, the monomer may not have time to reach the surface before TOPO recombines. In summary, the short distance that TPPO extends from the surface and the large cone angle will contribute to more poorly regulated and rapid growth.

2.5 Our Method of Synthesizing $LiNbO_3$

In this work, two nonhydrolytic decomposition processes were explored for the synthesis of crystalline $LiNbO_3$. As described, these reactions both employed a solution of TPPO as a non-surface selective capping agent. Only one of these approaches was successful in the production of $LiNbO_3$; the other synthesis produced crystalline Nb_2O_5 (**Figure 2.6**).[74] The later route was based on the cross-reaction of metal halides with metal alkoxides. This reaction is believed to result in the elimination of volatile haloalkanes while forming oxo-bridges between metal centers.[57] Several authors have reported the successful synthesis of both homo and heterometallic group IV oxides by this technique,[66, 70, 71] but the technique has not been demonstrated on heterometallic materials containing alkali metals. The chemical inertness and stability of these halides hindered the formation of $LiNbO_3$ by this method. The alternative approach requires the use of only metal alkoxides. This decomposition is thought to be initiated by the removal of a γ-hydrogen on an adjacent alkoxide ligand. This process produces gaseous alkenes and alcohols in addition to the metal oxide, $LiNbO_3$.[57]

In the chloride-based route, 4 mmol of niobium and lithium each were added to a mortar in the form of 0.91 g (2 mmol) lithium niobium isopropoxide ($LiNb(OPr^i)_6$, Chemat Technology, 99.9 %), 0.08 g (2 mmol) anhydrous lithium chloride (LiCl, Alfa Aesar, 99 %), and 0.54 g (2 mmol) niobium chloride ($NbCl_5$, Alfa Aesar 99.9 %). This mixture was ground in the glovebox with 12.80 g (46 mmol) of TPPO (Aldrich 98 %) until thoroughly blended. The chloride-free process was prepared in a similar fashion, except with 1.82 g (4 mmol) $LiNb(OPr^i)_6$ to account for the lack of chloride precursors. For either method, the ground mixture was loaded into a 3-neck 50 mL round-bottom flask containing a glass-coated stir bar and heated to 360 ^oC at a rate of 3.3 ^oC/min (for setup see **Figure 4.11**). Both mixtures form homogenous solutions near the melting point of TPPO. Crystalline materials were obtained from these solutions without the need to sinter at higher temperatures. Inert conditions (N_2, 4.8 grade, dried gas) were rigorously maintained during precursor mixing and during the course of the reaction.

Samples were prepared for electron microscopy and powder diffraction analysis by extracting the excess TPPO three times with acetone. Later experiments performed purification using a 3:1 (v/v) acetone/hexanes solution that was found to isolate the product in a higher yield (see **Chapter 4**). Diffraction of the isolated powder was integrated over the course of 20 min using a Rigaku R-Axis Rapid diffractometer equipped with a 3 kW sealed tube copper source (Rigaku long fine; 46 kV, 42 mA) collimated to 0.5 mm. The sample was analyzed in a 3 mm diameter by 5 mm deep hole in a glass sample holder. The

resulting spectra were characterized using an indexing routine in MDI Jade 5.0 software.[75] Transmission electron microscopy studies were performed using a Tecnai G2 electron microscope (FEI) operating at 200 kV. Sample grids (Formivar carbon-backed 400 mesh Cu) used in this analysis were prepared by dipping the grid into an ethanol suspension of the reaction products. The grid was air-dried under the heat of a halogen desk lamp positioned ~5 cm away.

2.6 Concluding Remarks

In this section, the processes that have produced nanocrystalline $LiNbO_3$ were introduced. From a wide range of methods only the hydrothermal and the sol-gel templated techniques emerged as capable of producing anisotropic nanoparticles of $LiNbO_3$. In the sol-gel templated technique, difficulties surround the removal of the template and in the hydrothermal technique high pressure bomb-reactors were an unattractive alternative for the synthesis of $LiNbO_3$. The nonhydrolytic solution-phase synthesis of $LiNbO_3$ performed in this research was a promising method that had not yet been explored. The solution-phase route has been known to controllably synthesize high quality heterometallic oxides with various nanocrystal morphologies, and as a result, it was well suited for our goals in this research. The reaction parameters for the solution-phase synthesis of $LiNbO_3$ were described in this section in relation to the theory of nonhydrolytic solution phase syntheses. A pure triphenylphosphine oxide solution was chosen to decompose $LiNb(OPr^i)_6$ at a temperature of 360 ^oC in this reaction. In **Chapter 3**, attention is directed to the synthesis, characterization, and optimization of $LiNb(OPr^i)_6$ for the purposes of use in our solution-phase synthesis of $LiNbO_3$.

CHAPTER 3 – OPTIMIZATION OF $LiNb(OPr^i)_6$ FOR THE SOLUTION-PHASE SYNTHESIS OF $LiNbO_3$ NANOPARTICLES

3.1 Introduction

The precursor, $LiNb(OPr^i)_6$, used in the synthesis of $LiNbO_3$ nanocrystals is a complex compound with a degree of OH^- or O^{2-} in the place of isopropoxy groups. When $LiNb(OPr^i)_6$ is purchased from commercial sources, the extent of OH^- and/or O^{2-} substitution varies, and the material contains varied amounts of solvent residue. These facts have led to inconsistent results when commercial $LiNb(OPr^i)_6$ precursors are reacted in the solution-phase reaction described in **Chapter 2**. Specifically, the solution-phase reaction produces $LiNbO_3$, but the amount of $LiNbO_3$ relative to other impurity phases varies batch to batch and company to company. Formerly, $LiNb(OPr^i)_6$ was purchased via Chemat Technology Inc. (Northridge, CA) and Alfa Aesar, but there was visible inconsistencies in the color, habit, and homogeneity of the precursor batch to batch. This variability became increasingly evident as the synthesis of high purity precursors was investigated in this research. It is for this reason that **Chapter 3** is devoted to the synthesis and characterization of the alkoxides relevant to the synthesis of $LiNbO_3$. These investigations would eventually lead to an understanding of how the solution-phase synthesis of $LiNbO_3$ could be optimized. In addition, this Chapter also introduces my study of other alkoxides such as

$Bi(OPr^i)_3$, $B(OPr^i)_3$, and $K(OPr^i)$ that are important components in the precursors of other relevant second harmonic materials. A number of standard inert-reaction methods (SIM) are also introduced in this Chapter. These techniques have been summarized in **Appendix 2** of this work. The bracketed SIM notation appears periodically and is used to avoid the repeated discussion of the same reaction procedures. Unless stated otherwise, all of the reaction solvents have been purified by the process described in SIM-B, and all of the inert gases are 99.998 % pure and have been passed through a Drierite column and a copper-based oxygen scrubber.

3.2 Synthesis of Lithium Isopropoxide ($LiOPr^i$)

The synthesis of lithium isopropoxide was pursued by two methods in this research. The first method involved a redox reaction between metallic lithium and an alcohol of choice as shown below:[76]

$$2Li + 2Pr^iOH \xrightarrow{\textit{reflux, heptane}} H_{2(g)} + 2LiOPr^i \qquad (14)$$

The described reaction is driven to completion by the continuous generation of $H_{2(g)}$. The rate of the reaction depends on the tendency of the alcohol to ionize and the ease of which the metal will oxidize. Alcohol pKa values can be used to describe this ionization potential. Larger and more highly branched alkyl groups, inductively donate electron density to the alcohol oxygen better than straight chain isomers. Consequently, the oxygen draws less electron density from the OH bond reducing its polarity, acidity, and reactivity in the above

reaction. The choice of isopropanol, therefore, results in a longer reaction time. As for the metal reactivity, the electronegativity can be used as a measure of the electron donor capability. As the top-most member of its group, lithium has the highest electronegativity of alkali metals, meaning it reacts the slowest in its group. The overall result of this is a slow reaction that takes 24-72 h to complete.

In a typical synthesis of $LiOPr^i$ ~2.0 g (0.29 mol) of lithium rod (Alfa Aesar, 99.9 %, 0.5” dia) is washed three times in the glovebox with 5 mL of heptane to remove any packing oil. The rod is then cut into 1/8” pieces and added with a stir bar to a dry 500 mL Schlenk flask. The flask is sealed with a sleeve septum then removed from the box, and attached to a Schlenk line where nitrogen flow is applied through the side stopcock. Dried heptane (100 mL, Caledon, 99.8 %) is then transferred into the flask via a procedure outlined in SIM-C. This transfer is followed by the addition of a mixture of 20 mL (0.26 mol) dried isopropanol (Caledon, 99.7 %) and 100 mL of dried heptane via the same procedure. Under positive nitrogen flow, the septum is removed from the reaction flask. The flask is attached promptly to an evacuated (SIM-A) water-jacketed condenser that also has a positive nitrogen flow through a top inlet adaptor. Once connected, the flask stopcock is closed and the flask is set into a 380 W Glas-Col heating mantle. The temperature of the reaction is gradually brought to 110 ^oC to avoid the loss of refluxing isopropanol as a result of rapid hydrogen evolution. The solution is stirred for a minimum of 24 h. Longer reaction times in further studies can lead to coloration through hydrolysis and oxidation events that will be described later in further detail.

The procedure outlined in SIM-D is used to isolate the filtrate from the excess lithium. The reaction product is collected as a white crystalline powder after vacuum distillation of the filtrate solvent at 50 ^{o}C. The product normally appears faint yellow (48 h) and light orange (72 h) in color when the reaction time is extended beyond 24 h. After further pumping by vacuum for 24 h at 50 ^{o}C, the product is then stored in the glove box. The yield is close to quantitative and there is little evidence to support Kamienski and Lewis'[76] claim for a reaction time greater than 24 h.

The second method of preparing lithium isopropoxide is cleaner and faster, but is also more expensive. As it turns out, the synthesis of high purity $LiOPr^{i}$ by the preceding metal redox method is not possible. Lithium rod always comes with a slight black tarnish on the surface that is the result of trace hydroxides and oxides of lithium. The use of butyl lithium removes this source of impurity and results in a higher purity product. The described reaction involves an acid/base type reaction between an alkyl lithium (base character) and an alcohol (acid character):[77]

$$Bu^{n}Li + Pr^{i}OH \xrightarrow{-78\ ^{o}C,\ heptane} Bu^{n}H + LiOPr^{i} \qquad (15)$$

In a typical experiment, 5.0 mL of distilled isopropanol is transferred to a dry and evacuated 250 mL Schlenk flask (SIM-A) with the use of a dry gas-tight 5 mL syringe. The flask is then submersed in a dry-ice/acetone bath with stirring. Once cooled, a clean 5 mL gas-tight syringe is used to deliver 20.0 mL of 2.5 M

Bu^nLi (in hexanes) drop-wise. Violent steaming was observed during this addition. Once the addition was complete, the acetone bath is removed and the reaction is allowed to warm to room temperature. A filtration step (SIM-D) was performed to remove any solid impurities that may have formed, and the product was isolated after vacuum distillation of the reaction solvent at 50 ^oC. $LiOPr^i$ is collected as a white powder in a total reaction time of about 2-3 h. The isolated powder is dried under vacuum at 50 ^oC for 24 h prior to storage in the glove box.

3.3 The Origin of Color in Lithium Isopropoxide

In this research, $LiOPr^i$ was synthesized primarily by the metal redox method because of its low cost, ease of synthesis, and suitability in the production of $LiNbO_3$ by our solution-phase synthesis. One of the biggest mysteries surrounding this product is the origin of color as the reaction time is increased (**Figure 3.1**). The answer to the origin of color was important to this research because the solution-phase synthesis of $LiNbO_3$ worked optimally when the darker red $LiOPr^i$ ("super-red")[78] was used in preparing the $LiNb(OPr^i)_6$. Several hypotheses were formed about the origin of color including: ketone contamination, the

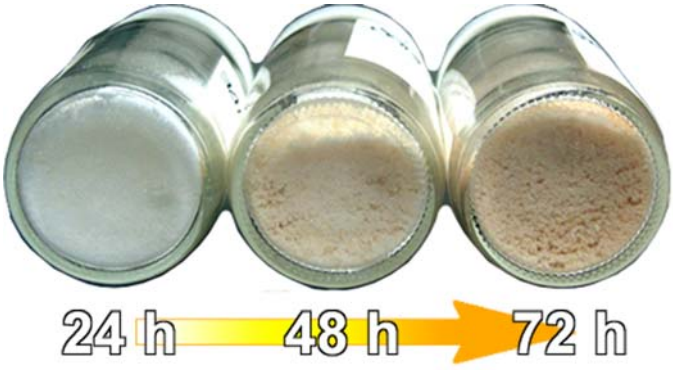

Figure 3.1 **Color of the $LiOPr^i$ after 24, 48, and 72 h of synthesis by the metal redox method [equation (14)].**

black Li-rod tarnish, temperature, a photochemical reaction, water contamination, and oxygen contamination.

The first of these hypotheses was suggested by Dr. Nabyl Merbouh of the Department of Chemistry at SFU, who pointed out that the isopropanol (Caledon) contains a small ketone impurity that might undergo a series of base catalyzed aldol addition and condensation reactions to form large conjugated organic compounds. To test this hypothesis a small reaction (50 % scale) was performed according to the same experimental procedure as before except it was deliberately tainted with 1 mL of dry acetone. After 3 days at 120 ^{o}C, there was no presence of color. However, after one month on the benchtop, a faint yellow coloration was observed. This result appeared to disprove the ketone hypothesis, but possibly provided evidence of exposure to light, oxygen, or water that could have occurred over the course of a month on the benchtop. The possibility of a photochemical reaction was soon eliminated from this list by performing another reaction shrouded in aluminum foil. Subsequent experiments were performed to explore the remaining possibilities.

Temperature was suspected to affect the molecular structure of the isolated LiOPr^{i}, which could have an impact on the absorption characteristics of the molecule. As the state of oligomerization in LiOPr^{i} increases, it is expected that the HOMO-LUMO gap decreases, and the absorption will red-shift. Since the perceived color of the compound has a complementary relationship to the compound absorption, a yellow 48 h LiOPr should have a violet absorption, and

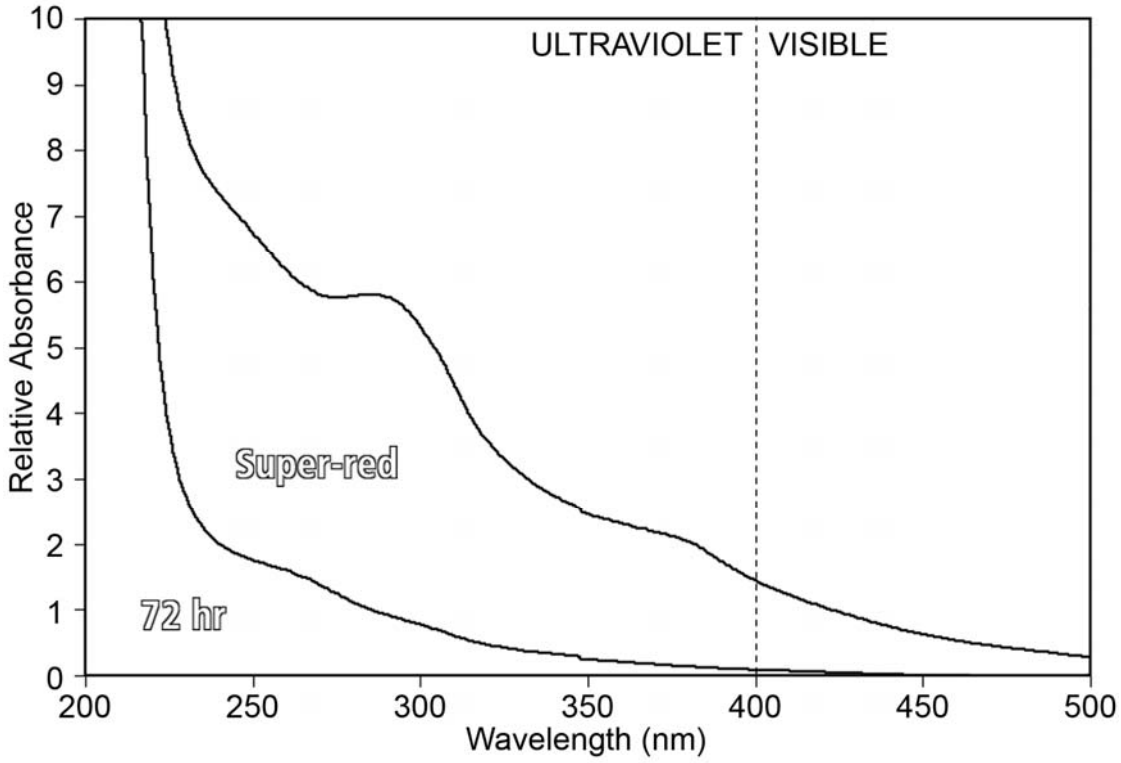

Figure 3.2 **UV-Visible spectra for a 72-h sample of LiOPr^{i} and a "super-red" sample of LiOPr^{i}. As time progresses the ultraviolet absorption tails deeper into the visible spectrum**

the "super-red" compound should have a blue absorption. This theory agrees with the observed UV-visible absorption spectra of the two samples (**Figure 3.2**). The EI-MS data of Kahn *et al*. shows that reaction temperature does influence the molecular complexity of LiOPr^{i}.[77] In Kahn's work, higher preparation temperatures favoured the formation of cubic tetramers and at lower reaction temperatures hexameric complexes were formed. LiOPr^{i} can complex to form a large array of oligomeric structures including square (2 units), hexagon (3 units), cube (4 units), hexagonal prism (6 units), and fused hexagon-cube prism (8 units).[79] Infinite polymeric chain molecules of LiOPr^{i}·5Pr^{i}OH are also known.[80] Since larger complexes are expected to have a greater degree of absorption in

the visible spectrum, the temperature used for the synthesis of $LiOPr^i$ was reduced to just 80 ^oC. After 72 h, the reaction looked typical of observations at 24 h from any other higher temperature reaction. The powder isolated from this reaction was without a trace of color. Further reactions were performed at several higher temperatures that were only able to establish that refluxing is mandatory (>100 ^oC) for the creation of color in $LiOPr^i$. Here, the absorption and temperature studies suggest that large complexes are present, but beyond a threshold temperature heat is not contributing to their formation. Complexes larger than hexamers and tetramers are likely present here. The minimum temperature of 100 ^oC seems to suggest these complexes could have been the product of initial water contamination that is followed by a subsequent condensation reaction to eliminate isopropanol.

Water contamination, oxygen contamination, and the black lithium rod are all related to the atmospheric conditions of the reaction and of the stored reagents. Since black lithium can be produced by deliberate exposure of lithium to atmospheric oxygen and moisture, only the previous two factors were deemed necessary to study. As a quick check of this hypothesis, a small reaction was performed without concerns for atmospheric purity. The lithium rod was handled in air, and the reaction was assembled without purging with nitrogen (SIM-A not performed). After 72 h of reaction at 100 ^oC, a faint yellow solution was observed, and suggests that oxygen or moisture contamination is necessary.

Water contamination was considered the most likely culprit because of observations seen in the formation of the “super-red” $LiOPr^i$ compound. The

lithium wire in the “super-red” reactions was originally stored on the benchtop, and the solvents were only treated by primary drying. As a result, significant amounts of white hydrolyzed precursor precipitated in the first few hours. During the next 48 h, however, the precipitate progressively dissolved back into solution to give a red solution. Assuming that condensation reactions were occurring between hydrolyzed and non-hydrolyzed $LiOPr^i$, an inert reaction was performed where the trace amount of LiOH precipitate was filtered from the reaction (SIM-D). The clear filtrate was refluxed for an additional 48 h. At the end of this reaction, the solution was colorless. This result supported the hypothesis that water was necessary for the formation of “super-red” $LiOPr^i$. However, when 1 mL of distilled deionized H_2O (18 MΩ) was subsequently added, the resulting solution remained colorless even after 24 h of reflux. This conflicting result led to the suggestion that another factor was involved in forming color in $LiOPr^i$.

To test the theory of oxygen derived red coloration, a small amount of white 24 h $LiOPr^i$ was placed in a scintillation vial in the glovebox, dissolved in distilled heptane, and sealed with a sleeve septum. This solution was refluxed under a dry oxygen atmosphere. No color change was observed, but once a small amount of distilled deionized H_2O was added, LiOH immediately forms and the solution became yellow then dark orange with time (~5 min). These results suggested that both water and oxygen impurities are necessary for the formation of colored $LiOPr^i$. In a series of quickly executed experiments, it was further found that only a small amount of oxygen is necessary to form a colored solution, that the solvent polarity is important, and that temperature only seems to

increase the rate of coloration under these conditions (high O_2 / H_2O concentration). In more polar solutions that contained isopropanol, the reaction was much slower. After 24 h of heating at 100 ^oC only a dark yellow solution was obtained. One suggestion for the slow formation of color in the presence of isopropanol could be that neutral O_2 and Pr^iOH donors compete for a lithium site in the initial stages of the unknown reaction mechanism.

Little precedent exists in the literature for the reaction between lithium alkoxides, atmospheric oxygen, and moisture to help support a mechanistic discussion. Lambert, appears to be one of the few to study these conditions by crystallizing "$(Bu^tOLi)_{10}\cdot(LiOH)_6$" (**Figure 3.3**).[81] In their work nothing was suggested about the role of oxygen despite the fact that lithium alkoxides are known to produce oxide bonds through a radical reaction with oxygen.[82] Since the hydrogen atoms were never identified by X-ray diffraction as all OH-based, an alternative interpretation could be the $(Bu^tOLi)_8(Li_2O)_2(Bu^tOH)_2(LiOH)_4$ structure. This interpretation seems more reasonable than to suggest that two of the hydroxyl groups occupy unusually high six-coordinate sites, and also agrees with the anticipated production of oxide bonds. It is

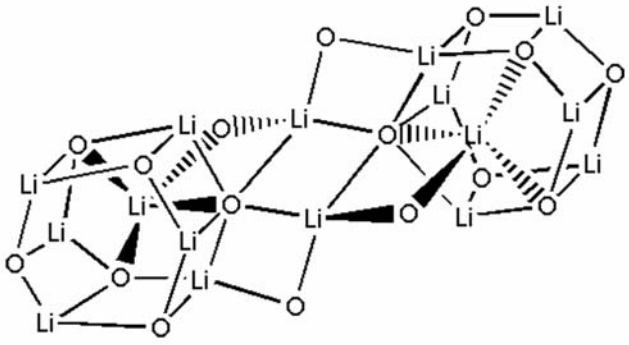

Figure 3.3 Structural representation of "$(Bu^tOLi)_{10}\bullet(LiOH)_6$", a compound created by reaction of O_2 and lithium t-butoxide. The t-butyl groups have been omitted for clarity. They can be found on the five oxygen atoms (with CN < 6) of each hexamer.

interesting to observe that every alkoxide-based lithium is stable enough to exist in a three-coordinate geometry, whereas, OH-based lithium sites require a fourth donor (CN4) for stability. The correlation between increasing coordination number and OH at a lithium site implies a change in the electrophilic strength of the alkoxide lithium. The cause of this change is a weaker inductive donation character in OH^- groups relative to OPr^{i-} groups. From previously described experiments it is known that water (causing the formation of OH bonds) is a required contaminant prior to the possibility of reaction with O_2 to form a colored complex. It is reasonable to suggest that these two observations are not coincidental, and that the mechanism of color formation involves O_2 reacting with three-coordinate $LiOPr^i$ sites once they become hydrolyzed.

3.4 Characterization of Lithium Isopropoxide

Proton NMR of $LiOPr^i$ at various times was hoped to provide some structural evidence towards our current theory. The ^{1}H-NMR of 24, 48, 72 h, and "super-red" $LiOPr^i$ are shown in **Figure 3.4**. The main signals in all spectra are a methyl doublet and methyne septet, with integration that would be expected for $LiOPr^i$. The methyl peak appears distorted such that the upfield peak is higher in intensity, and it is not the result of peak overlap in all cases (**Figure 3.4A**). The distortion is not fully understood, but it was observed in standard samples of isopropanol. The methyl and methyne peaks also appear to shift downfield slightly which could be an indication of a slightly more electron withdrawing environment caused by the introduction of OH^- groups and additional lithium bonds over time. In addition, the spectra are further complicated by additional

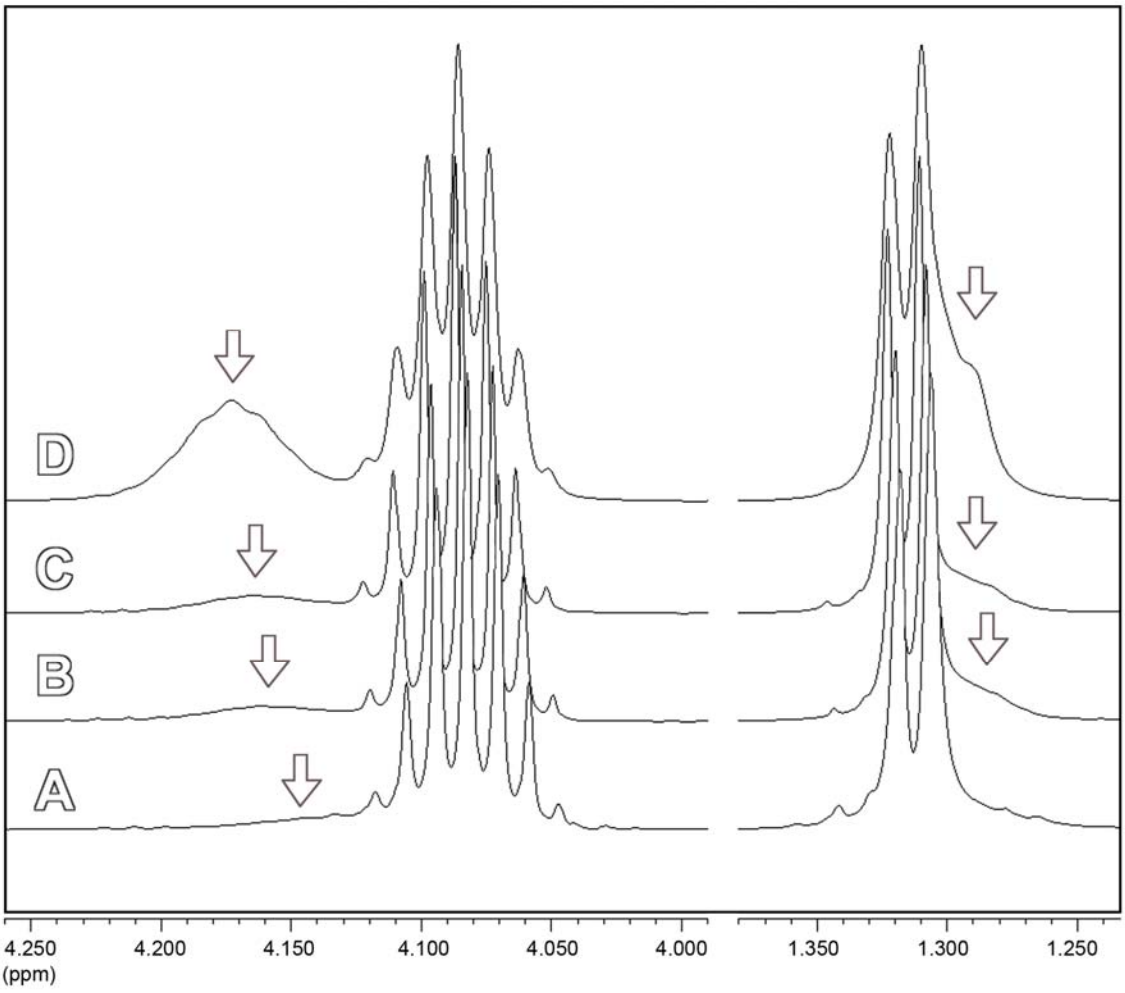

Figure 3.4 **^{1}H-NMR (500 MHz) of LiOPr^{i} in d_6-benzene.[83] Samples were prepared via equation (14) after (A) 24, (B) 48, and (C) 72 h of reaction. (D) represents an advanced stage of the compound and is called "super-red" for its dark orange-red appearance. Note the rise of a second set of methyne and methyl peaks as the intensity of coloration increases (arrows).**

bands, upfield of the doublet and downfield of the septet. The intensity of these unknown bands (arrows in **Figure 3.4**) grows over time, and they are consequently expected to be related to the observed color changes of the product. These broad peaks also have a faintly observable coupling that appears to correlate with an approximated 6:1 intensity ratio for the methyl and methyne peaks, respectively. This data, as well as ^{13}C-NMR, suggests that another

isopropoxide environment exists in the oxidized compound. The difficulty with this assessment is that the shielding effects seen for the methyl and methyne of this additional isopropoxide environment appear to contradict one another. The methyl signal is shielded while the methyne region is deshielded.

To answer this contradiction, one needs to take a comparative look at the ^{1}H-NMR of another more electropositive alkoxide such as $Nb(OPr^i)_5$ (discussed later in more detail). The ionic radii of Li^+ and Nb^{5+} are similar, so one can expect that the electron-withdrawing nature of niobium is much higher than that of lithium on account of a greater charge density. The ^{1}H-NMR methyne region of monomeric $Nb(OPr^i)_5$ and the 24 h $LiOPr^i$ product reveal septets centered at 4.829 ppm and 4.082 ppm, respectively, and the niobium has caused a more significant deshielding effect as expected. The chemical shifts in the methyl region are quite the opposite. Methyl signals of $Nb(OPr^i)_5$ occur at 1.280 ppm versus 1.311 ppm for $LiOPr^i$. If this deshielding effect was simply the result of bridging $LiOPr^i$, one would expect to have seen an even stronger deshielding in the methyne protons that are more closely situated to the bridging bond. One rationalization for the observed trend is that the structure of $LiOPr^i$ positions methyl protons such that intramolecular dipole bonding occurs within the oligomer. Once oligomers become cross-linked by condensation and/or reactions with O_2 (not shown), sterics may contribute to disrupting the original dipole bond (**Figure 3.5**). In addition, the new oxide bridge has a stronger electron-withdrawing effect that would cause the associated adjacent methyne protons to deshield. As a result, a new ^{1}H-NMR signal is produced downfield of the methyne

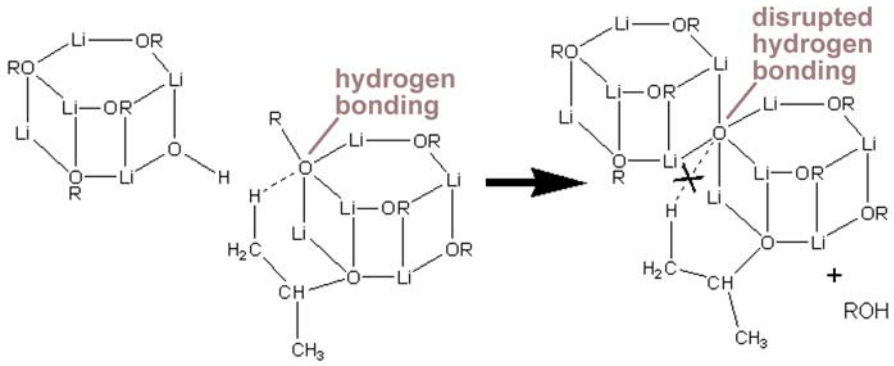

Figure 3.5 Model displaying dipole bonding within oligomeric LiOPr^i and the disruption of those bonds following a condensation reaction.

and upfield of the methyl for the affected isopropoxides.

From the spectral experiments with LiOPr^i, we have identified that color develops due to a broad absorption that protudes deeper into the visible spectrum as it grows in intensity. The reason the absorption grows in intensity has been speculated through ^{1}H-NMR studies to be the result of cross-linking multiple LiOPr^i oligomers through condensation and/or oxygen-related reactions. Aside from the reaction requirements, a clear mechanism to the formation of color is still unknown.

3.5 Synthesis and Characterization of Na, K, and Ba Isopropoxides

Sodium, potassium and barium alkoxides are synthesized by the direct addition of the metal to the alcohol as in the synthesis of lithium alkoxides in **equation (14)**. Our interest in these compounds is to use them as metathesis reagents or as components in precursors to SHG materials such as $KNbO_3$ or β-BaB_2O_4. Unlike the lithium alkoxides, these metals form alkoxides with noticeably different solubility properties. In particular, $Ba(OPr^i)_2$ was not easily solubilized and the synthesis of NaOPr^i and KOPr^i were no longer performed in a hexane

solution. Instead, an excess of isopropanol solution was necessary in the synthesis to keep the products solubilized. In this section, the synthesis and characterization of these materials is described.

In this research sodium alkoxides were used as metathesis reagents, specifically for the synthesis of $Nb(OPr^i)_5$ and $Bi(OPr^i)_3$. The synthesis of $Bi(OPr^i)_3$ is relevant to future work that may involve BiB_3O_6 as a NLO nanocrystal. The preparation of $Bi(OPr^i)_3$ is described further in the following sections of this Chapter. For the synthesis of $NaOPr^i$, 1.00 g (43.5 mmol) of sodium (Aldrich, cubes 99.95 %) was removed from the packing oil and washed three times with ~3 mL of dried heptanes in the glovebox. The clean sodium cube was then transferred to a 250 mL Schlenk flask containing a Teflon stir bar and capped with a sleeve septum. The flask was attached to the Schlenk line and a strong nitrogen gas flow was applied through the side-arm. The sleeve septum was then replaced with a dry condenser that, once purged of oxygen, was capped by a sleeve septum. The nitrogen supply was then switched from the side-arm to the top septum and 75-100 mL of distilled isopropanol (Caledon, 99 %) was slowly transferred to the flask via canula. Some precipitate ($NaOPr^i$) forms during this addition, but it redissolves upon excess addition of isopropanol. After 4-5 h of gentle warming at 40 ^oC, all of the sodium was dissolved. The solution was then filtered according to the procedure outlined in SIM-D. The isolated filtrate was vacuum distilled until all of the solvent had been removed. The isolated finely powdered $NaOPr^i$ was placed under vacuum for an additional 24 h at ~50 ^oC to ensure the complete removal of solvent.

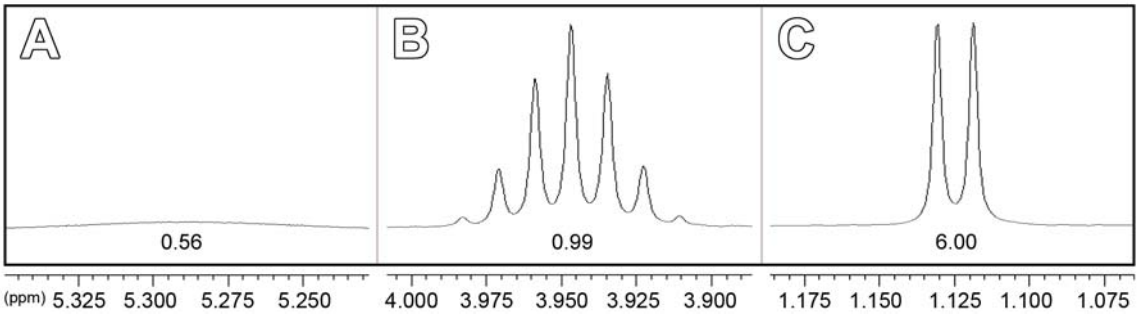

Figure 3.6 **^{1}H-NMR (500 MHz) of NaOPr^{i} samples dissolved in d_6-benzene.[83] Peak integrations are provided below (A) an unknown (trace OH?), (B) the NaOPr^{i} methyne proton, and (C) the NaOPr^{i} methyl protons.**

The ^{1}H-NMR spectrum of NaOPr^{i} (**Figure 3.6**) identifies that the isolated product was ~97 % pure. The spectrum reveals an unobstructed methyl doublet and methyne septet with ideal integration (6:1) as one would expect, but there was a further broad peak at 5.29 ppm (**Figure 3.6A**) that remains unidentified. The integration of the unknown peak does not appear to correlate with any other signal. The chemical shifts of the ^{1}H-NMR peaks show that NaOPr^{i} behaves similarly to LiOPr^{i} by oligomerizing to complete the coordination sphere around the metals of the complex. Compared with LiOPr^{i}, the methyne peak in the NaOPr^{i} ^{1}H-NMR spectrum (3.946 ppm, **Figure 3.6B**) is found in nearly the same position (4.086 ppm, **Figure 3.4**). Like LiOPr^{i}, a high chemical shift for the methyne proton is suggestive that the isopropoxy groups are bridging in dissolved NaOPr^{i} and that indicates a oligomeric structure. The small difference in chemical shift can be attributed to the reduced electronegativity of sodium. Hexamers, and nonamers of NaOBu^{t} have been shown to crystallize for the compound.[84] Smaller tetramers have not been previously shown, and that is likely the result of size constraints for packing a much larger sodium atom into a small cubic tetramer.The chemical shift of the NaOPr^{i} methyls at 1.123 ppm

contrasts significantly to that of $LiOPr^i$ (1.314 ppm). This shift suggests a loss of the formerly described hydrogen bonding, possibly as a result of the drop in sodium electronegativity. It is interesting that the synthesized $NaOPr^i$ is suggested by these results to have a similar structure to $LiOPr^i$, and yet have a sharply contrasted solubility in polar solvents. $LiOPr^i$ is highly insoluble in isopropanol. The effect is believed to be the result of the larger size of the sodium atom. The larger atom is believed to open the oligomer enough such that polar solvents can penetrate to access the polar core of the structure.

In the future, following the investigation of $LiNbO_3$ in our group $KNbO_3$ and $LiTaO_3$ may be alternative materials of interest with respect to the production of SHG. The synthesis of precursors to these materials required little additional research to access. $Ta(OPr^i)_5$ is prepared identically to $Nb(OPr^i)_5$ (see **Section 3.6.1**) and $KOPr^i$ is prepared according to the same procedure as for $NaOPr^i$. In preparation for this future work the synthesis of $KOPr^i$ was carried out here. The only exceptions to the $NaOPr^i$ procedure were a small amount of benzene (20-30 mL) to start in the reaction flask, and that flask was submerged in an ice-water bath for the addition of isopropanol. The addition of benzene was adapted to the $NaOPr^i$ procedure as a hydrocarbon “safety-blanket” in the odd chance the potassium was exposed to air. Benzene also acts to solubilize the initially formed $KOPr^i$ in the reaction. The addition of isopropanol was slow with caution to maintain a slow rate of reaction. Once all of the isopropanol was added, the reaction flask was slowly allowed to warm to room temperature and then stirred for another 30 min prior to filtration and isolation as described above. $KOPr^i$ is

also a white powder. Characterization of $KOPr^i$ was not performed since $KNbO_3$ was not pursued in this work. In the future, its characterization by ^{1}H-NMR would enable an interesting contrast and comparison with the spectra of lithium and sodium alkoxides already presented.

The synthesis of $Ba(OPr^i)_2$ from barium metal[85,86] is slow compared with the reactions described above. In this reaction, 5.1 g (37 mmol) of solid barium was sawed from an ingot (Aldrich, 99 %) and added, with a stir bar, to a 250 mL Schlenk flask in the glovebox. A noticeable tarnish was visible on the surface of the ingot and it was removed by scraping the surface with scissors prior to portioning. This tarnished surface was most likely hydrolyzed metal and would not be desirable for the preparation of pure $Ba(OPr^i)_2$.The flask containing the barium was sealed with a sleeve septum, removed and connected to the Schlenk line. A 10 % molar excess of dry isopropanol was added to the reaction flask with 100 mL of dry heptane (SIM-B) via the canula transfer method (SIM-C). After 24 h of reflux, all of the barium had dissolved to leave a grey-white precipitate. This precipitate was isolated as a fine white powder after vacuum distillation of the reaction solvent and 24 h of further vacuum drying at 55-60 ^oC. Other literature reactions using $Ba(OH)_2$[87] and BaO[88] as starting reagents are known, however, it is unclear if all of the residual oxygen bonds are removed by the process.

The precipitation of $Ba(OPr^i)_2$ observed during the reaction is a result of the large atomic size of barium requiring more than two isopropoxide ligands for stability. As a result, $Ba(OPr^i)_2$, bridges to form large ladder-like polymeric structures that are typically insoluble.[93, 95, 97] Alcohol adducts (1:1) of $Ba(OBu^t)_2$[89]

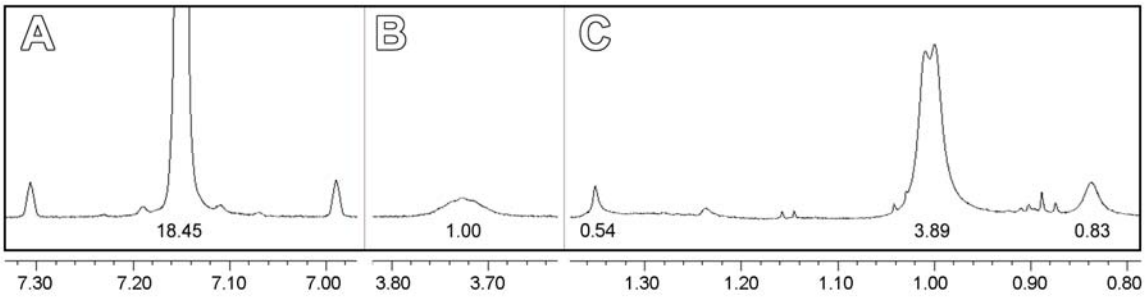

Figure 3.7 **^{1}H-NMR (500 MHz) of Ba(OPr^i)$_2$. Peak integrations are provided below (A) the C_6HD_5 solvent impurity, and what is believed to be (B) the Ba(OPr^i)$_2$ methyne protons and (C) the Ba(OPr^i)$_2$ methyl protons in addition to other unknown signals. The Ba(OPr^i)$_2$ signal intensity is very low with respect to the intensity of the solvent impurity. The low intensity is a result of solubility difficulties.**

and barium products of chelating alcohols (e.g., 2-methoxylethanol) have been shown to be soluble in hydrocarbon solutions.[93]

The ^{1}H-NMR of spectrum of Ba(OPr^i)$_2$ was hampered by this mentioned insolubility. The ^{1}H-NMR was performed in d_6-benzene solvent[83] and very little remains to be analyzed from the spectrum (**Figure 3.7**). The extremely low analyte concentration is evident by the intensity of the d_6-benzene impurity relative to any other signal (**Figure 3.7A**). The multiplet seen in **Figure 3.7B** and the doublet in **Figure 3.7C** were believed to be the result of Ba(OPr^i)$_2$, but the peak integration ratio is not as expected (expected 1:6, respectively). Further ^{1}H-NMR studies may have more success if they utilize a solvent that can act as a stable neutral donor to help disassemble the insoluble polymer (e.g., d_8-THF) and boost the analyte signal.

3.6 Synthesis of Niobium Isopropoxide [$Nb(OPr^i)_5$]

3.6.1 Synthesis of $Nb(OPr^i)_5$ by the Amine Method

The synthesis of niobium alkoxides was performed by the "*ammonia route*" and first introduced by Bradley *et al*.[90,91] The following reaction scheme outlines their method, but has been modified to represent our work with other amines and our suspicion of an amine or alcohol-based intermediate that is likely removed during the vacuum drying step of this procedure:

$$NbCl_5 + n\ R'OH \underset{}{\overset{0\ ^\circ C,\ benzene}{\rightleftharpoons}} Nb(OR')_nCl_{(5-n)} + n\ H^+ + n\ Cl^-$$

$$Nb(OR')_nCl_{(5-n)} + n\ H^+ + n\ Cl^- + 6NR''_3 \xrightarrow{0\ ^\circ C,\ benzene} Nb(OR')_5NR''_3 + NR''_3HCl_{(s)}$$

$$Nb(OR')_5NR''_3 \xrightarrow{40\ ^\circ C,\ vacuum} Nb(OR')_{5(s)} + NR''_3 \qquad (16)$$

This method is entirely based on the ability of the chosen alcohol (R' = Et or Pr^i) to displace the chloride ligands and the ability of dissolved amine (NR''_3) to remove HCl from solution. As before, the reaction rate is influenced by the sterics and the acidic property of the alcohol as described for the reaction of lithium alkoxides. In the first stage of the reaction, a red-orange solution of $NbCl_5$ in benzene is formed. The reaction transitions to a yellow color once the alcohol is added, and it is followed by the formation of a colorless solution with time. The latter color change corresponds to the ligand exchange reaction shown in the first line of **equation (16)**. Addition of an amine in the second reaction above, results in the precipitation of HCl in the form of $NR_3HCl(s)$. That acid-by-product can be

filtered from reaction relatively easily. The final $Nb(OPr^i)_5$ is isolated from its amine adduct, following vacuum distillation of the reaction solvent.

In this reaction, we have utilized the method as described by Bradley *et al*.,[90] but also explored this reaction through substitution of benzene for heptane or toluene and triethyl amine (TEA) in place of ammonia. As a result of this study, it was concluded that the substitution of benzene, while less toxic, either results in a hindered $NbCl_5$ solubility or higher NH_4Cl solubility. Both of these results reduced the overall yield for the reaction. Furthermore, a benzene-based reaction benefited by a fluffy crystal habit for the precipitated NH_4Cl crystals. The porous structure of the precipitated crystals facilitated in their removal by the filtration process. The cost associated with the use of ammonia caused us to explore the possibility of alternative HCl scrubbing agents. Three of the immediate benefits associated with the use of TEA were the immediate availability, the ease of handling liquid reagents over a gas and, according to pKa tables, TEA is a stronger base than ammonia (pKa NH_3 = 9.21; NEt_3 = 10.63).[92] While these benefits were found to be true, there were some unfavourable results. Filtration difficulties were experienced as a result of a more waxy Et_3NHCl precipitate. This problem was eventually overcome as described below. As a stronger neutral donor, TEA was also believed to form a stronger association with $Nb(OR)_5$ and it was not as easily removed by vacuum drying. The crude product, believed to contain $Nb(OR)_5NEt_3$, has a faint orange-pink color, but the impurity was removed by a more careful vacuum sublimation procedure that is also outlined below.

In a typical synthesis of $Nb(OPr^i)_5$, 7.00 g (0.026 mmol) $NbCl_5$ (99.9 % powder, Alfa Aesar) and a stir bar was loaded into a 250 mL Schlenk flask in the glovebox. The top of the flask was sealed by a sleeve septum secured with a wire prior to removal from the glove box. The Schlenk flask was removed from the box, attached to the Schlenk line, and submerged in an ice-water bath. Using a 100 mL graduated cylinder and the procedure outlined in SIM-C, 100 mL of distilled benzene (SIM-B) was transferred to the reaction flask with a dry and purged 18-gauge canula. An orange-red solution formed after stirring for ~10 min. Once the solution was cooled, 23 mL (0.300 mol, roughly 2.25 times stoichiometric amount) of dried isopropanol is added via the same method (SIM-C). After ~15 min, 4 mL of TEA was slowly added to the reaction with 4 aliquots from a 1 mL gas tight syringe. Once the white vapors had subsided, another 32 mL of TEA was added slowly via a thin 20-gauge canula from the same graduated cylinder used above (during SIM-C). After 15 min of stirring, the reaction is removed from the ice bath and allowed to settle for roughly 30 min.

The crude $Nb(OPr^i)_5$ was obtained in solution following a series of two filtration steps outlined in the technique section of the appendix (SIM-D). The first filtration utilizes a coarse porosity filter stick and the second filtration utilizes a medium porosity filter. If the precipitate has settled well, a single filtration using a medium porosity filter stick can be performed while taking care not to resuspend the precipitate. To isolate the crude powder, the solvent was vacuum distilled and the resulting powder was vacuum dried for 24 h at 40 ^oC. Due to potential losses in yield during two filtration steps, it is believed that the experiment could be

ideally performed in large glass centrifuge tubes, capped by sleeve septa. After the precipitation event, centrifugation can be used to create a dense precipitate pack and the reaction solvent can be directly removed by canula techniques and concentrated to dryness in the receiving flask.

Pure $Nb(OPr^i)_5$ was isolated by our method in roughly 68 % yield after careful vacuum distillation. This yield identifies that there is no benefit to the use of ammonia (~65 % yield) in the synthesis of $Nb(OPr^i)_5$ except for the convenience it provides for filtration. In our procedure, the crude material and a small stir bar was loaded and sealed in a cold finger apparatus in the glovebox. The cold finger was removed, attached to the vacuum of the Schlenk line and water flow, then submerged in an 80 ^oC oil bath with stirring. Strict adherence to the stated temperature is critical for the isolation of only $Nb(OPr^i)_5$. Once collected, $Nb(OPr^i)_5$ was removed as a moisture sensitive white crystalline powder, and it was stored in sealed vials in the glovebox until required.

3.6.2 A Metathesis Approach to $Nb(OPr^i)_5$

Due to the success of the metathesis approach in the synthesis of $Ti(OR)_4$ from $TiCl_4$,[93] it was believed that the same approach could be applied to the synthesis of niobium alkoxides from $NbCl_5$. The synthesis of $Ti(OPr^i)_4$ by the following procedure may be useful to our group in the future if they decide to pursue the synthesis of $KTiOPO_4$ as an NLO nanocrystal. If the metathesis approach was capable of forming $Nb(OPr^i)_5$, it was believed that our chosen precursor, $LiNb(OPr^i)_6$, could be prepared in heptane via a one step reaction with

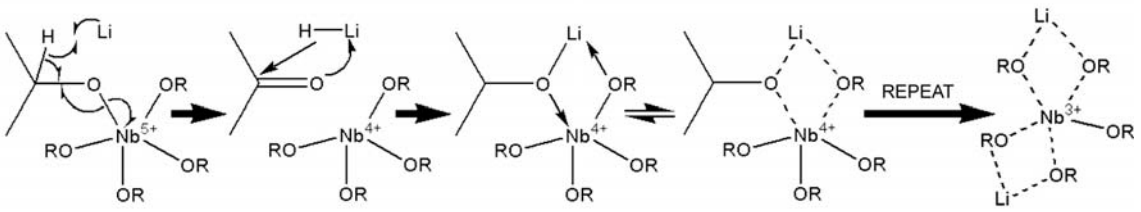

Figure 3.8 **A proposed mechanism for the reduction of $Nb(OPr^i)_5$ in the metathesis reaction. The generation of acetone is only necessary in this reaction if lithium cannot access the inner Nb-O bond. The first four steps of the mechanism result in a blue Nb^{4+} molecule. If the steps are repeated once more the Nb^{4+} product can be reduced further to a green Nb^{3+} molecule.**

$LiOPr^i$. This was a possibility worth exploring. The two salt metathesis reactions investigated in this research are outlined here:

$$NbCl_5 + 5/n\ M + 5Pr^iOH \xrightarrow{0\,^\circ C,\ benzene} Nb(OPr^i)_5 + 5/n\ MCl_n + 5/2\ H_{2(g)} \quad (17)$$

$$NbCl_5 + 5/n\ M(OPr^i)_n \xrightarrow{0\,^\circ C,\ benzene} Nb(OPr^i)_5 + 5/n\ MCl_n \quad (18)$$

In both these reactions, M = Li or Na so n = 1. In the first reaction, the lithium or sodium is used in 10 % excess and the alcohol was the limiting reagent. Excess metal was expected to be inactive following the consumption of ROH by the redox outlined in the synthesis of lithium isopropoxide. This assumption was, however, not correct. Lithium and sodium continued to react by reducing Nb to a blue Nb^{4+} and further to a green Nb^{3+} alkoxide (**Figure 3.8**). In the suggested mechanism, the metal (Li in this case) initiates a radical reaction with the methyne proton of an isopropoxide ligand. This immediately results in reduction to Nb^{4+}. Acetone generated by this reaction would react quickly with the generated hydride to form $LiOPr^i$ that coordinates to $Nb(OPr^i)_4$ through oxygen π-

bonding. Repeating the process generates $Nb(OPr^i)_3$ adducts.

Following these results, attention was turned to reaction in **equation (18)** where the excess reductant was removed. This route was performed using a 10 % excess of the alkali alkoxide. In a promising observation, the solution remained transparent yellow while a white precipitate was formed. The precipitate was collected and confirmed by X-ray powder diffraction to be 9.8 % LiCl [Fm$\bar{3}$m (#225)] and 90.2 % $LiCl{\cdot}H_2O$ [$P4_2/nmc$ (#137)] after drying for 24 h (**Figure 3.9**).[94] The hydrated LiCl crystals are expected to be the result of washing the precipitate with wet solvents and not a result of the reaction. Assuming success,

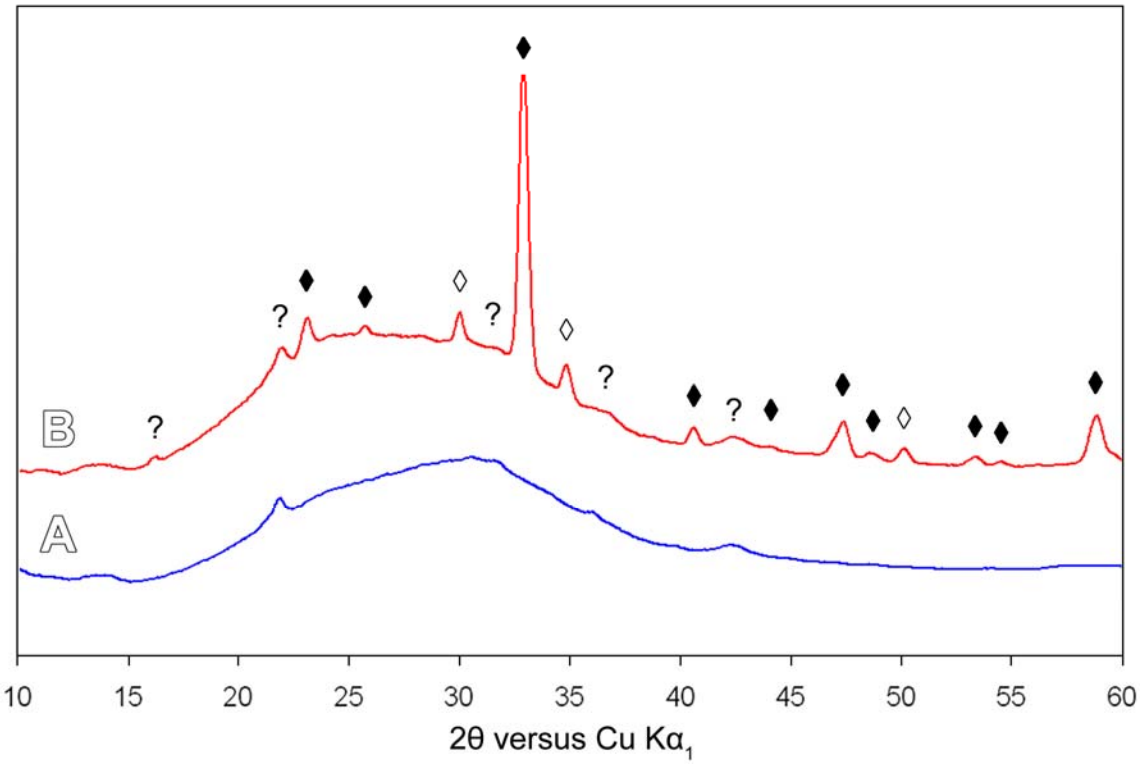

Figure 3.9 **X-ray powder diffraction (XRD) spectra of the salt metathesis by-products. (A) The XRD spectrum of the precipitate collected from the reaction and air-dried 4 h and (B) the spectrum of the oven dried by-product (120 °C, 2 h). Peaks identified with hollow diamonds (◊) represent LiCl [Fm$\bar{3}$m (#225)] and those of filled diamonds (♦) represent $LiCl{\bullet}H_2O$ [$P4_2/nmc$ (#137)]. Others (?) are still unidentified.**

the filtrate was distilled to dryness and the resulting powder treated for use in our solution-phase synthesis. This reaction was, however, not successful in the production of $LiNbO_3$. Residual chloride was believed to be the cause of this failure so the reaction was set to be repeated using $NaOPr^i$ as a more typical metathesis reagent. Also, instead of a lengthy solution-phase reaction, this new reaction would be evaluated by exploiting the difference in volatility between niobium and alkali alkoxides. In general, alkali alkoxides are non-volatile, so vacuum sublimation should be capable of extracting $Nb(OPr^i)_5$ as an indication of reaction success. The treatment of $NbCl_5$ with $NaOPr^i$ had observations consistent with that of the $LiOPr^i$-based reaction. The crude reaction product was isolated from the reaction filtrate following vacuum distillation of the reaction solvent. Subsequent cold-finger sublimation of the crude material was performed at 80 ^oC, but no $Nb(OPr^i)_5$ could be isolated or observed. Furthermore, no volatiles at all were isolated up to 120 ^oC. This result was unexpected, and the metathesis reaction was abandoned as a possible route to $Nb(OPr^i)_5$.

3.7 Characterization and Reactivity of Niobium Isopropoxide

Characterization of $Nb(OPr^i)_5$ structure and reactivity was performed by ^1H-NMR spectroscopy. The structure of the ethoxide, $Nb(OEt)_5$, is known to exist as a dimer[95,96] in solution, but sterically hindered alcoholates are known to form monomers or a mixture of monomers and dimers.[97,98] The isopropoxide has been seen to crystallize as a dimer.[99] The concentration of either the monomer and dimer is believed to be due to the following equilibrium:[97]

$$2Nb(OR')_5 \rightleftharpoons Nb_2(OR')_{10} + \textit{heat} \qquad (19)$$

As the size of R′ increases, the compound favors the left side of this equilibrium.

The ^{1}H-NMR spectra of the methyl and methyne regions are shown in **Figure 3.10** and **Figure 3.11**, respectively. The bottom and middle spectra from both figures represents crude and purified $Nb(OPr^i)_5$, respectively. In each of these spectra methyne septets occur for each of the methyl doublets and they

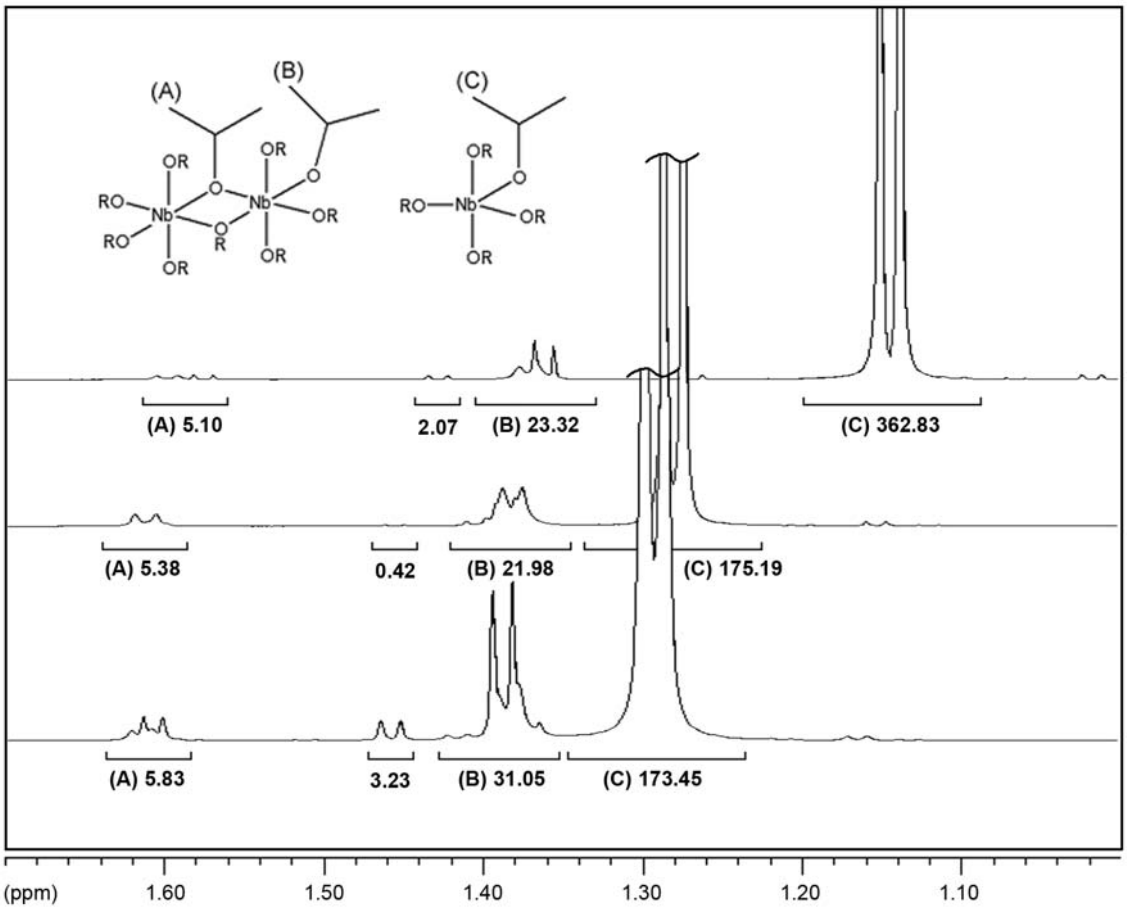

Figure 3.10 ^{1}H-NMR (500 MHz) of the methyl region of $Nb(OPr^i)_5$ (bottom) as synthesized by the amine route, (middle) after vacuum distillation, and (top) after addition of isopropanol in an amount equal to five times the monomer concentration. Removing isopropanol contribution in the top spectrum, the 362.83 integration decreases to 207.07. Spectra were obtained in d_6-benzene.[83]

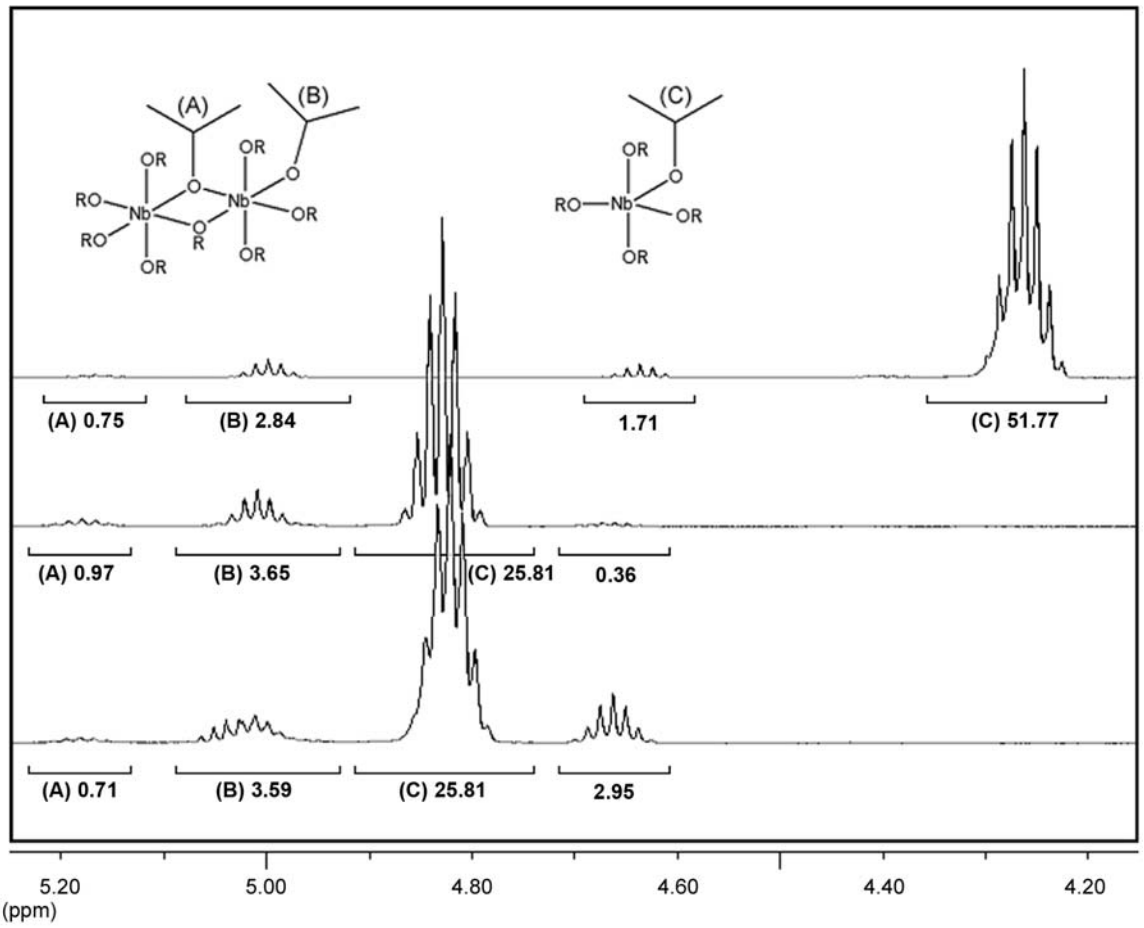

Figure 3.11 **^{1}H-NMR (500 MHz) of the methyne region of Nb(OPr^i)$_5$ (bottom) as synthesized by the amine route, (middle) after vacuum distillation, and (top) after addition of isopropanol in an amount equal to five times the monomer concentration. Removing isopropanol contribution to in the top spectrum, the 51.77 integration decreases to 25.81 as observed in the other spectra. Spectra were obtained in d_6-benzene.[83]**

have a complementary chemical shift. The integration of the methyl peaks to the methyne peaks is ~6:1, respectively, and it agrees with the integration expected from isopropoxide groups. As a result of purification, the peak positions remain relatively stationary and the fine structure becomes clarified. An impurity, with a methyl peak at ~1.46 ppm and a methyne peak at ~4.66 ppm is shown to reduce in intensity as a result of the purification. The impurity was suspected to be NbO(OPr^i)$_3$ because of the upfield position of the methyne septet, but the

corresponding methyl integration and chemical shift do not support this conclusion. The impurity still remains unknown as a result. Aside from the impurity, the two most deshielded septets or doublets of the methyne or methyl regions, respectively, have a clear 1:4 integration ratio that identifies these peaks as the bridging and peripheral groups of the dimer molecule (**Figure 3.10** and **3.11**). The high chemical shift of these peaks indicate that the addition of a second niobium atom has a strong electron withdrawing effect on the attached isopropoxide groups. The remaining upfield peaks represent that of the monomer unit, and their intensity identifies that the monomer is the most abundant species in solution. Upon purification, the lower molecular weight monomer is the volatilized compound, but **Figure 3.10** and **Figure 3.11** show that the equilibrium in **equation (19)** is quick to restablish the dimer. The ^{1}H-NMR results for the purified compound indicate that it is 98.6-99.8 % pure.

According to the crystal structure of $LiNb(OPr^{i})_6$ (**Figure 3.12**), there is no presence of directly bridged $Nb(OPr^{i})_5$ molecules. It appears as though two molecules of $LiOPr^{i}$ have been inserted between what was $Nb_2(OPr^{i})_{10}$. Therefore, it appears as though the dimer must be broken to expose a coordination site for reactivity with $LiOPr^{i}$. Once the coordination site is available, $LiOPr^{i}$ can coordinate to form a $LiNb(OPr^{i})_6$

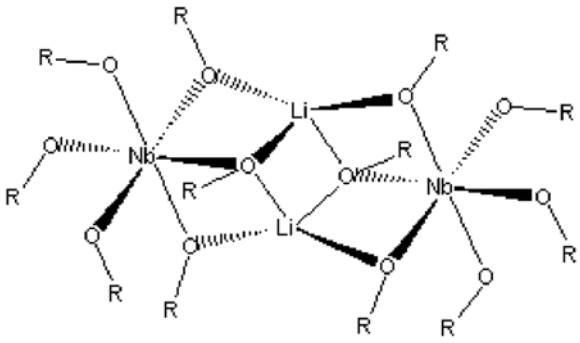

Figure 3.12 Structural representation of crystalline $LiNb(OR)_6$ where R = Pr^{i}. Note the separation of niobium centers by a $LiOPr^{i}$ dimer. This observation implies that $Nb_2(OPr^{i})_{10}$ must be cleaved to form the precursor.

unit. To study the reactivity of the dimer molecule, isopropanol was added to the NMR tube to act as a weak donor molecule (**Figure 3.10** and **3.11 top**). According to the ^{1}H-NMR, the monomer molecule, $Nb(OPr^{i})_5$, reacts to form $HNb(OPr^{i})_6$ in solution. The extra donor molecule has a shielding effect on the molecule that causes the methyne signal to move upfield from 4.79 to 4.26 ppm, and the methyl signal to move upfield from 1.27 to 1.14 ppm. According to the integration of the isopropanol hydroxyl peak, a five-fold excess of isopropanol was added, yet an independent set of peaks for isopropanol was not observed. In order to create a single homogeneous signal, this means that the $Nb(OPr^{i})_5$ molecules are rapidly exchanging the added isopropanol, and it identifies how $Nb(OR)_5$ molecules are capable of further modification by alcohol exchange:[100]

$$Nb(OEt)_5 + 5R'OH \longrightarrow Nb(OR')_5 + 5EtOH \qquad (20)$$

Equation (20) highlights the fact that this research can emphasize on the development of one type of alkoxide. Since primarily $Nb(OPr^{i})_5$ was used in this research, it has not been necessary to use this reaction yet.

The strongly bridged dimer molecule does not appear to degrade rapidly in the presence of the coordinating molecule. Its integration and chemical shift remain roughly constant after the addition of isopropanol. The small chemical shift change could be due to a slight change in solvent composition. In order to react the dimer molecule, it is clear that heat is needed to overcome the energy of the bridging bonds according to the preceding equilibrium [**equation (19)**]. If

heat is applied and an excess of isopropanol is present, the molecule can remain trapped in the monomeric form. The necessity of heating $Nb(OPr^i)_5$ in the presence of a donor group is apparent in a study by Shinichi.[96] When LiOEt and $Nb(OEt)_5$ were refluxed in a 1:1 ratio for longer periods of time, the fraction of $LiNbO_3$ produced in that synthesis increased relative to other phases such as Li_3NbO_4 and $LiNb_3O_8$. The Nb-rich phases were likely the result of $Nb_2(OEt)_{10}$ rich sites that still existed within the sol produced. Consequently, in a 1:1 Li:Nb ratio, every threefold Nb-rich site produces a complementary threefold Li-rich site and the Li_3NbO_4 phase also forms. When the heating was sufficient to disassemble all of the dimers (24 h), Shinichi produced a homogenous sol that formed pure $LiNbO_3$.[96] The synthesis of $LiNb(OR)_6$ ($R = Pr^i$) for the synthesis of $LiNbO_3$ will be discussed further in the last section of this Chapter.

3.8 Synthesis of Boron Isopropoxide [$B(OPr^i)_3$]

Since a variety of SHG crystals contain boron as part of their composition, the synthesis of $B(OPr^i)_3$ became an interest for the use in future studies in BBO, LBO, LTB and BiBO (**Appendix 1.1**). The synthesis of boron alkoxides is relatively straightforward because it does not rely on inert conditions during the start of the reaction. The reaction performed makes use of the following equilibria to obtain $B(OPr^i)_3$:[101]

$$B(OH)_3 + 3R'OH \underset{}{\overset{\text{reflux, benzene}}{\rightleftharpoons}} B(OR')_3 + 3H_2O \quad (21)$$

$$B_2O_3 + 6\ R'OH \underset{}{\overset{\text{reflux, benzene}}{\rightleftharpoons}} 2\ B(OR')_3 + 6H_2O \quad (22)$$

In our work we utilized $B(OH)_3$ and a 10 % excess of isopropanol[102] as starting materials, but both of these equilibria are expected to be relevant because $B(OH)_3$ may contain oxides as well. Evidence of oxide contamination is seen in the amount of water collected in this reaction. For our reaction scale we anticipate roughly 9 mL of H_2O, but collect about 11 mL upon completion.

Several reaction modifications were tried and/or added to optimize the procedure for synthesizing $B(OPr^i)_3$. One difficulty with this reaction is that the boron alkoxide forms a strong association with benzene, and proper isolation requires distillation through a fractionating column. If distillation is applied without a column white string-like crystals are isolated in a 5 % yield (assuming a $B(OPr^i)_3$ composition). The crystalline nature of the product is unusual because $B(OPr^i)_3$ is known to be a liquid at room temperature. The crystalline nature appears to be due to what is believed to be the presence of hydroxide impurities that form stronger bridging bonds that facilitate crystallization (see below for more information). The reaction was also attempted with toluene. After 3 days of reaction, the volume of water collected indicated that the reaction was only 40 % complete. In one article, the use of benzene is specific to the reactions above where R = Pr^i.[103] Without justification Kuivila *et al.* also state that if R = Me or Et toluene should be used. Upon our investigation, the reason for the solvent change appears to be the degree solubility of the alcohol in the hydrocarbon. Since the reaction requires the use of a Dean-Stark (DS) apparatus, the success of the reaction relies on the separation of water and hydrocarbon/alcohol fractions, and that the alcohol is returned to the reaction vessel with the

hydrocarbon. The alcohol is returned more effectively when using a solvent of appropriate polarity.[104] The second modification we attempted was to use a large excess of the alcohol (>10 % standard[102]) in attempt to push the equilibrium toward the reaction products. The addition of excess alcohol negatively affected the ability of water and benzene to fractionate in the cold finger of the DS apparatus.

In a typical synthesis of $B(OPr^i)_3$, 10.0 g (0.162 mol) $B(OH)_3$ (Caledon 99.3 %) was added to a dry 250 mL Schlenk flask. To this flask was added a oven-dried stir bar, 41 mL of distilled isopropanol (Caledon 99 %, SIM-B), and 110 mL of benzene (Caledon 99 %) that has been dried with anhydrous $MgSO_4$. This flask was connected to the DS assembly, atop which was attached a condenser and a gas inlet adaptor. All joints were covered with Teflon in order to maintain a tight seal for the system. A head pressure of dry nitrogen was maintained over the course of the reaction through the attached a gas inlet adaptor. The DS assembly was wrapped in aluminum foil and the cold finger was placed in an ice bath. The base temperature for the reaction was increased until the distillate reached the upper condenser (160 ^oC) and the reaction held at that temperature for a minimum of 24 h. The majority of the water was collected over the first 24 h of reaction. No further water was observed to be collected after 2 days. In the future, this reaction could be improved if the cold finger of the DS-assembly was drained after 24 h and then filled with a clean dry dessicant.

To isolate the product, a strong nitrogen flow was applied through the side arm of the 250 mL flask and the DS-assembly was replaced with a 30 cm

Vigreux column, distillation adaptor (with thermometer), condenser, and collection flask, in that order respectively, such that the connected glassware was purged of any atmospheric H_2O and O_2. Alternatively, the distillation apparatus can be treated separately according to SIM-A. Once connected, the base temperature of the distillation setup was gradually increased until each fraction was collected. The first fraction was small and appears at a thermometer reading of 65 ^oC and it likely represents a benzene/water (91/9) fraction or[104] a isopropanol-water-benzene ternary azeotroph. This fraction was followed by two larger fractions at 70 ^oC and 80 ^oC, which likely represent a isopropanol/benzene (33/67) azeotroph and pure benzene, respectively.[104] Since, $B(OPr^i)_3$ is highly susceptible to hydrolysis to form white $B(OH)_3$, a small amount of the collected distillate was deliberately spilled on the black fume hood surface as a qualitative check for the presence of $B(OPr^i)_3$. No white residue formed from this test indicating the distillate was only solvent. After ~1 h of distillation, $B(OPr^i)_3$ remained a clear solution in the bottom flask.

3.9 Characterization of Boron Isopropoxides

Characterization of $B(OPr^i)_3$ was performed by ^1H-NMR. It was originally believed that the presence of hydrolyzed $B(OPr^i)_3$ would be easily detectable by the appearance of three sets of methyl doublets produced by the species, $B(OPr^i)_3$, $B(OPr^i)_2(OH)$, and $B(OPr^i)(OH)_2$. The fully hydrolyzed form, boric acid ($B(OH)_3$), would not be soluble in d_6-benzene that was used in the analysis. This hypothesis was complicated by the fact that any two of these compounds may

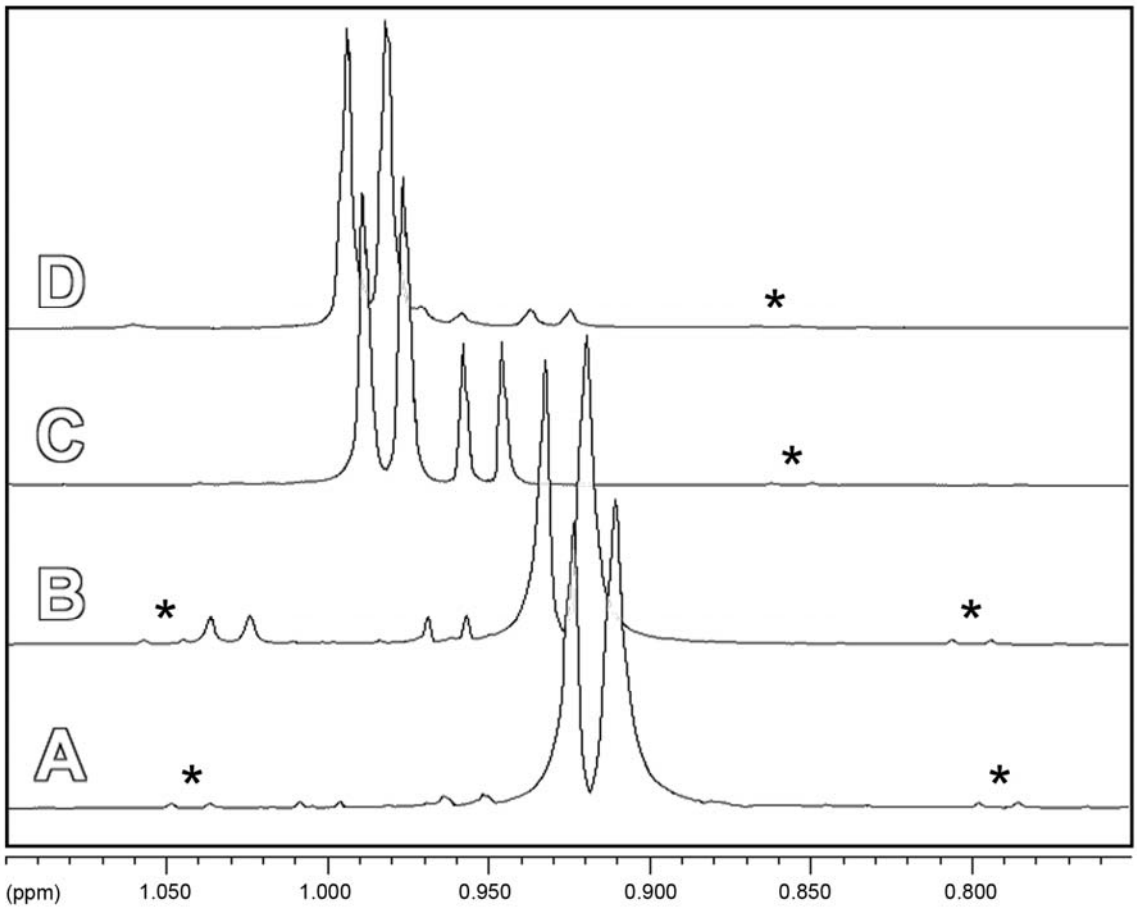

Figure 3.13 **^{1}H-NMR (500 MHz) spectra of (A) an Aldrich standard of $B(OPr^{i})_3$, (B) our prepared $B(OPr^{i})_3$, (C) deliberately hydrolyzed $B(OPr^{i})_3$, (D) and the hydrolyzed sample after 24 h reflux. All the compounds were analyzed in d_6-benzene.[83] The stars represent ^{13}C satellite peaks and are not to be confused with the other methyl doublets that are discussed in the body of the main text. The large doublet in the later two spectra (C & D) is due to the presence of the isopropanol liberated during hydrolysis.**

undergo a condensation reaction to generate a bridging oxygen bond (e.g., $(OPr^{i})_2B\text{-}O\text{-}B(OPr^{i})_2$). A cyclic metaborate, $(OBOPr^{i})_3$, is also possible by condensation.[104]

As a result, analysis of the ^{1}H-NMR obtained was more difficult than originally believed. **Figure 3.13** shows four ^{1}H-NMR methyl spectra of (A) a standard $B(OPr^{i})_3$ (Aldrich, 98 %), (B) our sample prepared as described above,

(C) our sample deliberately treated with H_2O, (D) and the deliberately hydrolyzed sample after a subsequent 24 h of reflux. Our sample and the Aldrich standard appear to be similar, but the peaks of our sample occur at a slightly higher chemical shift. We believe this discrepancy is the effect of a decreased amount of molecular association (through vacant p-orbital bridging) in our $B(OPr^i)_3$ as a result of a lower concentration in our sample (~30 % diluted by the reaction solvent) versus the 98 % pure standard. Aside from the major product, our main concern was to identify the origin of two significant doublets at higher chemical shift (0.96 and 1.03 ppm). The outermost weak doublets near 1.05 and 0.80 ppm are only ^{13}C satellites of the major product.

Each of the unknown sets has a complementary methyne septet, with an integration that indicates all of the proton signals originate as part of isopropoxide units. Suspecting the unknown signal in our reaction product was hydrolyzed $B(OPr^i)_3$, such as $B(OPr^i)_2(OH)$ or $B(OPr^i)(OH)_2$, another reaction was deliberately tainted with approximately 1 mL of H_2O. This addition resulted in the immediate formation of white precipitate in solution [presumed to be $B(OH)_3$]. The ^1H-NMR of the solution (**Figure 3.13C**) contained a doublet at 0.98 ppm from isopropanol (a hydrolysis product), and another doublet (0.95 ppm) that did not correspond to any of the peaks in the original reaction. Knowing that $B(OPr^i)_3$ was hydrolyzed, either $B(OPr^i)_2(OH)$ and/or $B(OPr^i)(OH)_2$ should be present in **Figure 3.13C**. The appearance of only a single doublet in the ^1H-NMR spectrum identifies that either both are present in rapid ligand exchange or only one is present because the other was insoluble in benzene. Unexpectedly, the

hydrolyzed doublet at 0.95 ppm does not appear to be one of the unknown doublets in the synthesized $B(OPr^i)_3$ (**Figure 3.13B**). The unknown $B(OPr^i)_3$ peaks were now believed to be condensation products on account of the high reaction temperature. To investigate that possibility the hydrolyzed sample (C) was refluxed for 24 h to facilitate condensation. The new ^{1}H-NMR spectrum, **Figure 3.13D**, reveals that isopropanol was liberated during the refluxing period. This result is indicative of a condensation event. In **Figure 3.13D** the result of condensation was to split the original doublet of the hydrolyzed product to form isolated doublets at 0.93 and 0.96 ppm. While the chemical shifts of this pair of peaks appears to coincide with the original synthesis of $B(OPr^i)_3$, the actual composition is still not known. This splitting could indicate a restricted degree of rotational freedom in methyl units possibly as a result of forming a multicentered metaborate complex.[104]

Unfortunately, the results of the tests with $B(OPr^i)_3$ did not provide any information about the origin of the unknown doublet at a chemical shift of 1.03 ppm in the ^{1}H-NMR spectrum of our product. Both unknown peaks are tentatively assigned as condensation products, but their structure is not known. Since the identity of the methyl signals is not fully understood, only minimum purity values can be stated. The Aldrich sample appears to be +96 % pure whereas ours is only +90 % pure. In the future, this synthesis should be attempted with a 15 % excess of isopropanol, and incorporate a desiccant during a second 24 h of the reaction. These suggestions are believed to help eliminate more water that would avoid the possibility of condensation products. Attention should also be made

towards a prolonged distillation procedure since the solvent content of our product (30 % volume) is a considerable concern.

3.10 Synthesis of Bismuth Isopropoxide

The interest in bismuth alkoxides is related to possible future studies in our group with BiB_3O_6 (BiBO). As an SHG crystal, BiBO has a high damage threshold, broad transparency region, and the highest nonlinear optical coefficient of the borates (**Appendix 1.1**). The synthesis of bismuth alkoxides is performed by the following sodium salt metathesis reaction:[105]

$$BiCl_3 + 3NaOR' \xrightarrow{\textit{isopropanol / benzene}} Bi(OR')_3 + 3NaCl \qquad (23)$$

The above reaction was difficult because neither NaOR or $Bi(OPr^i)_3$ is very soluble in benzene.[106] The solubility of $Bi(OPr^i)_3$ is also poor in isopropanol, and the compound only remains soluble while the solution is near reflux. The reaction was further complicated by the clogging of the filter-stick with finely precipitated NaCl (SIM-D). Prior to filtration, the solution was attempted to be transferred off of the precipitate via canula to avoid this problem, but the product would either crystallize out of solution or crystallize and clog the canula before the transfer could be completed. Below is an outline of the most optimal approach at this point in time. Future work may want to devise a heated filterstick for use in this reaction as mentioned in the literature.[105] This process is reported to have high (80-90 %) yields. An alternative approach may also be to allow the solution to

grow large crystals of $Bi(OPr^i)_3$ by a slow cooling process and then rinse the $Bi(OPr^i)_3$ through the filterstick with boiling isopropanol.

The synthesis of $NaOPr^i$ is outlined in section 3.5 of this Chapter. In this reaction, 1.00 g (43.5 mmol) of sodium (Aldrich, cubes 99.95 %) was converted to the isopropoxide. The only alteration in the procedure for $NaOPr^i$ was that the reaction solvent contained 100 mL of distilled benzene (Caledon, 99 %) and 75 mL of distilled isopropanol (Caledon, 99 %) in order to promote NaCl crystallization in the metathesis reaction that follows. On the bench-top, 4.60 g (14.6 mmol) $BiCl_3$ (Aldrich, 98 %) was weighed out and added to a dry 500 mL Schlenk flask with a stir bar. This flask was sealed with a condenser fitted with a sleeve septum, and cycled according to SIM-A. Thereafter, 75 mL of distilled isopropanol (Caledon, 99 %) was transferred to this flask through the top septum with the use of a canula (SIM-C). A head-pressure of nitrogen was applied through the septum using the Schlenk line, and the solution was heated to reflux. Using a hot wide-boar canula (16 gauge), the hot benzene/isopropanol solution of $NaOPr^i$ was transferred to the $BiCl_3$ flask through the top septum. This transfer is performed quickly to avoid $NaOPr^i$ precipitation inside the canula. The solution in the $BiCl_3$ flask forms a milky solution soon after this addition. To complete the metathesis reaction, the combined solution was refluxed for 16 h.

By morning the solution had a blue appearance indicative of the reaction product. To isolate the product from the reaction mixture, a filtration was performed (SIM-D) under conditions that were as hot as possible. A medium porosity filter stick and a generous amount of Celite was used in this reaction, but

NaCl and crystallization of the reaction product in the filter stick caused clogging soon after starting the filtration process. In the product flask, the transparent blue fitrate quickly transforms to a yellow solution upon rapid precipitation of white $Bi(OPr^i)_3$ crystals. These crystals were isolated after vacuum distillation of the solvent and further drying of the resulting powder at 40 ^oC under vacuum 16 h. After 2 days in a sealed Schlenk flask, the white $Bi(OPr^i)_3$ product decomposes to a light brown color. After 7 days it decomposes further to a dark purple color. A $Bi(OPr^i)_3$ standard was purchased from Alfa Aesar (purity unlisted) as a comparison to our own. The dark purple color of this purchased precursor shows that it would be an unsuitable comparison to our own because of exposure to air.

More work is required to characterize the synthesized compound. ^{1}H-NMR analysis has been complicated by the lack of solubility of the reaction product, but solvents, such as d-chloroform are yet to be explored. A trace amount of the product has been found to dissolve in d_6-benzene, but the intensity of the benzene impurity peak saturates the instrument before the fine-structure of peaks becomes obtainable. Approximate peak positions of 1.20 ppm for CH_3 and 4.20 ppm for CH are similar to the ethoxide reported elsewhere.[106] If a heated filter stick is not obtainable, the reaction should be carried out at 50 % the current reaction scale. This should keep the product solubilized for a slightly longer working time. The use of a coarse filtration stick may also shorten the filtration time and thus decrease the chance for product precipitation.

3.11 Synthesis and Characterization of Lithium Niobium Isopropoxide

3.11.1 Purification of Chemat Compound

As shipped the lithium niobium isopropoxide ($LiNb(OPr^i)_6$) supplied from Chemat Technology, Inc. (Northridge, CA) had an inconsistent viscosity and purity between manufactured lots. The supply of this compound has been discontinued, presumably as a result of these inconsistencies and possible complaints. The optimal compound for the solution-phase synthesis of $LiNbO_3$ nanocrystals, had a light orange color, a glassy appearance, and a very high viscosity (hard like a solid, but it would flow over the course of days). Alkoxides are known to form homogenous sols of tunable viscosity with their parent alcohol so it was anticipated that the Chemat precursor often contained dissolved solvent that could compromise our reaction. Often the precursor would also be delivered with the appearance of a crusted surface. These white hydrolysis products were the result of improper conditions for storage or synthesis (e.g., H_2O impurities) on the part of Chemat. Unless removed, these insoluble particles would act as nucleation centers in our reaction, and result in micron-sized anomalously-shaped crystals.

For consistency, it became necessary to purify the Chemat compound before use in our reaction. Each gram of the $LiNb(OPr^i)_6$ reagent was originally dissolved in 30 mL distilled heptane (SIM-B). This solution was stirred under inert conditions for 15 min and filtered through dry celite to remove solid impurities (SIM-D). Excess solvent was subsequently removed by placing the sample under vacuum at 40-50^oC. The temperature was carefully maintained during the course

of drying because of the possibility of disproportionation and volatilization of $Nb(OPr^i)_5$ from the precursor (at temperatures greater than 80 ^oC). During the course of evaporation, the solution darkened to a deep red color from which a generous amount of fine crystals precipitated. Separation of the crystalline and liquid phases was then performed such that both could be investigated on their own.

To separate the two phases, a canula was inserted into the reaction vessel through a rubber septum, and the deep red solvate was transferred off the crystals into a small 100 mL Schlenk flask (SIM-C). Using the same canula, a small amount of cold dry heptane was transferred to the crystals to rinse the crystals of the remaining dark red solvent. This rinse was also added to the 100 mL Schlenk flask. The cleaned crystals were then dissolved in a minimum amount of hot heptane and allowed to recrystallize slowly in a three-stage cooling process. After 1 day, 3-5 mm long, transparent, and slightly yellow crystals were isolated from the cold solution by removal of the solvent with a canula. The dark red solution was concentrated to yield a resinous mass that then dried to form an amorphous orange powder. A small amount of fine crystals were observed to form again during the concentration of this solution.

Soon after, a new purification was adapted using the same procedure as above except 30 mL distilled isopropanol was used (SIM-B) per gram of precursor instead of heptane. The coordinating nature of isopropanol, functions to re-network the crystalline and amorphous components of the precursor as the solution was concentrated, and no precipitation was observed during

evaporation. As the solution was concentrated at 40 ^{o}C, a homogenous yellow-orange resinous solution is formed that dries to give a beige-colored powder over the course of 2 days. This new method of purification would become the standard method in this research. However, in the following section (**3.11.2**) the heptane purification did reveal some valuable information about optimizing a precursor for this reaction.

3.11.2 Characterization of the Chemat Precursor

With the assistance of Edwin Wong, in Professor Leznoff's laboratory at SFU, a primitive crystal structure was elucidated for the crystals isolated from the Chemat precursor. $LiNb(OPr^{i})_6$ crystallizes as a symmetric dimer, which is quite different from the polymeric chain nature of the previously reported $LiNb(OEt)_6$ compound.[98] In this dimer, each lithium tetrahedron shares an edge with the other and both tetrahedra share an edge with each of the niobium octahedra. The coordination sphere of both metals is filled with the isopropoxide groups, and the crystal is therefore not hydrolyzed or oxidized. While full crystal structure refinements were not performed, the approximate positions of the atoms were adequately identified. A representation of the structure was previously shown in **Figure 3.12**. It is similar to previously crystallized dimers of $LiNb(OEt)_6$ by Antipin,[99] $LiNb(OCHCMe_3)_6$ by Goel,[107] and alkali titanium alkoxides crystallized elsewhere.[108]

Both the isolated crystalline and amorphous precursor were used in separate solution-phase syntheses that were described in **Chapter 2**. The stoichiometric crystalline sample was expected to perform the best on account of

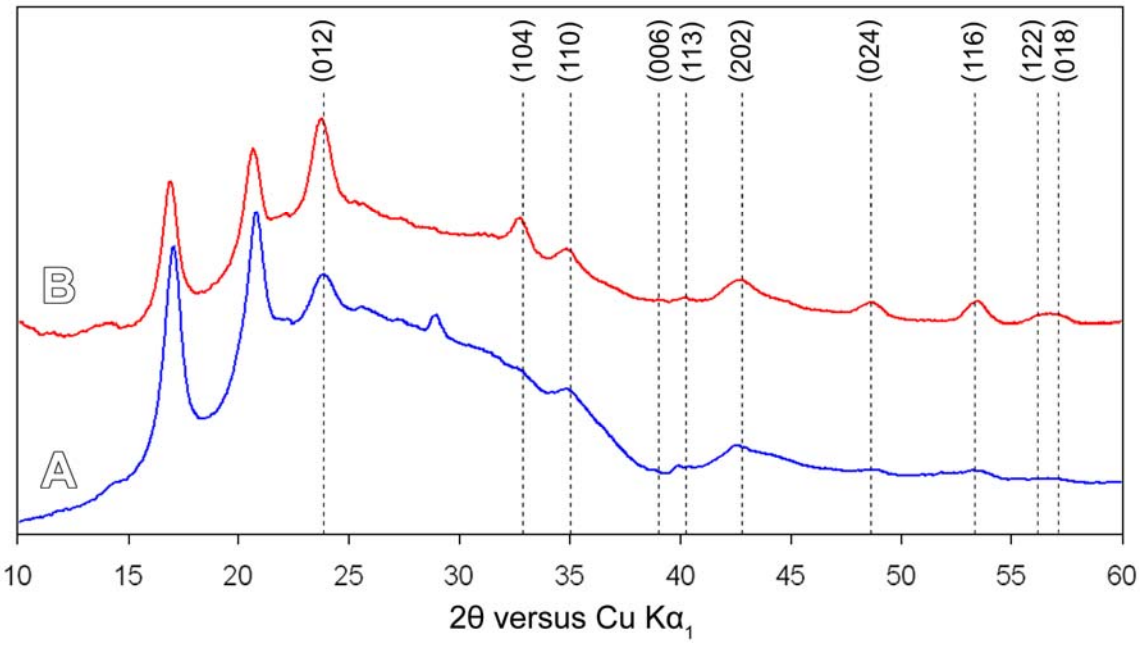

Figure 3.14 X-ray powder diffraction spectra of the crystalline (A) and polymeric (B) components of Chemat's $LiNb(OPr^i)_6$ precursor after they have been subjected to 20 h of reaction at 360 °C in TPPO. The dashed lines have been included to indicate the required peak positions for $LiNbO_3$. More $LiNbO_3$ and less of the impurity (17 and 22°) appear with the use of the polymeric precursor.

purity, but this was not the case. The powder diffraction patterns shown below are that for the products from the crystalline and amorphous precursors after 20 h at 360 °C (**Figure 3.14**), respectively. In both cases the intensity of the $LiNbO_3$ peaks increase with time, but the amorphous precursor always shows a more significant yield of $LiNbO_3$, and less of the undesired impurity phase (remaining peaks).

In order to investigate the composition of the Chemat precursor and to help us design a better precursor, a purified sample was submitted for CHN analysis. This sample was purified by the new, isopropanol procedure in order to give us an overall composition of the Chemat precursor. This analysis revealed that the mass percent of carbon and hydrogen in the purified precursor were

45.65 % and 9.03 %, respectively (expected 47.58 % and 9.32 %). The carbon and hydrogen deficiency are assumed to be the result of exposure to trace water, presumably in the glovebox or solvents of the manufacturer. The partial hydrolysis of the precursor results in the dissociation of an isopropyl group and its replacement by a hydroxide group. Subsequent heating in the processing procedure at Chemat would result in the partial condensation of those hydrolyzed bonds. If the assumption is made that the carbon and hydrogen deficiency is due to the loss of isopropoxy groups, as a result of hydrolysis and condensation reactions, a molecular formula can be derived for the Chemat precursor (**Appendix 3.5**). The overall formula for the Chemat precursor was found to be $LiNb(OH)_{0.389}(O)_{0.088}(OPr^i)_{5.435}$ (MW = 429.0305 g/mol). This analysis shows that hydrolysis has resulted in the loss of one isopropoxide ligand per dimer (12 OPr^i expected and 10.87 seen; **Figure 3.12**) and that condensation is 31 % complete.

With respect to the solution-phase synthesis of $LiNbO_3$, it will be shown that more $LiNbO_3$ is formed as a result of a partially hydrolyzed or condensed red precursor. The presence of hydroxyl and oxide bridging bonds are stronger than alkoxide bonds, and these enable the formation of more $LiNbO_3$ by maintaining more lithium–oxygen-niobium segments. In the following section the synthesis and decomposition of our own high purity and partially oxidized $LiNb(OPr^i)_6$ is described. This work clearly identifies the need for stronger oxide-linked metal centers to form more $LiNbO_3$ and limit the appearance of the impurity phase seen in the powder diffraction pattern of many samples, including **Figure 3.14**.

3.11.3 Preparation of Lithium Niobium Isopropoxide

The synthesis of our own $LiNb(OPr^i)_6$ became a necessary task in this research to overcome the lack of commercial availability and inconsistent purity. Our first synthesis of $LiNb(OPr^i)_6$ was according to Mehrotra *et al*. who reacted lithium with isopropanol to form the $LiOPr^i$ *in situ* during the reaction:[109]

$$Li + Pr^iOH + Nb(OPr^i)_5 \xrightarrow{\textit{isopropanol / benzene}} LiNb(OPr^i)_6 \qquad (24)$$

Our previous research involving $Nb(OPr^i)_5$ reactivity (**Section 3.7**) allowed us to establish that $Nb(OPr^i)_5$ needs to be converted to the monomer to be effectively reacted with $LiOPr^i$. Reflux and the presence of isopropanol are necessary for the formation of $LiNb(OPr^i)_6$. This reaction [**equation (24)**] was performed first with excess lithium then with excess isopropanol. The latter was adopted to prevent the possible reduction of Nb^{5+} to Nb^{4+} by lithium. This reduction was known to be possible from the metathesis reaction described earlier in this section.

In both reactions, bubbles of $H_{2(g)}$ form once the lithium rod is added to the solution of $Nb(OPr^i)_5$, and the solution takes on an orange color. The color seen after 1 h of reaction is typical of solubilized niobium oxo-alkoxide complexes,[110] in this case possibly $LiNbO(OPr^i)_4$. This observation highlights the possibility that $Nb(OPr^i)_5$ used in this experiment may have become partially hydrolyzed (e.g., $NbOH(OPr^i)_4$) because the resulting hydroxyl group would have reacted first because it is much more acidic than the available isopropanol proton. As the reaction refluxes overnight the two tested conditions differ greatly in appearance.

In excess lithium, refluxing overnight produces a brown-green solution and less lithium metal remained than expected from reaction stoichiometry. This observation may have resulted from further reaction between lithium and the niobium alkoxide to produce blue Nb^{4+} and green Nb^{3+} complexes. In excess isopropanol, the initial red color fades to produce a clear solution. This observation is believed to be the result of intermolecular bonding between $LiNbO(OPr^i)_4$ and $LiNb(OPr^i)_6$. In this second reaction, the formation of blue Nb^{4+} and green Nb^{3+} appears to have been prevented by the protection of niobium with additional acidic isopropanol groups. During concentration of this precursor a viscous transparent gel forms that is further dried into a dry white powder. The suitability of the latter precursor was tested by using the isolated powder in the solution-phase synthesis described in **Chapter 2** (**Figure 3.15A**).

Since the use of elemental lithium posed an oxidation risk to the precursor, another method of preparation was required. The first method was adapted with the substitution of lithium for butyl lithium to avoid the possibility of reduction:

$$Bu^nLi + Pr^iOH + Nb(OPr^i)_5 \xrightarrow{0\,^\circ C,\ heptane} LiNb(OPr^i)_6 + Bu^nH \qquad (25)$$

The addition of the first few drops of Bu^nLi to this solution was surprisingly accompanied by a color change to a yellow-green color. Over time (30 min) the greenish color fades to leave a yellow solution. The powder obtained from this reaction had a yellow appearance. The failure of this attempt to produce $LiNbO_3$

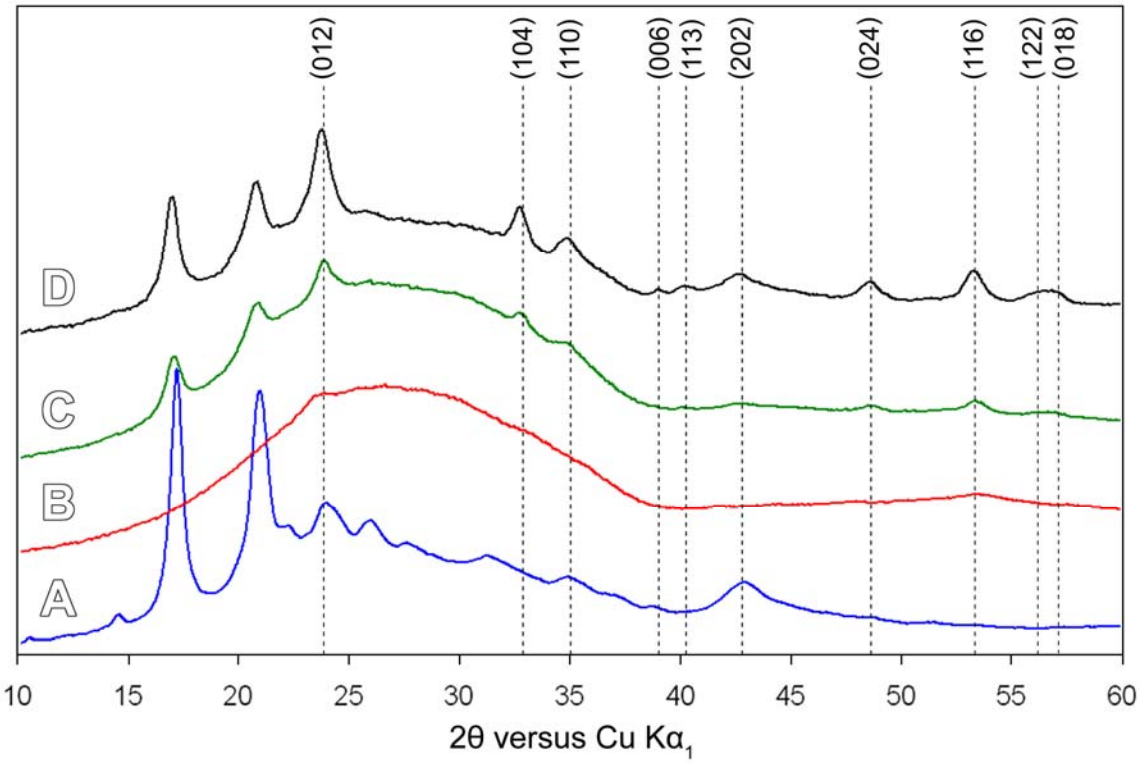

Figure 3.15 A XRD of solution-phase reaction products using $LiNb(OPr^i)_6$: (A) derived reaction with Li and $Nb(OPr^i)_5$, (B) derived after 2 h of reaction between Bu^nLi and $Nb(OPr^i)_5$, (C) derived from 24 h of reflux of orange $LiOPr^i$ [i.e. 72 h of reaction in equation (14)] in and $Nb(OPr^i)_5$, and (D) derived after purification of the Chemat precursor.

from the isolated precursor, was reason to dismiss this technique (**Figure 3.15B**). The use of $LiOPr^i$ in place of Bu^nLi would be the last method applied in this research and it became the standard practice of preparing the precursor:

$$LiOPr^i + Nb(OPr^i)_5 \xrightarrow{reflux,isopropanol} LiNb(OPr^i)_6 \qquad (26)$$

This reaction is similar to that of Hirano and Kato,[96] but unlike the $Nb(OEt)_5$ used in their reaction, $Nb(OPr^i)_5$ is mostly monomeric at equilibrium. This property leads to a complete reaction in much less than 24 h. After 1 h of reflux light

orange $LiOPr^i$ [after 72 h of **equation (14)**] and $Nb(OPr^i)_5$ converge to form a single methyne septet and a single methyl doublet (**Figure 3.16A and D,** respectively). The small broad shoulder seen in the methyne spectrum may represent a small amount of $LiOPr^i$ that has not fully integrated with the precursor. The peak area of this shoulder must be included for a calculation of a 1:6 peak area ratio between the methyne and the methyl protons, respectively. The endpoint of the reaction is easily identified because $LiOPr^i$ is insoluble in isopropanol until it has reacted with $Nb(OPr^i)_5$. Both the methyl and methyne signals of the product occur downfield of the previous niobium monomer signals as would be expected by the presence of a second bridging metal atom, but the magnitude of the shifts is not proportional nor clearly understood. The methyl peaks shift 0.121 ppm downfield and the methyne peaks shift just 0.024 ppm

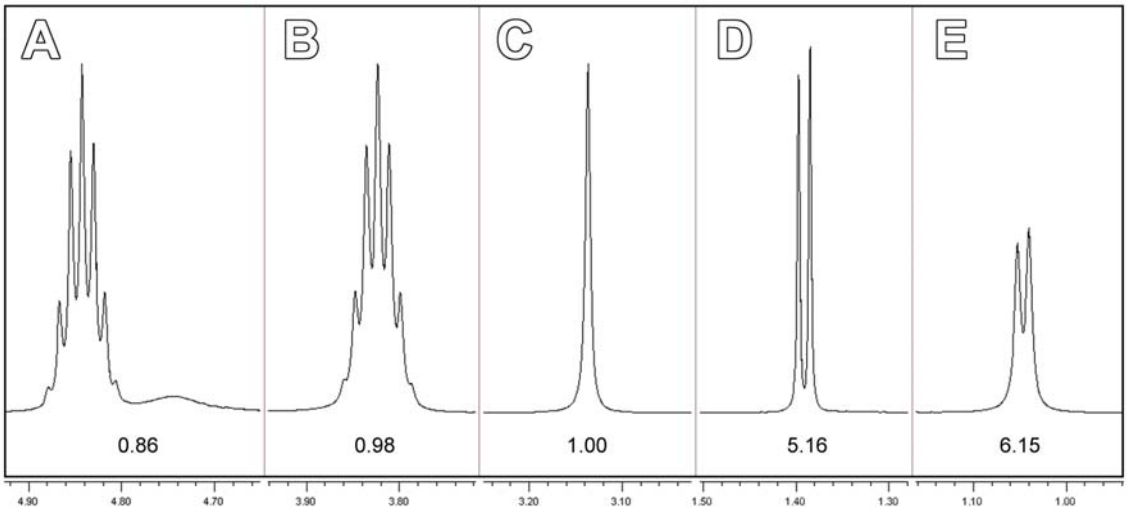

Figure 3.16 **^{1}H-NMR (500 MHz) spectra of $LiOPr^i$ reacted with $Nb(OPr^i)_5$ for 1 h in refluxing isopropanol. Peaks are identified as a (A) septet for the precursor methynes and possibly unincorporated $LiOPr^i$ (shoulder), (B) a septet for isopropanol methyne, (C) a singlet for the isopropanol hydroxyl proton, (D) a doublet from the precursor methyls, and (E) a doublet for the isopropanol methyls.**

downfield, relative the monomeric $Nb(OPr^i)_5$ peaks. The methyl shift is the opposite to what would be expected for the complex because distal methyl positions should not be as electronically influenced as the methyne positions that are adjacent the new bridging bonds. In the work of Hirano and Kato[111], they observe the expected shift magnitudes where the methyl remain relatively stationary. The shift discrepancy could be the result of the same intramolecular hydrogen bonding that was present in the $LiOPr^i$. After a further 24 h of reflux the solvent was removed by vacuum distillation. The solution concentrates to a yellow gel that dries to yield a light beige powder. This precursor was also tested for adequacy in the solution-phase synthesis of nanoscale $LiNbO_3$ (**Figure 3.15C**). Between the precursors tested, the use of $LiOPr^i$ as a lithium reagent had the highest yield of $LiNbO_3$ with respect to the impurity phase (seen below 23^o). None of the prepared precursors were as effective at producing $LiNbO_3$ as the purified commercial source (**Figure 3.15D**).

3.11.4 Optimization of the Bonding within Prepared $LiNb(OPr^i)_6$

From the powder diffraction patterns of Chemat-derived $LiNbO_3$ and our precursor derived $LiNbO_3$, it became apparent that a more deeply colored precursor was better for producing $LiNbO_3$ with less observable secondary phases. This result was attributed to the stronger oxide links holding lithium and niobium centers together. Since former methods used a light orange $LiOPr^i$ that had an unknown state of hydrolysis or oxidation, only white $LiOPr^i$ prepared in >24 h would be used herein. ^{1}H-NMR was used to test the suitability of the lithium reagent by inspecting for any additional hydrolysis-based peaks

(described in **Section 3.4**). The synthesized high-purity $LiNb(OPr^i)_6$ [via **equation (26)**] was then treated by several methods to controllably introduce oxygen bridging sites.

The first method employed the simple addition of water; either neat, through a carrier gas, or as a trace component in isopropanol. The hydrolysis and condensation reactions are represented, respectively, as:

$$LiNb(OPr^i)_6 + n\ H_2O \xrightarrow{isopropanol} LiNb(OH)_n(OPr^i)_{(6-n)} + nPr^iOH \qquad (27)$$

$$LiNb(OH)_n(OPr^i)_{(6-n)} \xrightarrow{reflux,\ isopropanol} LiNbO_n(OPr^i)_{(6-2n)} + nPr^iOH \qquad (28)$$

The condensation reaction [**equation (28)**] is not restricted to only intermolecular processes as suggested here. In the first step [**equation (27)**], the hydrolysis reaction is much faster for $LiNb(OPr^i)_6$ than $LiNb(OEt)_6$ and this can lead to the creation of less compositionally homogeneous gels.[119] In our work, $LiNb(OPr^i)_6$ hydrolzed so fast that precipitates formed instantly in all the cases studied. Reflux could also not redissolve the precipitates regardless time or precipitate abundance. To slow the rate of H_2O addition, an inert experiment was modified to carry humidified $N_{2(g)}$ through a isopropanol solution of the high-purity $LiNb(OPr^i)_6$ precursor. The concentration of H_2O in the vapour phase was controlled by the temperature of the water source. Precipitate forms more slowly in this case and is less abundant. None of the dried precursors extracted from these solutions were capable of producing an appreciable amount of $LiNbO_3$ by the solution-phase reaction (e.g., **Figure 3.17A**).

Two other methods to introduce oxide bonds in $LiNb(OPr^i)_6$ used time as the controlling variable and they were based on either the thermal elimination of diisopropyl ether or alcohol and an alkene from the complex:

$$LiNb(OPr^i)_6 \xrightarrow{\textit{reflux, heptane}} LiNbO(OPr^i)_4 + O(Pr^i)_2 \quad (29)$$

$$LiNb(OPr^i)_6 \xrightarrow{\textit{reflux, heptane}} LiNbO(OPr^i)_4 + CH_2{=}CHCH_3 + Pr^iOH \quad (30)$$

These methods of decomposition are known to occur for a number of alkoxides.[67, 74, 120, 121] Essentially, these reactions are just the addition of a prolonged high temperature reflux in **equation (26)**. The physical appearance of the isolated $LiNb(OPr^i)_6$ powder did not change significantly as a result of these reactions, but the solutions did appear slightly more yellow in color. The result of using this precursor in the solution-phase synthesis is presented in **Figure 3.17B**. This method represents the most optimal route of preparing $LiNb(OPr^i)_6$ in terms of the amount of $LiNbO_3$ produced relative to the impurity.

The fourth method of introducing oxide bonding was to reflux $LiNb(OPr^i)_6$ in the presence of varying concentrations of $O_{2(g)}$. Time and solvent polarity can be examined as control variables. While this reaction has been identified in one article as capable of producing $LiNbO(OEt)_4$ crystals, the mechanism is not known or discussed.[110] The capability of $LiOPr^i$ to participate in radical reactions has already been discussed and may be responsible for this reaction. More commonly, the reaction is seen in metal alkoxides that have at least one valence electron to initiate the reaction.[112] The other alternative is that the reaction is

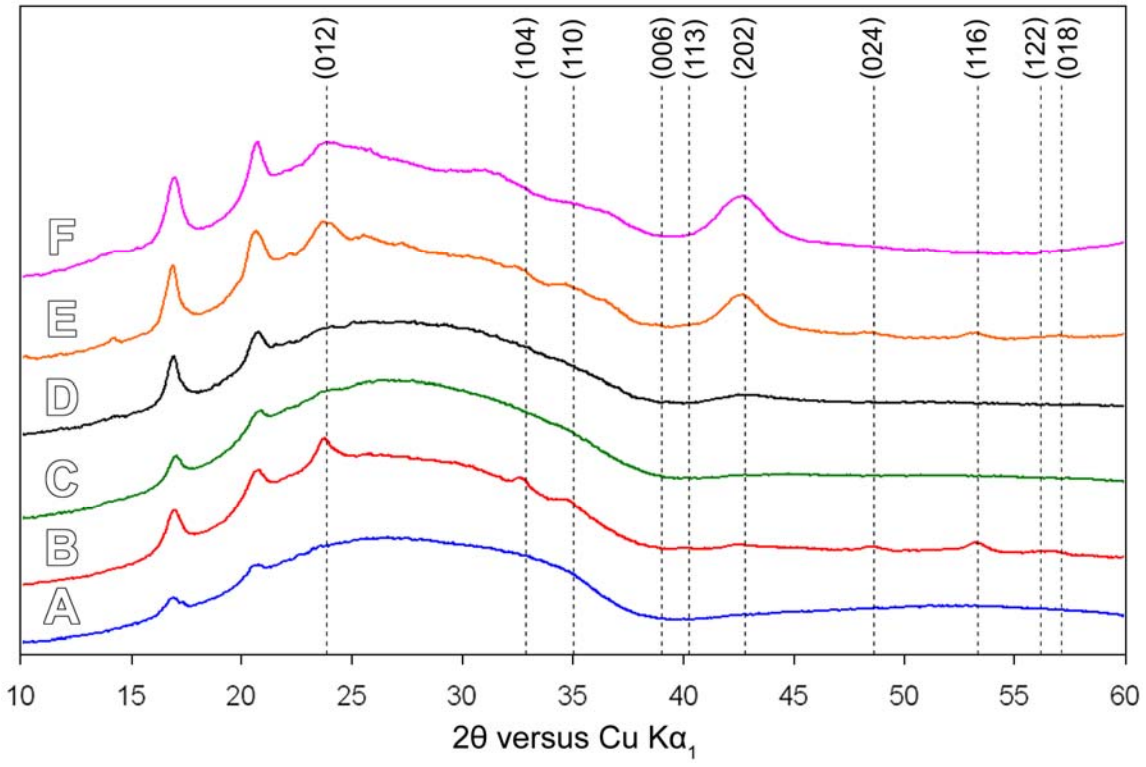

Figure 3.17 The X-ray powder diffraction spectra of decomposition products from different precursors used in the solution-phase synthesis of $LiNbO_3$. All precursors were first derived from equation (26) then reacted to form oxide bonds by a number of methods: (A) by typical H_2O hydrolysis [equation (27) and (28)], (B) 24 h reflux [equation (29) and (30)], (C) by reflux of precursor in O_2, (D) by a slow 4-week exposure to atmosphere, (E) by a 3 day exposure of isopropanol wetted powder to trace atmosphere, (F) by reflux and purification of (D) in isopropanol.

simply the product of a light combustion that is controlled by temperature. Regardless of the nature of the reaction, a noticeable red-colored solution was observed, to our surprise, within a few minutes of reflux in dry heptanes under pure O_2. Once isolated, the precursor reacts to form only trace quantities of $LiNbO_3$ after 24 h of reaction in TPPO (denoted by the 012 peak **Figure 3.17C**).

The final method was to leave pure powdered $LiNb(OPr^i)_6$ in sealed scintillation vials on the counter to react with atmospheric water and oxygen over different periods of time. This process was believed to mimic how the precursor

may have been handled at the manufacturing plant. Unfortunately, the vial seals were not consistent enough to act as a control-variable. The vials stored for 1 to 4 weeks had varying degrees of orange color and they remained a loose powder that was not capable of producing $LiNbO_3$ (**Figure 3.17D**). If a trace amount of isopropanol is left in the powder, the color change occurs in a much shorter time frame and it is more capable for use in the solution-phase reaction (**Figure 3.17E**). If that precursor is redisolved in isopropanol, refluxed, filtered, and reconcentrated the results do not appear to significantly change (**Figure 3.17F**). The peak heights for $LiNbO_3$ in this set of reactions indicates that solvent facilitates the creation of an optimized precursor, possibly by homogenizing the distribution of hydrolyzed/oxidized bonds in the precursor.

Since the polymeric Chemat precursor still superseded our own precursors ability to generate $LiNbO_3$, a technique was needed that would allow us to compare the structural differences between our material and that of Chemat. This type of comparison would allow us review the adequacy of our chosen solvents, atmospheres, and refluxing time and help to identify the best possible process. Since all precursors are soluble in benzene, ^{1}H-NMR was used as an effective tool for qualitatively comparing the effects of the preceding variables. Four different conditions were tested in this work that are characterized according to the refluxing solvent, the atmosphere, and the length of reaction, respectively. These reactions include: (B) isopropanol/N_2/4 h, (C) isopropanol/N_2/24 h, (D) heptane/1 % O_2 in N_2/24 h, and (E) heptane/O_2/1 h (**Figure 3.18 and 3.19**). The commercial source of $LiNb(OPr^i)_6$ (Chemat) is

shown as Figure 3.18A for comparison. Broad peaks and peak overlap rendered peak integration data difficult to extract for a meaningful discussion so it has been excluded from the spectra.

In the methyl region, the Chemat precursor appears as two triplet-like peaks that are likely the result of two separate isopropoxide environments where the methyls have confined mobility. Relative to the main precursor doublet at roughly 1.40 ppm, refluxing the precursors can be observed to generate the necessary second methyl environment, but it occurs at a lower chemical shift than expected (1.34 ppm). The reason for the observed shift is believed to be due to a decomposition similar to that of **equation (29)** or **(30)** where some Nb=O bonds are formed. These would partially alleviate the electron-withdrawing effect of the highly positive Nb^{5+} atoms. Oxygen is not necessary for this step to occur and that was demonstrated in **Figure 3.18B** through **3.18D** where oxygen is present in only 0-1 %. Notably, the peaks of (D), with just 1 % O_2, start to deshield to more closely resemble the Chemat structure. This shift is accompanied by the appearance of a broad shoulder that could indicate O_2 starts to hinder the mobility of isopropoxyl methyls. The use of pure O_2 in heptane results in a much greater concentration of the second methyl environment. Two triplet-like ensembles at 1.37 and 1.43 ppm are also observed that, although at a higher chemical shift, appear similar in structure to the spectrum of the Chemat precursor.

The methyne region of the ^{1}H-NMR provides a complementary story to that seen in the methyl region. In the Chemat precursor, all peaks are broadened

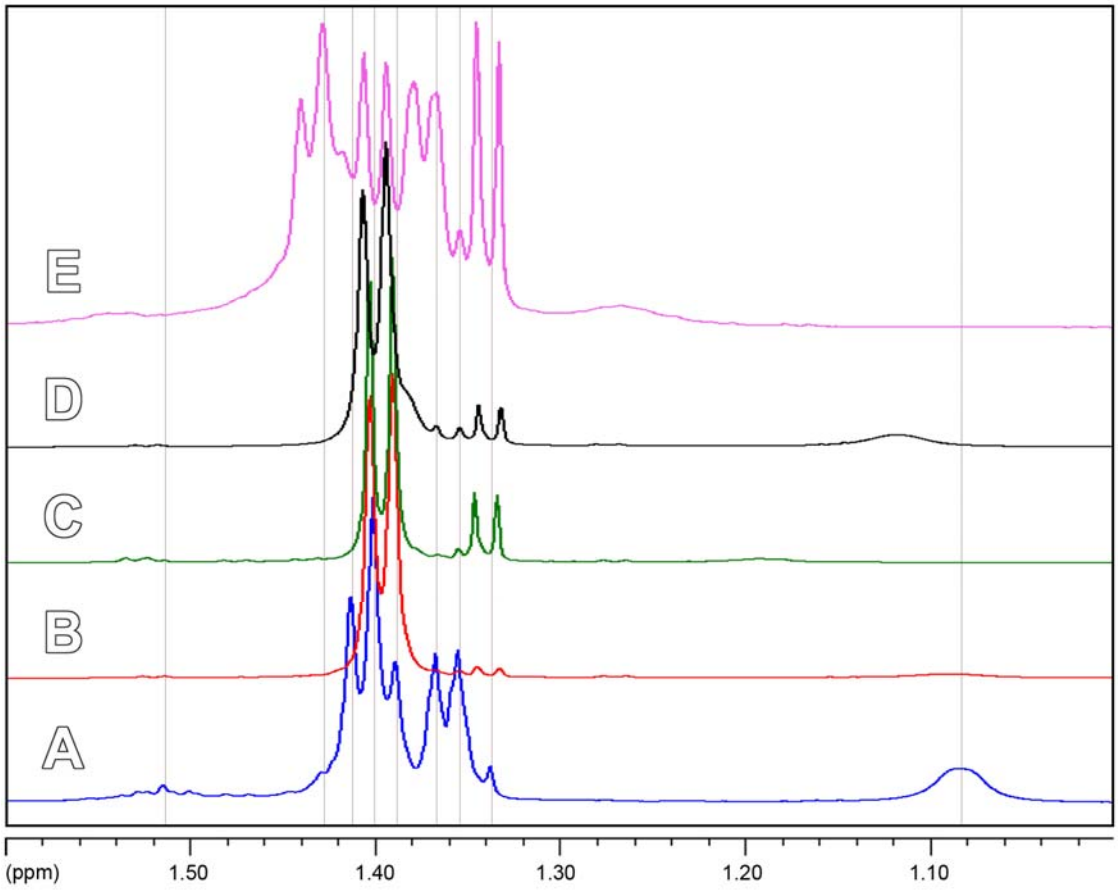

Figure 3.18 **^{1}H-NMR (500 MHz) spectra of the methyl region for (A) the purified CHEMAT precursor and high-purity LiOPr^{i} reacted with Nb(OPr^{i})$_5$ according to the following conditions: (B) heptane/O_2/1 h reflux, (C) isopropanol/N_2/4 h reflux, (D) isopropanol/N_2/ 24 h reflux, and (E) heptane/1 % O_2 (in N_2) /24 h reflux. All samples were analyzed in d_6-benzene.[83]**

revealing a high state of disorder as would be expected from the structure of a sol. By comparison with the synthesized samples, the broad peak at higher chemical shift in the Chemat precursor looks as though it can be deconvoluted into two “methyne” regions. Peaks protruding from the bulge at high chemical shift resemble those of a more crystalline precursor, such as that of (B) that has been lightly processed. The majority of the bulge resembles the peaks that form upon more heavy processing. Without a high concentration of O_2, samples B

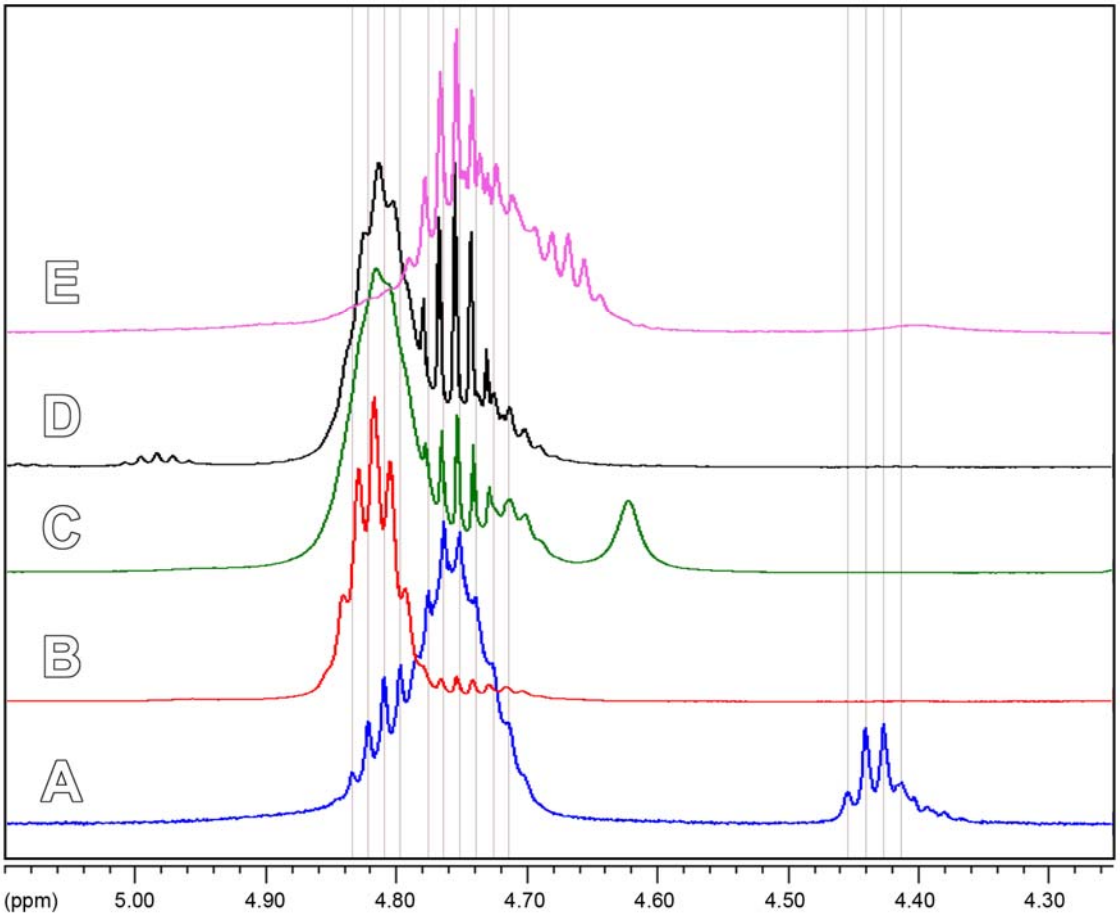

Figure 3.19 **^{1}H-NMR (500 MHz) spectra of the methyne region for (A) the purified CHEMAT precursor and high-purity LiOPr^{i} reacted with Nb(OPr^{i})$_5$ according to the following conditions: (B) heptane/O_2/1 h reflux, (C) isopropanol/N_2/4 h reflux, (D) isopropanol/N_2/ 24 h reflux, and (E) heptane/1 % O_2 (in N_2) /24 h reflux. All samples were analyzed in d_6-benzene.[83]**

through D produce the same peak positions seen to protrude in the Chemat compound, but the sharpness of peaks shows that the modified structure still has too much order. The only sample that notably resembles Chemat is that of (E); synthesized in pure O_2. Coupling these findings with that of the methyl region, it looks as though the isopropoxide groups restructure in a beneficial way through the action of refluxing. While the structure has been altered, it still contains too

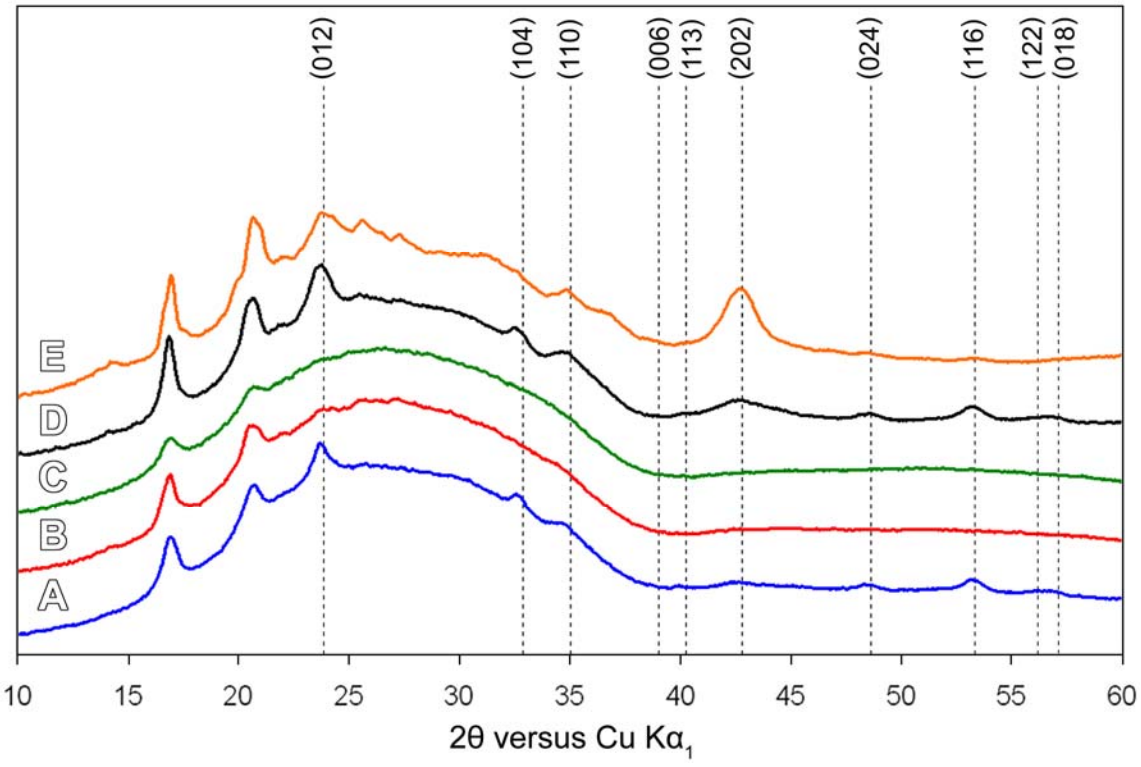

Figure 3.20 **X-ray powder diffraction spectra of $LiNbO_3$ synthesized in the solution-phase reaction using (A) $LiNb(OPr^i)_6$ derived from orange $LiOPr^i$ in equation (26), (B) $LiNb(OPr^i)_6$ after substitution of 12 % of the isopropoxides with ethylene glycol, (C) $LiNb(OPr^i)_6$ after substitution of 50 % of the isopropoxides with ethylene glycol, (D) $LiNb(OPr^i)_6$ after substitution of 12 % of the isopropoxides with 1-methoxy-isopropanol, and (E) 12 % substitution of isopropoxides with 1-methoxy-isopropanol followed by reflux in air 30 min.**

much regularity. Mass disorder and cross-linking in the structure appears to be the necessary role of oxygen. More work is needed to examine the length of oxygen exposure more closely. Future experiments that explore isopropanol/O_2 reactions and mixed polarity solutions would make a good accompaniment to the research presented here.

If oxide links were difficult to introduce reproducibly, another way to strengthen the links between lithium and niobium atoms was through doping with chelating molecules.[113] These bichelate (trichelate, etc.) molecules displace isopropanol to tether together separate $LiNb(OPr^i)_6$ centers. These types of

additives have proven to be an effective way of maintaining product stoichiometry with the use of alkoxides in chemical vapour deposition.[113] To further improve our precursor, chelates were doped in to represent 12 % to 50 % of the previously attached alkoxy groups. These precursors were used in the solution-phase reaction to test their effect on the solution-phase synthesis of $LiNbO_3$ (**Figure 3.20**). The use of 12 % 1-methoxy-isopropanol was the only dopant that can be argued to produce less of the impurity phases and more $LiNbO_3$. The failure of ethylene glycol to produce any $LiNbO_3$, indicates that it has disrupted the decomposition mechanism in some way. The hypothesized mechanism for this reaction (**Figure 2.6**) reveals that a γ-H position is required on the precursor for decomposition to occur. The mechanism of decomposition will be discussed further in **Chapter 4**.

3.12 Concluding Remarks

In this Chapter, the synthesis and characterization of a number of alkoxide and mixed oxo-alkoxide precursors have been discussed. In general, the work here has found that commercially sourced precursors, including $LiNb(OPr^i)_6$ (Chemat, Alfa Aesar) and $Bi(OPr^i)_3$ (Alfa Aesar), are not the compounds specified. Instead, they have partially decomposed to form mixed oxo-alkoxides.

In the synthesis of $LiNb(OPr^i)_6$, it was discovered that oxygen and the surface hydroxide impurities of lithium rod lead to the generation of a colored $LiOPr^i$ precursor. If the lithium rod is sufficiently cleaned, and the conditions are rigorously maintained, there is no need to use the more expensive alternative of synthesizing $LiOPr^i$ with butyl lithium. The key requirement in the synthesis of

$LiOPr^i$ is purity because consistent $LiOPr^i$ reagents are necessary to ensure a reproducible quality in the prepared precursor. Oxide linkages that result in the observed coloration can be added controllably at a later stage using a number of discussed techniques. Characterization of niobium isopropoxide reveals that it recrystallizes in high purity in a mixed monomeric and dimeric crystallline form. In order for a complete reaction of $Nb(OPr^i)_5$ with $LiOPr^i$, isopropanol and refluxing conditions (<2 h) are necessary to cleave the dimeric structure of $Nb_2(OPr^i)_{10}$. Thereafter, the most optimal precursor is obtained by a partial decomposition caused by a prolonged reflux in a heptane dominant solution where the atmosphere is regulated to contain a specific amount of O_2. To date, this precursor and others synthesized by the preceding reactions have not compared to the suitability of the polymeric component of the commercial material.

The synthesis and characterization of a number of other SHG relevant alkoxides was also discussed. Bismuth, barium, boron, potassium and sodium alkoxides were among those materials synthesized, and the reaction procedures were scrutinized. Namely, the synthesis of $Bi(OPr^i)_3$ is hindered by solubility issues, and may require alternative equipment to produce in the future. The ethoxide is claimed to be more soluble[105] and may be a good alternative to pursue if difficulties with the isopropoxide derivative continue. For the synthesis of $B(OPr^i)_3$, several condensation impurities were suggested in the product as a result of an incomplete removal of water. Several easily implemented changes to the reaction procedure could help to improve the purity in the future syntheses of this compound.

The following Chapter is devoted to a detailed examination of the solution-phase synthesis of $LiNbO_3$ based on the precursor, $LiNb(OPr^i)_6$, discussed here. In particular, justification is provided for the temperature, time, solvent, and atmosphere of reaction, and the purification procedure required to isolate the most product with the least amount of impurity phases. The composition of the reaction product and by-products are also described to provide a complete story about the processes occurring during the solution-phase synthesis of $LiNbO_3$ nanocrystals.

CHAPTER 4 – CHARACTERIZATION OF THE REACTION PROCESSES, PRODUCTS, AND BY-PRODUCTS

4.1 Introduction

In this Chapter the products of $LiNb(OPr^i)_6$ decomposition are explored in detail for both the chloride-based and choride-free reactions. This discussion includes the products remaining in solution and the volatiles that were eliminated during the decomposition of $LiNb(OPr^i)_6$ under different reaction conditions. Together, the information obtained about the reaction products and byproducts offer a description about the manner in which Nb_2O_5 and $LiNbO_3$ come about in the chloride-based and choride-free reactions, respectively. Through understanding, the steps required to optimize the process also become apparent in this Chapter.

4.2 The Chloride-Based Route to Pseudohexagonal Nb_2O_5

One of the nonhydrolytic syntheses of $LiNbO_3$ attempted in this work was based on a cross-reaction between stoichiometric quantities of $LiNb(OPr^i)_6$, $NbCl_5$ and LiCl. The specific details of this experimental procedure were introduced earlier in **Chapter 2**. The product from this process crystallized to form nanocrystals of Nb_2O_5 after just 2 h of reaction in TPPO.[74] While Nb_2O_5 was not the target compound of this reaction, it has a variety of interesting applications that justify further discussion about this product. Nanocrystals of

Nb_2O_5 are particularly interesting because the majority of applications are based on thin nanostructured films. The thermal, acid, base, air and moisture stability, in addition to the redox[114] capabilities of Nb_2O_5 make it an ideal coating that has found uses as an electrochromic film in smart windows,[124, 125] as a wide band-gap semiconductor in photovoltaic cells,[115] and as a component of oxide-based catalysts[116,117] and gas sensors.[118] In this section the structure and composition of synthesized Nb_2O_5 will be discussed utilizing X-ray powder diffraction and electron microscopy as the primary tools of characterization.

To evaluate the effect of the solution-phase process on crystal size and morphology, the reaction product was examined by transmission electron microscopy (TEM). Images obtained by this technique **(Figures 4.1A and B**) reveal a complex mixture of small and large nanocrystals with a variable degree of anisotropy. The product containing the smaller Nb_2O_5 particles is composed of crystallites with a diameter of 2.2 ± 0.6 nm. Many of these crystallites have an oblong shape or elongated structure (**Figure 4.1A inset**) with an average aspect ratio of 1.9 ± 0.9. The larger crystals of this composition are 30 ± 8 nm in diameter with average lengths of 100 nm. These rod-like structures also appear to be coarsely textured.

Electron diffraction can be observed as lattice fringe patterns in high-resolution TEM images (**Figures 4.1B**). These fringe patterns are useful for qualitative crystal identification and they also act to identify the crystal growth direction. The continuous extension of this pattern across the entire nanoparticle identifies that they are single crystal grains, although close examination can

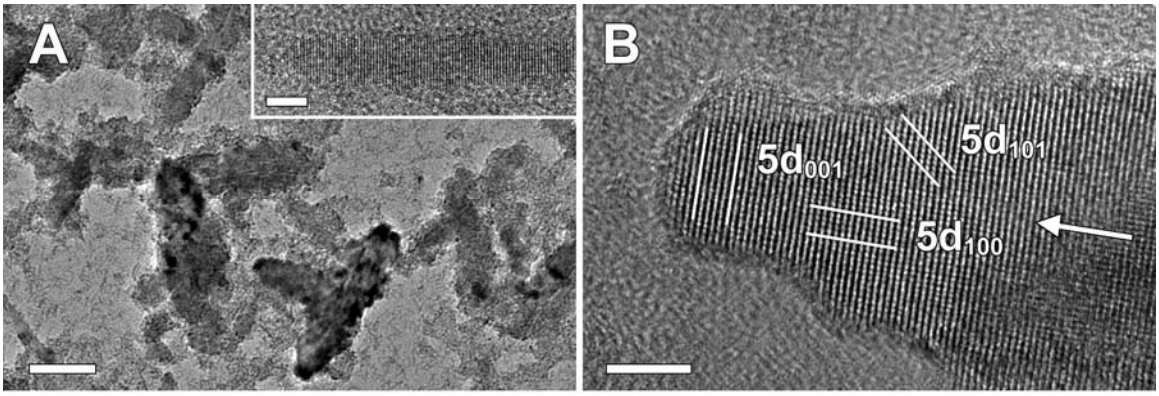

Figure 4.1 **(A) A transmission electron micrograph showing a broad view of the product morphology. (insert) A typical elongated morphology from the smaller crystals. (B) Electron diffraction observed by high resolution TEM can be associated to crystalline planes in Nb_2O_5 and they indicate *c*-axis growth (arrow). Scale bars are 50 nm (A) and 5 nm (B, insert). Reprinted with permission from the Materials Research Society © 2008.[74]**

find the rare stacking defect. Three sets of planes were observed in this image and they are estimated to have periodicities of 4.07 ± 0.07, 3.21 ± 0.06, and 2.44 ± 0.04 Å which correspond reasonably well to the observed d-spacing of the (001), (100), and (101) planes in pseudohexagonal Nb_2O_5, respectively (see **Appendix 3.6**). Their orientation relative to the observed crystal morphology indicates that anisotropy is along the [001] direction, and that growth has preferentially occurred along the *c*-axis of the hexagonal cell.

The composition and crystallinity of Nb_2O_5 were further evaluated by X-ray powder diffraction and subsequent computational analysis. With the use of indexing software,[75] the major peaks observed in the powder diffraction spectrum (**Figure 4.2**) are indexed to a hexagonal cell with cell parameters of a = 3.598 Å, c = 3.904 Å, and γ = 120 ^{o}. The values obtained for the crystal are in good agreement with those previously reported for Nb_2O_5 [119]. The d-spacing calculated for the 001, 100, and 101 planes in the spectrum are 3.92, 3.12, and

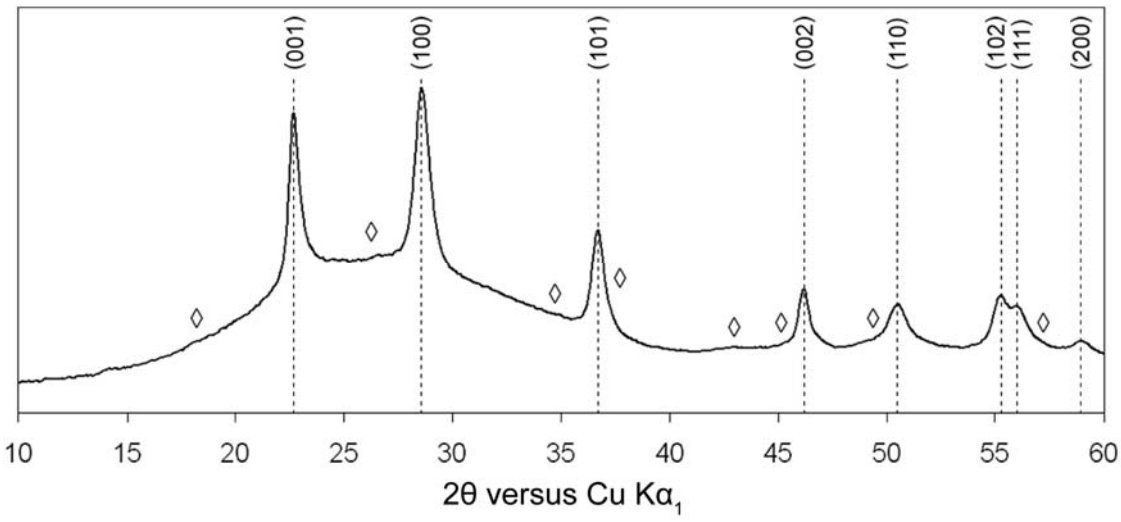

Figure 4.2 **X-ray powder diffraction of the synthesized pseudohexagonal Nb_2O_5 nanocrystals. Dashed lines represent the literature peak positions and they are shown with their respective miller indicies. Diamonds (◊) mark peaks that represent the onset of a phase transition to γ-Nb_2O_5. Reprinted with permission from the Materials Research Society © 2008.**[74]

2.45 Å, respectively, and they are in agreement to those calculated previously by electron diffraction. A further look at the spectrum reveals the absence of any lithium-based phases. This result suggests that LiCl has remained unreactive during the course of the reaction. The lithium alkoxide precursor is also believed to be consumed in LiCl production through a salt metathesis reaction. The lithium-free product of that reaction, $(RO)_5Nb$-(OR)-$NbCl_4$, would then decompose to give the observed Nb_2O_5.

The analysis of the X-ray powder diffraction pattern above has led to the belief that Nb_2O_5 crystallizes as the hexagonal δ-phase. However, at 360 ^oC a phase transition to the monoclinic γ-Nb_2O_5 phase is possible.[119,120] Such a transition could be responsible for the appearance of several low intensity peaks and shoulders (**Figure 4.2** diamonds) that were neglected during indexing.

Despite these peaks, this intermediate (δ/γ) form of Nb_2O_5 is indexed by many according to the major signals of the spectrum. Since this intermediate is not wholly represented by the hexagonal indexing, the structure is typically referred to as pseudohexagonal.

A rationale for the observed anisotropic crystal morphology can be hypothesized using some of the fundamentals of the coordinating solution approach described in **Chapter 2**. As a hexagonal crystal, Nb_2O_5 is predetermined to contain different surface energies for the exposed planes, and this is a necessary feature to create elongated structures. The kinetically high rate of monomer production for this reaction is suggested by the brief 2 h reaction time. The reaction was sufficiently fast to have resulted in the anisotropic growth seen in some of the small particles (**Figure 4.1A** inset). Usually, a high concentration of capping agent results in the formation of larger nanocrystals after growth is complete, but here very small nanocrystals resulted. It is believed that the reason for this observation may be that the high capping agent concentration was offset by the fast reactivity of precursor. In other words, the critical saturation level was elevated by the capping agent concentration (a high concentration causes less nucleation), but a high rate of monomer production means that the nucleation event plateaus at a higher monomer concentration (causes more nucleation events). The metathesis reaction, which is believed to initiate the decomposition, is a fast reaction even at room temperature. In fact, so many nucleation events are believed to have occurred that few monomers were available for growth. If the starting concentration of precursor is increased in this

reaction in the future, it may result in more material for growth and subsequently produce larger rod-shaped nanocrystals.

The sharp bimodal size distribution of particles seen by electron microscopy can not be rationalized in terms of the coordinating solution theory. It is believed that the high surface area of the small crystals resulted in a thermodynamically unstable state. The resulting aggregation of nuclei may be facilitated by insufficient steric resistance and/or surface-coordinating strength of TPPO at the chosen reaction temperature. Like growth, aggregation would be directed preferentially to the sites of highest surface energy. The observation of *c*-axis elongation in **Figure 4.1B** indicates that the *c*-axis of Nb_2O_5 has a higher chemical potential when compared with other exposed planes. Interestingly, the edges of the large nanocrystal in **Figure 4.1B** reveal 3-4 nm steps that could be suggestive of aggregation between ~2-3 nm nanocrystals.

The chloride-based nonhydrolytic reaction, used here was unsuccessful in incorporating the lithium ion to generate $LiNbO_3$. In spite of this, a commercially relevant material was produced. The analyses performed here identify that the synthesis resulted in the formation of pseudohexagonal Nb_2O_5 nanocrystals. If the concentration of the precursor is explored, along with changing the capping agent to one with greater steric bulk, this synthesis could be viable in the future for the production of monodisperse Nb_2O_5 nanocrystals of controllable size and shape. Size and shape control are specifically relevant to the current uses of Nb_2O_5 as a catalyst. The synthesis of monodisperse Nb_2O_5 nanocrystals would also be more applicable in the current use of the material in thin film applications.

4.3 The Chloride-Free Route to $LiNbO_3$

The second of the nonhydrolytic routes explored in this research was adapted to improve the probability of lithium uptake in the composition of the resulting crystal. This required the complete absence of chloride-based reagents to avoid the possibility of forming LiCl. Once this choice was made, $LiNbO_3$ was synthesized in addition to a number of secondary phases that are the topic of more discussion in the following section. Since the crystal structure and composition of $LiNbO_3$ can have implications on SHG, they are also discussed; including the effect of time and temperature on the product morphology. As a result of secondary phases, there is also considerable discussion in the following sections about the work that was performed to optimize the process either by identifying the reaction mechanism, by changing the reaction setup, or by changing the purification procedure.

4.4 The Morphology of the $LiNbO_3$ Nanocrystals

In order to optimize SHG performance for $LiNbO_3$ it was important that this reaction resulted in the production of morphologically anisotropic crystals. This property would facilitate the simple gravity-based ordering of crystals in a powder, and create localized breaks in inversion symmetry. The direction of anisotropy was also important because elongation of the crystal is most desirable in the direction of propagation for the second harmonic. In the simple case of SHG, the d_{31} or d_{33} coefficient would be utilized in $LiNbO_3$ by *a*- or *b*-axis illumination; therefore, *a*- or *b*-axis elongation is preferable. In this section,

electron microscopy reveals that our synthesis produces anisotropic nanocrystals of $LiNbO_3$. The lattice diffraction patterns obtained from these structures identify that they are single crystalline and have *c*-axis anisotropy. The impact of temperature and time on the resulting morphology is also discussed, in addition to a possible mechanism for the formation of these structures.

The morphology of the synthesized crystals was examined by transmission electron microscopy (TEM). Once the maximum reaction temperature is met (defined as the 0 h mark), the product is composed of 6 ± 1 nm particles with a poorly defined surface (**Figure 4.3**). The hazy surface-boundary of the crystallites indicate that the particles are still an amorphous material. An average aspect ratio for these crystals was also calculated to be 1.4 ± 0.3 and it indicates that they have a fairly isotropic shape. If the reaction temperature is changed between 360 and 380 ^{o}C it does not seem to greatly impact the surface texture or size of these particles (note the reduced size of the scale in the 360 ^{o}C sample). An additional 1 h reaction time in the 370 ^{o}C sample can, however, be seen to degrade the amorphous appearance of these particles to form more distinct surfaces. At roughly 19 h reaction time, all of the particles are clearly defined suggesting the onset of crystallinity. More importantly though, new anisotropic structures can be seen to develop in all of the images. These structures appear to be rod-like in shape, and they are favoured by the higher reaction temperatures. After further reaction time, this favourability becomes clearer as there is a marked difference in the particle-to-rod ratio at roughly 48 h. During the course of this additional day, these anisotropic structures continue to

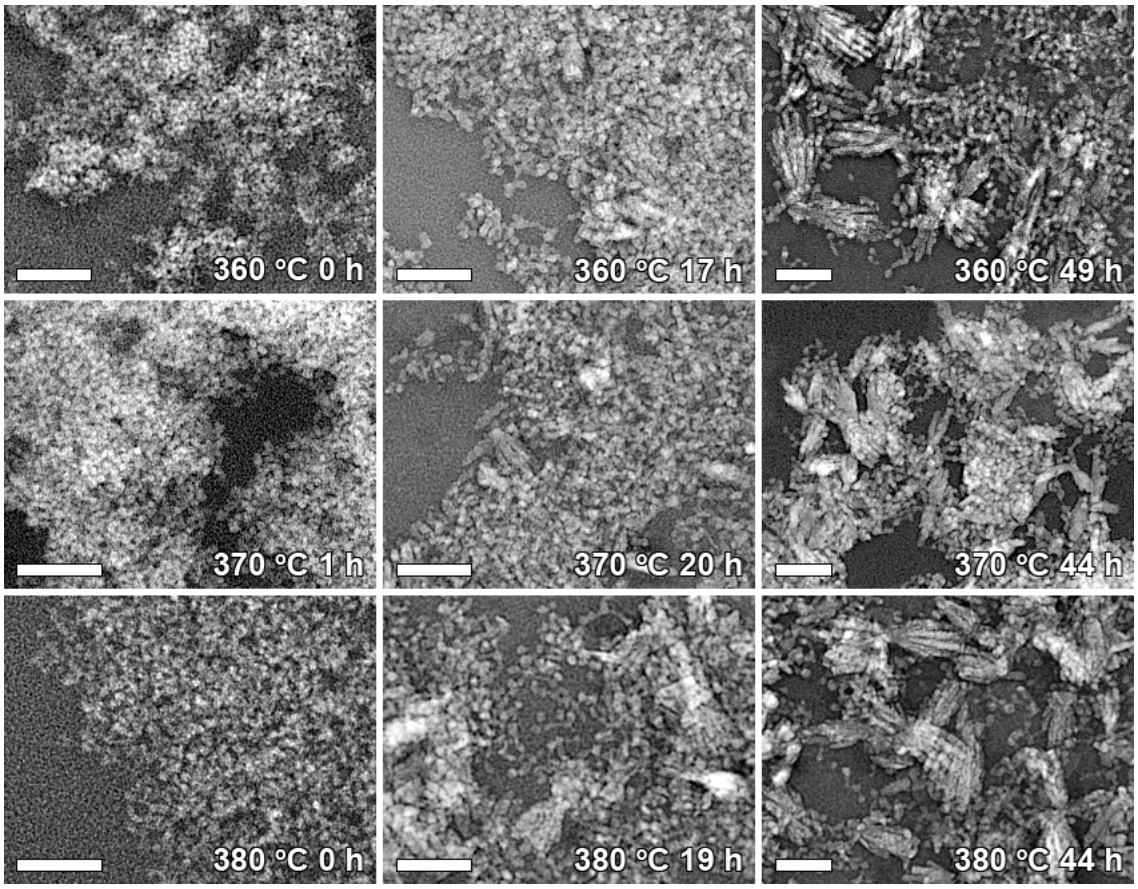

Figure 4.3 **A series of transmission electron micrographs that display the effect of time (horizontal) and temperature (vertical) on the morphology of the synthesized $LiNbO_3$ nanocrystals. All scale bars represent 50 nm. In all cases, an increase in time leads to crystallinity and an increase in the amount of anisotropic structures. An increase in reaction temperatures also appears to favour the formation of the anisotropic structures.**

grow in number and size. The length and number of rods found in the structures of each sample appears to have grown with reaction time. The rods of these structures are an average of 7 ± 1 nm in diameter and have average lengths of 51 ± 16 nm. Some of the largest particles reach 80 nm in length and can contain up to 13 visible rods. These particles are best described as fan-like in appearance. The rods that compose these fan-like structures are normally found

to share a common apex, and some apexes are shared by multiple fan-like structures.

The anisotropic structures were a surprising result. Further insight into the growth mechanism could be obtained through establishing a better understanding of the product. Of particular interest is the determination of the direction of anisotropy. The nanocrystals were examined by high resolution transmission electron microscopy (HRTEM) to obtain lattice fringe patterns for these particles. As in the case of Nb_2O_5, electron diffraction is observed from the niobium-dense planes within the crystal. The fan-like 3-dimensional structure of the nanocrystal creates a difficulty for this analysis because overlapping rods create two sets of diffraction patterns, and a suitable rod orientation must be

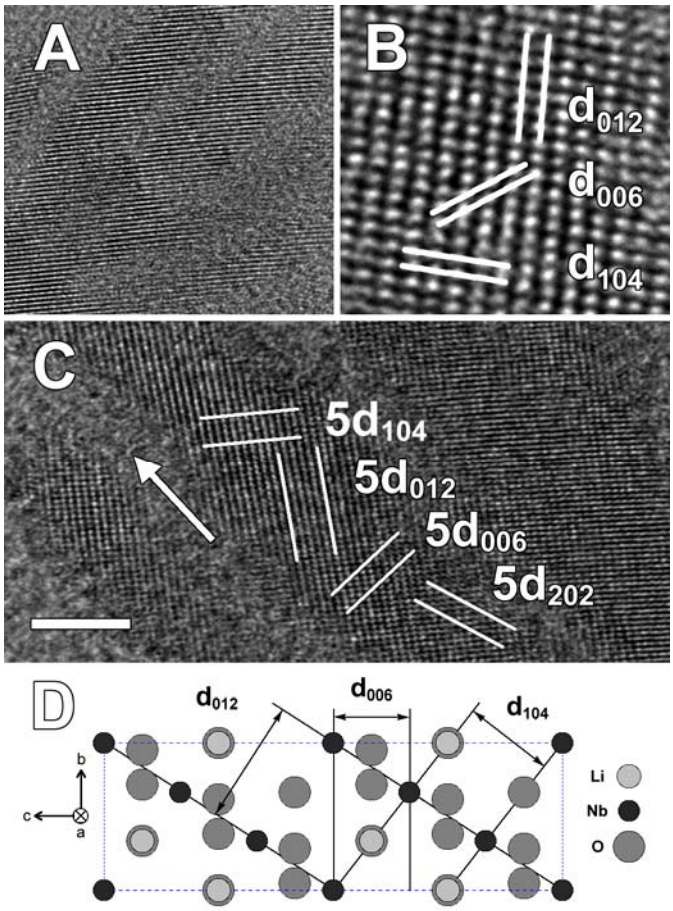

Figure 4.4 **(A) HRTEM image of an anisotropic structure indicating single crystallinity. (B) HRTEM image of a nanocrystal segment identifying single plane spacing. (C) orientation of the identified planes with respect to the growth direction marked by an arrow. Reprinted with permission from the Materials Research Society © 2008.[74] (D) A model of $LiNbO_3$ that identifies the diffracting planes in the images. Reprinted with permission from Wiley-VCH Verlag GmbH & Co. © 2008.[47]**

found such that at least three crystalline planes are orthogonal to the electron beam. This requirement is necessary because three vectors are needed to describe the spatial orientation of the nanocrystal. In many cases, non-overlapping rods could be found, however, only one diffracting plane is visible (**Figure 4.4A**). In this particular case, the lattice fringe pattern is continuous along the entire length of multiple rods indicating that it is a single crystal. Once a rod is found to identify all of the requirements, as in **Figure 4.4B**, lattice spacings of 3.76 ± 0.10, 2.85 ± 0.09, 2.37 ± 0.08 Å was calculated (see **Appendix 3.6**). These calculations correspond well to the expected d-spacing for the (012), (104), and (006) planes in $LiNbO_3$ (anticipated to be 3.75, 2.74, and 2.31 Å, respectively). Observation of the 012 and 104 planes orthogonal to the source beam is enough to identify that we are viewing the crystal along either the positive *a*- or *b*-axis, but the additional 006 plane is needed to identify the crystal orientation relative to the growth direction. The growth direction in this case is indicated by an arrow in **Figure 4.4C**, and it is oriented perpendicular to the set of 006 diffracting planes. This assignment indicates that the *c*-axis is the direction of anisotropy in these structures.

A plausible mechanism for the formation of the observed nanoparticles can be developed, through the use of the coordinating solution theory introduced in **Chapter 2**. Unlike the Nb_2O_5 synthesis, the long reaction time for the synthesis of $LiNbO_3$ indicates that the chloride-free mechanism of decomposition is much slower. The slower decomposition indicates that the precursor is more stable without the chloride present and a slower monomer flow is produced as a result.

In **Chapter 2**, the stabilization of precursors leads to less material being nucleated during the nucleation stage (**Figure 2.5**). With less material nucleated, more material is available for growth, and as a result the $LiNbO_3$ nanocrystals are approximately three times larger than those of the Nb_2O_5 synthesis. The $LiNbO_3$ nanocrystals are also observed to be rounded in shape (**Figure 4.3**, 0-1h), which is attributed to a number of factors, including a slow production of monomers imposing a thermodynamic growth scheme (see **Chapter 2**), and/or the non-surface specific binding of TPPO. Anisotropic structures are observed after ~19 h time, which is long after decomposition of the precursor is complete (noted by the completion of off-gassing). These anisotropic shapes are, therefore, not a result of the growth phase. Instead, the anisotropic shapes appear during aging, which suggests they are the result of aggregation.

Electron microscopy provides several indications that the process of nanorod formation is the result of the directed aggregation of crystals. This technique also reveals the possible origin of their fan-like appearance.

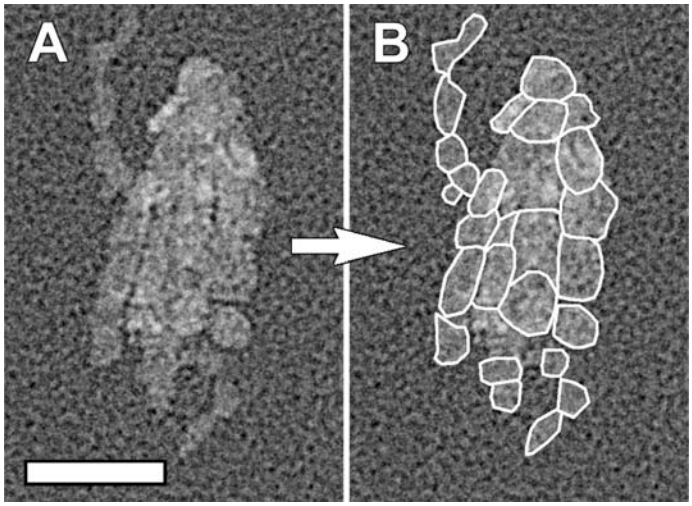

Figure 4.5 **(A) The nodular shape of the anisotropic structure is the result of aggregation between several nanocrystals. The adjacent nanoparticle (B) shows how the crystal can be deconvoluted into its hypothetical particle-components. Lines were overlaid where density changes appear in the nanocrystal. The scale bar is 25 nm.**

The first indication of aggregation is that the diameter of the rods is very similar to those of the particles.[121] The second is that the length of the rod appears nodular in shape and density (**Figure 4.5**). Thirdly, there is a marked increase in the rod-to-particle concentration as time progresses[122] and no additional source of material is being supplied to support their growth by another mechanism. A further proof is also suggested by some authors to be made by dividing the rod length by the average nanocrystal length.[121,123] If nanocrystals are aggregating, a large frequency of these calculations will result in whole numbers. In the case of our $LiNbO_3$, only 30 nanorods have been analyzed relative the thousands that would be required to obtain a trend with any statistical merit. Therefore, this calculation could not be applied in this research. The mechanism responsible for the formation of the fan-like appearance of the rod assemblies is attributed to differing rates of aggregation on the different crystal planes identified by HRTEM. Clearly, the *c*-axis elongation indicates that there is a higher surface potential observed for the (006) plane than the others. However, this elongation is intuitively strange since the surface energy is expected to be proportional to the planar niobium density. That density is just 0.0218 Nb/Å^2 for the (006) plane relative 0.0354 and 0.0258 Nb/Å^2 for the (012) and (104) planes, respectively.[124] The reason for the enhanced chemical activity is believed to be the result of surface charges generated by the intrinsic polarization along the *c*-axis of $LiNbO_3$.[125] Opposite sides of each nanocrystal would carry an opposing charge that would facilitate their assembly and eventual aggregation (**Figure 4.6**). Examples of the dipole-assisted aggregation behavior have also been observed

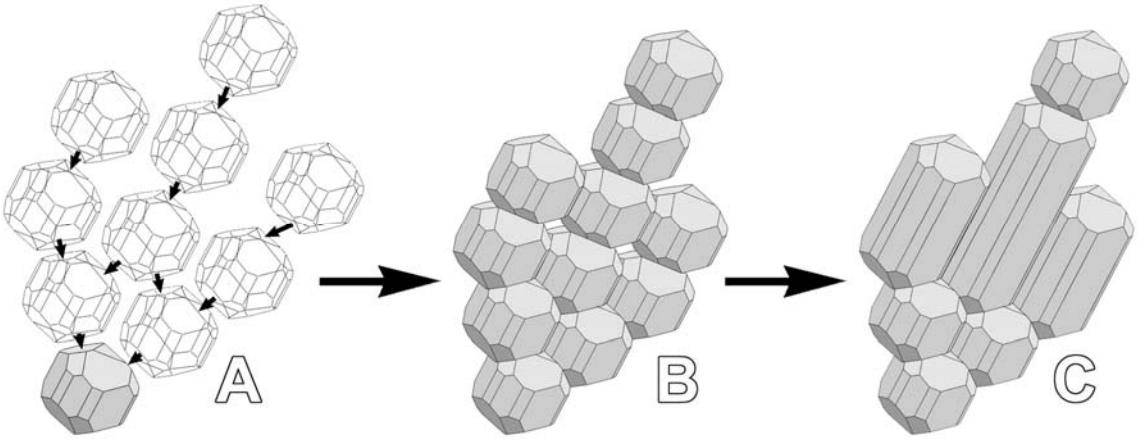

Figure 4.6 Schematic of the proposed mechanism for the formation of the anisotropic nanoparticles. (A) The hypothetical nanocrystals in this image have been created by cropping an ideal $LiNbO_3$ crystal to expose several native planes. (B) The directed aggregation of 006 planes is shown to generate the rod shape in the 006 direction, while aggregation in the 104 and 012 planes contribute to the observed branching. (C) The final structure is smoothened by the redistribution of material by Ostwald ripening.

for ZnO, ZnS, and PbSe nanocrystals.[45,125] Once assembled, the process of Ostwald ripening redistributes material to the connection point between the nanocrystals. This process aids to secure aggregation while also leading to a smoother surface texture.[121] The branching observed in the product could be attributed to a competitive but slower aggregation rate on the 104 and 012 planes. The observation of shared apexes between multiple fan-like structures could be the result of the fact that 104, 012, and 006 planes can aggregate on both sides of a seeding nanocrystal.

The results of this analysis indicate that anisotropic structures of $LiNbO_3$ were formed by the solution-phase process. The observed *c*-axis anisotropy appears to be the result of aging rather than any growth phase mechanism. The elongated structure of the crystals is useful to SHG because it would impose a pseudo-orientation in the powder. Furthermore, the observation of a dipole-based

aggregation mechanism is promising for the possibility of nanocrystal alignment with the use of electric fields. For more efficient SHG production, *a*- or *b*- axis anisotropy would have been preferable. The loss to SHG yield as a result of *c*-axis anisotropy is not expected to be a function of the amount of light that reaches the *a*- or *b*-axis because the diameter of the laser beam will most likely exceed that of the crystals. Rather, the loss of SHG would be the result of the fundamental and second harmonic waves passing through more crystal interfaces on account of the thin ab-planes. Scattering would increase and beam coherency is not expected to be maintained as a result.

4.5 The Phase Composition of the Nanocrystals

To review the overall phase composition of the nanocrystals, X-ray powder diffraction patterns were obtained for the samples prepared by the solution-phase synthesis at 360, 370, 380, and 390 ^{o}C at different times. The results of this work are displayed in **Figure 4.7** in three time intervals. A comparison of the samples at the initial maximum temperature (bottom) show that $LiNbO_3$ is still amorphous. The 370 ^{o}C reaction is an exception, with a small broad 012 peak, because it represents a further 1 h of reaction. The initial spectra are also marked by two notable impurity peaks that will be discussed in detail in the sections to come. The difference in peak intensity for the impurity does not appear to follow any recognizable trend with temperature. Within the next 20 h, crystalline $LiNbO_3$ appears in nearly equal abundance among the temperatures tested, with exception to the 390 ^{o}C experiment. $LiNbO_3$ continues to have difficulty forming at 390 ^{o}C for unknown reasons. The higher reaction

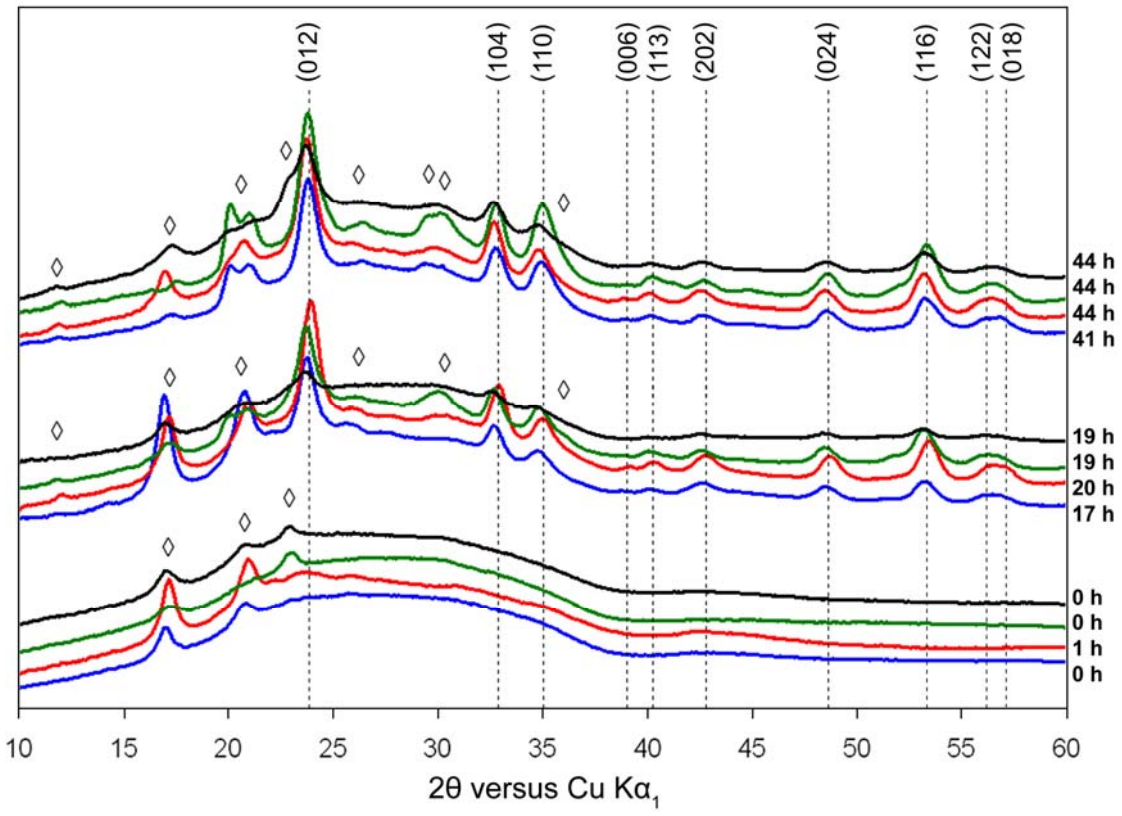

Figure 4.7 **The X-ray powder diffraction pattern of $LiNbO_3$ synthesized in the solution-phase process at 360 (blue), 370 (red), 380 (green), and 390 °C (black). The spectra have been assembled according to increasing time. Dashed lines identify the expected peak positions for $LiNbO_3$. Diamonds indicate the peaks from an impurity that is identified later in this chapter (primary peaks at 17.3 ° and 21.2 °), and from an impurity believed to be $LiNb_3O_8$ (primary peak at 30.4 °).**

temperatures do appear to have less of the observed impurity phase (e.g., peaks at 17.3 ° and 21.2 °), but it is difficult to evaluate this because the impurity also appears to be involved in a phase transition (denoted by splitting of 21.2 ° peak). If there is a benefit, it is certainly opposed by the formation of a new impurity that is believed to be $LiNb_3O_8$ (denoted by a primary peak at 30.4 °). An increased lithium mobility at higher temperatures could explain the prevalence of $LiNb_3O_8$ at 380 °C. By approximately 44 h $LiNb_3O_8$ is observable in all the samples. On a

whole, the 360-370 ^{o}C range appeared to be the most optimal at producing $LiNbO_3$ with less impurities. The reaction time should also be kept to a minimum (≤48 h) to reduce the possibility of forming significant amounts of $LiNb_3O_8$. Further reactions were limited to these guidelines for temperature and time.

4.6 The Liquid By-products and a Proposed Decomposition Mechanism

In order to derive a possible mechanism for the solution-phase decomposition reaction, the reaction setup was altered to condense and trap volatiles as the reaction progressed. Within the trap, a typical reaction collects 1-1.5 mL of liquid by-products that have a yellow appearance and an unpleasant phosphine smell that was discovered accidentally. To analyze the components of this mixture, a 1 µL sample was injected (neat) into a 30 meter GC-MS column at 250 ^{o}C (**Figure 4.8**). The compounds volatilized at this temperature are the topic of the following analysis.

The chromatogram of the liquid by-products is shown in **Figure 4.8**, and it reveals three main peaks at 0.63 min, 0.71 min, and one between 0.81-1.60 min.

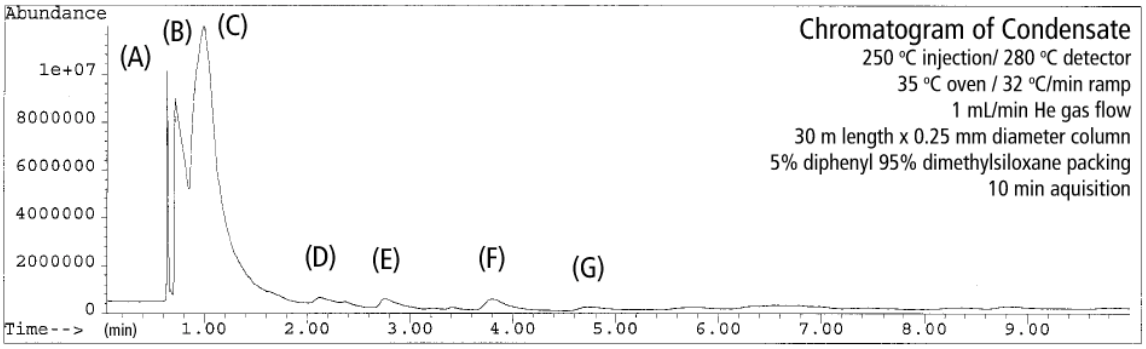

Figure 4.8 Gas chromatogram of the trapped reaction byproducts from the solution-phase synthesis of $LiNbO_3$ nanoparticles. Peaks discussed in detail have been denoted with a reference letter. Some of the experiment parameters are listed on the chromatogram.

The separation between the second and third peaks appears to be distinct when in fact the separation between the peaks is a discontinuity in the graph. The discontinuity is believed to be the result of detector saturation. One of these peaks is an impurity that requires little discussion. The impurity eluting at 0.63 min (A) is identified as common atmospheric gases, including N_2 (28 m/z), O_2 (32 m/z), and an injection chamber contaminant of CO_2 (44 m/z). The first main peak of interest elutes at 0.71 min and the fragmentation pattern is easily attributed to acetone (58 m/z; b.p. 57 ^oC; **Figure 4.9B**).[126] While acetone was used to clean the injection syringe, it was then baked at 140 ^oC in an oven for 30 min. The residual acetone could not be responsible for the observed acetone abundance. Acetone is one of the reaction by-products. The second most peak, eluting at 0.81 min, offers an explanation to the origin of the acetone. Like the acetone signal, this compound is also in great abundance in the analyzed liquid, and the peak trails late into the chromatogram as a result. Analysis of the mass spectra from several points along this peak identify that it is isopropanol (60 m/z; b.p. 82 ^oC; **Figure 4.9C**).[126] As with typical alcohols, isopropanol is identifiable by a large M-1 peak and an almost nonexistent molecular ion peak. The 45 m/z base peak is also distinctive, representing the loss of $\cdot CH_3$ from either side of the molecule to create the $CH_3CH{=}OH^+$ ion. Less favourably, the C-O bond can cleave heterolytically to generate neutral $\cdot OH$ and the $(CH_3)_2CH^+$ ion found at 43 m/z. This mass peak could also be represented by the dehydrogenation ($- H_2$) of the base peak to yield $CH_3C{\equiv}O^+$ (43 m/z). At the high temperature of the solution-phase reaction, alcohols like isopropanol are prone to dehydrogenation to create

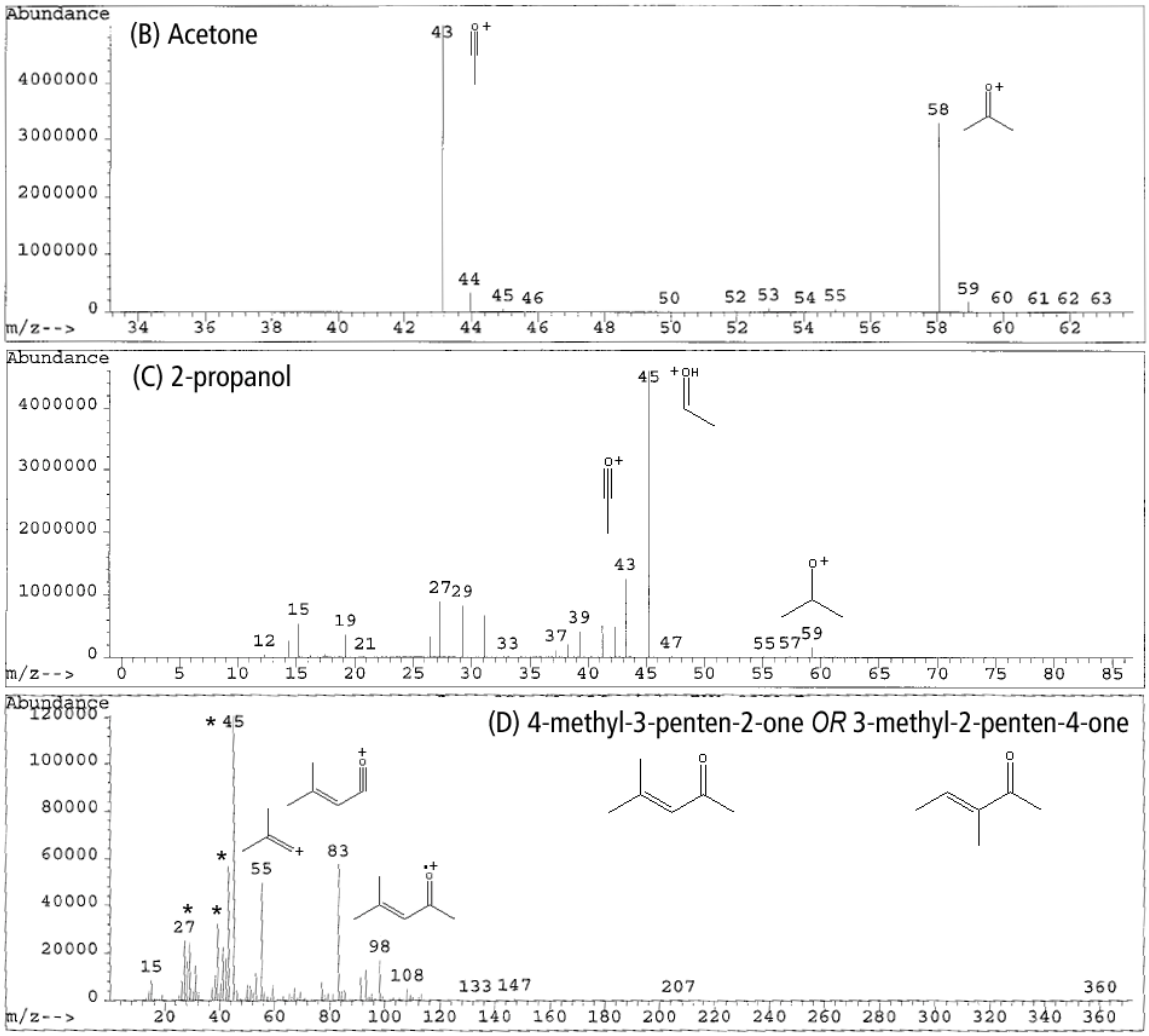

Figure 4.9 Mass spectra of the major byproducts denoted by (B), (C), and (D) in the gas chromatogram of Figure 4.8. Those peaks have been identified as acetone (B), isopropanol (C), and 3-methyl-2-penten-4-one or 4-methyl-3-penten-2-one (D). Stars are the result of overlap with the large isopropanol peak.

ketones. This reduction is favourable at high temperature because delocalization of the π-electron pair provides better thermal stability in the molecule.[59]

At higher retention times, smaller by-product signals are also detected and examined by mass spectroscopy. Interference from the tail-end of the large isopropanol fraction and the significant background-to-signal ratio at these higher retention times does, however, impede much of this analysis. The first notable

peak occurs at 2.13 min (**Figure 4.9D**) and it has a fragmentation pattern that appears to be the cross-product of two isopropyl or isopropoxy molecules. A dominant loss of M-15 (98-83 m/z; $\cdot CH_3$) in this product suggests that a methyl is situated favourably for elimination. Another loss of M-43 (98-55 m/z) has a lower peak height, that indicates loss of $(CH_3)_2CH\cdot$ or $CH_3CO\cdot$ fragments as an alternative, but slightly less favourable, decomposition for the parent molecular ion. Since $(CH_3)_2CH\cdot$ is a more stable radical than $\cdot CH_3$ the loss of M-43 is attributed to $CH_3CO\cdot$. A loss of $CH_3CO\cdot$ also seems likely considering M-15 could also lose a common CO fragment to form the 55 m/z ion. If the composition of the 55 m/z ion is $C_4H_7^+$, rather than a less obvious $C_3H_3O^+$ ion, two possible identifications can be made for the product by the addition of $CH_3CO\cdot$ to form the parent ion. The first of these products is 3-methyl-2-penten-4-one (98 m/z; b.p. 138 ^oC) that forms a more favourable $CH_3CH{=}CCH_3^+$ ion for C_4H_7, but it is difficult to see how isopropanol could have eventually resulted in the proposed 3-methyl position. The second possible product for this retention time is 4-methyl-3-penten-2-one (98 m/z; bp 129 ^oC).[126] It creates a primary $(CH_3)_2C{=}CH^+$ ion, and it appears to more closely resemble the addition of two isopropyl-based units. Such a compound may be the result of an aldol addition and condensation reaction between thermally generated acetone ($(CH_3)_2CHOH \rightarrow H_2 + (CH_3)_2C{=}O$) and eliminated isopropanol. At 2.75 min another considerable peak is seen in the chromatogram, and the mass spectrum (**Figure 4.10E**) is composed of three main peaks at 85, 91, and 106 m/z. The 91 and 106 m/z peaks are typically indicative of a stable aromatic tropillium ($C_7H_7^+$) and methylated tropillium ions,

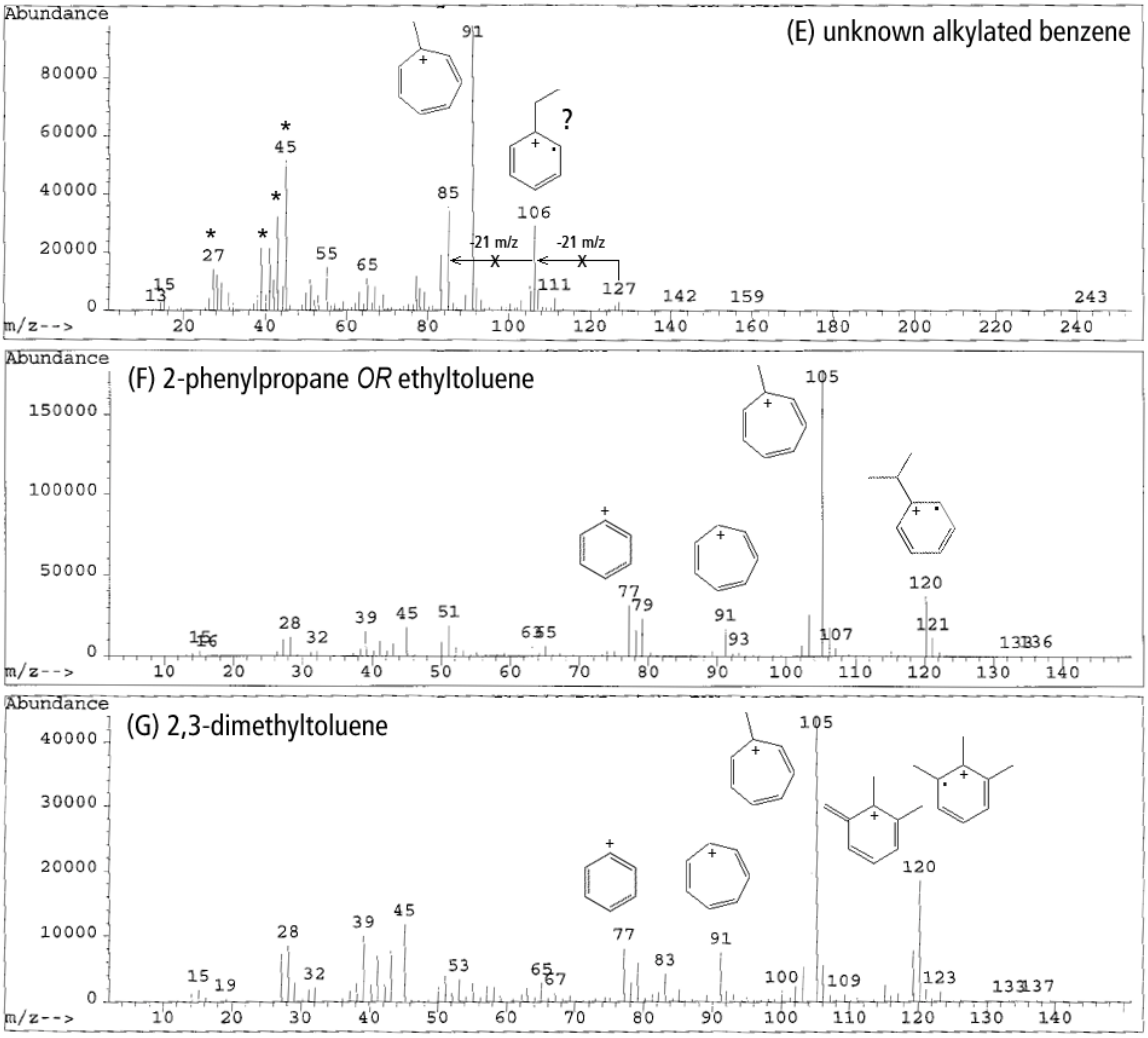

Figure 4.10 Mass spectra of the minor byproducts denoted by (E), (F), and (G) in the gas chromatogram of Figure 4.8. The tropillium ion at 91 m/z indicates that these fragmentation patterns originated from alkylated phenyl compounds. The compounds responsible for these patterns are identified or suspected as isomers of 2-phenylpropane.

respectively. These peaks indicate that the product is phenyl-based and alkylated. This finding also reveals that triphenylphosphine oxide is reacting. The actual identification of this compound still remains unknown because of an unusual (and typically forbidden) mass loss of 21 m/z (H_2O +H_3?) that appears at least twice in the spectrum (106 to 85 and 127 to 106 m/z). At 3.81 min, another product elutes and it also contains peaks indicative of phenyl groups (**Figure**

4.10F). The mass-to-charge peak positions and intensities indicate that this compound is 2-phenylpropane (120 m/z; b.p. 152 ^{o}C).[126] To account for some of the minor peak height differences, a contribution may exist from its isomer, m-ethyltoluene (b.p. 159 ^{o}C)[126] with nearby boiling point. Both of these compounds could be conceived as being the product of a reaction between TPPO and $LiOPr^{i}$ or $Pr^{i}OH$. P-O bond formation and the relief of sterics around the phosphorus would create a strong driving force for this reaction at high temperature. The final compound in this discussion elutes at 4.75 min and has nearly the same mass spectrum (**Figure 4.10G**). This similarity could possibly indicate another of the C_9H_{12} isomers. In this case, a high peak-height ratio of 119/120 m/z is distinctive of 2,3-dimethyltoluene (b.p. 176 ^{o}C),[126] although the observed ratio is higher than expected. This identification is still questioned due to miscellaneous peaks at 53 and 83 m/z that could not be rationalized.

The analysis of condensed volatiles from the solution-phase reaction of $LiNbO_3$ by GC-MS has led to the identification of some of the decomposition by-products. The key identification being that the majority of trapped condensate was composed of isopropanol. In **Section 3.12.2** it was discovered that the precursor contains 0.389 mol of OH ligands per mol of monomeric $LiNb(OPr^{i})_6$, and it was discussed that heating would cause condensation and the release of $Pr^{i}OH$. Based on stoichiometry, condensation of the hydroxyl groups would only generate 0.13 mL of isopropanol, and this is not nearly enough to account for the 1.5 mL of isolated by-products. The discovery of isopropanol is, therefore, in strong support of the alcohol/alkene elimination mechanism shown in **Figure 2.6**.

Propene was not trapped by our methods as a result of its low boiling point. Additional side products appear in trace quantities, and they are either the result of the reaction between two isopropoxide groups or the reaction between triphenylphosphine oxide and an isopropoxide source. The phenylated by-products have identified that the phosphine capping agent is playing an active role in the decomposition of $LiNb(OPr^i)_6$.

4.7 Examining Changes in the Experimental Setup

After some preliminary experiments, it was decided that the gaseous by-products could be removed from the reaction more effectively if the condenser in our setup was moved from the center of the 3-neck reaction vessel (**Figure 4.11A**) to the side-neck of the reaction vessel (**Figure 4.11B**). This new setup was no longer clogged by the refluxing triphenylphosphine oxide and the attached collection flask allowed us to isolate the reaction by-products easily. The new reaction setup also used a stopcock type inlet adaptor that excludes the

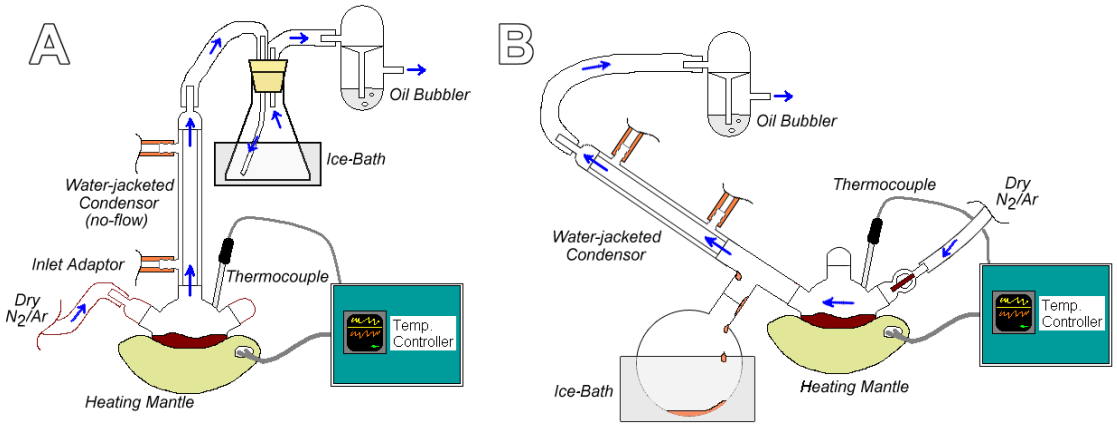

Figure 4.11 The two reaction setups used in the synthesis of $LiNbO_3$ nanocrystals. (A) represents the old method, while (B) became the standard reaction setup because it removed and trapped the reaction byproducts more effectively.

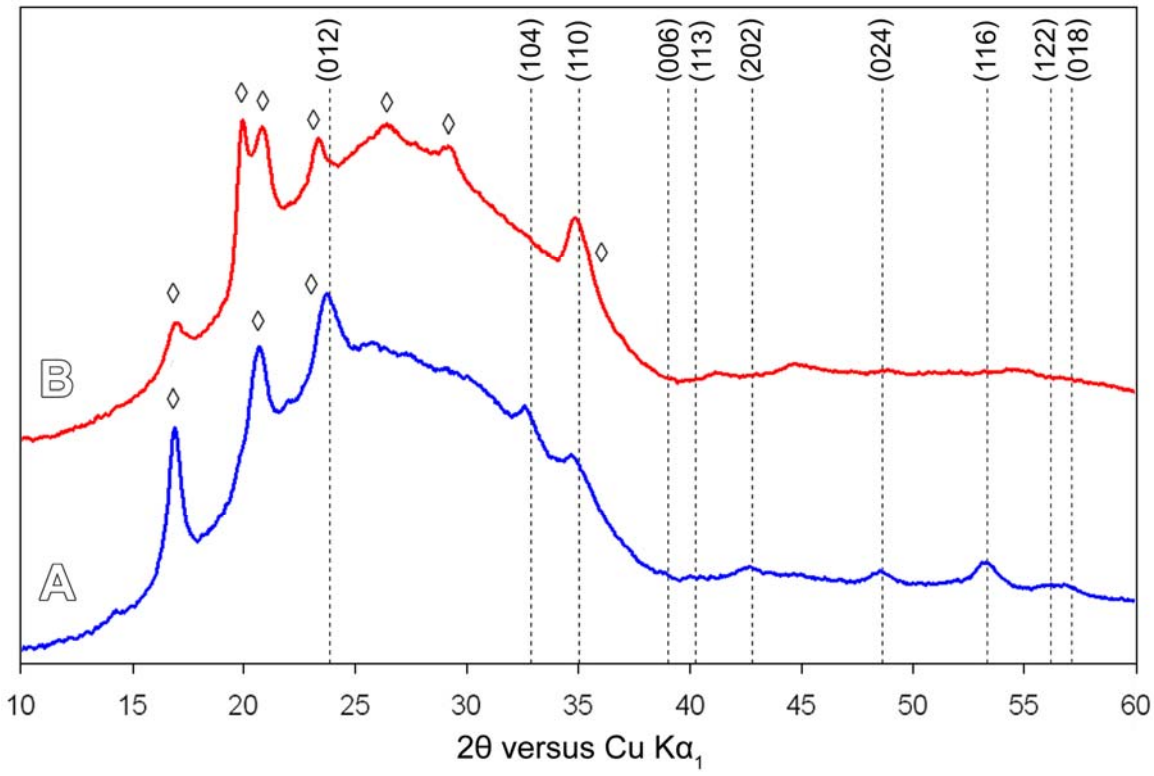

Figure 4.12 X-ray powder diffraction patterns of $LiNbO_3$ synthesized by the solution-phase process using (A) the new reaction setup or (B) the old reaction setup described in Figure 4.11.

possibility of exposure to air. Interestingly, the solution-phase reaction performed differently depending on the choice of setup, and the new setup was found to be optimal (**Figure 4.12**). By comparing the powder diffraction patterns of the products from the two setups, it is clear that $LiNbO_3$ formation is favoured by the new position of the condensor. The impact of this alternative setup is significant, and most likely due to an increased efficiency for the removal of isopropanol. At the temperature of the reaction, alcohols can combust under their own oxygen supply, or some (e.g., ethylene glycol) are also known to act as mild reducing agents in the polyol process.[127] One of these theoretical reaction conditions

resulted in the complete absence of $LiNbO_3$ formation and a large impurity phase (**Figure 4.12B**).

Since the combustion hypothesis is strongly linked to the presence of an internal oxygen supply, the purity of the inert atmosphere during reaction was brought into question. Three solution-phase reactions were run using 99.9 % nitrogen passed through a drying column, 99.998 % nitrogen passed through oxygen and moisture traps, and 99.998 % argon passed through oxygen and moisture traps (**Figure 4.13**). The difference is evident. High purity atmospheres are preferred for the formation of $LiNbO_3$. The presence of oxygen in up to 0.1 %

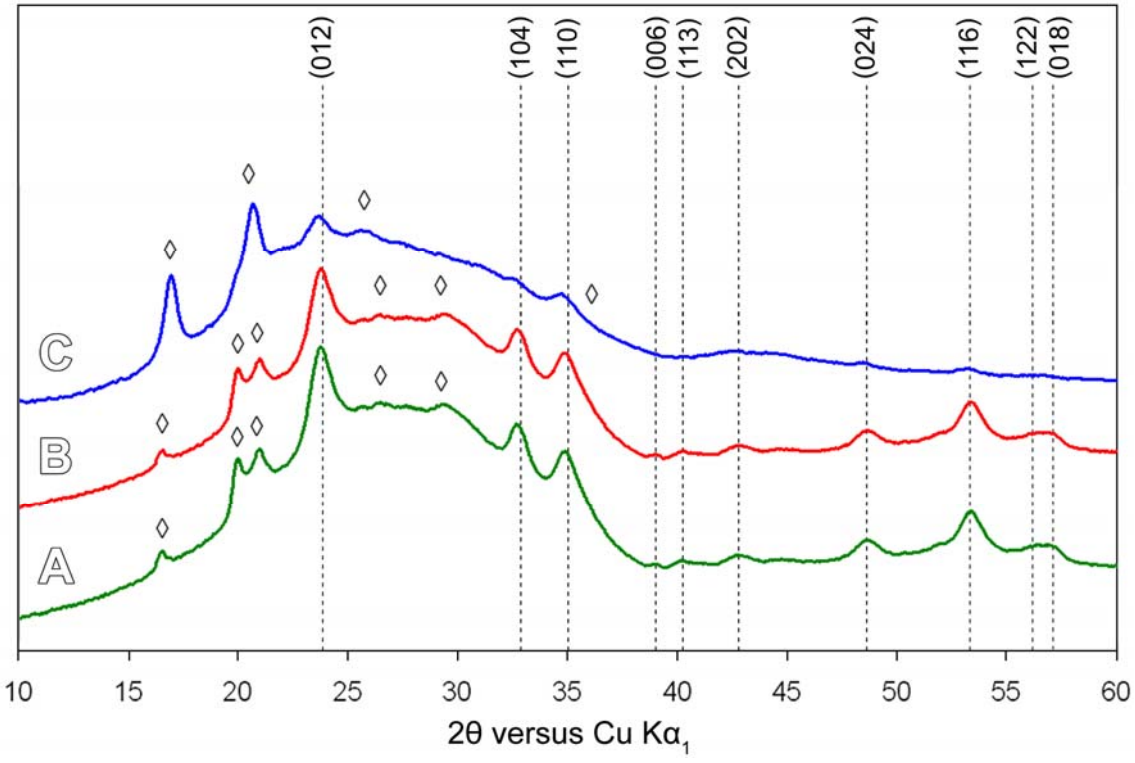

Figure 4.13 X-ray powder diffraction patterns displaying the effect of atmospheric purity on the synthesis of $LiNbO_3$. Dashed lines indicate the position of peaks for the desired phase. Atmospheres were (A) 99.998 % (or 4.8 grade) N_2 or (B) 99.998 % (or 4.8 grade) Ar both passed through an O_2 and moisture trap, and (C) 99 % (or regular grade) N_2 that was passed through a moisture trap only. The 1 % O_2 impurity of regular grade N_2 negatively impacts the yield of $LiNbO_3$.

concentration in low-grade nitrogen appears to hamper the growth of $LiNbO_3$ while promoting the growth of the unknown impurity phase. Similarly, the presence of isopropanol also promoted the growth of this impurity phase. It is clear that optimal results require that oxygen impurities of any kind are avoided during the solution-phase process. Still, it is unclear how Li_2O, isopropanol, and/or oxygen are reacting to form the impurity.

One further modification that was performed on the solution-phase reaction was to use trioctylphosphine oxide (TOPO) as the reaction solvent instead of TPPO. While the two capping groups have nearly identical surface coordination strength, they differ greatly in the amount of steric bulk they possess. From theory, the additional bulk of TOPO is expected to contribute to the formation of larger $LiNbO_3$ nanocrystals, but this was not the result. $LiNbO_3$

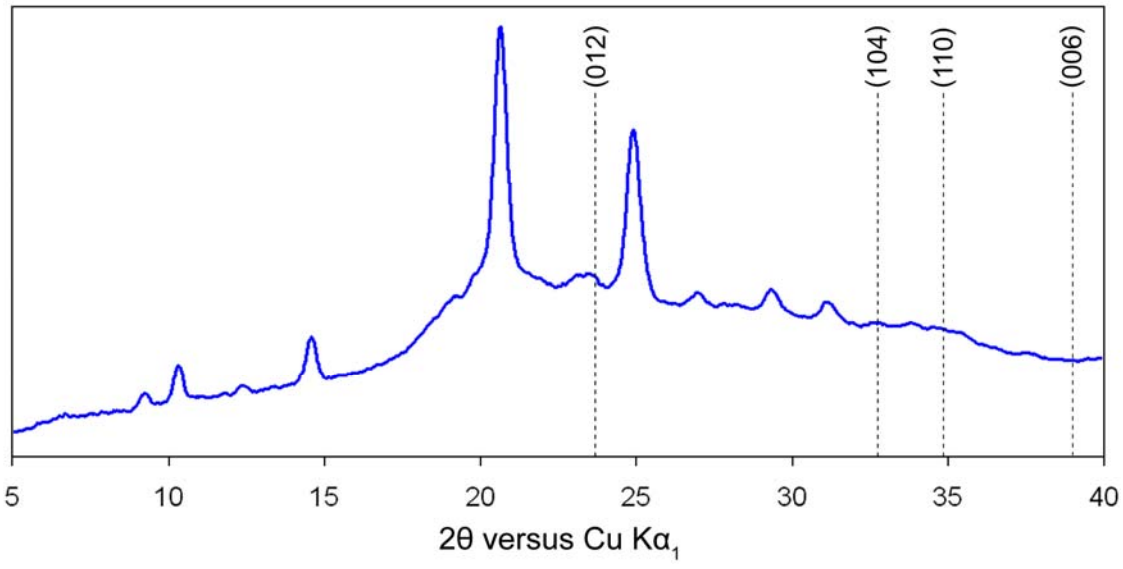

Figure 4.14 X-ray powder diffraction pattern of the product of the TOPO-based solution-phase synthesis. A trace indication of the desired phase, $LiNbO_3$, may be indicated by small peaks in the appropriate positions (dashed lines). The majority of the spectrum remains unidentified after thorough investigation.

was not the major phase from this reaction, as is seen in **Figure 4.14**. Despite the simple appearance of the powder diffraction of the main product, it has been referenced against every Li-based, Nb-based, and Li-Nb-based oxide in the PDF4+ literature library without a promising lead. Indexing of the spectrum was also attempted[75] with hopes of identifying the type of crystal lattice in the product, but this investigation was also inconclusive. The reason this study has been included in this discussion is that these results appear to suggest that TPPO is a necessary contributor to the reaction mechanism that forms $LiNbO_3$.

The surface chemistry of the reaction flask was also thought to have an impact on the reaction because of the hydrolytic sensitivity of the $LiNb(OPr^i)_6$ precursor. It is not uncommon that nanoscale reactions are strongly affected by trace ions at the surface of the reaction vessel. The standard method of creating scrupulously clean glass surfaces for nanoscale reactions is by treatment with piranha (7:2 H_2SO_4/H_2O_2) then aqua regia (4:1 HCl/HNO_3). The acid residue is rinsed from the flask using only 18 MΩ water. In this case, it was noticed that glassware treated by KOH and the high purity water performed differently in the solution-phase synthesis of $LiNbO_3$ than glassware treated by the standard method outlined above. The base treated flasks always contained a residual solid on the wall of the flask, while the flask cleaned by the standard method did not. The solution-phase product and the product adhered to the flask were purified and examined by X-ray powder diffraction (**Figure 4.15**). The most noticeable difference is that the “adhered” product was much more rich in $LiNbO_3$ than either of the solution-phase products. In addition, the formation of the impurity phase

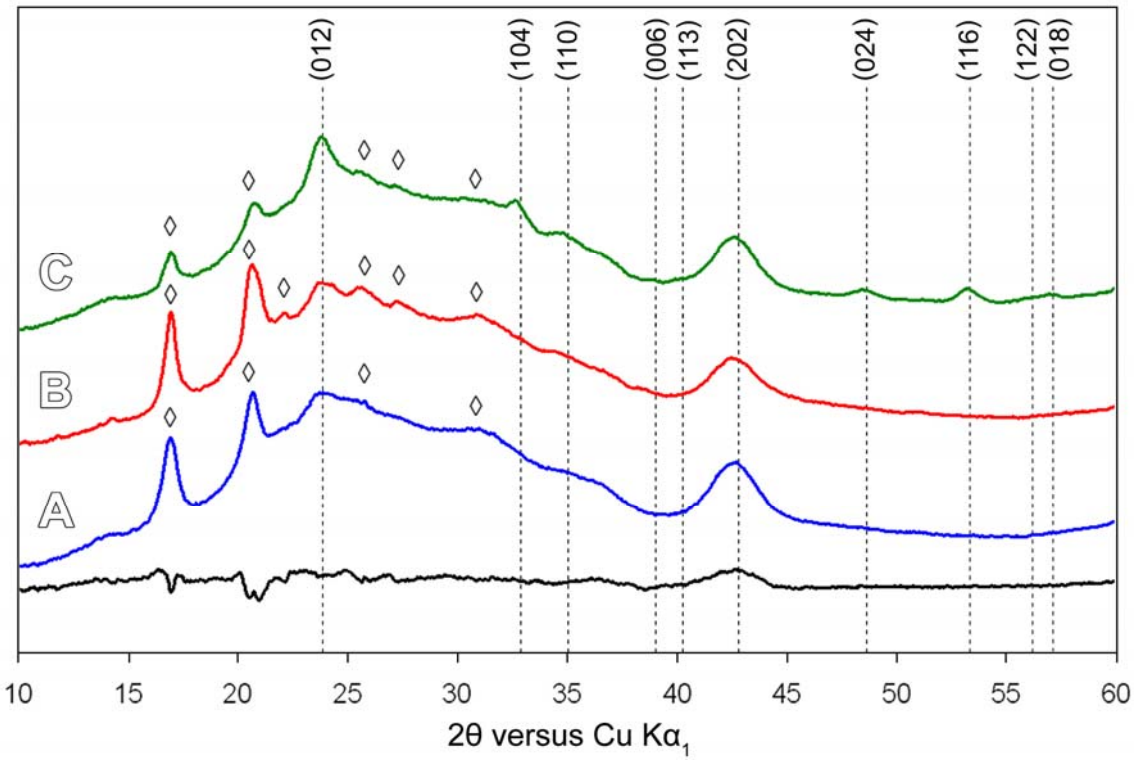

Figure 4.15 **The effect of glassware surface chemistry demonstrated by X-ray powder diffraction patterns of the isolated products. The bottom-most trace represents the difference between the products from a $LiNbO_3$ synthesis in (A) glassware cleaned with H_2O_2/H_2SO_4 and HNO_3/HCl, and (B) glassware cleaned by KOH. (C) Product that adhered to the KOH treated flask walls is rich in $LiNbO_3$ (dashed lines) because surface hydroxide preferentially reacts with the precursor.**

appeared to be minimized. The reason for these effects is likely due to the fact that KOH-treated glassware contains a large concentration of surface-bound hydroxides that are capable of hydrolyzing $LiNb(OPr^i)_6$. The hydrolysis reaction between the precursor and the flask wall is the reason for the adhesion. Once hydrolyzed the metal centers of the precursor are firmly linked together and this reduces the accessibility of Li for the development of the impurity phase. A comparison of the two solution-phase samples is less noteworthy, but the glassware treated by standard cleaning methods appears to have produced

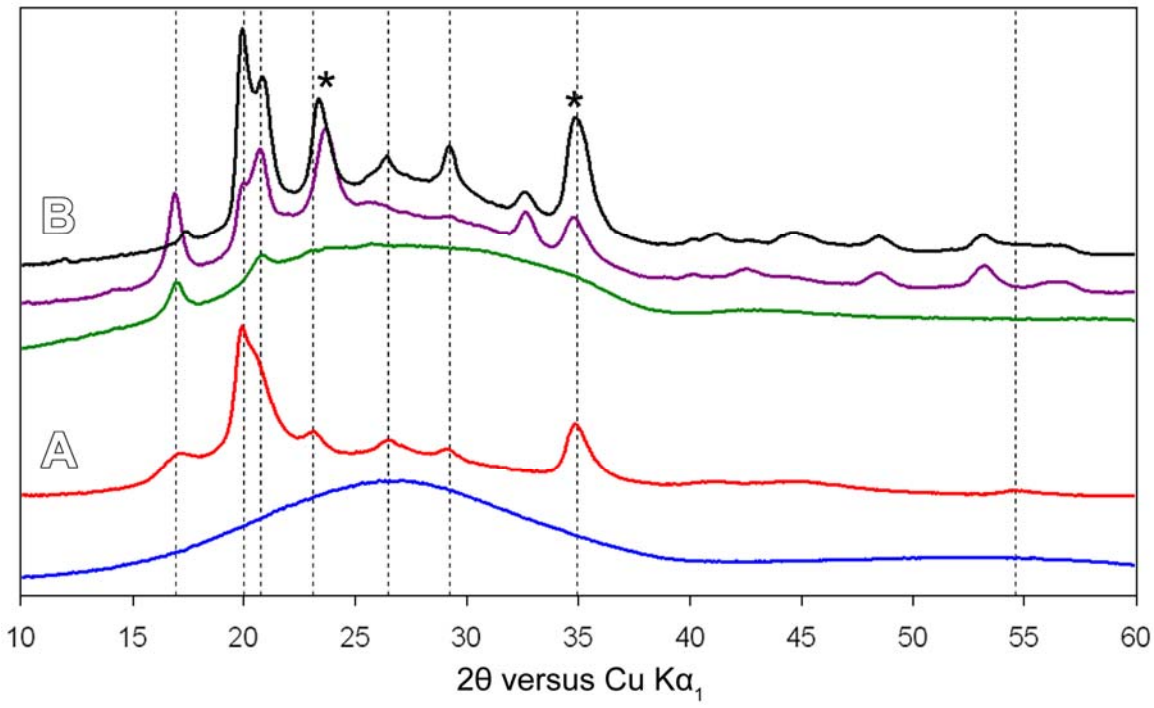

Figure 4.16 (A) The X-ray powder diffraction pattern of $Nb(OPr^i)_5$ (blue) and $LiOPr^i$ (red) each reacted independently in TPPO. The peak positions of the $LiOPr^i$ product (dashed lines) agree well with the impurity phase observed at 48 (purple) and 72 h (black) for the reaction utilizing the normal $LiNb(OPr^i)_6$ precursor (B). The amorphous product resulting from the decomposition of $Nb(OPr^i)_5$ could contribute to some of the observed background signal in the 0 h and the other X-ray spectra. The two stars, left and right mark the position of the (012) and (110) peak positions in $LiNbO_3$.

slightly less of the impurity and more of the $LiNbO_3$ phase. It is for this reason that the standard method was maintained for all solution-phase reactions.

4.8 The Origin and Identity of the Impurity Phase

Identifying the composition of the impurity phase became a necessary task in this research in order to either eliminate its ability to form, or to facilitate the possibility of its removal. Through studies in the reaction setup, it has already been shown that the development of the impurity is linked to sources of oxygen. This link suggests that oxygen is a likely component of the impurity. In addition to

oxygen, lithium is also implicated in the impurity composition by the appearance of $LiNb_3O_8$ in the phase analysis of the solid reaction product (**Figure 4.7**). $LiNb_3O_8$ results from a loss of Li_2O from $LiNbO_3$, and no additional phases could be found to represent the missing lithium or oxygen. The relationship between $LiNb_3O_8$ and the impurity could be related to the fact that the impurity shares a number of close diffracting planes to those of $LiNbO_3$ (e.g., 012 and 110, see **Figure 4.16** stars). Through lithium deintercalation, the impurity could develop epitaxially while consequently producing $LiNb_3O_8$. In this section, further origins of the impurity phase are investigated. As a result of this work, the composition of the impurity is identified and a molecular structure is suggested.

In **Chapter 3**, it was identified that the red oxidized $LiOPr^i$ suppresses the formation of the impurity. The cause of this effect could be due to the presence of stronger oxide bonds that hinder the dissociation of the precursor back to its parent lithium and niobium alkoxides. This dissociation process occurs at high temperatures and has been recognized by several authors.[115, 116, 123, 138] To explore the possibility that precursor decomposition leads to the formation of the impurity, two reactions were performed using $LiOPr^i$ and $Nb(OPr^i)_5$ separately in the same solution-phase process. The powder diffraction pattern of the $LiOPr^i$-generated product (**Figure 4.16A** red) reveals a striking similarity to the unknown impurity phase of a normal solution-phase reaction after 72 h (**Figure 4.16B** black). This result confirms that precursor dissociation is occurring, and $LiOPr^i$ is contributing to the development of the impurity. The decomposition of $Nb(OPr^i)_5$ alone resulted in the formation of a hard amber-colored glass that is amorphous

in the X-ray diffraction pattern (**Figure 4.16A** blue). The amorphous nature of the $Nb(OPr^i)_5$ product is similar to the observations of Kominami, who found that the decomposition products of niobium alkoxides remain amorphous until a temperature of 600 ^oC.[41] The niobium glass may be responsible for part of the amorphous background in **Figure 4.16B** (green) and in the other spectra of $LiNbO_3$ products. Another contributor to the background signal can be attributed to the glass sample holder used to obtain the X-ray diffraction patterns.

The first attempt to identify the true composition of the impurity was made by way of crystallography. Under higher temperatures, it was hoped that the crystallinity of the impurity phase could be improved to enable identification by comparison to a literature diffraction pattern. To explore this avenue, a sample of impurity-rich $LiNbO_3$ from the solution-phase reaction was loaded into a crucible and heated in an oven to 600 ^oC under an air atmosphere for 12 h. After this time, a new 3-phase diffraction pattern resulted that did not contain $LiNbO_3$ (**Figure 4.17**). Two of the three phases were phosphates identified as 59.8 % Li_3PO_4 [Pnma (#62)] and 40.2 % $NbO(PO_4)$ [P21/c (#14)].[94] The third phase could not be identified, but for cation balance it is assumed that the other phase is niobium-rich. The results of this experiment were exceptionally useful in that they identified a number of key points. The first point was that the crystalline impurity-phase was phosphine-based. Second, the impurity is a predecessor to Li_3PO_4. Thirdly, this reaction links oxygen sources to the impurity phase by way of combusting surface-bound phosphines. The final point made by this reaction is that $LiNbO_3$ is parasitized by the growth of the Li_3PO_4 and the amorphous

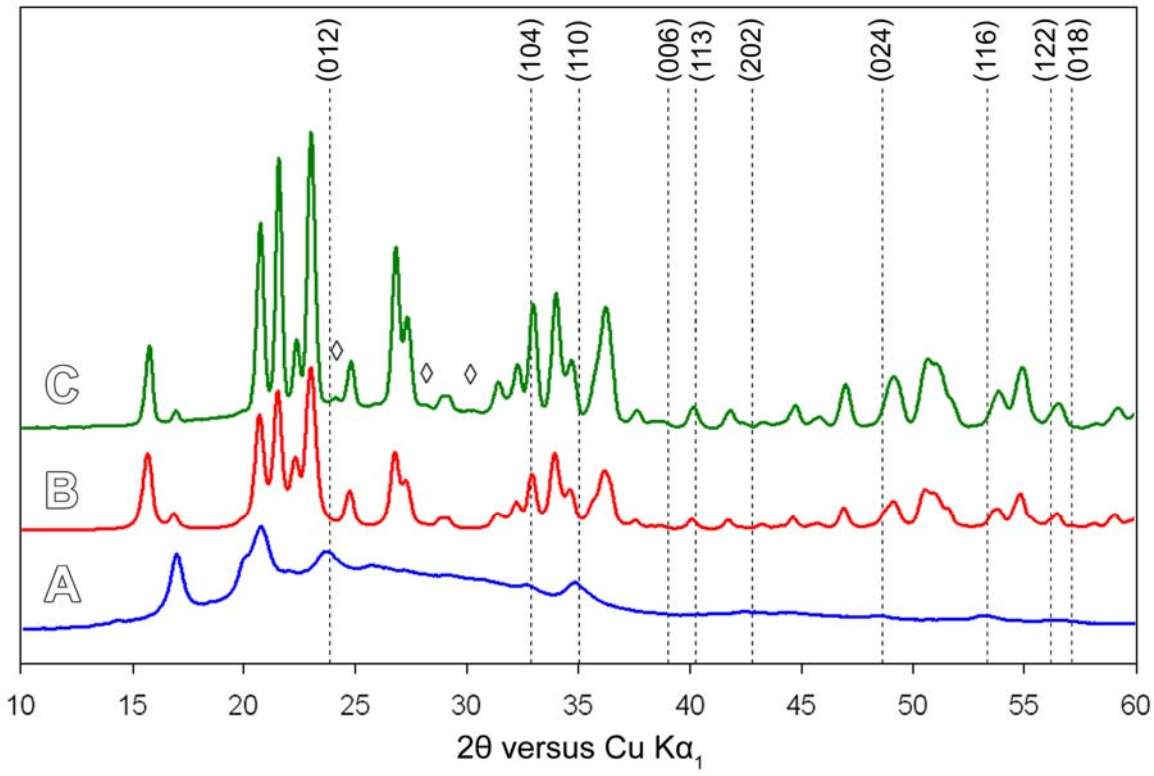

Figure 4.17 The X-ray powder diffraction pattern of (A) a 48 h sample of $LiNbO_3$, (B) a simulation using 59.8 % Li_3PO_4 [Pnma (#62)] and 40.2 % $NbO(PO_4)$ [P21/c (#14)], and (C) the 48 h sample following 12 h at 600 ^oC in air. Diamonds highlight a few spurious peaks that were not identified.

$NbO(PO_4)$ impurity phases. In otherwords, the impurity is the result of a slow destruction of the synthesized $LiNbO_3$.

The second attempt to identify the composition of the Li_3PO_4 predecessor was pursued by elemental analysis using X-ray photoelectron spectroscopy (XPS). Two samples were prepared for this analysis in the following way: (A) A standard sample of Li_3PO_4 was prepared by treating Li_2CO_3 with a stoichiometric amount of H_3PO_4. An additional drop of H_3PO_4 was used to ensure all of the Li_2CO_3 was reacted. The precipitate collected at pH 5 was isolated by centrifugation and washed repeatedly until the wash solution was pH 7. The resulting isolated powder was dispersed in methanol and added dropwise to a

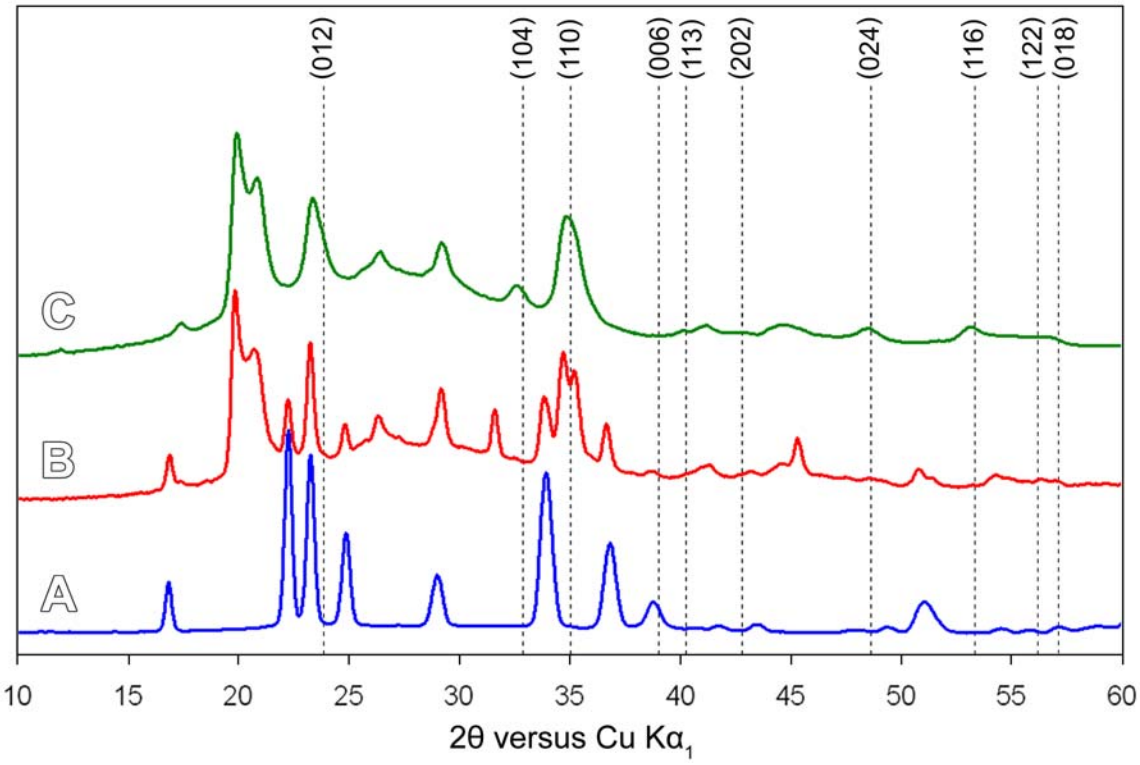

Figure 4.18 X-ray powder diffraction pattern of the synthesized Li_3PO_4 (A) and of the extracted impurity (B). The impurity was extracted from a 72 h sample of a 360 ^oC reaction (C). Dashed lines indicating $LiNbO_3$ have been included to assist the eye at identifying the peaks of the impurity. The appearance of Li_3PO_4 in (B) is not a result of the solution-phase process, but a result of the sample preparation.

heated silicon wafer. (B) The "Li_3PO_4" from the solution-phase synthesis of $LiNbO_3$ was obtained from a 72 h sample of a 360 ^oC reaction. To isolate the "Li_3PO_4" exclusively, excess TPPO was first removed by three wash and centrifugation cycles with 3:1 (v:v) acetone/hexanes. The solvent was drained and 2 M acetic acid was added to the solids. This acidic solution was sonicated, centrifuged, and finally isolated from the remaining solids. The acid was diluted with deionized distilled water resulting in a precipitation of "Li_3PO_4". This sample was isolated by centrifugation, neutralized, and coated on a silicon wafer in the

same manner as the standard. Both of these samples were examined by X-ray powder diffraction to verify the preservation of the processed impurity and the adequacy of the standard (**Figure 4.18**). This analysis reveals that the prepared standard is Li_3PO_4 [$Pmn2_1$ (#31)], with lattice parameters of a = 4.860, b = 5.264, and c = 6.105 Å.[75] For the most part, the structure of the impurity has been retained. A small portion of the impurity appears as Li_3PO_4, but it should be noted that this phase was not present in the original sample (**Figure 4.18C**). Li_3PO_4 occuring in the impurity was the result of the processing applied here, and will be noted but disregarded in the following XPS analysis.

The O 1s, Li 1s, and P 2p XPS core level spectra of the

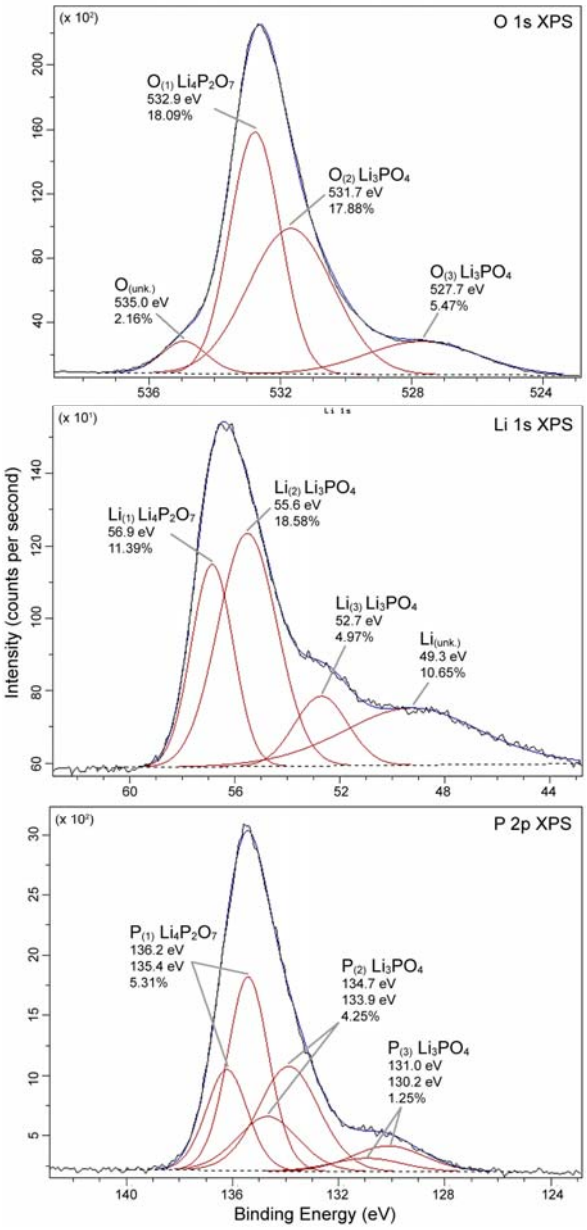

Figure 4.19 X-ray photoelectron spectra of the O 1s, Li 1s, and P 2p, binding energy regions for the prepared standard of Li_3PO_4. Peaks are provided with an identification, binding energy, and relative atomic abundance.

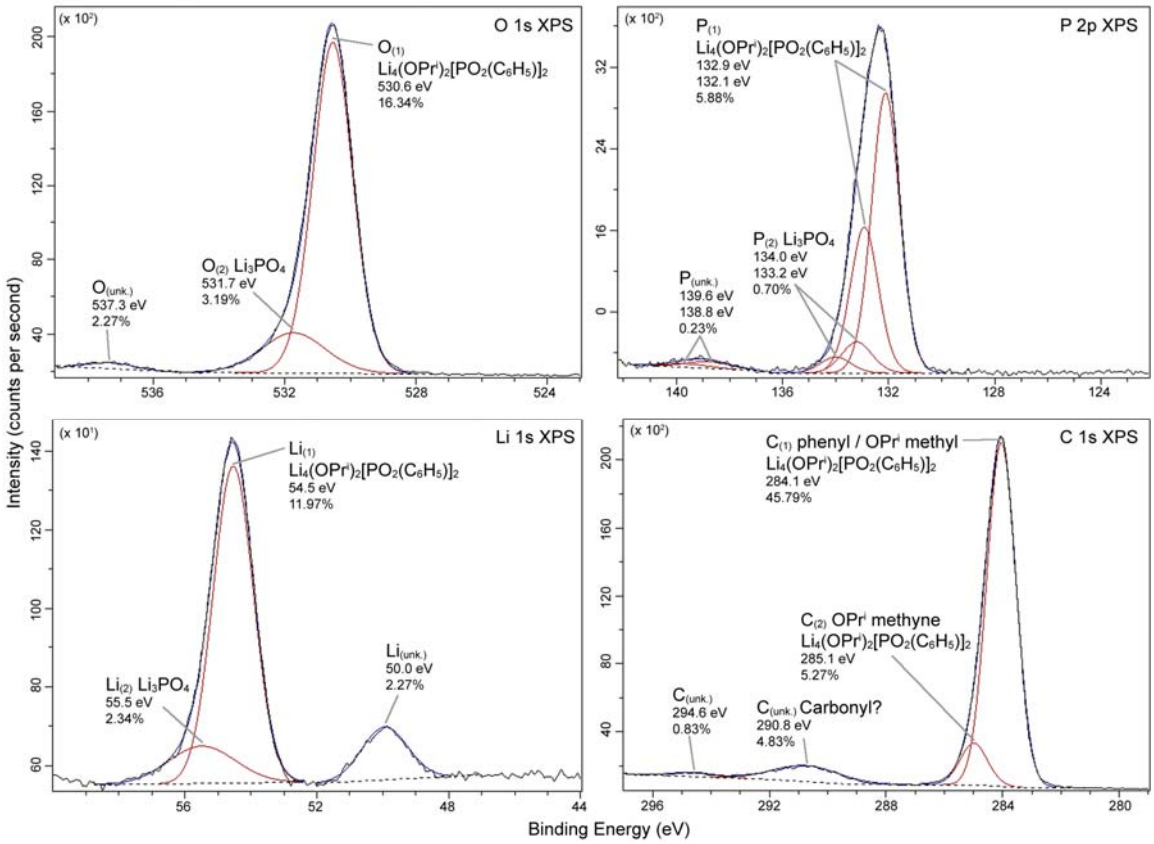

Figure 4.20 X-ray photoelectron spectra of the O 1s, Li 1s, P 2p, and C 1s binding energy regions for the extracted $LiNbO_3$ impurity. Peaks are provided with an identification, binding energy, and relative atomic abundance.

standard appear in **Figure 4.19**. Each spectrum was fitted using a linear background and 70 % Gaussian-30 % Lorenztian peaks. For the P 2p spectrum, the spin 3/2 and 1/2 doublet was always positioned 0.800 eV apart with equal peak widths. The peak heights were also maintained with a constant peak-area-ratio of 0.540, that is close to what would be expected from the multiplicity of the spin states.[128]

Interestingly, the standard sample was not as easily analyzed as expected by the purity revealed by X-ray powder diffraction. In fact, three phases were identified. A surface coating of $Li_4P_2O_7$ was found to represent 26.6 % of the

analyzed material depth due to a $P_{(1)}/O_{(1)}$ ratio of 0.294 (expected 0.286) and $Li_{(1)}/P_{(1)}$ ratio of 2.145 (expected 2.000). The peak energy difference values of 397.4 eV and 475.9 eV for Δ(O-P) and Δ(O-Li) match well with literature values for the phase (397.4 and 476.1 eV, respectively).[129] The $Li_4P_2O_7$ is found to contain the highest binding energy components (i.e., peaks) of the spectra because of the reduced oxygen and higher phosphorus concentrations that combine to create a more tightly bound electron environment. The remaining 73.4 % of the composition is identified by $P_{(2)}/O_{(2)}$ and $P_{(3)}/O_{(3)}$ ratios of 0.238 and 0.229 (expected 0.250) that indicate Li_3PO_4. The respective Li/P ratios are not as ideal at 4.372 and 3.976 (expected 3.000), and this error may be due to the large unknown signal overlapping the lithium region. Peak energy difference values for the Li_3PO_4 phases were calculated to be 397.8 and 397.5 for Δ(O-P) (expected 397.9 eV), and 476.1 and 475.0 eV for Δ(O-Li) (expected 476.1 eV). One of the Li_3PO_4 phases does not appear to match well with literature peak energy difference values, but this is believed to be due to the fact that it may be a hydrate. As such, this phase would be expected to appear at a lower binding energy, as it does in this set of spectra.

The XPS O 1s, Li 1s, P 2p, and C 1s core level scans for the extracted impurity was processed in the same manner as described for the prepared standard. These spectra appear in **Figure 4.20**. Using the binding energy values for Li_3PO_4 from the analysis of the standard, the Li_3PO_4 that formed during the extraction procedure was identified. $P_{(2)}/O_{(2)}$ and $Li_{(2)}/P_{(2)}$ ratios of 0.219 and 3.343 (expected 0.250 and 3.000) were found as a result of this process and they

are correlated to Li_3PO_4. According to the analyzed material, this phase represents approximately 20.7 % of the total composition. The remainder of the XPS spectrum represents the impurity phase of interest. A $P_{(1)}/O_{(1)}$ and a $Li_{(1)}/P_{(1)}$ ratio of 0.360 and 2.036 appear to indicate proportions of 1/3 and 2/1 for the atoms discussed. In addition to P, O, and Li, the impurity also contains a substantial amount of carbon. The $C_{(1)}$ peak occurs at the lowest binding energy and it is believed to contain both the alkyl and alkene carbons of any phenyl and isopropyl methyl carbons. In order to deduce the phenyl contribution to $C_{(1)}$ the isopropyl contribution needs to be removed, and it can be elucidated from $C_{(2)}$. This higher binding energy peak is believed to represent the C-O environment (the methyne) of the isopropyl group. With the propyl component removed $[(1/6)C_{(1)}-(2)C_{(2)}]/P_{(1)}$ reveals a phenyl/P ratio of almost 1 (observed 0.999). The $C_{(2)}/P_{(1)}$ ratio is a direct measure of the isopropyl/P ratio and it is also found to be ~1 (observed 0.896). From these calculations the empirical formula for the impurity is suggested to be $Li_4(OPr^i)_2[PO_2(C_6H_5)]_2$. The connectivity implied by this formula has taken several assumptions. Two of those assumptions are that the phenyl substituents have remained attached to the phosphorous atoms, and that

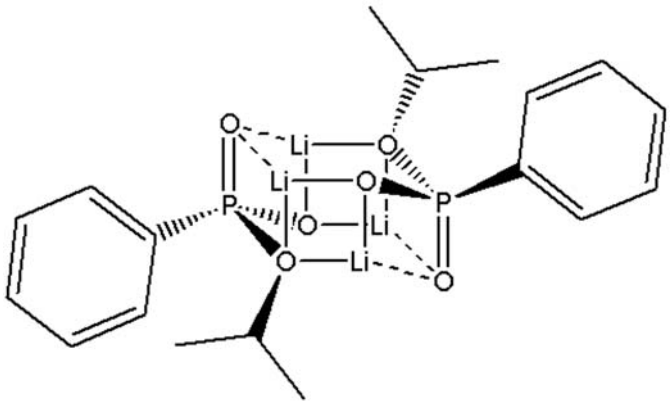

Figure 4.21 A proposed molecular structure for the identified impurity phase from the synthesis of $LiNbO_3$ nanocrystals.

the isopropyl components have remained associated to the lithium atoms. The third assumption is that the state of oxidation of each phosphorus is equal because there is no apparent reason that one would combust more than the other. If this formula also represents the molecular formula, the structure (**Figure 4.21**) can be reasonably assumed by maintaining a 4-coordinate environment for those parties involved. This proposed structure is similar to that of oligomeric $LiOPr^i$.

From the analyses performed here, the origin of the impurity phase appears to be initiated by a reaction between TPPO and $LiOPr^i$. A possible mechanism for this reaction may be that the phosphoryl is attacked by thermally phase segregated $LiOPr^i$, to form a 5-coordinate intermediate. Thereafter a phenyl group eliminates, possibly by a radical mechanism.[59] The phenyl group has been detected in the preceding mass spectral analyses to form isopropyl benzene or another of the phenyl-isopropyl derivatives. Once the initial thermal decomposition is complete and the majority of alkyl components have been removed from the reaction, further loss of phenyl groups is believed to be the result of oxidation with Li_2O or O_2 that diffuses out of $LiNbO_3$.

The identification of the impurity and the processes that lead to its formation raise concerns about the future prospects of this method for the production of $LiNbO_3$. The major concern is that the impurity cannot be avoided. Precautions can be taken for the use the most optimized $LiNb(OPr^i)_6$ precursor and to ensure the purest of reaction atmospheres, but $LiNbO_3$ will still feed the growth of the impurity phase with Li_2O. Questions about the necessity of TPPO in

the reaction mechanism are also troubling, since it is apparent that TOPO cannot be used as a substitute. Is it simply the larger cone angle of TPPO that facilitates in the removal of Pr^iOH or does TPPO react with the precursor to form an encapsulating micelle? The answer to these questions are difficult to obtain.

4.9 Optimizing the Purity of the Prepared $LiNbO_3$

As prepared, $LiNbO_3$ was incased in TPPO and contained a Li_3PO_4-based impurity. In addition, the Li:Nb ratio and the concentration of Nb^{4+} in the prepared $LiNbO_3$ was also in question.

Once the identity of the unknown impurity was identified as a predecessor to Li_3PO_4, its selective removal from the reaction product became possible. Under acidic conditions, Li_3PO_4 is soluble, whereas $LiNbO_3$ is not. A thorough examination of available acids was performed and tested for suitability in our procedure. Acids tested included HCl, H_3PO_4, H_2SO_4, HNO_3, acetic acid, citric acid, and oleic acid. The powder diffraction pattern of samples treated by these acids are shown in **Figure 4.22** except for H_2SO_4 or citric acid. These treatments could not be examined because the $LiNbO_3$ remained in suspension and could not be isolated. HCl, H_3PO_4, and HNO_3 all result in irreparable damage to the $LiNbO_3$ crystal. This damage is seen in **Figure 4.22** by the complete destruction of $LiNbO_3$ upon exposure to HCl and the shifting of peaks after treatment with H_3PO_4 or HNO_3. Acetic acid became the acid of choice for our purification because $LiNbO_3$ was unaffected and, unlike oleic acid, "Li_3PO_4" could be removed completely by a single rinse. Interestingly, the use of oleic acid in place of acetic acid has a notable effect on the surface polarity of the $LiNbO_3$.

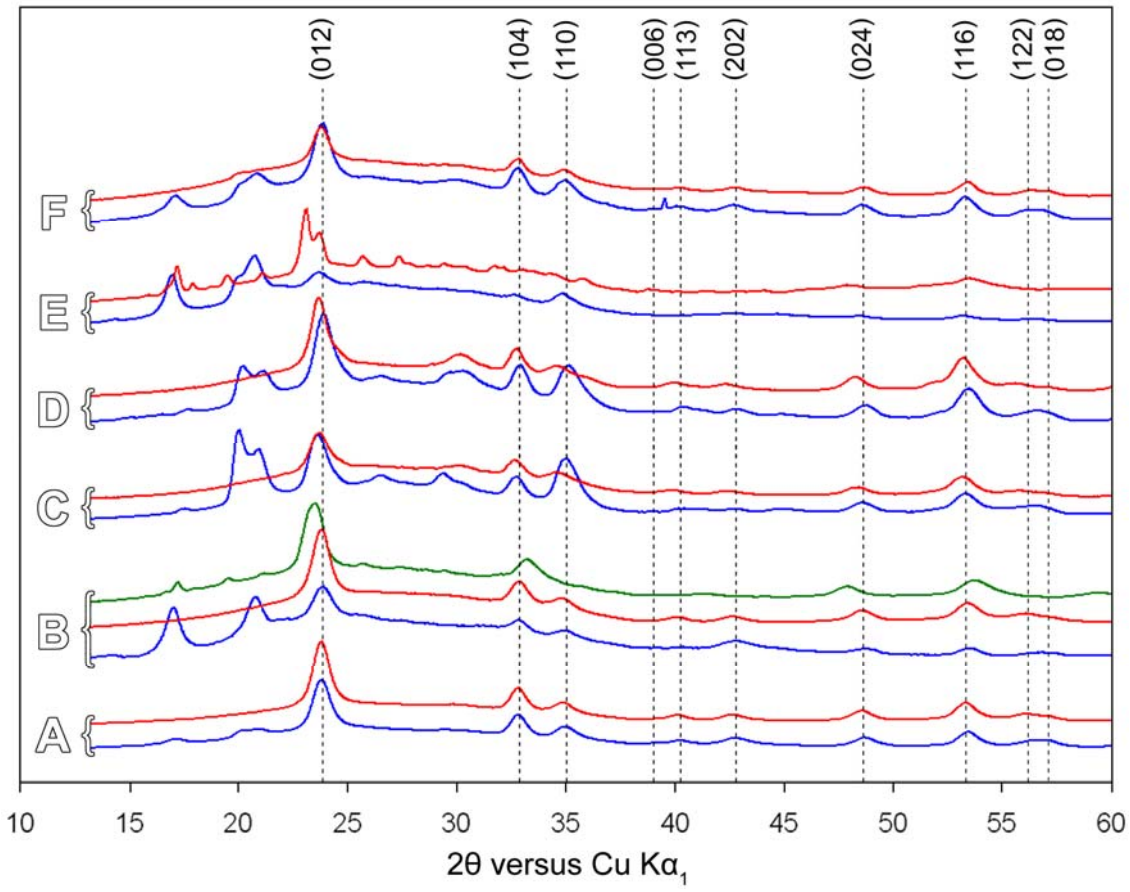

Figure 4.22 Identification of the ideal purification procedure by examination of X-ray powder diffraction spectra of non-acid treated (blue) and acid-treated (red) $LiNbO_3$. The tested wash solutions include: (A) 2 M acetic acid, (B) 17 M acetic acid and 5 M nitric acid (green), (C) 1 M nitric acid, (D) 15 M phosphoric acid, (E) 12 M hydrochloric acid, and (F) a 50 % oleic acid solution.

Following treatment with acetic and oleic acid, the prepared $LiNbO_3$ is dispersible in ethanol and hexanes, respectively.

The removal of TPPO from the reaction product was initially performed with three wash and centrifuge cycles with acetone, but $LiNbO_3$ product was lost by this method because it remained as a black suspension in the second and third wash cycles (**Figure 4.23C**). Several wash solutions, capable of dissolving TPPO were explored as alternatives to acetone including, benzene (A), 2-

Figure 4.23 Solutions tested for the removal of TPPO from the reaction product. Each solution was used three times to completely remove all traces of TPPO. Each of the three washes are shown left to right for (A) benzene, (B) isopropanol, (C) acetone, (D) 2:1 (v:v) acetone/hexane, and (E) 3:1 (v:v) acetone/hexane. Any black material appearing in the third wash is suspended $LiNbO_3$.

propanol (B), 2:1 acetone/hexane (D), 3:1 acetone/hexane (E), and methanol (not shown). The results of methanol are similar to that of the isopropanol wash solutions. Out of the tested washes, benzene was the most effective system for the extraction of TPPO, but its benefit was limited because the polarity of benzene hindered the subsequent use of aqueous acetic acid described earlier. The acetone/hexane blends were also successful in that the reduced polarity of hexanes forced $LiNbO_3$ out of suspension, while acetone solubilized the excess TPPO. Only the 3:1 (v:v) mixture was found to be compatible with the aqueous acid rinse procedure so it was adopted as the standard purification solvent.

4.10 The Composition of Synthesized $LiNbO_3$: The Li-to-Nb Ratio and the Nb^{4+} Concentration

The main importance in optical crystals is that they contain a high compositional regularity. This fact poses a problem to the synthesized $LiNbO_3$ nanorods because the aggregation process likely resulted in various anomalous inclusions. Aside from regularity, stringent compositional requirements do limit the ability of $LiNbO_3$ to produce SHG. Since a given refractive index is dependant on the composition of a specific crystal direction, it is relatively easy to see how

changes in composition can seriously impact the phasematched condition for SHG. A simple change in refractive index, as a result of compositional changes is enough to upset the fine balance between dispersion and birefringence. The temperature or angle of the SHG experiment would need to be adjusted to re-establish optimal SHG emission. Considering the lenient conditions required for phasematching nanocrystals, the greater concern of a compositional change is that the polarizability of the crystal is also affected along that direction. As a result, the d-tensor values are affected.[65] In our case, if the value of d_{31} or d_{33} is reduced, there will be a negative consequence to SHG efficiency. The optimal case for d_{31} is actually one where the Li/(Li+Nb) ratio is 52 % in a bulk crystal.[65] The reduction of $LiNbO_3$ to form Nb^{4+} sites also cause problems for SHG. Aside from a change in polarizability, the introduced electron acts as an absorption center for a variety of wavelengths. This reduced cation results in a decrease in the material transparency such that the source may be absorbed before a second harmonic is generated, or the produced second harmonic is reabsorbed and never emitted. As a result of these factors, determining the Li-to-Nb ratio and Nb^{4+} concentration were important endeavors in this research. The methods and results of those analyses are described in this section.

Compositional limitations exist with regards to the Li-to-Nb ratio and the stability of $LiNbO_3$. At room temperature, $LiNbO_3$ can persist between 48-50 mol percent lithium [Li/(Li+Nb)],[130] but it has also been demonstrated that this range can extend to be as low as 47 %.[131] The process by which lithium is lost from the crystal is facilitated by heat and it is shown below:

$$LiNbO_3 \xrightarrow{heating} Li_{(x)}NbO_{(3-x/2)} + (x/2)Li_2O \qquad (0.89 < x < 1) \quad (31)$$

Once the low-end of this range is met, lithium deficient phases such as $LiNb_3O_8$ begin to appear upon further loss of Li_2O. The appearance of $LiNb_3O_8$ in the prepared $LiNbO_3$ samples is alarming because it implies that the material is lithium deficient and this negatively impacts d_{31}. The appearance of $LiNb_3O_8$ in our samples dictates that our $LiNbO_3$ is as much as 3 % deficient in lithium after 48 h at lower reaction temperatures. The whereabouts of the released Li_2O has already been identified as part of the $Li_4(OPr^i)_2[PO_2(C_6H_5)]_2$ impurity.

Many techniques are available to investigate the Li-to-Nb ratio in $LiNbO_3$, but only one was found to be useful as a result of complications that surrounded the use of other methods. For instance, optical properties such as birefringence and the phasematching temperature for SHG are highly accurate and commonly employed methods.[143-146] None of our structures were, however, found to be capable of SHG using 1335 or 1064 nm peak laser wavelengths, regardless of laser intensity. A number of other articles describe the use of Raman spectroscopy to determine $LiNbO_3$ stoichiometry.[146-149] The linewidth of peaks at 876 cm^{-1} and 152 cm^{-1} are highly sensitive to the Li-to-Nb ratio, and can be used to determine the metal composition with an accuracy of 0.05 mol %.[132,133] Several of our samples were analyzed in the Raman spectroscopy laboratory of Dr. Michael Chen in the Department of Physics at SFU, but none of these attempts could identify the referenced absorptions. Low field ^{93}Nb-NMR

linewidths have also been used by a number of researchers successfully,[134,135] however a solid state NMR for this analysis was not readily available. Another popular and quick assessment of the Li-to-Nb ratio is normally done by examination of the Curie temperature that normally occurs at 1180 ^{o}C for stoichiometric samples.[135,136] Unfortunately, this analysis was also not possible because of a limited temperature stability (< 600 ^{o}C) observed by our sample.

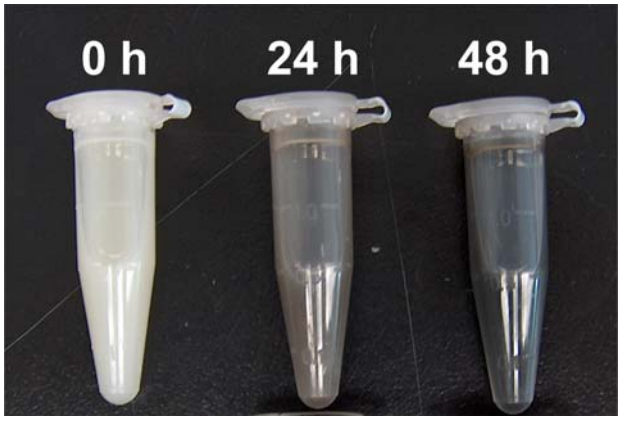

Figure 4.24 Physical observation of the darkening seen in the purified $LiNbO_3$ powder as time progresses. Samples have been suspended in ethanol.

The relationship between lithium vacancy and crystal lattice parameters of $LiNbO_3$ has also been shown to be linear and it allowed for a qualitative assessment of this deficiency.[37, 141, 142] After 24 h of reaction at 360 ^{o}C, our samples were indexed to cell parameters of a = 5.153 Å and c = 13.884 Å.[75] Using the linear relationship from the *a*- and *c*-axis values of Iyi[35] and Xue,[131] our $LiNbO_3$ was extrapolated to contain 47 ± 4 % mol percent lithium according to the *a*-axis and 46 ± 11 % according to the *c*-axis.

Three points led to the opinion that the synthesized $LiNbO_3$ contained Nb^{4+} impurities. The first was apparent after the $LiNbO_3$ was purified to remove the excess TPPO (**Figure 4.24**). The gradual darkening of the sample is the result of increasing the concentration of absorption centers. The black

appearance of the $LiNbO_3$ at later times is the result of a wide range of wavelength absorption, and it implies that the nanocrystals still contain a band-structure of molecular orbitals. The second indication was the observation of $LiNb_3O_8$, that is described by Courths to be the preliminary step in a three-stage reduction mechanism:[137]

$$\textbf{Stage I – 3 } LiNbO_3 \xrightarrow{vacuum,\ heat,\ inert\ gas} \textbf{ } LiNb_3O_8 \text{ (“}LiNbO_3 \cdot Nb_2O_5\text{”) + } Li_2O \quad (32)$$

$$\textbf{Stage II – } LiNb_3O_8 \xrightarrow{vacuum,\ heat,\ inert\ gas} \textbf{ } LiNbO_3 \cdot 2NbO_2 + \tfrac{1}{2}\ O_2 \quad (33)$$

$$\textbf{Stage III – } 2NbO_2 \xrightarrow{vacuum,\ heat,\ inert\ gas} \textbf{ } Nb_2O_3 + \tfrac{1}{2}\ O_2 \quad (34)$$

In Stage I, $LiNbO_3$ loses Li_2O to form $LiNb_3O_8$ or, in other words, surface sites of Nb_2O_5 are formed within $LiNbO_3$. Since surface Nb^{5+} atoms have an incomplete coordination sphere, they are also surrounded by the least electron density, and they are the most prone to reduction. In Stage II that reduction occurs to form Nb^{4+} ions, that are shown as a distinct NbO_2 phase, but could alternatively be explained as surface sites of NbO_2 in $LiNbO_3$. This process leads to the generation of O_2 that has now been proven to contribute to the degradation of $LiNbO_3$, the combustion of TPPO, and the generation of $Li_4(OPr^i)_2[PO_2(C_6H_5)]_2$. Once the Nb^{5+} sites become exhausted, Stage III initiates at the Nb^{4+} sites, and the reduction continues. The final point that suggested the presence of Nb^{4+} was that high temperatures and inert conditions, are known to cause the reduction of oxides by the diffusion of oxygen out of the structure (analogous to Stage II

above).[138,139] Since, heat and inert conditions are necessary for this type of nonhydrolytic reaction, it is difficult to see how Nb^{4+} might be avoided.

To test for the presence of Nb^{4+} ("NbO_2") in the prepared $LiNbO_3$, a sample was first analyzed by electron-spin resonance spectroscopy by Dr. Charles Walsby of the Department of Chemistry at SFU. The results of this test (**Figure 4.25**) indicate that the sample does contain a large paramagnetic impurity but the results could not be attributed to Nb^{4+} or quantified.

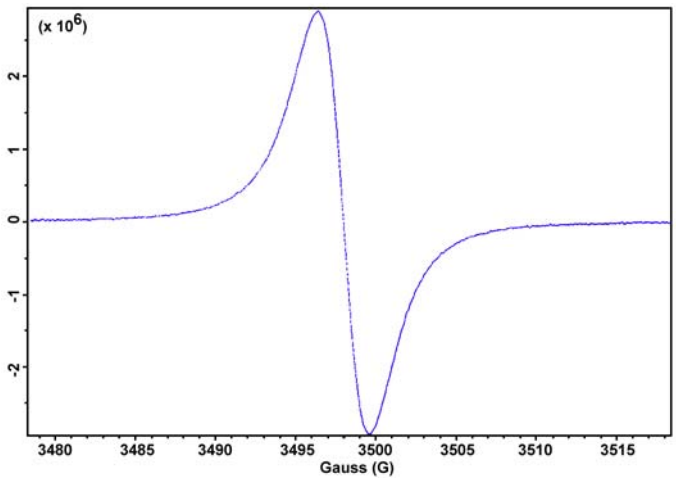

Figure 4.25 Electron-spin resonance (ESR) spectrum of a sample of $LiNbO_3$ powder taken from a 360 °C reaction after 48 h. A large paramagnetic impurity is detected without observation of any fine-structure.

Although the paramagnetic source is difficult to conceive as anything but Nb^{4+}, one would have expected the spectrum to also contain fine structure with 11 lines (I_{Nb} = 9/2).[126] Following this experiment, a quantitative analysis by impedance spectroscopy was sought, but a suitable sample wafer could not be constructed from the small amount of material on hand (~20 mg). More material would have been synthesized to perform this analysis if difficulties with the commercial availability and consistency of $LiNb(OPr^i)_6$ were not encountered. As a final approach to determine the composition of Nb^{4+} in the synthesized $LiNbO_3$, seven samples

were analyzed for C, P, O, Nb, Li, and other trace ions by X-ray photoelectron spectroscopy (XPS). Caution was taken in this analysis because the detected photoelectrons only represent the composition at a depth of a few angstroms.[140] If electron mobility is assumed to be free in the structure, then the detected Nb^{4+} concentration will also be indicative of the bulk Nb^{4+} concentration. This assumption is made here on the basis of the grey color of $LiNbO_3$ nanocrystals (**Figure 4.24**) that implies electrons occupy a conduction band.

The initial sample analyzed by XPS was a $LiNbO_3$ standard supplied by Aldrich (99.9 % powder). This sample allowed the identification of peak positions and peak spacings that are indicative to $LiNbO_3$. In this analysis, all spectra were fitted with linear backgrounds and 70 % Gaussian-30 % Lorenztian peaks with an exception for the Li 1s spectrum where the background is more suitably represented by a “simple” background that is part of the supplied Kratos Axis Ultra XPS analysis software. The choice of a “simple” background was made for all the Li 1s spectra in this study because the scattered electrons (background) have a nonlinear increase in concentration and binding energy. The Nb $3d_{5/2}$ and $3d_{3/2}$ spin doublet of all spectra is fitted with peaks of equal width that are separated by 2.750 eV apart. A peak-area-ratio of 0.650 (expected 0.666)[128] was also maintained for all the doublets. After fitting, the relative peak positions, $\Delta[avg.O_{(2,3)} - Nb_{(1)}]$ and $\Delta[avg.O_{(2,3)} - Li_{(1)}]$, obtained for the standard match well with those expected from literature $LiNbO_3$ data (**Table 4.1**).[129] With this fitting, two niobium environments were found in the standard. The lowest energy doublet was the dominant signal, believed to originate from $LiNbO_3$. The second

Table 4.1 **Binding energy gaps and peak area ratios summarizing the results of 35 X-ray photoelectron spectra. The data is tabulated from a 99.9 % powdered sample of $LiNbO_3$ (Std), 0, 24, and 72 h samples of a reaction at 360 °C, a 48 h sample from a 370 °C reaction (A), a 48 h sample using an optimized precursor at 360 °C (B), and a 48 h sample that was not rinsed by acetic acid (C). The expected binding energy gaps were found in the online NIST database for XPS data.[129]**

Binding Energy Gaps	**0 h**	**24 h**	**72 h**	**48 h (A)**	**48 h (B)**	**48 h (C)**	**Std**	**Expected**
$\Delta[O_{(1)} - Nb_{(3)}]$	320.8	320.9	320.0	321.0	-	323.3	-	324.6
$\Delta[O_{(4)} - Nb_{(2)}]$	325.3	325.2	324.4	325.8	324.9	325.6	324.4	323.0
$\Delta[avgO_{(2,3)} - Nb_{(1)}]$	324.5	324.1	323.5	324.7	323.6	324.5	323.4	323.2
$\Delta[avgO_{(2,3)} - Li_{(1)}]$	-	475.7	475.4	475.9	475.9	475.6	475.5	475.5
Peak Area Ratios								
$(1/6)C_{(2)} / P_{(1)}$	2.03	1.75	0.96	1.51	1.17	0.95	N/A	3.00
$Nb_{(1)}/[O_{(2)} + O_{(3)}]$	0.28	0.30	0.27	0.25	0.27	0.14	0.34	0.33
$Nb_{(1)}/[O_{(2)}+ O_{(3)}+ O_{(4)} - (5/2)Nb_{(2)} - (4-(1/6)C_{(2)}]$	0.30	0.34	0.31	0.32	0.32	0.24	0.34	0.33
$Nb_{(1)}/[O_{(2)} + O_{(3)} + O_{(4)} - (8/3)Nb_{(2)} - (4-(1/6)C_{(2)}]$	0.30	0.35	0.31	0.32	0.32	0.24	0.34	0.33
$Nb_{(2)} / O_{(4)}$	0.37	0.63	0.02	1.16	0.57	0.19	0.37	0.38-0.40
$Nb_{(3)} / [Nb_{(1)} + Nb_{(2)} + Nb_{(3)}]$	0.01	0.06	0.07	0.00	0.01	0.04	0.00	0.00
$Li_{(1)} / [Li_{(1)} + Nb_{(1)}]$	0.00	0.11	0.16	0.18	0.18	0.65	0.50	0.50
$[Li_{(1)} + Li_{(2)}] / [Nb_{(1)}]$	0.00	0.12	0.27	0.31	0.32	2.61	1.53	1.00
$[Li_{(1)} + Li_{(2)}] / [Nb_{(1)}+(1/3)Nb_{(2)}]$	0.00	0.12	0.27	0.28	0.31	2.57	1.49	1.00

Nb^{5+} environment at higher binding energy is thought to signify a more electron withdrawing environment such as that from a Nb-rich phase like $LiNb_3O_8$ or Nb_2O_5. The oxygen O 1s spectrum occurs as three main peaks denoted as $O_{(2)}$, $O_{(3)}$ and $O_{(4)}$ that describe the same story. Calculating the $Nb_{(1)}/[O_{(2)}+O_{(3)}]$ ratio from this data obtains a value of 0.336 that is suggested here to be due to $LiNbO_3$ (expected 0.333). A ratio of 0.370 for the high binding energy pair, $Nb_{(2)}/O_{(4)}$, is estimated to be the result of a niobium-rich phase such as Nb_2O_5 (expected 0.400) or $LiNb_3O_8$ (expected 0.375). The Li 1s spectrum was difficult to deconvolute for comparison because of an overlapping Li_2CO_3 signal, that is believed to be a reactant in the process of forming the standard $LiNbO_3$ powder. A reasonably good agreement was, however, still found with $Li_{(1)}/(Li_{(1)}+Nb_{(1)})$

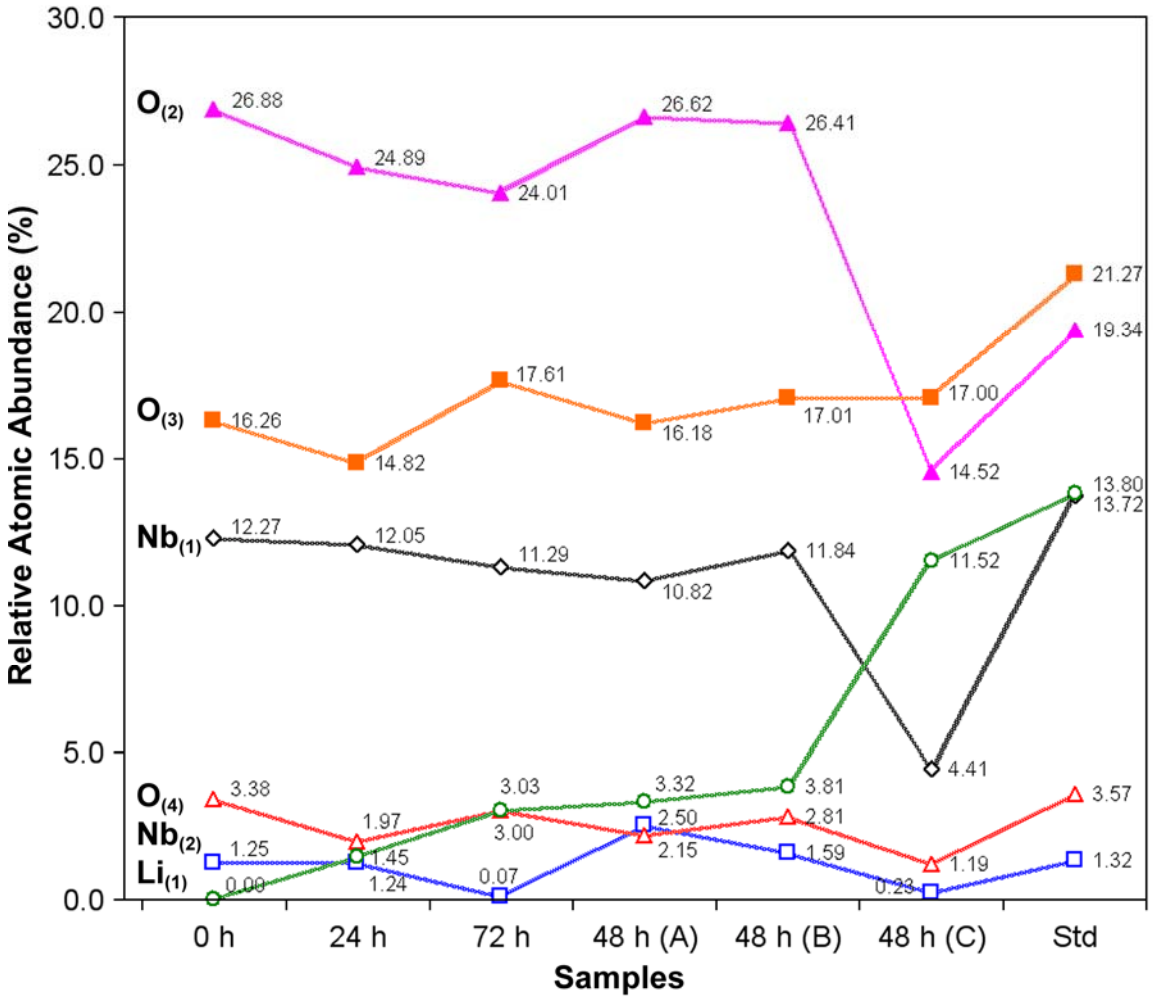

Figure 4.26 **The relative atom abundance (%) calculated from peaks detected in the analysis of Nb 3d, O 1s and Li 1s X-ray photoelectron spectra. Lines have been included to guide the eye and they do not represent a linear connectivity between the samples. The spectra represent a 99.9 % powdered sample of $LiNbO_3$ (Std), 0, 24, and 72 h samples of a reaction at 360 ^{o}C, a 48 h sample from a 370 ^{o}C reaction (A), a 48 h sample using an optimized precursor at 360 ^{o}C (B), and 48 h sample that was not rinsed by acetic acid (C). The $Nb_{(3)}$ intensity is too low to be shown in this figure, but data can be viewed in Table 4.1.**

equal to 50.1 %. Using the same peak spacings and peak-height ratios obtained here, samples prepared from our $LiNbO_3$ synthesis were also analyzed by XPS.

Out of the six remaining samples, three are from a single reaction that represents the composition at roughly 0, 24, and 72 h reaction time at 360 ^{o}C.

The remaining three samples fill in the 48 h gap, but for comparison purposes they differ in temperature of reaction, the nature of the precursor, and in post-reaction treatment. The spectra of reaction samples are far more convoluted than that of the standard due to surface-bound organo-phosphine oxides, and the additional set of peaks that can be attributed to Nb^{4+} ("NbO_2") impurity sites. Since the spectra are so complex, peak associations were assessed by a comparison of the changes in relative peak area percentages (**Figure 4.26**). The 48 h samples identified as (A) and (C) in this figure used the same precursor as the 0, 24, and 72 h samples, but (A) was run at 370 ^{o}C and (C) was not washed by acetic acid. The 48 h sample identified as (B) represents a sample prepared with a more polymeric and oxide rich precursor. By examining **Figure 4.26**, the $Nb_{(1)}$ and $O_{(2)}$ traces share a similarity in shape that suggests they are associated as in the $LiNbO_3$ standard. The calculation of $Nb_{(1)}/[O_{(2)}+O_{(3)}]$ (**Table 4.1**) and the shape of the $O_{(3)}$ trace relative $Nb_{(1)}$ suggests that there are other contributions to the $O_{(3)}$ signal. Notably, the phosphine impurity is expected to contribute, and the $P_{(1)}$ profile does have a similar shape to $O_{(3)}$ (**Figure 4.27**). Due to the complexity of the O 1s spectrum and the close proximity of peaks, it is also likely that the peak fitting has assigned a small amount of $O_{(4)}$ peak intensity under the $O_{(3)}$ peak or vice versa. As a result of these two factors, two corrections are applied to the oxygen term of $Nb_{(1)}/[O_{(2)}+O_{(3)}]$. One adds in $O_{(4)}$ then subtracts the expected oxygen from either Nb_2O_5 (i.e., $5/2Nb_{(2)}$) or $LiNb_3O_8$ (i.e., $8/3Nb_{(2)}$). The second adjustment subtracts out the phosphine contribution by assuming P remains 4-

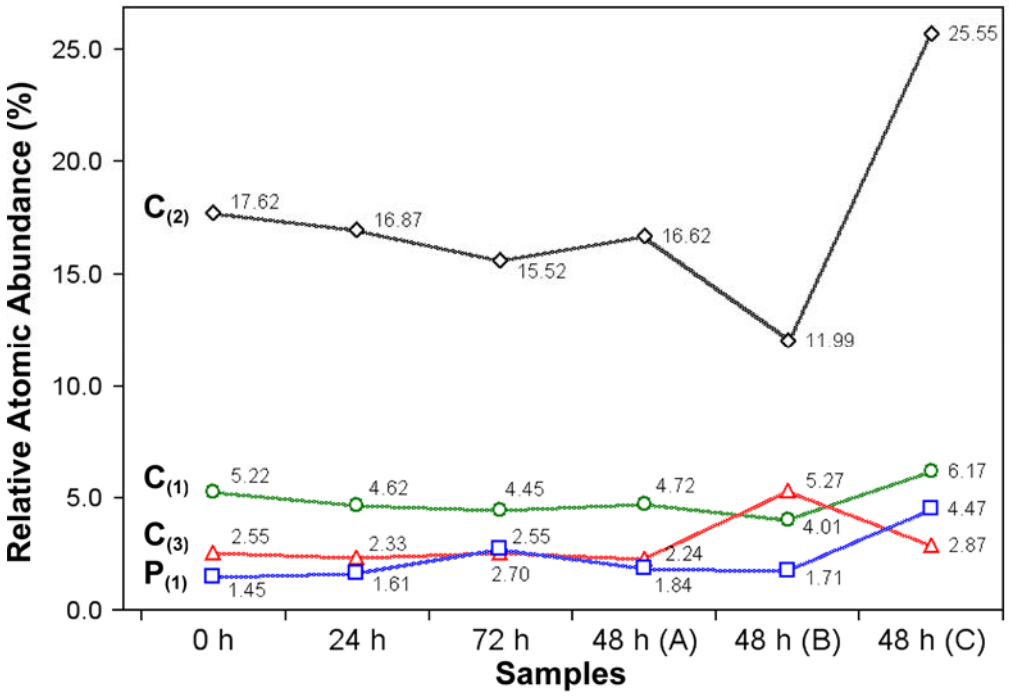

Figure 4.27 The relative atom abundance (%) calculated from peaks detected in the analysis of C 1s and P 2p X-ray photoelectron spectra. The plot contains the prepared samples of LiNbO3 described in Figure 4.26.

coordintate and replaces each phenyl by an oxygen (i.e., 4-(1/6)$C_{(2)}$). With both these factors removed the adjusted $Nb_{(1)}/[O_{(2)}+O_{(3)}]$ values in all samples agree very well for that expected for $LiNbO_3$. The data obtained from Li 1s spectra indicate that the surface of the synthesized $LiNbO_3$ is highly Li deficient. As soon as the reaction reaches the maximum temperature (0 h), no lithium is detectable in the surface of the acid purified sample. The former impurity study, and the non-acid rinsed 48 h (C) sample (**Figure 4.26**), identify that the loss of lithium is occurring in the formation of the phosphine impurity phase. Interestingly, as time progresses, it appears as though lithium reappears. The $Li_{(1)}/(Li_{(1)} + Nb_{(1)})$ ratio increases to 10.7 % after 24 h to 16.2 % after 72 h. This process may be the result of the redistribution of lithium from the bulk of the nanocrystal, and it would

result in the reformation of lithium-based phases at the surface. A second lithium peak, $Li_{(2)}$, was identified in all cases within 1 eV of $Li_{(1)}$, but was never identified. If this is assumed to be due to $LiNbO_3$ or $LiNb_3O_8$, the results are slightly improved for all synthesized materials. These results are shown in two additional calculations for lithium included in **Table 4.1**.

The XPS results for the 0, 24, and 72 h reaction show a trend in compositional change that is somewhat consistant with the mechanism of reduction introduced earlier. Initially, no Nb^{4+} is detected ($Nb_{(3)}$ in **Table 4.1**) but the formation of the impurity has deprived the surface of the necessary Li and O atoms to form $LiNbO_3$ and a niobium-rich phase such as $LiNb_3O_8$ forms (Stage I). By 24 h, Stage II has commenced and it coincides with Stage I such that the concentration of $LiNb_3O_8$ remains roughly constant despite its consumption to produce NbO_2. As a result of Stage II, the concentration of Nb^{4+} has increased to 5.7 % of the surface niobium. By 48 h later, Stage II has increased this concentration to 7.1 %. The decline in $LiNb_3O_8$ concentration by 72 h also marks the end of Stage I. The P 2p spectrum for all acid treated samples reveals that TPPO is still attached to the surface in some form. Since acid has removed the lithium-based impurity, the detected surface phosphines are believed to be associated with the surface niobium ions as part of the amorphous glass identified earlier (**Figure 4.16A** blue spectrum). Phenyl groups from TPPO can still be detected in the C 1s spectrum as a peak labeled $C_{(2)}$. By the time the maximum reaction temperature has been reached, this analysis shows that TPPO has reacted to leave an average of two phenyl groups on the complex

(**Table 4.1**). The remainder of the valency can be assumed to be filled with the oxygen atoms that are contained within the area of the $O_{(3)}$ peak. The $(1/6)C_{(2)}/P_{(1)}$ ratio continues to decrease as time goes on to a limit of one phenyl per phosphorus after 72 h. The second phenyl group is believed to be lost as a result of slow combustion with oxygen liberated in a Stage II-like process.

The 48 h samples used as a comparison in this study offer some confusing results that are difficult to rationalize. Most of the data for samples (A) and (B) appears to fit the trend seen in the 0-72 h time span. This trend includes the $1/6C_{(2)}/P_{(1)}$ ratio representing the state of phosphine combustion, and the Nb-to-O ratios expected for $LiNbO_3$. Both have a higher Li-to-Nb ratio, but this is believed to be the result of a more rapid rate of lithium redistribution at higher temperatures (A) and a better ability of oxide linked precursors to firmly hold "$LiOPr^i$"(B). The amount of Nb^{4+} seen in **Table 4.1**, however, does not appear to follow any recognizable trend. For example, the lithium deficient phase in (A) (i.e., $Nb_{(2)}/O_{(4)}$) is present in double the concentration of as the 24 h sample. The higher $Nb_{(2)}$ concentration signifies that the $LiNbO_3$ has lost a significant amount of lithium and oxygen relative the 24 h sample. Considering this advanced state of Stage I, the complete absence of $Nb_{(3)}$ (i.e., Nb^{4+}) in this sample is surprising because the higher reaction temperature should more easily mobilize O_2 and cause Stage II. With the use of a better precursor, the $Nb_{(3)}$ and $Nb_{(2)}$ concentrations in (B) look as though they might represent the early part of the Stage I reduction process. This result seems to contradict the advanced stages of oxygen-fed phosphine decomposition indicated by the $1/6C_{(2)}/P_{(1)}$ ratio.

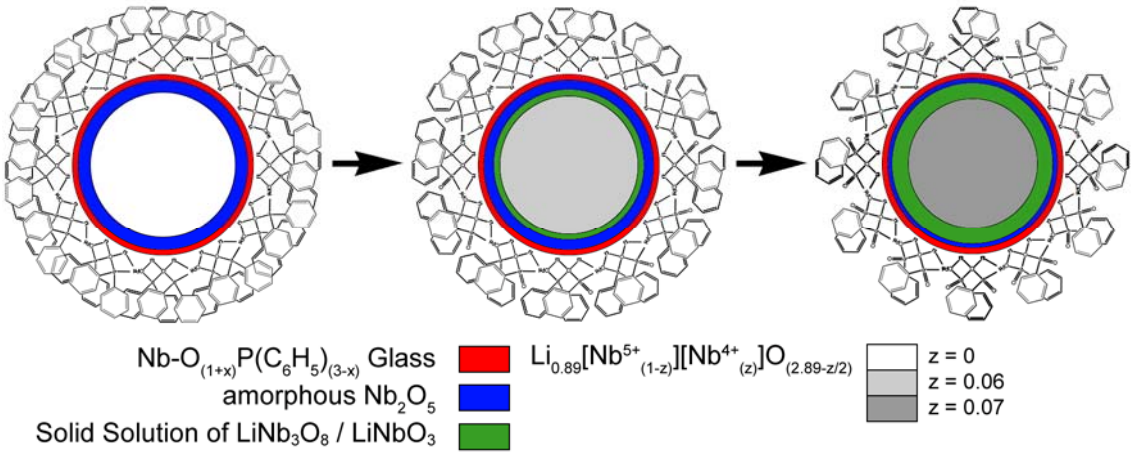

Figure 4.28 The proposed compositional evolution of $LiNbO_3$ synthesized by the solution phase process at 0 (left), 24 (mid), and 72 h (right). The size of the outer layers has been exaggerated for clarity. The Li-phosphine impurity is shown on the surface of the particle and it loses phenyl groups as it continues to oxidize over time. Below is found layers of the detected Nb-phosphine glass impurity and an amorphous Nb_2O_5 that are both the result of lithium loss. Over time the bulk $LiNbO_3$ is seen to reduce in volume to form $LiNb_3O_8$ by the redistribution of bulk lithium towards the depleted surface.

The results of this work suggest a time-dependant evolution in the composition of the synthesized $LiNbO_3$. Initially the amorphous $LiNbO_3$ reacts to lose a significant amount of Li and O from the surface (**Figure 4.28**). These atoms are reacted to become part of $Li_4(OPr^i)_2[PO_2(C_6H_5)]_2$ that has formed a capsule around the material. Beneath the impurity is believed to be an amorphous surface coating of Nb_2O_5. When the material crystallizes by 24 h later, the lattice constants identify that the bulk $LiNbO_3$ stoichiometry has reached the limit of lithium depletion as a result of the surface impurity. By this point in the reaction, XPS reveals that lithium has started to diffuse from the bulk to the surface as a result of the established lithium gradient. At the same time, O_2 is also being lost to the impurity to form an overall 5.7 % Nb^{4+} concentration in the amorphous niobium surface layers. As time progresses to 48 h, lithium continues

to redistribute to produce a crystalline $LiNb_3O_8$ phase observable by XRD. By 72 h O_2 has been sufficiently removed to increase the Nb^{4+} concentration to 7.1 %.

4.11 The Reoxidation of $Li_{(x)}[Nb^{5+}_{(1-y)}][Nb^{4+}_{(y)}]O_{(3-x/2-y/2)}$

The presence of free electrons within black $LiNbO_3$ is the greatest concern to the ability of our material to produce SHG. It has been briefly mentioned that the prepared $LiNbO_3$ was not capable of generating SHG and here the problem is attempted to be corrected. Reoxidation of Nb^{4+} in black $LiNbO_3$ is known to occur by heating the material in an oxygen-rich atmosphere.[155-158] At 600 ^oC this treatment was already shown to destroy the $LiNbO_3$ (**Figure 4.17**), but this sample was coated in an abundance of the decomposed phosphines. To avoid the degradation observed earlier, lower temperatures were explored from 200-400 ^oC. These temperatures were assumed to be sufficient because oxygen was known to be mobile at the lowest reaction temperature (360 ^oC). Prior to this heat treatment, an acetic acid wash was applied to remove the surface impurity that is the source of phosphate anions.

A $LiNbO_3$ sample was heated in air at several temperatures until the sample oxidation was observed by a visible change in color. At 200 and 250 ^oC no oxidation of $LiNbO_3$ was observed so the reaction temperature was further increased to 300 ^oC and left for 18 h. A slight lightening in the color of the sample may have occurred, but rate of reoxidation was not practical. At 400 ^oC it took only 3 h to visually remove the Nb^{4+} impurities, however, the material structure was damaged (**Figure 4.29**). Furthermore, the sample remains incapable of producing SHG. The substantial structural rearrangement is likely a result of Li

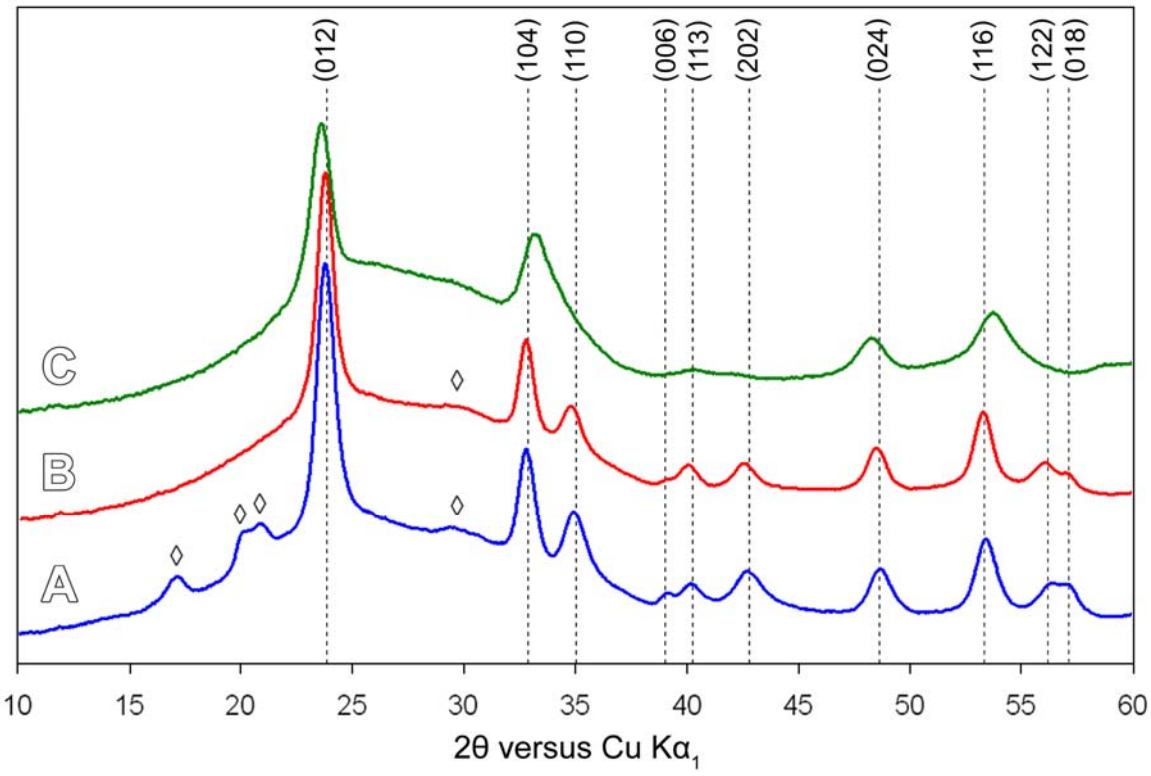

Figure 4.29 X-ray powder diffraction patterns for $LiNbO_3$ after 48 h at 360 °C (A), for the sample following a wash with acetic acid (B), and following a subsequent 3 h 400 °C thermal treatment (C).

and O redistribution to form a more homogenous composition. The shifting of several peaks in **Figure 4.29**, likely represents a loss of inversion symmetry rendering the material incapable of SHG.

4.12 Concluding Remarks and the Prospect of this Synthesis

In this Chapter, the chloride-based and chloride-free decompositions of $LiNb(OPr^i)_6$ were described, and their reaction products were examined by a number of techniques. In the chloride-based route, $LiNbO_3$ was not produced due to the formation of a stable LiCl phase. The result of this synthesis was, instead, nanocrystals of pseudohexagonal Nb_2O_5. These crystals had a bimodal size

distribution containing nanocrystals ~2 nm in diameter and nanorods ~30 by 100 nm with *c*-axis anisotropy. The large crystals were suggested to be the result of nanocrystal aggregation. Upon removal of chlorine, the chloride-free route produced $LiNbO_3$ that also contained a bimodal particle size distribution. Nanocrystals of ~6 nm in diameter and nanorod complexes ~7 nm by 50 nm were the result. The formation of these crystals was also described to be the result of nanocrystal aggregation that occurred preferentially along the *c*-axis.

The successful synthesis of $LiNbO_3$ was examined in further detail to characterize the reaction mechanism and to learn how to optimize the process. Experiments included examination of the atmosphere purity, surface chemistry of the reaction glassware, the reaction temperature, time, and solvent, and the purification procedure. These tests identified that synthesis of $LiNbO_3$ was best achieved using acid-cleaned glassware, an oxygen-free atmosphere, a reaction setup that removes volatile by-products, a reaction temperature of 360-370 °C, and a reaction time less than 48 h. TPPO was also identified as an essential solvent in this reaction because it is believed to play a role in the decomposition of the precursor. The crystalline product was isolated from the reaction, in the highest yield and in the purest form, by removal of excess TPPO with 3:1 (v:v) acetone/hexanes followed by a rinse with 2 M acetic acid and 18 MΩ water.

The compositional purity of the synthesized $LiNbO_3$ was also investigated since the composition of $LiNbO_3$ is strongly linked to the optical properties of the material.[141] This analysis revealed that several impurity phases form during the synthesis. The major impurity, identified as $Li_4(OPr^i)_2[PO_2(C_6H_5)]_2$ was removed

once acetic acid was used for the purification of the reaction product. The remaining phases including "$LiNbO_3$" are believed to compose a nanocrystal with a stratified composition. At the surface, a Nb-phosphine analog to $Li_4(OPr^i)_2[PO_2(C_6H_5)]_2$ was detected by XPS, and it is believed to overlay another niobium-rich layer of an amorphous niobium oxide. The core of the synthesized nanocrystals is composed of reduced and highly lithium deficient $LiNbO_3$. Over time, the state of reduction worsens and lithium migration continues towards the surface causing the formation of $LiNb_3O_8$. Lithium nonstoichiometry is not expected to positively affect the SHG intensity, nor is the fact that Nb^{4+} acts as a broad and efficient light-absorbing impurity in the middle of the visible spectrum. These attributes of the product composition are believed to be the cause of the absence of SHG in our synthesized $LiNbO_3$. In the following Chapter, suggestions are offered for the future solution-phase synthesis of $LiNbO_3$. These suggestions address the current compositional obstacles, and may result in the formation of an SHG active nanocrystal for the future use in SHG microscopy.

CHAPTER 5 – FUTURE RECOMMENDATIONS AND PROSPECTS OF THE SOLUTION-PHASE SYNTHESIS OF $LiNbO_3$ FOR NONLINEAR OPTICAL MICROSCOPY

5.1 Introduction

The latest solution-phase synthesis of $LiNbO_3$, has been shown in **Chapter 4** to require improvement in both the morphological and compositional aspects of the synthesized material. The crystal morphology was revealed to be anisotropic in shape and only partially aggregated, which would benefit the task of pseudo-orienting the nanocrystals for efficient SHG. The direction of anisotropy could be improved, however, if *ab*-plane expansion was exhibited by the crystals instead of *c*-axis elongation. The crystal composition was suggested to be stratified into various layers of different Li-to-Nb and metal-to-oxygen stoichiometries. At the extreme, metal nonstoichiometries are resulting in the formation of centrosymmetric crystal phases such as amourphous Nb_2O_5 and $LiNb_3O_8$ that do not exhibit a SHG emission. Furthermore, the loss of oxygen from the structure results in niobium reduction. The introduction of electrons, as a result of reduction, has caused the synthesized $LiNbO_3$ to efficiently absorb visible wavelengths. This absorption results in a complete loss in the ability of the crystal to emit SHG. In this Chapter, the future direction of the solution-phase synthesis of $LiNbO_3$ is discussed with respect to the foregoing concerns.

Methods of achieving an SHG active nanocrystal might be possible through a modification of the current synthetic approach.

5.2 Reaction Modifications that may Favourably Improve the Product Morphology

While the overriding concern of this research is the lack of SHG as a result of composition, the crystal morphology will become a future focus with the anticipation that composition can be improved. The directed aggregation of $LiNbO_3$ nanocrystals was not an expected result in this research, and it caused the formation of the less-favourable *c*-axis structural anisotropy. The current solution-phase synthesis of $LiNbO_3$ needs to be modified to encourage growth of the crystal along the *ab*-plane where the second harmonic will travel. While any anisotropic morphology encourages a natural ordering of a random powder, *ab*-plane anisotropy will result in the most intense SHG response for each individual crystal. To achieve this goal, the directed aggregation of nanocrystals along *c*-axis needs to be opposed and a kinetic growth regime should be encouraged to produce *ab*-plane growth. It is believed that this goal can be targeted by changing the temperature of reaction, choice of precursor, and choice of capping agent type, concentration, and sterics in the solution-phase reaction.

The long aging time in the current solution-phase synthesis of $LiNbO_3$ is required to promote crystallinity in the synthesized $LiNbO_3$, but it is also resulting in processes, such as aggregation, that reduce the surface energy of the system. To avoid aggregation, the reaction time must be shortened, but not at the expense of product crystallinity. To shorten the reaction time, maintain

crystallinity, and impose a kinetic growth regime, a more suitable precursor is required. To achieve these goals, the new precursor must have a more facile decomposition, and a structure that more closely resembles the bond structure inherent to $LiNbO_3$. A more easily decomposed precursor acts to support kinetic growth by a higher rate of monomer production at lower reaction temperatures.

Any alkoxide precursor must undergo C-O bond cleavage at some stage of the reaction to form a purely oxide-based product. To reduce the decomposition temperature and increase the rate of decomposition, choices must be made in precursor design to facilitate this important reaction step. In our case, an isopropoxide-based precursor was chosen rather than the ethoxide because the additional steric bulk would apply more stress to the C-O bond during thermal motion. In some other metal alkoxides, such as $Zr(O^iPr)_4 \bullet Pr^iOH$, $Hf(OEt)_4$, $Ti(O^nBu)_4$, $Ti(OCH_2Ph)_4$, $Sn(O^tBu)_4$ and $Sn(OCH_2Ph)_4$, a different decomposition mechanism can occur where the C-O bond cleaves more readily (**Figure 5.1**).[64] This new mechanism, called ether elimination, generates dialkyl ether as the reaction byproduct. The precursor decomposition appears to occur under two circumstances. In the S_N1-like scenario, the attached metal atom is smaller than Nb^{5+} (0.51 Å for Ti^{4+} and 0.55 Å for Sn^{4+} relative to 0.64 Å),[142] but the attached alkoxide is larger than isopropoxide. The larger alkoxide groups are more capable of generating stable carbocations due to induction (as in the O^tBu ligand) or resonance (as in the OCH_2PH ligand) and that appears to enable the C-O bond to cleave. In the second scenario, smaller alkoxides (like OPr^i and OEt) function with larger metal cations like Zr^{4+} or Hf^{4+} (0.72 and 0.71 Å,

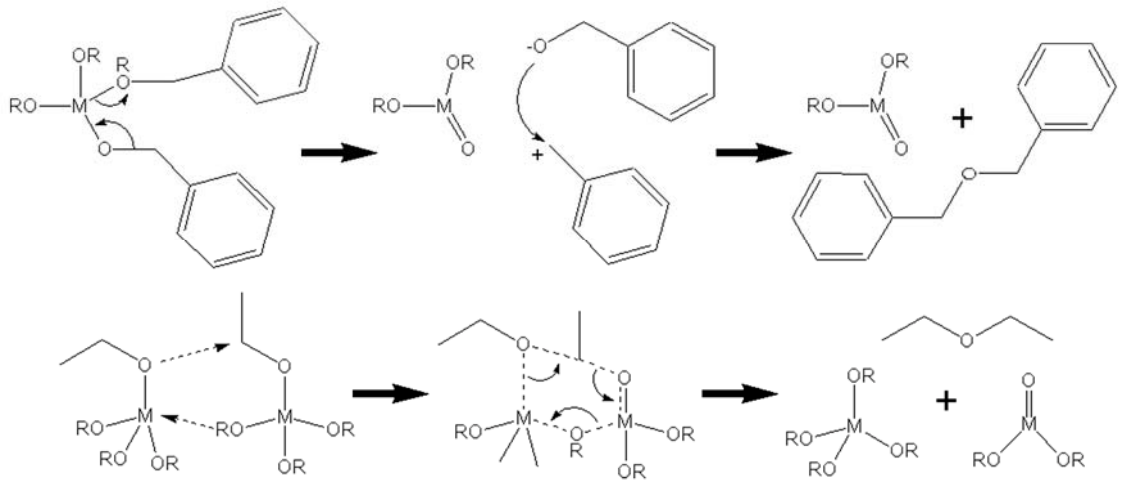

Figure 5.1 The first step in the ether elimination reaction to for metal (M) oxides. The steps could be presumed to repeat until the oxide is formed. (top) The S_N1-like reaction with bulky alkyl groups and small metals (R = CH_2Ph). (bottom) The S_N2-like reaction for small alkyls and large cations (R = Et).

respectively) to produce the same result presumably by S_N2-like reactions. The cause of this reaction may be that an open metal core allows ligand mobility, which facilitates the possibility of S_N2-like geometries. It is unknown why $LiNb(OPri)_6$ did not result in ether byproducts. As smaller cations with six attached ligands, the precursor would be best suited to an S_N1-like scenario, but the C-O bond is still too strong under the present conditions. Therefore, a search for new reaction precursors must focus on a further increase in alkoxide sterics to weaken the bond further and electronic support to stabilize the generated cation.

A new precursor should also be sought that has a structure similar to $LiNbO_3$ because in those precursors less ion mobility would be required following decomposition to form a crystalline product.[143] The alternating oxygen-lithium-oxygen-niobium layers of the chain-like or dimeric structure of $LiNb(OR)_6$

resembles the $LiNbO_3$ *c*-axis (**Figure 1.7B**),[98,99] and therefore, the alkoxides were believed to be the ideal precursor. The drawback of the chosen precursor structure was discovered to be weak $LiNbO_3$-like bonds (i.e., the Li-OR-Nb bridging bonds). During heating these bonds dissociate to form separate molecules of $LiOPr^i$ and $Nb(OPr^i)_5$. Suitable single-source precursors should employ a combination of both weak and strong bonds. The strong bonds should be localized on the precursor where the bonding needs to be maintained during decomposition.[143] The flaw in $LiNb(OPr^i)_6$ is that only one type of bonding is present and a stronger bond is not available to help maintain the mandatory link between the lithium and niobium atoms.

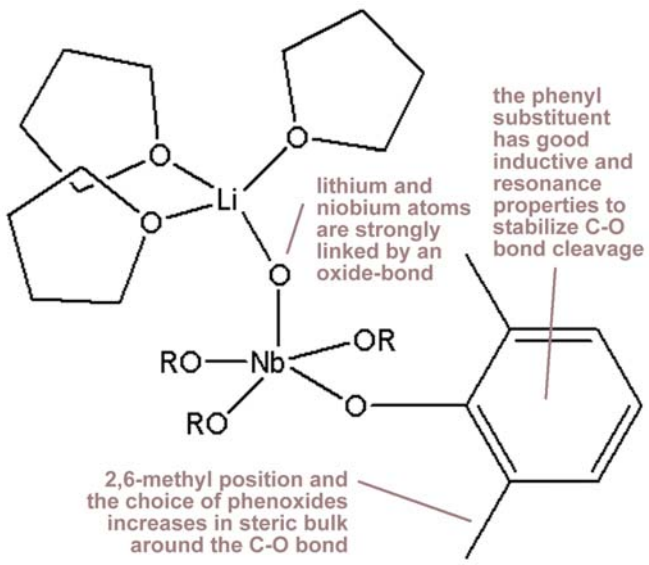

Figure 5.2 **A crystal structure model for $LiNbO(O\text{-}2,6\text{-}PhMe_2)_4$•3THF. Some 2,6-dimethylphenoxide groups have been shown as "OR" for clarity. The properties that make $LiNbO(O\text{-}2,6\text{-}PhMe_2)_4$•3THF an attractive crystal in the solution-phase synthesis of $LiNbO_3$ have been indicated in the figure.**

One precursor, exhibiting all of the desired properties is $LiNbO(O\text{-}2,6\text{-}PhMe_2)_4$•3THF, and it has received less attention than deserved in the literature utilizing single-source molecular $LiNbO_3$ precursors.[144] Large 2,6-dimethylphenoxide groups in this precursor provide enhanced steric and

electronic properties that would facilitate C-O bond cleavage, and a strong oxide-bridged lithium-niobium bond ($LiNbO_3$-like) is already present in its structure (**Figure 5.2**). In a promising observation, the decomposition of $LiNbO(O\text{-}2,6\text{-}PhMe_2)_4 \bullet 3THF$ was shown by Park to form $LiNbO_3$ in just 3 h of decomposition at 300 ^oC in an air atmosphere.[145] This attractively low decomposition temperature does not necessarily apply to nonhydrolytic inert reactions, but the precursor does hold qualities that are expected to outperform the current use of $LiNb(OPr^i)_6$. The work to synthesize $LiNbO(O\text{-}2,6\text{-}PhMe_2)_4 \bullet 3THF$ is currently underway in our group, and it is hoped to have an effect on the product growth direction and significantly reduce the reaction time required to produce crystalline $LiNbO_3$ nanoparticles.

The other factor leading to a less advantageous *c*-axis elongation was the choice of capping agent type, concentration, and sterics. The GC-MS (**Figure 4.8**) and XPS spectra (**Figure 4.18**) of the TPPO-based solution-phase synthesis of $LiNbO_3$, and the XRD spectra for the TOPO-based synthesis of $LiNbO_3$ (**Figure 4.12**) all imply that TPPO has a mechanistic role in the reaction with $LiNb(OPr^i)_6$, so it is not clear how changes in the capping agent will affect the current synthesis of $LiNbO_3$. In solution-phase syntheses, theory states that a high TPPO concentration (1:12-1:10 precursor to capping agent mole ratio) is good for hindering nucleation and reserving precursor for a growth, but the nonselective coordinating property, short phenyl backbone, and poor surface-packing density of TPPO are not capable of regulating the deposition of the remaining material to any particular set of planes (**Figure 5.3**). These properties

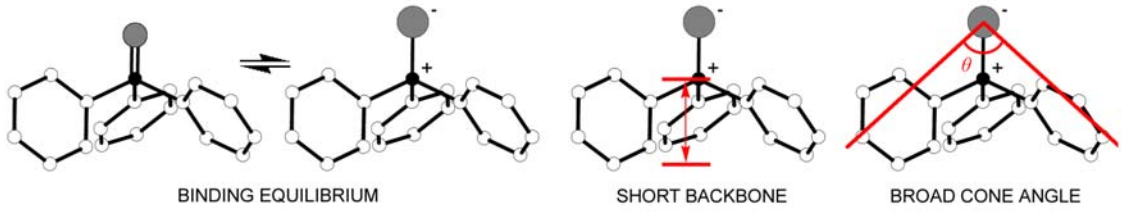

Figure 5.3 The triphenylphosphine oxide (TPPO) molecule showing the binding equilibrium that favours the unbound state (i.e., left), the short length of the phenyl substituent, and a broad rigid cone angle that leads to low surface packing density.

resulted in the isotropic growth of nuclei to form roughly spherical crystals that eventually aggregated along the *c*-axis (**Figure 4.3**). While a long period of time is necessary before aggregation is observed (24 h at 360-380 ^{o}C), the appearance of aggregation is still an indicator of insufficient sterics. The aggregation event was only delayed as a consequence of the high capping agent concentration. To produce anisotropic structures during the growth phase of our synthesis, a new set of capping agent variables should be chosen to facilitate a change from a thermodynamic to a kinetically driven growth regime.

To encourage a kinetic growth regime, the first suggested change in the capping agent would be to increase its steric bulk such that aggregation is more effectively avoided. Bulkier capping agents position nanocrystals further apart, which results in a reduced probability of aggregation, even if the concentration is lowered. The high concentration of TPPO currently forces the capping agent binding equilibrium [**equation (13)**] towards the surface-bound form (SL) where all of the planes are blocked. With a larger steric bulk, the excessive concentration is no longer necessary to prevent aggregation. The second

suggested change in the capping agent condition is, therefore, to reduce the concentration. This would enable planes with a lower binding affinity for the capping agent to be exposed and experience more growth. The extent of exposure for a given set of planes will rely strongly on the temperature of the reaction [**equation (13)**]. The principle of different binding affinities, implies the third change that would be to employ a surface selective capping agent. The choice of TPPO as a nonselective capping agent was intended to allow the intrinsic surface energy differences in $LiNbO_3$ (**Figure 2.2**) to facilitate anisotropic growth. The result of the reaction, however, was isotropic particles as a result of the high reaction temperature causing the surface energies to equalize. If nonselective capping agents are going to be explored further in the solution-phase synthesis of $LiNbO_3$, the reaction temperature will have to be lowered so that the crystal surface energies are no longer thermally equal. Such a temperature change may be possible through the use of alternative precursors such as $LiNbO(O\text{-}2,6\text{-}PhMe_2)_4 \bullet 3THF$ that was previously mentioned. It is not clear, however, whether or not nonselective precursors could ever result in *ab*-plane growth in the case of $LiNbO_3$. The preferential growth of the *ab*-plane would rely on a higher suface energy for *a*- and *b*- dominant lattice planes (e.g., the 110 plane). This may not be the case, however, because the 012 and 006 planes have some of the highest planar Nb^{5+} density[124] and half of the oxygen coordination sphere for each niobium is vacant (**Figure 4.4**). The combination of these properties can be expected to result in relatively high surface energies for these *c*-axis dominant planes. To stop the growth of these planes at lower

temperatures, a selective capping agent, like a long-chain carboxylic acid, may be a better choice. These types of capping agents bond strongly with high surface energy planes by filling the vacant coordination sphere of the metal atoms. Through bonding, the growth of these *c*-axis dominant planes could be selectively blocked. A simple switch to a selective capping agent, such as oleic acid, may not necessarily work in the case of $LiNbO_3$ either because the development of a dipole in $LiNbO_3$ complicates the surface bonding interaction. While a long-chain carboxylic acid may be attracted to the positively charged side of the growing crystal, the negative charge on the complementary side of the crystal can be expected to repel the capping ligands and *c*-axis growth may still result. If this difficulty is encountered in further research, the answer may be to use a certain amount of tetradecyl(trihexyl)phosphonium decanoate, (CYPHOS® 103). This ionic liquid is soluble in organic media, has a high thermal stability, and provides both a bulky anionic and cationic counterpart that can each act as capping agents.

According to our present knowledge, the SHG efficiency of $LiNbO_3$ prepared by the solution-phase synthesis may be improved if an *a*- and *b*- plane dominant crystal morphology can be synthesized. The method of achieving this goal is to encourage a kinetic growth and to prevent the directed aggregation that resulted in *c*-axis anisotropy. The solution suggested in this section is to use more volatile precursors that increase the rate of monomer production, bulkier capping agents that reduce the tendancy for aggregation, and a lower concentration of capping agents such that planes become selectively exposed.

The use of a more selective capping agent may help to ensure the selectively exposed planes are those with higher *a*- and *b*- axis characteristics.

5.3 Reaction Modifications that may Favourably Influence the Product Composition

The current failure of the of solution-phase synthesis to produce SHG-active $LiNbO_3$ is a result of both metal and oxygen nonstoichiometry. In terms of the lithium-to-niobium ratio, an excessive loss of lithium is resulting in the formation of centrosymmetric niobium-rich phases that do not produce bulk SHG. Furthermore, our attempt to reoxidize the material (**Figure 4.26**) appears to be hampered by the inhomogeneous distribution of lithium and niobium, and the serious lithium depletion at the surface of the nanocrystals. Since even centrosymmetric materials can give rise to an SHG response, the largest issue in the current approach appears to be the introduction of absorption centers as a result of niobium reduction. In this section, the changes that may help to correct the present compositional difficulties will be discussed.

If the lithium to niobium ratio of the material can be maintained throughout the current reaction time, the Nb^{4+} absorption centers can be removed by the low temperature gas-phase reoxidation treatment described in **Section 4.11**. A solution-phase reoxidation using a mild oxidant such as trimethylamine oxide, may also be worth exploring. The oxidation/reduction treatment of $LiNbO_3$ is fully reversible[146] as long as oxygen-deficiency is the only nonstoichiometry in the material. In order to maintain the lithium-to-niobium ratio, a precursor with strong lithium-to-niobium connections must be used and an alterative to TPPO is also

advisable. The importance of oxide linkages between lithium and niobium has already been discussed in **Section 3.12.4** for the use of the current precursor, $LiNb(OPr^i)_6$. Oxide links in $LiNb(OPr^i)_6$ have been shown in this research to result in the supression of the lithium-based impurity phase, $Li_4(OPr^i)_2[PO_2(C_6H_5)]_2$. A soluble single-source precursor with all oxygen-bridged lithium and niobium atoms would be the ideal precursor to correct the current lithium deficiency. Again, $LiNbO(O\text{-}2,6\text{-}PhMe_2)_4 \bullet 3THF$ appears to be the solution because the likelihood of lithium and niobium segregation is reduced due to the strength of oxide bridging bonds. The choice of capping agent is going to depend highly on the maximum reaction temperature. In the current reaction, TPPO is forced to function at and above its threshold for decomposition (360 ^oC). The only hinderance to immediate decomposition is the availability of oxygen to TPPO, but the combustion of TPPO is occurring instead by drawing Li_2O from the surface of the synthesized nanocrystal. If the reaction temperature is not reduced, another capping agent must be found with a higher thermal stability than TPPO. It is the future recommendation of this research, however, to persue a synthesis between 300 and 320 ^oC, where a larger variety of capping agents is available for exploration. The use of a new precursor may no longer require a 360 ^oC reaction temperature, and that alone could avoid the difficulties that are experienced with TPPO decomposition.

The immediate obstruction to the successful generation of SHG is not metal stoichiometry, but the presence of free electrons introduced by the loss of oxygen at the reaction temperature. The introduction of Nb^{4+} centers results in

the rapid appearance of a broad absorption band at ~500 nm in $LiNbO_3$ that corresponds with the targeted green SHG emission wavelengths.[158, 163, 164] In **Section 4.8** and **4.11**, the diffusion of oxygen out of $LiNbO_3$ was found to be temperature dependant, and at 300 ^oC the rate of diffusion appears to be minimal. Higher processing temperatures are known to yield darker, more heavily reduced $LiNbO_3$.[146] The future direction of the solution-phase preparation of $LiNbO_3$ should therefore be aimed at reducing the reaction temperature to near 300 ^oC where the loss of oxygen by diffusion is less prevalent. A shorter reaction time is also suggested for future reactions because it would also result in less oxygen loss (**Figure 4.22**). Both of these suggestions should be achievable through the use of a new precursor such as $LiNbO(O\text{-}2,6\text{-}PhMe_2)_4 \bullet 3THF$.

5.4 Concluding Remarks

The solution-phase synthesis of $LiNbO_3$ by decomposition of $LiNb(OPr^i)_6$ in TPPO at 360 ^oC resulted in nanocrystals that were not suitable for SHG. The primary obstacle hindering the production of SHG was the formation of Nb^{4+} as a result of oxygen loss over the course of the reaction. A significant lithium deficiency has worsened the problem because the reduced $LiNbO_3$ can no longer be reoxidized to become SHG-active. The key changes that need to take place in order to correct the both these compositional problems are a reduction in the reaction temperature and in the reaction time. A reduction in temperature permits the use of TPPO without worry for its combustion drawing lithium and oxygen resources from the surface of the synthesized $LiNbO_3$. Even if a small amount of combustion is occurring, the effect can be limited by a short reaction time. The

only method of accomplishing both of these changes in the solution-phase synthesis of $LiNbO_3$ is to explore alternative precursors. One potential precursor that was discussed in this Chapter is $LiNbO(O\text{-}2,6\text{-}PhMe_2)_4 \bullet 3THF$, and it appears to meet all of the desired criteria. Work is currently underway to synthesize this compound in our laboratory.

As a secondary goal, the future solution-phase synthesis of $LiNbO_3$ would preferably produce a crystal morphology with an emphasis in the *a*- and *b*- unit cell directions. The nonlinear coefficient that is most relevant in the production of SHG is the d_{33} coefficient that will produce a second harmonic travelling in the *a*- or *b*-axis direction. The optimum SHG response is, therefore, achieved if the direction of anisotropy corresponds with the direction of propagation for the second harmonic. To influence *a*- or *b*-axis growth, it was suggested in this Chapter that the directed aggregation of nanocrystals along the *c*-axis must first be avoided. This may be accomplished by shortening the reaction time required for crystallinity through the use of new precursors and by employing a more sterically guarded capping agent to maintain a distance between nanocrystals. Once aggregation is addressed, changes have to be made to stimulate a kinetic growth regime. This requires a fast rate of monomer production and a selective capping agent at a suitable concentration to expose the required low energy planes. Temperature will play a key role in determining the extent to which a given plane is exposed by regulating the surface binding equilibrium of the capping agent.

The current solution-phase synthesis of $LiNbO_3$ was chosen because the adjustable reaction parameters are attractive to the production of a tunable crystal morphology. If the rate of monomer production required to produce *a*- or *b*-plane anisotropy is still unachievable, a new method should be explored. Notably, the current method may be coupled with a reaction bomb in a non-aqueous hydrothermal process that is similar to Niederberger *et al.* except a capping agent would be employed.[42] The benefit provided by this route is that temperature increases can be substituted with pressure, and lower reaction temperatures should avoid the current compositional challenges. Higher reaction pressures should support the formation of dense products from the decomposed precursor, and therefore facilitate the formation of crystalline solids despite the lower reaction temperatures. A hydrothermal process may still pose challenges. For example, if the decomposition mechanism involves an equilibrium step with gaseous products, the higher pressures of the hydrothermal process may act to hinder product formation. To avoid this obstacle, pressure can be adjusted by exploring different head-space volumes in the reaction bomb. Whether or not the synthesis of $LiNbO_3$ nanocrystals proceeds by the solution-phase synthesis or follows a new route, by incorporating a reaction bomb, challenges will be met. The compensation for this effort may prove to be the development of a new aid for the difficulties that face tissue imaging.

REFERENCE LIST

(1) Campagnola, P. J.; Millard, A. C.; Terasaki, M.; Hoppe, P. E.; Malone, C. J.; Mohler, W. A. *Biophys. J.* **2002**, *82*, 493-508.

(2) Zoumi, A.; Yeh, A.; Tromberg, B. J. *Proc. Nat. Acad. Sci. U.S.A.* **2002**, *99*, 11014-11019.

(3) Larson, D. R.; Zipfel, W. R.; Williams, R. M.; Clark, S. W.; Bruchez, M. P.; Wise, F. W.; Webb, W. W. *Science* **2003**, *300*, 1434-1436.

(4) Bonacina, L.; Mugnier, Y.; Courvoisier, F.; Le Dantec, R.; Extermann, J.; Lambert, Y.; Boutou, V.; Galez, C.; Wolf, J. P. *Appl. Phys. B* **2007**, *87*, 399-403.

(5) Bruchez, M.; Moronne, M.; Gin, P.; Weiss, S.; Alivisatos, A. P. *Science* **1998**, *281*, 2013-2016.

(6) Murray, C. B.; Norris, D. J.; Bawendi, M. G. *J. Am. Chem. Soc.* **1993**, *115*, 8706-8715.

(7) Cho, S. J.; Maysinger, D.; Jain, M.; Roder, B.; Hackbarth, S.; Winnik, F. M. *Langmuir* **2007**, *23*, 1974-1980.

(8) Chang, E.; Thekkek, N.; Yu, W. W.; Colvin, V. L.; Drezek, R. *Small* **2006**, *2*, 1412-1417.

(9) Campagnola, P. J.; Loew, L. M. *Nat. Biotechnol.* **2003**, *21*, 1356-1360.

(10) Abe, S.; Kajikawa, K. *Phys. Rev. B: Condens. Matter* **2006**, *74*, 035416.

(11) Campagnola, P. J.; Wei, M. D.; Lewis, A.; Loew, L. M. *Biophys. J.* **1999**, *77*, 3341-3349.

(12) Gu, M.; Fu, L. *Opt. Expr.* **2006**, *14*, 1175-1181.

(13) Lin, M.-G.; Yang, T.-L.; Chiang, C.-T.; Kao, H.-C.; Lee, J.-N.; Lo, W.; Jee, S.-H.; Chen, Y.-F.; Dong, C.-Y.; Lin, S.-J. *J. Biomed. Opt.* **2006**, *11*, 064006.

(14) Cao, L.; Panoiu, N. C.; Osgood, R. M. *Phys. Rev. B* **2007**, *75*, 205401-205407.

(15) Hubert, C.; Billot, L.; Adam, P. M.; Bachelot, R.; Royer, P.; Grand, J.; Gindre, D.; Dorkenoo, K. D.; Fort, A. *Appl. Phys. Lett.* **2007**, *90*, 181105-181107.

(16) Zavelani-Rossi, M.; Celebrano, M.; Biagioni, P.; Polli, D.; Finazzi, M.; Duo, L.; Cerullo, G.; Labardi, M.; Allegrini, M.; Grand, J.; Adam, P. M. *Appl. Phys. Lett.* **2008**, *92*, 093119.

(17) McMahon, M. D.; Ferrara, D.; Bowie, C. T.; Lopez, R.; Haglund, R. F. *Appl. Phys. B* **2007**, *87*, 259-265.

(18) Nakayama, Y.; Pauzauskie, P. J.; Radenovic, A.; Onorato, R. M.; Saykally, R. J.; Liphardt, J.; Yang, P. D. *Nature* **2007**, *447*, 1098-1101.

(19) Chan, S. W.; Barille, R.; Nunzi, J. M.; Tam, K. H.; Leung, Y. H.; Chan, W. K.; Djurisic, A. B. *Appl. Phys. B* **2006**, *84*, 351-355.

(20) Zhao, Q. R.; Zhu, X.; Bai, X.; Fan, H. H.; Xie, Y. *Eur. J. Inorg. Chem.* **2007**, *2007*, 1829-1834.

(21) Le Xuan, L.; Zhou, C.; Slablab, A.; Chauvat, D.; Roch, J. F. *Ann. Phys.* **2007**, *32*, 99-101.

(22) Risk, W. P.; Gosnell, T. R.; Nurmikko, A. V. *Compact Blue-Green Lasers*; Cambridge University Press: New York, 2003.

(23) Koechner, W.; Bass, M. *Solid-State Lasers: A Graduate Text*; Springer-Verlag New York Inc.: New York, 2003.

(24) Baldwin, G. C. *An Introduction to NONLINEAR OPTICS*; Plenum Press: New York, 1969.

(25) Boyd, R. W. *Nonlinear Optics*; 2nd ed.; Academic Press: San Diego, 2003.

(26) Byer, R. L. *Parametric Oscillators and Nonlinear Materials*; Academic Press Inc.: San Francisco, 1977.

(27) Weber, M. J. (ed.) *Handbook of Optical Materials*; CRC Press LLC: Boca Raton, 2003; Vol. III: Optical Materials.

(28) Weis, R. S.; Gaylord, T. K. *Appl. Phys. A* **1985**, *37*, 191-203.

(29) Dougherty, J. P.; Kurtz, S. K. *J. Appl. Cryst.* **1976**, *9*, 145-158.

(30) Teyssier, J.; Le Dantec, R.; Galez, C.; Mugnier, Y.; Bouillot, J.; Plenet, J. C. *J. Non-Cryst. Solids* **2004**, *341*, 152-156.

(31) Zhang, H.; Wang, X. M.; Zhang, K. C.; Teo, B. K. *J. Solid State Chem.* **2000**, *152*, 191-198.

(32) Finazzi, M.; Biagioni, P.; Celebrano, M.; Duo, L. *Phys. Rev. B* **2007**, *76*, 125414-125421.

(33) Alford, W. J.; Smith, A. V. *J. Opt. Soc. Am. B: Opt. Phys.* **2001**, *18*, 524-533.

(34) Bonacina, L.; Mugnier, Y.; Courvoisier, F.; Le Dantec, R.; Extermann, J.; Lambert, Y.; Boutou, V.; Galez, C.; Wolf, J. P. *Appl. Phys. B* **2007**, *87*, 399-403.

(35) Iyi, N.; Kitamura, K.; Izumi, F.; Yamamoto, J. K.; Hayashi, T.; Asano, H.; Kimura, S. *J. Solid State Chem.* **1992**, *101*, 340-352.

(36) Please see the calculation section of this paper for further information regarding the formulation of these values.

(37) Boysen, H.; Altorfer, F. *Acta Crystallogr.* **1994**, *B50*, 405-414.

(38) Kong, L. B.; Zhang, T. S.; Ma, J.; Boey, F. *Prog. Mater Sci.* **2008**, *53*, 207-322.

(39) Ono, S.; Hirano, S. *J. Am. Ceram. Soc.* **1997**, *80*, 2533-2540.

(40) Zhao, L. L.; Steinhart, M.; Yosef, M.; Lee, S. K.; Schlecht, S. *Sens. Actuators, B* **2005**, *109*, 86-90.

(41) Kominami, H. *Catal. Today* **1993**, *16*, 309-317.

(42) Niederberger, M.; Pinna, N.; Polleux, J.; Antonietti, A. *Angew. Chem. Int. Ed.* **2004**, *43*, 2270-2273.

(43) Liu, M. N.; Xue, D. F. *J. Phys. Chem. C* **2008**, *112*, 6346-6351.

(44) Park, J.; Joo, J.; Kwon, S. G.; Jang, Y.; Hyeon, T. *Angew. Chem. Int. Ed.* **2007**, *46*, 4630-4660.

(45) Jun, Y. W.; Choi, J. S.; Cheon, J. *Angew. Chem. Int. Ed.* **2006**, *45*, 3414-3439.

(46) Lamer, V. K.; Dinegar, R. H. *J. Am. Chem. Soc.* **1950**, *72*, 4847-4854.

(47) Wood, B. D.; Mocanu, V.; Gates, B. D. *Adv. Mater.* **2008**, *20*, 4552-4556.

(48) Peng, X. G. *Adv. Mater.* **2003**, *15*, 459-463.

(49) Yin, M.; Willis, A.; Redl, F.; Turro, N. J.; O'Brien, S. P. *J. Mater. Res.* **2004**, *19*, 1208-1215.

(50) Xia, Y. N.; Yang, P. D.; Sun, Y. G.; Wu, Y. Y.; Mayers, B.; Gates, B.; Yin, Y. D.; Kim, F.; Yan, Y. Q. *Adv. Mater.* **2003**, *15*, 353-389.

(51) Jun, Y. W.; Lee, J. H.; Choi, J. S.; Cheon, J. *J. Phys. Chem. B* **2005**, *109*, 14795-14806.

(52) Seo, J. W.; Jun, Y. W.; Ko, S. J.; Cheon, J. *J. Phys. Chem. B* **2005**, *109*, 5389-5391.

(53) Murray, C. B.; Sun, S. H.; Gaschler, W.; Doyle, H.; Betley, T. A.; Kagan, C. R. *IBM J. Res. Dev.* **2001**, *45*, 47-56.

(54) Park, J.; An, K. J.; Hwang, Y. S.; Park, J. G.; Noh, H. J.; Kim, J. Y.; Park, J. H.; Hwang, N. M.; Hyeon, T. *Nat. Mater.* **2004**, *3*, 891-895.

(55) Manna, L.; Milliron, D. J.; Meisel, A.; Scher, E. C.; Alivisatos, A. P. *Nat. Mater.* **2003**, *2*, 382-385.

(56) Tang, J.; Fabbri, J.; Robinson, R. D.; Zhu, Y. M.; Herman, I. P.; Steigerwald, M. L.; Brus, L. E. *Chem. Mater.* **2004**, *16*, 1336-1342.

(57) Vioux, A. *Chem. Mater.* **1997**, *9*, 2292-2299.

(58) Yanovskaya, M. I.; Turevskaya, E. P.; Leonov, A. P.; Ivanov, S. A.; Kolganova, N. V.; Stefanovich, S. Y.; Turova, N. Y.; Venevtsev, Y. N. *J. Mater. Sci.* **1988**, *23*, 395-399.

(59) Johns, I. B.; Smith, J. O.; McElhill, E. A. *Ind. Eng. Chem. Prod. Res. Dev.* **1962**, *1*, 2-6.

(60) Joo, J.; Yu, T.; Kim, Y. W.; Park, H. M.; Wu, F. X.; Zhang, J. Z.; Hyeon, T. *J. Am. Chem. Soc.* **2003**, *125*, 6553-6557.

(61) Trentler, T. J.; Denler, T. E.; Bertone, J. F.; Agrawal, A.; Colvin, V. L. *J. Am. Chem. Soc.* **1999**, *121*, 1613-1614.

(62) Hyeon, T.; Lee, S. S.; Park, J.; Chung, Y.; Bin Na, H. *J. Am. Chem. Soc.* **2001**, *123*, 12798-12801.

(63) Park, J.; Lee, E.; Hwang, N. M.; Kang, M. S.; Kim, S. C.; Hwang, Y.; Park, J. G.; Noh, H. J.; Kini, J. Y.; Park, J. H.; Hyeon, T. *Angew. Chem. Int. Ed.* **2005**, *44*, 2872-2877.

(64) Pinna, N.; Niederberger, M. *Angew. Chem. Int. Ed.* **2008**, *47*, 5292-5304.

(65) Miller, R. C.; Nordland, W. A.; Bridenbaugh, P. M. *J. Appl. Phys.* **1971**, *42*, 4145-4147.

(66) Kim, C. D.; Joo, G. T.; Kim, H. G. *Jpn. J. Appl. Phys., Part 1* **1997**, *36*, 5555-5557.

(67) Jun, Y. W.; Casula, M. F.; Sim, J. H.; Kim, S. Y.; Cheon, J.; Alivisatos, A. P. *J. Am. Chem. Soc.* **2003**, *125*, 15981-15985.

(68) Bannister, E.; Cotton, F. A. *J. Chem. Soc.* **1960**, 2276-2280.

(69) Brown, D.; Easey, J. F.; du Preez, J. G. H. *J. Chem. Soc.* **1966**, *A*, 258-261.

(70) Deacon, G. B.; Green, J. H. S. *Spectrochim. Acta* **1968**, *A24*, 845-852.

(71) Deacon, G. B.; Green, J. H. S. *Spectrochim. Acta* **1969**, *A25*, 355-364.

(72) Lorenz, J. K.; Ellis, A. B. *J. Am. Chem. Soc.* **1998**, *120*, 10970-10975.

(73) Park, J.; Kang, E.; Son, S. U.; Park, H. M.; Lee, M. K.; Kim, J.; Kim, K. W.; Noh, H. J.; Park, J. H.; Bae, C. J.; Park, J. G.; Hyeon, T. *Adv. Mater.* **2005**, *17*, 429-434.

(74) Wood, B. D.; Gates, B. D. *Mater. Res. Soc. Symp. Proc.* **2008**, *1087V*.

(75); Program Release 5.0.36; Materials Data, Inc.: Livermore, CA, USA, 1995, XRD powder indexing software.

(76) Kamienski, C. W.; Lewis, D. H. *J. Org. Chem.* **1965**, *30*, 3498-3504.

(77) Kahn, J. D.; Haag, A.; Schleyer, P. V. *J. Phys. Chem.* **1988**, *92*, 212-220.

(78) During the initial syntheses of lithium isopropoxide the isolated powder was red in color. Due to its success in precursors for the preparation of lithium niobate, it has since been referred to as "super-red".

(79) Boyle, T. J.; Alam, T. M.; Peters, K. P.; Rodriguez, M. A. *Inorg. Chem.* **2001**, *40*, 6281-6286.

(80) Mehring, M.; Berkei, M.; Schurmann, M. *Z. Anorg. Allg. Chem.* **2002**, *628*, 1975-1978.

(81) Lambert, C.; Hampel, F.; Schleyer, P. V.; Davidson, M. G.; Snaith, R. *J. Organomet. Chem.* **1995**, *487*, 139-141.

(82) Wheatley, A. E. H. *Chem. Soc. Rev.* **2001**, *30*, 265-273.

(83) Cambridge Isotope Laboratories supplied 99.5% d6-benzene for this experiment. The solvent was dried prior to use with oven-dried type 5A molecular sieves, but trace moisture is expected to be present. The concentration of moisture is relatively low with respect to the concentration of the analyte such that hydrolysis products should only appear in trace quantities.

(84) Davies, J. E.; Kopf, J.; Weiss, E. *Acta Cryst.* **1982**, *B38*, 2251-2253.

(85) Mehrotra, R. C.; Singh, A.; Sogani, S. *Chem. Soc. Rev.* **1994**, *23*, 215-225.

(86) Suyama, Y.; Nagasawa, M. *J. Am. Ceram. Soc.* **1994**, *77*, 603-605.

(87) Veith, M.; Mathur, S.; Lecerf, N.; Huch, V.; Decker, T.; Beck, H. P.; Eiser, W.; Haberkorn, R. *J. Sol-Gel Sci. Technol.* **2000**, *17*, 145-158.

(88) Ritter, J. J.; Roth, R. S.; Blendell, J. E. *J. Am. Ceram. Soc.* **1986**, *69*, 155-162.

(89) Borup, B.; Samuels, J. A.; Streib, W. E.; Caulton, K. G. *Inorg. Chem.* **1994**, *33*, 994-996.

(90) Bradley, D. C.; Chakravarti, B. N.; Wardlaw, W. *J. Chem. Soc.* **1956**, 2381-2384.

(91) Bradley, D. C.; Chakravarti, B. N.; Chatterjee, A. K.; Wardlaw, W.; Whitley, A. *J. Chem. Soc.* **1958**, 99-101.

(92) Hall, H. K. *J. Am. Chem. Soc.* **1957**, *79*, 5441-5444.

(93) Speer, R. J. *J. Org. Chem.* **1949**, *14*, 655-659.

(94) Kraus, W.; Nolze, G.; Version 2.4 ed. Berlin, Germany, 2000.

(95) Eichorst, D. J.; Payne, D. A. *Mat. Res. Symp. Proc.* **1990**, *180*, 669-673.

(96) Shinichi, H. *Adv. Ceram. Mater.* **1987**, *2*, 142-145.

(97) Bradley, D. C.; Holloway, C. E. *J. Chem. Soc.* **1968**, *A*, 219-223.

(98) Eichorst, D. J.; Payne, D. A.; Wilson, S. R.; Howard, K. E. *Inorg. Chem.* **1990**, *29*, 1458-1459.

(99) Antipin, M. Y.; Starikova, Z. A.; Yanovskii, A. I.; Dolgushin, F. M.; Lysenko, K. A.; Khrustalev, V. N.; Vorontsov, II; Korlyukov, A. A.; Andreev, G. B.; Neretin, I. S. *Russ. J. Coord. Chem.* **2001**, *27*, 221-258.

(100) Mehrotra, R. C.; Kapoor, P. N. *J. Less-Common Met.* **1966**, *10*, 354-361.

(101) Lappert, M. F. *Chem. Rev.* **1956**, *56*, 959-1064.

(102) Scattergood, A.; Miller, W. H.; Gammon, J. *J. Am. Chem. Soc.* **1945**, *67*, 2150-2152.

(103) Kuivila, H. G.; Slack, S. C.; Siiteri, P. K. *J. Am. Chem. Soc.* **1951**, *73*, 123-124.

(104) Steinberg, H. *Organoboron Chemistry*; John Wiley & Sons Inc.: London, 1964; Vol. 1 - Boron-oxygen and Boron-sulfur Compounds.

(105) Mehrotra, R. C.; Rai, A. K. *Indian J. Chem.* **1966**, *4*, 537-539.

(106) Suzuki, H. (ed.); Matano, Y. (ed.) *Organobismuth Chemistry*; 1 ed.; Elsevier: Amsterdam, 2001.

(107) Goel, S. C.; Hollingsworth, J. A.; Beatty, A. M.; Robinson, K. D.; Buhro, W. E. *Polyhedron* **1998**, 781-790.

(108) Veith, M.; Mathur, S.; Mathur, C. *Polyhedron* **1998**, *17*, 1005-1034.

(109) Mehrotra, R. C.; Agrawal, M. M.; Kapoor, P. N. *J. Chem. Soc. A* **1968**, 2673-2676.

(110) Turevskaya, E. P.; Turova, N. Y.; Korolev, A. V.; Yanovsky, A. I.; Struchkov, Y. T. *Polyhedron* **1995**, *14*, 1531-1542.

(111) Hirano, S.; Hayashi, T.; Nosaki, K.; Kato, K. *J. Am. Ceram. Soc.* **1989**, *72*, 707-709.

(112) Kessler, V. G.; Shevelkov, A. V.; Bengtsson-Kloo, L. A. *Polyhedron* **1998**, *17*, 965-968.

(113) Gleizes, A. N. *Chem. Vap. Deposition* **2000**, *6*, 155-173.

(114) Leite, E. R.; Vila, C.; Bettini, J.; Longo, E. *J. Phys. Chem. B* **2006**, *110*, 18088-18090.

(115) Lenzmann, F.; Krueger, J.; Burnside, S.; Brooks, K.; Gratzel, M.; Gal, D.; Ruhle, S.; Cahen, D. *J. Phys. Chem. B* **2001**, *105*, 6347-6352.

(116) George, P. P.; Pol, V. G.; Gedanken, A. *Nanoscale Res. Lett.* **2007**, *2*, 17-23.

(117) Pinna, N.; Antonietti, M.; Niederberger, M. *Colloid. Surface. A* **2004**, *250*, 211-213.

(118) Hyodo, T.; Ohoka, J.; Shimizu, Y.; Egashira, M. *Sens. Actuators, B* **2006**, *117*, 359-366.

(119) Frevel, L. K.; Rinn, H. W. *Anal. Chem.* **1955**, *27*, 1329-1330.

(120) Terao, N. *Jpn. J. Appl. Phys.* **1963**, *2*, 156-174.

(121) Pacholski, C.; Kornowski, A.; Weller, H. *Angew. Chem. Int. Ed.* **2002**, *41*, 1188-1191.

(122) Halder, A.; Ravishankar, N. *Adv. Mater.* **2007**, *19*, 1854-1858.

(123) Yu, J. H.; Joo, J.; Park, H. M.; Baik, S. I.; Kim, Y. W.; Kim, S. C.; Hyeon, T. *J. Am. Chem. Soc.* **2005**, *127*, 5662-5670.

(124) Zhang, X.; Xue, D. F.; Liu, M. N.; Ratajczak, H.; Xu, D. L. *J. Mol. Struct.* **2005**, *754*, 25-30.

(125) Cho, K. S.; Talapin, D. V.; Gaschler, W.; Murray, C. B. *J. Am. Chem. Soc.* **2005**, *127*, 7140-7147.

(126) Lide, D. R. (ed.) *CRC Handbook of Chemistry and Physics (Internet Version)*; 89th Edition ed.; CRC Press/Taylor and Francis: Boca Raton, FL, 2009.

(127) Siekkinen, A. R.; McLellan, J. M.; Chen, J. Y.; Xia, Y. N. *Chem. Phys. Lett.* **2006**, *432*, 491-496.

(128) Steiner, P.; Hochst, H. *Z. Phys. B: Condens. Matter* **1979**, *35*, 51-59.

(129); Version 3.5; National Institute of Standards and Technology: Gaithersburg, 2003, http://srdata.nist.gov/xps/.

(130) Lerner, P.; Legras, C.; Dumas, J. P. *J. Cryst. Growth* **1968**, *3/4*, 231-235.

(131) Liu, M. N.; Xue, D. F.; Zhang, S. C.; Zhu, H. Y.; Wang, J. Y.; Kitamura, K. *Mater. Lett.* **2005**, *59*, 1095-1097.

(132) Chen, Y. L.; Zhang, W. L.; Shu, Y. C.; Lou, C. B.; Kong, Y. F.; Huang, Z. H.; Xu, J. J.; Zhang, G. Y. *Opt. Mater.* **2003**, *23*, 295-298.

(133) Schlarb, U.; Klauer, S.; Wesselmann, M.; Betzler, K.; Wohlecke, M. *Appl. Phys. A* **1993**, *56*, 311-315.

(134) Peterson, G. E.; Carruthers, J. R. *J. Solid State Chem.* **1969**, *1*, 98-99.

(135) Carruthers, J. R.; Peterson, G. E.; Grasso, M.; Bridenbaugh, P. M. *J. Appl. Phys.* **1971**, *42*, 1846-1851.

(136) Xia, H. R.; Sun, S. Q.; Cheng, X. F.; Dong, S. M.; Xu, H. Y.; Gao, L.; Cui, D. L. *J. Appl. Phys.* **2005**, *98*, 033513-033516.

(137) Courths, R.; Steiner, P.; Hochst, H.; Hufner, S. *Appl. Phys.* **1980**, *21*, 345-352.

(138) Fay, H.; Alford, W. J.; Dess, H. M. *Appl. Phys. Lett.* **1968**, *12*, 89-92.

(139) Atuchin, V. V.; Kalabin, I. E.; Kesler, V. G.; Pervukhina, N. V. *J. Electron. Spectrosc. Relat. Phenom.* **2005**, *142*, 129-134.

(140) Chab, V.; Kubatova, J. *Applied Physics a-Materials Science & Processing* **1986**, *39*, 67-71.

(141) Rauber, A. *Chemistry and Physics of Lithium Niobate*; North-Holland Publishing Company, 1978; Vol. 1.

(142) Shannon, R. D.; Prewitt, C. T. *Acta Crystallogr. B* **1969**, *25*, 925-946.

(143) Maury, F. *J. Phys. IV* **1995**, *5*, 449-463.

(144) Park, S. K.; Koo, S. M.; Lee, Y. E. *Polyhedron* **2000**, *19*, 1037-1041.

(145) Park, S. K.; Park, J. W.; Koo, S. M. *J. Ceram. Process. Res.* **2001**, *2*, 21-26.

(146) Bordui, P. F.; Jundt, D. H.; Standifer, E. M.; Norwood, R. G.; Sawin, R. L.; Galipeau, J. D. *J. Appl. Phys.* **1999**, *85*, 3766-3769.

(147) Luo, C.; Xue, D. F. *Langmuir* **2006**, *22*, 9914-9918.

(148) An, C. H.; Tang, K. B.; Wang, C. R.; Shen, G. Z.; Jin, Y.; Qian, Y. T. *Mater. Res. Bull.* **2002**, *37*, 1791-1796.

(149) Liu, M. N.; Xue, D. F. *Mater. Lett.* **2005**, *59*, 2908-2910.

(150) Chien, C. H.; Chang, Y. H.; Tsai, C. P.; Peng, C. W.; Wang, L. S.; Sheng, P. S.; Lee, C. Y.; Chiu, H. T. *J. Chin. Chem. Soc.* **2006**, *53*, 287-292.

(151) Bouquet, V. L., E.; Leite, E. R.; Varela, J. A. *J. Mater. Res.* **1999**, *14*, 3115-3121.

(152) Bouquet, V.; Bernardi, M. I. B.; Zanetti, S. M.; Leite, E. R.; Longo, E.; Varela, J. A.; Viry, M. G.; Perrin, A. *J. Mater. Res.* **2000**, *15*, 2446-2453.

(153) Simoes, A. Z.; Zaghete, M. A.; Stojanovic, B. D.; Riccardi, C. S.; Ries, A.; Gonzalez, A. H.; Varela, J. A. *Mater. Lett.* **2003**, *57*, 2333-2339.

(154) Simoes, A. Z.; Zaghete, M. A.; Stojanovic, B. D.; Gonzalez, A. H.; Riccardi, C. S.; Cantoni, M.; Varela, J. A. *J. Eur. Ceram. Soc.* **2004**, *24*, 1607-1613.

(155) Dey, D.; Kakihana, M. *J. Ceram. Soc. Jpn.* **2004**, *112*, 368-372.

(156) Cheng, Z. X.; Ozawa, K.; Miyazaki, A.; Kimura, H. *J. Am. Ceram. Soc.* **2005**, *88*, 1023-1025.

(157) Wang, L. H.; Yuan, D. R.; Duan, X. L.; Wang, X. Q.; Yu, F. P. *Cryst. Res. Technol.* **2007**, *42*, 321-324.

(158) Lanfredi, S.; Folgueras-Domingueza, S.; Rodrigues, A. C. M. *J. Mater. Chem.* **1995**, *5*, 1957-1961.

(159) Hur, N. H.; Park, Y. K.; Won, D. H.; No, K. S. *J. Mater. Res.* **1994**, *9*, 980-985.

(160) Zeng, H. C.; Tung, S. K. *Chem. Mater.* **1996**, *8*, 2667-2672.

(161) Ono, S.; Hirano, S. *J. Am. Ceram. Soc.* **1997**, *80*, 2869-2875.

(162) Ono, S.; Hirano, S. I. *J. Ceram. Soc. Jpn.* **2007**, *115*, 801-807.

(163) Rao, A. V. P.; Paik, D. S.; Komarneni, S. *J. Electroceram.* **1998**, *2*, 157-162.

(164) Ono, S.; Hirano, S. *J. Mater. Res.* **2001**, *16*, 1155-1162.

(165) Hreniak, D.; Strek, W.; Speghini, A.; Bettinelli, M.; Boulon, G.; Guyot, Y. *Appl. Phys. Lett.* **2006**, *88*, 161118-161120.

(166) Hreniak, D.; Speghini, A.; Bettinelli, M.; Strek, W. *J. Lumin.* **2006**, *119*, 219-223.

(167) Steinhart, M.; Wehrspohn, R. B.; Gosele, U.; Wendorff, J. H. *Angew. Chem. Int. Ed.* **2004**, *43*, 1334-1344.

(168) Zhao, L. L.; Steinhart, M.; Yosef, M.; Lee, S. K.; Geppert, T.; Pippel, E.; Scholz, R.; Gosele, U.; Schlecht, S. *Chem. Mater.* **2005**, *17*, 3-5.

(169) Chadwick, A. V.; Savin, S. L. P.; O'Dell, L. A.; Smith, M. E. *J. Phys.: Condens. Matter* **2006**, *18*, L163-L170.

(170) Edwards, G. J.; Lawrence, M. *Opt. Quantum Electron.* **1984**, *16*, 373-375.

APPENDICES

Appendix 1: Tables

Table A1.1 Common materials and their properties with respect to the generation of a second harmonic.

Compound Name and Acronym		Transparency Window (μm)	Effective Nonlinear Coefficients (pm/V)			Tolerances:[b] Δθ (mrad cm) ΔT (oC nm) Δλ (nm cm) ρ (degrees)	Damage Threshold[b] (GW/cm^2 10 ns pulse)
			d_{eff} ($\lambda_{SHG} \approx$ 655 nm)	d_{eff} ($\lambda_{SHG} \approx$ 535 nm)	d_{eff} ($\lambda_{SHG} \approx$ 490 nm)		
Lithium Niobate	LN	0.3-5.0 [o]	4.05 [c] 3.7 [d]	5.9 [e] 4.4 [d]	6.3 [d]	Δθ = 33 [r] ΔT = 0.75 [r] Δλ = 0.31 [r] ρ = 0 [r]	≤ 0.04 [g] 0.3 [s]
Potassium Niobate	KN	0.4-4.5 [o] 0.4-5.5 [r]	10.7 [d] 5.00 [c]	13.8 [d] ≤ 20 [g]	8.62 [c]	Δθ = 9 [r] ΔT = 17 [r] Δλ = 0.46 [r] ρ = 0 [r]	≤ 0.4 [g] >7 [s]
Lithium Iodate	$LiIO_3$	0.38-5.5 [o] 0.28-6.0 [h]	1.83 [c]	4.1 [d,j]	-	Δθ = 0.34 [r] ΔT = 23 r Δλ = 0.82 [r] ρ = 4.3 [r]	0.12 [h] ≤ 0.05 [g]
Potassium Dihydrogen Phosphate	KDP	0.18-1.5 [o] 0.17-1.6 [h]	0.23 [c]	0.27 [c] 0.38 [j]	-	Δθ = 0.84 [g] ΔT = 11.5 g Δλ = 10.6 [g]	0.25 [h] 0.4 [g]
Potassium Dideuterium Phosphate	KD*P	0.2-1.5 [h]	-	0.37 [j]	-	Δθ = 2.3 [r] ΔT = 12 [r] Δλ = 5.6 [r] ρ = 1.4 [r]	0.4 [g]
Potassium Titanyl Phosphate	KTP	0.35-4.5 [p]	2.5 [d]	3.8 [d] 3.2 [j] 3.35 [p]	-	Δθ = 9 [r] ΔT = 17 [r] Δλ = 0.46 [r] ρ = 0.27 [r]	0.9 [h] ≤ 1.0 [g]
β-Barium Borate	BBO	0.19-3.5 [h] 0.2-2.6 [r]	1.8 [c] 1.7 [i]	2 [i] 2.2 [j]	2.08 [k]	Δθ = 0.92 [h] ΔT = 37.1 [h] Δλ = 2.1 [h] ρ = 3.2	5 [h] ≤ 5 [g]
Lithium Triborate	LBO	0.16-2.6 [g]	-	0.85 [h]	0.92 [k]	Δθ = 72 [s] ΔT = 3.9 [s] Δλ = 3.6 [s] ρ = 0 [s]	>0.9 [k] ≤ 10 [g]
Lithium Tetraborate	LTB	0.17-3.5 [h]	-	0.07 [h]	-	Δθ = 0.05 [h] ΔT = 21 [h]	40 [h]
Bismuth Borate	BiBO	0.3-2.5 [o]	-	3.2 [l]	-	Δθ = 0.92 [h] ρ = 3.2	High

[a] All nonlinear coefficient values are based on a type I (o + o → e) SHG processes but include both critically and noncritically phasematched crystals. The SHG wavelength is approximately ± 5 nm so that more laser lines could be incorporated in a single column of this table.
[b] Tolerances and damage thresholds are according to use of a 1064 nm laser for SHG.
[c] Alford, W. J.; Smith, A. V.; *J. Opt. Soc. Am. B* **2001**, *18*, 524.
[d] Shoji, I.; Kondo, T.; Kitamoto, A.; Shirane, M.; Ito, R.; *J. Opt. Soc. Am. B* **1997**, *14*, 2268.

[e] Klein, R. S.; Kugel, G. E.; Maillard, A.; Polgar, K.; Peter, A.; *Opt. Mat.* **2003**, 22, 171.
[g] Lin, J. T.; *Opt. Quantum Electron.* **1990**, *22*, S283.
[h] Becker, P.; *Adv. Mater*. **1998**, *10*, 979.
[i] Shoji, I.; Nakamura, H.; Ohdaira, K.; Kondo, T.; Ito, R.; Okamoto, T.; Tatsuki, K.; Kubota, S.; *J. Opt. Soc. Am. B* **1999**, *16*, 620
[j] Eckardt, R. C.; Byer, R. L.; *Proc. SPIE* **1991**, *1561*, 119.
[k] Kellner, T.; Heine, F.; Huber, G.; *Appl. Phys. B*, **1997**, *65*, 789.
[l] Chen, C.; Wu, Y.; Jiang, A.; Wu, B.; You, G.; Li, R.; Lin, S.; *J. Opt. Soc. Am. B*, **1989**, 6, 616.
[o] Weber, Marvin J; *Handbook of Optical Materials*, CRC Press LLC, New York, **2003**.
[p] Bierlein, J. D.; Vanherzeele, H.; *J. Opt. Soc. Am. B*, **1989**, *6*, 622.
r Boulanger, B.; Zyss, J.; *Nonlinear Coefficients*. In: Authier, A.; *International Tables for Crystallography* **2006**, *D*, ch. 1.7, pp. 212-214.
s Fejer, M; Bordui, P. F.; *Annu. Rev. Mater. Sci.* **1993**, *23*, 321.

Table A1.2 A comprehensive summary of the methods and methodologies that have been applied to synthesize nanocrystals of $LiNbO_3$. A list of acronyms applied in this table can be found at the very end of the table.

Method	*Year*	*Description*	*Crystal Specifics*	*Ref.*
Hydrothermal (non-aqueous)	1993	1) add $Nb(OBu^n)_5$ and LiOAc to BG in a sealed autoclave 2) heat at 300 ^oC for 2 h	0.7-1.5 um, elliptically shaped	41
	2004	1) add Li to benzyl alcohol 2) add lithiated benzyl alcohol to $Nb(OEt)_5$ in a sealed autoclave 3) heat at 220 ^oC for 4 d	20-60 nm, PD, prism-like crystals, independent	42
Hydrothermal (aqueous/non-aqueous)	2006	1) digest Nb_2O_5 in HF solution 2) precipitate $Nb(OH)_5$ with NH_4OH, filter and wash 3) Add precipitate to LiOH solution and EG in a sealed autoclave 4) Add CTAB or SDS (optional) 5) heat 200-250 ^oC for 3-5 d	100 nm PC, MD hollow spheres	147
Hydrothermal (aqueous)	2002	1) add LiOH solution to Nb_2O_5 in a sealed autoclave 2) heat 250 ^oC for 5-10 h	10-400 nm, PD, spherically shaped	148
	2005	1) dissolve Li_2CO_3 in OA solution 2) add to Nb_2O_5 in a sealed autoclave 3) heat 340 ^oC for 10 h	0.4-2.1 um cubic shaped crystals	149
	2008	1) digest Nb_2O_5 in HF solution 2) precipitate $Nb(OH)_5$ with NH_4OH, filter and wash 3) Add precipitate to LiOH solution in a sealed autoclave 4) Add small amount of ED, BA^n, TEA, or EA to the system 5) heat at 220 ^oC for 1-4 d	0.8 x 3 um PC, MD rods with ED; 0.3 x 1 um PC, MD rods with EA; 1.5-2 um and 0.4 um PC hollow spheres with BA^n and TEA.	43
Miscellaneous	2001	1) add Li to 2,6-dimethylphenol 2) add $NbCl_5$ to THF 3) add Nb solution dropwise to the lithium alkoxide solution 4) Evaporate THF, filter LiCl, evaporate to dryness 5) heat >300 ^oC in air for 3 h	40-50 nm ball-like crystals, appear aggregated	145
	2006	1) dissolve $NbCl_5$ in THF 2) add LiEt and stir 2 h then dry 3) heat 1h under vacuum at 600 ^oC	20-50 nm lightly aggregated, spherical particles, some Nb^{4+}	150
Sol-gel (Pechini method)	1999	1) add citric acid solution to Li_2CO_3 2) add citric acid solution to $Nb(OH)_5$ 3) mix Li and Nb-citrates with EG 4) dip coat film on substrate 5) sinter 400-900 ^oC in air 2-3 h	Size from ~20 to 500 nm with an increase in temperature, fairly spherical and highly aggregated	151
	2000			152
	2003	1) mix Li_2CO_3 and Nb_2O_5 with citric acid and heat with EG 2) spin coat thin film on substrate 3) heat film 500 ^oC for 3 h	70-100 nm highly fused crystals	153
	2004		40-60 nm highly fused crystals	154

Method	*Year*	*Description*	*Crystal Specifics*	*Ref.*
Sol-gel (peroxide route)	2004	1) hydrated Nb_2O_5 is added to H_2O_2 2) adjust the pH to 11 with NH_4OH 3) add LiOH solution 4) 30 min mixing then 10min at 70°C 5) wash and dry the precipitate 6) sinter 2 h in air at 400-600 °C	0.1-0.4 um spherical crystals, aggregated	155
	2005	1) add $Nb(OEt)_5$ and LiOEt to EtOH 2) add H_2O_2 with vigorous stirring 3) heat at 100°C for several hours 4) treat excess H_2O_2 with Pt foil 5) concentrate to dryness and sinter at 500 °C for several hours	60 nm highly fused crystal grains	156
	2007	1) $NbCl_5$ and LiOAc refluxed in H_2O_2 2) mix with CA to form a gel 3) dry gel for 15 h at 60 °C 4) sinter 500-700 °C for 5-6 h	40-60 nm spherical crystals lightly fused 100-200 nm at higher temperature	157
Sol-gel (oxalate route)	1995	1) add $LiNO_3$ to OA solution 2) adjust pH to 3 with NH_4OH 3) add $NH_4H_2[NbO(C_2O_4)_3]$ 4) heat 3 h at 80 °C, then dry 70 °C 5) grind and sinter 450-550 °C 5 h	88 nm fused crystals	158
Sol-gel (hydrolyzed alkoxide)	1988	1) dissolve LiOEt and $Nb(OEt)_5$ in EtOH and reflux >20 h 2) add NH_4OH solution 3) distill off solvent and dry powder 4) heat 500 °C in air 30 min	10-20 nm fused crystals with isotropic shape	58
	1994	1) dissolve $LiOPr^i$ and $Nb(OPr^i)_5$ in MeOH and a small amount of H_2O 2) reflux 5 h under Ar 3) spin coat substrate 4) sinter at 500 °C in air for 30min	<1 um fused crystals with isotropic shape	159
	1996	1) add $Nb(OEt)_5$ to i-PrOH and acac 2) add aqueous $LiNO_3$ dropwise 3) allow to gel and then dry over 5 d 4) heat 400 °C 4 h in air	230 nm fused crystal grains with rounded isotropic shape	160
	1997	1) dissolve LiOEt and $Nb(OEt)_5$ in EtOH and reflux >20 h 2) add H_2O to fully hydrolyze 3) add AcOH to neutralize 4) concentrate and coat substrate 5) heat 400-500 °C for 6 h	~20 nm fused crystals with isotropic shape	161,162
	1998	1) dissolve Li acac and $Nb(OEt)_5$ in separate MOE solutions 2) reflux 12 h then combine solutions and reflux for 6 h 3) add H_2O to fully hydrolyze 4) dry and sinter 500 °C for 6 h	60-400 nm	163
Sol-gel (non-hydrolyzed alkoxides)	2001	1) dissolve LiOEt and $Nb(OEt)_5$ in EtOH and reflux >20 h 2) add AcOH and concentrate to gel 3) spin coat or dip substrate 4) heat 500 °C	~40 nm fused crystals with rounded isotropic shape	164
	2006	1) above scheme heat 700 °C 2h	0.1-0.5 um fused spherical crystals	165,166

Method	*Year*	*Description*	*Crystal Specifics*	*Ref.*
Sol-gel (templated)	2004	1) dissolve $Nb(OEt)_5$ in EtOH and phenyl-acac 2) mix in EtOH solution of LiOEt 3) reflux for 24 h 4) add H_2O and reflux 24 h 5) drop solution on Al_2O_3 template 6) heat 550 ^oC for 5 h 7) KOH etch template away	0.1-0.4 um diameter PC, MD tubes	40,167
	2005	1) above scheme using Si template	1 um tubes up to 100 um long	168
	2006	1) add $Nb(OEt)_5$ to LiOEt in EtOH 2) add TEOS and stir to homogenize 3) dry then heat gel at 800 ^oC	44 nm crystals in a SiO_2 matrix	169

Acronyms (listed alphabetically): *Ac* – acetate, *acac* – 2,4-pentanedionate, BA^n – n-butylamine, *BG* – butylene glycol, *CA* – citric acid, *CTAB* – cetyltrimethylammonium bromide, *BG* – butylene glycol, *ED* – ethylenediamine, *EG* – ethylene glycol, *Et* – ethyl, *MD* – monodisperse, *Me* – methyl, *MOE* – 2-methoxyethanol, *OA* – oxalic acid, *PC* – polycrystalline, *PD* – polydisperse, Pr^i – i-propyl, *SDS* – sodium dodecyl sulphate, *TEA* – triethylamine, *THF* – tetrahydrofuran, *TEOS* – tetraethylortho silicate,

Appendix 2: Description of Standard Inert Methodology (SIM)

SIM-A: Creating and Maintaining an Inert Atmosphere

Any apparatus that will be used in an inert reaction and has been assembled outside of the glovebox will require the replacement of O_2 and H_2O (present in air) with purified nitrogen or argon. An inert and dry atmosphere can be created through a series of three evacuation and purge cycles using an attached Schlenk line. The Schlenk line can be attached to the sealed apparatus via a needle adaptor and septum or via a stopcock sidearm and clamp. In a single cycle, vacuum is created in the apparatus for several minutes, then the volume is refilled by purified nitrogen. Following three cycles the atmosphere has been replaced by purified nitrogen and is now suitable for use. When dry joints are being used or the intended reaction is long, a slight positive nitrogen pressure should be maintained following the 3rd cycle to ensure an outward flow at all times from potential leakage sites. The flask or assembly can be opened at this stage given that the N_2 flow rate is high enough to prevent air from entering the opening. Ideal work would employ the use of Ar because it is more dense than air, therefore resisting the intrusion of air through any opening.

SIM-B: Drying and Degassing Solvents for Use in Water and Oxygen Sensitive Reactions

A 1-2 L round-bottom flask is filled to 70 % capacity with a solvent that has already undergone primary dessication with anhydrous $MgSO_4$, $CaCl_2$ or NaOH. A stir-bar and an excess of drying agent is then loaded into the flask. Alcohols

are finely dried with Mg activated with I_2, amines by CaH_2, and hydrocarbons with freshly pressed Na wire. The salts produced in the reaction of the drying agent with water (e.g., $Mg(OH)_2$, $Ca(OH)_2$, and NaOH, respectively) are nonvolatile so they remain in the source flask as the solvent is distilled. An oven or flame dried distillation head is then attached to the ground-glass joint and attached to the Schlenk line. The condenser coil is attached to a cold water line and circulation is started.

The distillation head and solution are submitted to 5 pump and purge cycles as was previously described. Full vacuum is not obtainable due to the volatility of the solvent to be purified. In this case, vacuum is brought to the point of boil and it is recognized by solution degassing. Thereafter, a slight positive pressure of dry nitrogen is maintained during the course of drying. To dry the solvent, it is distilled into the condensing coil where it is returned to the source flask through a two-way stopcock. Typically it is found that the distillates on our common reaction solvents reach the condenser coils with a minimum base temperature of ~220 ^{o}C. Heating is applied through the use of a variac or suitable temperature controller attached to a 380 W heating mantle.

After 24 h, a collecting flask (Schlenk-type) can be attached to the collection arm of the distillation head. The side arm and volume of the attached flask and the collection arm are then required to be evacuated and purged three times with the use of the Schlenk line (SIM-A). A positive N_2 pressure is then maintained on the collection arm as a blow-off valve and the stopcock of the distillation head can be rotated to collect the distilled solvent. Once the collection

flask is 70 % full, the stopcock is rotated back. The Schlenk flask is removed and capped (with a wired sleeve septum) under a vigorous stream of N_2 gas supplied through the side-arm. For optimal results, solvents should be dried and degassed as required in small batches to avoid the need for lengthy storage. Molecular sieves that have been heated under vacuum can be added to the dry solvents and improve the length of time that they remain effectively dry.

SIM-C: The Canula for Transfer

Canula techniques are essential for a number of procedures related to solution transfer including the mixing of two solutions, the measurement of an aliquot, or for filtration under inert conditions. Canula techniques require sleeve septa or sure-seals to be fitted on all the flasks, graduated cylinders, or reagent bottles involved in the transfer. A solution is moved through a canula by a push or pull technique using a simple pressure gradient established by the Schlenk line. The solution is passed through a canula towards an area of lower pressure until the pressure of both sides has been equated.

SIM-D: Filtration Technique

Inert filtrations performed in this work require the use of a filter stick (a tube containing a porous ceramic filter and fitted with male ground glass joints) and a nonreactive filtering agent such as celite (high surface area SiO_2). This process requires that the reaction flask to be filtered is also a Schlenk flask and

works best when this flask is below half its capacity. An ideal filtration of this type would also employ the use of $Ar_{(g)}$ for reasons stated in SIM-A.

The filter stick is removed from the oven and attached immediately to a dry and hot Schlenk flask (collection flask). A volume of celite is loaded to the open end of the filter stick an amount equal to 1-2 times the tube diameter then the assembly is capped with a round bottom flask. SIM-A is performed hereafter using the stopcock of the attached collection flask. Once cycled, a strong dry N_2 pressure is maintained on the filtration assembly. The reaction flask to be filtered can be uncapped once a strong dry N_2 pressure is also applied. The round-bottom flask is then removed from the top of the filter stick assembly. N_2 flow should be rapid out of both the reaction flask and the filtration assembly at this point to maintain the inert condition of both vessels. The flask and filter stick assembly are connected at this stage with the filter stick angled down roughly 10^o to prevent the spillage of solution from the reaction flask. Before lifting the assembly upright, the stopcock of the reaction flask should be closed to prevent solution from entering the Schlenk line. The assembly is then lifted upright slowly so not to disturb the celite excessively. The filtration runs by gravity through the celite, but is accelerated using vacuum applied with the Schlenk line through the stopcock of the collection flask. Once transferred, the assembly can be disassembled, with a strong N_2 flow out of both the filter sick and the flask containing the filtrate. The product flask is capped followed by the filter stick. Depending of the by-product collected in the filter stick a careful ‘neutralization’ may be necessary before the waste can be disposed of.

Appendix 3: Calculations

3.1) Determining Phasematching Conditions for $LiNbO_3$

To assess the necessary phasematching conditions requires knowledge of how temperature and wavelength affect the indicies of refraction for $LiNbO_3$. Dispersion data for $LiNbO_3$ such as this is shown by Edwards and Lawrence[170] to follow the following equations:

$$n_o(T,\lambda) = 4.913 + \frac{117.3x10^3 + 1.65x10^{-2}T^2}{\lambda^2 - \left(212 + 2.17x10^{-5}T^2\right)^2} - 2.78x10^{-8}\lambda^2 \quad (35)$$

$$n_e(T,\lambda) = 4.5567 + 2.605x10^{-7}T^2\,\frac{97x10^3 + 2.7x10^{-2}T^2}{\lambda^2 - \left(201 + 5.4x10^{-5}T^2\right)^2} - 2.24x10^{-8}\lambda^2 \quad (36)$$

The noncritical phasematched temperature for a given laser is calculated by solving the temperature condition where $n_o(\omega) = n_e(2\omega)$ or $n_e(\omega) = n_o(2\omega)$ such that $\Delta n = 0$ in **equation (11)**. The "*solver*" or "*goal seek*" functions in Microsoft Excel facilitate in that calculation.

The critical phasematching angle for a specific laser and temperature is found trigonometrically using an equation provided by Boyd:[25]

$$\sin^2\theta = \frac{n_o(\omega)^2 - n_o(2\omega)^2}{n_e(2\omega)^2 - n_o(2\omega)^2} \quad (37)$$

Solving for θ requires the use of the correct indicies given by **equation (35)** and **(36)** above for the fundamental (ω) and second harmonic (2ω) wavelengths.

3.2) Radius Ratio Calculation for Li and Nb in the $LiNbO_3$ lattice

The minimum radius for a metal, r_M, to occupy an octahedral site is calculated theoretically by considering two hexagonally close-packed layers of anions with a radius of r_A. In an ideal octahedron a square cross-section can be drawn, which is composed of the octahedron center and four of its sides:

the length of a square cross-section:	$a = 2r_A$
the length of the square diagonal:	$\sqrt{2}a = 2r_A + 2r_M$
setting the expressions for *a* equal yields:	$2\sqrt{2}r_A = 2r_A + 2r_M$
simplifying gives:	$\sqrt{2}r_A - r_A = r_M$
dividing through by r_A gives:	$r_M/r_A = \sqrt{2} - 1 = 0.414$

Using the ionic radii of Li^{+}, Nb^{5+}, and O^{2-} from Shannon and Prewitt[142] r_M/r_A can be calculated. The radii of the three ions are 0.74, 0.64, and 1.40 Å, respectively. This gives a radius ratio of 0.53 for lithium and 0.46 for niobium, both > 0.414.

3.3) The Principle of Polyhedral Metal Spacing

For a generic metal *M* and anion *A* in fcc cubic lattice, let the bond length between them be d(M-X) = *L*, and let the distance to the next metal in an adjacent polyhedra be d(M-M) = *D*. If the polyhedra are linked by the following interactions, then D is calculated trigonometrically from L:

corner sharing = metals bridge with 1 connection; D = 2L
edge sharing = metals bridge with 2 connections; geometrically, a box with sides L has a diagonal D = √2L = 1.41 L
face sharing = metals bridge with 3 connections; geometrically, a cube where 1/3 the body diagonal is D; so D = 2(√3)/3 L; D = 1.15L

The result of these calculations show that the space between metals decreases as polyhedra share more atoms.

3.4) Dipole Calculation for Lithium Niobate

Dipole created in Li displacement = 1 q * (1.60218 E-19 C / 1 q) * -0.481E-10 m * (1 D / 3.33564E-30 C m) = -2.31 D (based on data provided by Iyi *et al.*[35])

Dipole created in Nb displacement = 5 q * (1.60218 E-19 C / 1 q) * 0.255E-10 m * (1 D / 3.33564E-30 C m) = 6.12 D

3.5) CHN Analysis of Chemat technologies "$LiNb(OPr^i)_6$"

The analysis found that the compound was 45.65 % C and 9.03 % H by mass.

The molecular weight of the Chemat precursor was unknown but the molecular formula is assumed to be $LiNb(OH)_x(O)_y(OPr^i)_{(6-x-2y)}$. The mass of 1 mol of this precursor is equal to the sum of all the masses (m) of each component:

$$m_{pre.} = (m_{Li}) + (m_{Nb}) + x(m_{OH}) + y(m_O) + (6-x-2y)(m_{OPri})$$
$$= 454.3753 - 42.0806x - 102.177y$$

Based on the above precursor stoichiometry, the mass of hydrogen and carbon in that precursor is then:

$m_H = 7(6-x-2y)(1.00794) + 1(x)(1.00794) = (42-6x-14y)(1.00794)$
$m_C = 3(6-x-2y)(12.011) = (18-3x-6y)(12.011)$

Our CHN results gives us two equations within which there are two unknowns; x and y:

$0.0903 = m_H/m_{pre.}$
$= (42.3348 – 6.0476x – 14.112y)/(454.3753 – 42.0806x – 102.177y)$
$0.4565 = m_C/m_{pre.}$
$= (216.198 – 36.033x – 72.066y)/(454.3753 – 42.0806x – 102.177y)$

There is only one unique solution for this linear equation and that is:

$x = 0.389$
$y = 0.088$

The Chemat precursor has the formula $LiNb(OH)_{0.389}(O)_{0.088}(OPr^i)_{5.435}$

3.6) Calculation of Lattice d-spacing from Electron Diffraction Images

Measurements of the interplanar distances (d-spacings) of Nb_2O_5 and $LiNbO_3$ were obtained using a minimum of 15 defect-free lattice fringe spots using the ''*Measure Tool*'' in Adobe Photoshop Version 8.0. The Photoshop (PS) ''*units*'' were converted to nanometers using the TEM scale bar as a reference. The TEM scale bar was calibrated using the diffracting planes of a silver standard. For our calculations, the measurement error was estimated as half the width of the lattice fringe spots and the width of the frame surrounding the TEM scale bar.

e.g. In Nb_2O_5, 71 parallel planes were identified to have a perpendicular distance of separation equal to 770.3 ± 2.2 PS units. The 5 nm scale bar in the diffraction image is measured as 137.2 ± 2.2 PS units. The interplanar distance is calculated as:

$(770.3 / 70) \times (0.5 Å / 137.2) = 4.01 Å$ space between planes

$error = 4.01 \times [(2.2 / 770.3)^2 + (2.2 / 137.2)^2]^{0.5} = 0.07 Å$

By Braggs Law this d-spacing of 4.01 ± 0.07 Å can be represents in terms of a 2θ range for identification in the X-ray powder diffraction pattern:

$n\lambda = 2d\sin\theta$ (first order diffraction n = 1)
$2\theta = 2 \times [(180/\pi) \times \sin^{-1}(\lambda/2d)]$

A 2θ range was found to be 21.79 to 22.52, which corresponds roughly to the (001) plane of pseudohexagonal Nb_2O_5 occurring at a 22.69. The actual 2θ value is outside the calculated range so the error in our measurement must be greater than 2.2 PS units.